Few Layered Graphene and Its Composites as Anode Materials in Li-ion Batteries and EMI Shielding Materials

A thesis submitted by

Sandeep Kumar Marka

in the partial fulfillment of the requirement for the award of the degree of

Doctor of Philosophy

in

Nano Science and Technology

Under the supervision of

Dr.-Ing. V. V. S. S. Srikanth

School of Engineering Sciences and Technology
University of Hyderabad
Central University (P.O.)
Hyderabad 500046
India

July 2017

Declaration

I, **Sandeep Kumar Marka**, declare that this thesis work entitled "**Few Layered Graphene and Its Composites as Anode Materials in Li-ion Batteries and EMI Shielding Materials**", submitted in partial fulfillment of the requirement for the award of **Doctor of Philosophy** (in **Nano Science and Technology**) in the School of Engineering Sciences and Technology, University of Hyderabad is completely my own work except for those referenced. This work was done under the supervision of **Dr.-Ing. V. V. S. S. Srikanth**. This report is a record of the bonafide research work carried out by me and the results incorporated in it have not been reproduced/copied from any source. This work has not been submitted to any other University or Institution for the award of any other degree or equivalent.

Sandeep Kumar Marka
Reg. No.: 11ENPT09
School of Engineering Sciences and Technology
University of Hyderabad

Certificate

This is to certify that the thesis entitled Few Layered Graphene and Its Composites as Anode Materials in Li-ion Batteries and EMI Shielding Materials Submitted by Sandeep Kumar Marka bearing registration number 11ENPT09 (Int. M.Tech./Ph.D. (Nano Science and Technology)) in partial fulfillment of the requirements for award of Doctor of Philosophy in the School of Engineering Sciences and Technology is a bonafide work carried out by him/her under my supervision and guidance.

This thesis is free from plagiarism and has not been submitted previously in part or in full to this or any other University or Institution for award of any degree or diploma.

Parts of this thesis have been:

A. published in the following publications:

1. *RSC Advances 6, 55167-55175 (2016) (ISSN number: 2046-2069), Chapter 4*
2. *Electrochimica Acta 178, 699-708 (2015) (ISSN number: 0013-4686), Chapter 4*
3. *RSC Advances 5, 36498-36506 (2015) (ISSN number: 2046-2069), Chapter 4*
4. *Superlattices and Microstructures 83, 530-537 (2015) (ISSN number: 0749-6036), Chapter 4*
5. *Nanoscience & Nanotechnology-Asia 5, 90-108 (2015) (ISSN number: 2210-6812), Chapter 1*

and

B. presented in the following conferences:

1. *NMEA-2017* (National)
2. *TNT-2016* (International)
3. *AMRP-2015* (National)
4. *IUMRS-ICA 2013* (International)

Further, the student has passed the following courses towards fulfilment of coursework requirement for Ph.D.

Course Code	Name	Credits	Pass/Fail
AC801	Research Methodology	4	Pass

and was exempted from doing coursework (recommended by Doctoral Committee) on the basis of the following courses passed during his M.Tech. program (in Int. M.Tech./Ph.D. program) and the M.Tech. degree was awarded:

Course Code	Name	Credits	Pass/Fail
NT401	Thermodynamics and Phase Equilibria	4	Pass
NT402	Concepts of Materials Science	4	Pass
NT403	Characterization of Materials	4	Pass
NT404	Seminar	2	Pass
NT405	Advanced Engineering Mathematics	2	Pass
NT406	Materials Processing and Characterization Laboratory	4	Pass
NT407	Concepts of Nano Science and Technology	4	Pass
NT408	Synthesis and Applications of Nanomaterials	4	Pass
NT451	Nano Biotechnology	4	Pass
NT452	Mechanical Behavior of Nanomaterials	4	Pass
NT453	Modeling and Simulation	4	Pass
NT454	MEMS AND NEMS Nanofabrication Technologies	4	Pass
NT455	Surface Engineering	4	Pass
NT456	Polymer Science and Technology	2	Pass
NT457	Laboratory	4	Pass
NT458	Seminar	2	Pass
NT550	Dissertation	18	Pass

Supervisor **Dean of School**

Acknowledgements

I express with great pleasure my sincere gratitude to my thesis supervisor Dr.-Ing. V. V. S. S. Srikanth for his patience, constant encouragement, constructive criticism, guidance, and timely and cheerful co-operation throughout my PhD studies. Very special thanks to my doctoral review committee (DRC) members, Prof. M Ghanashyam Krishna and Dr. Koteswararao V. Rajulapati for their valuable suggestions during the DRC meetings. I would also like to take this opportunity to sincerely thank Prof. M. Ghanashyam Krishna for his advice which initiated my admission into this school. My sincere thanks to Prof. K. C. James Raju, School of Physics, University of Hyderabad for readily allowing me to carry out experiments in his laboratory on vector network analyzer. It is my honor to acknowledge Prof. B. V. R. Chowdari, Senior Executive Director, President's Office, Nanyang Technological University, Singapore (formerly Head, Advanced Battery Lab and Executive Director of NUS-India Research Initiatives, National University of Singapore) with heartfelt thanks for giving me the opportunity to work at NUS under SIPIS-2013 programme and collaboration. I also sincerely thank Dr. M. V. Reddy, Senior Research Fellow, Advanced Battery Lab, NUS Singapore for his supervision during SIPIS-2013. I would like to express my gratitude to Dean (present and previous), faculty members, office staff, and lab assistants of School of Engineering Sciences and Technology, University of Hyderabad for their constant support. I am also thankful to Dr. Ahamed, and Mr. Muvva D Prasad for helping me in carrying out Raman spectroscopy and transmission electron microscopy experiments, respectively. I feel great to acknowledge Dr. K. Mohan Kumar, Dr. P. Shaikshavali, Mr. J. Ramakrishna, Mr. K. V. Sreenivasulu, and Mr. N. Charanadhar for helping me at various stages of my PhD studies. This work and my education would not have been the way it is now without the moral support and love of family members, whom I sincerely acknowledge.

Sandeep Kumar Marka

List of Publications

Journal Publications

1. **Marka, S. K.**; Petnikota, S.; Srikanth, V. V. S. S.; Reddy, M. V.; Adams, S.; Chowdari, B. V. R., $Co_2Mo_3O_8$/reduced Graphene Oxide Composite: Synthesis, Characterization and its Role as Prospective Anode Material in Lithium Ion Batteries, RSC Advances, **2016**, 6, 55167-55175.
2. Petnikota, S.; Keefe, W. T.; Luo, C.; Amos, S.; **Marka, S. K.**; Reddy, M. V.; Srikanth, V. V. S. S.; Adams, S.; Chowdari, B. V. R., Exfoliated Graphene Oxide/MoO_2 Composites as Anode Materials in Li Ion Batteries: An Insight into Intercalation of Li and Conversion Mechanism of MoO_2, ACS Applied Materials & Interfaces, **2016**, 8, 10884-10896.
3. Petnikota, S.*; **Marka, S. K.***; Srikanth, V. V. S. S.; Reddy, M. V.; Chowdari, B. V. R., Elucidation of Few Layered Graphene-Complex Metal Oxide ($A_2Mo_3O_8$, A = Co, Mn and Zn) Composites as Robust Anode Materials in Li Ion Batteries, Electrochimica Acta, **2015**, 178, 699-708. (*equally contribute)
4. **Marka, S. K.**; Srikanth, V. V. S. S., Graphene and Graphene/Binary Transition Metal Oxide Composites as Anode Materials in Li-Ion Batteries, Nanoscience & Nanotechnology-Asia, **2015**, 5, 90-108. (Invited review)
5. **Marka, S. K.**; Sindam, B.; James Raju, K. C.; Srikanth, V. V. S. S., Flexible Few-Layered Graphene/Poly Vinyl Alcohol Composite Sheets: Synthesis, Characterization and EMI Shielding in X-band through the Absorption Mechanism, RSC Advances, **2015**, 5, 36498-36506.
6. **Marka, S. K.**; Mohiddon, Md. Ah.; Prasad M. D.; Srikanth, V. V. S. S., Growth of MgO on Multi-Layered Graphene and Mg in PVA Matrix, Superlattices and Microstructures, **2015**, 83, 530-537.
7. Petnikota, S.; **Marka, S. K.**; Banerjee, A.; Reddy, M. V.; Srikanth, V. V. S. S.; Chowdari, B. V. R., Graphenothermal Reduction Synthesis of 'Exfoliated Graphene Oxide/Iron (II) Oxide' Composite for Anode Application in Li Ion Batteries, Journal of Power Sources, **2015**, 293, 253-263.
8. Inguva, S.; **Marka, S. K.**; Vijayaraghavan, R. K.; McGlynn, E.; Srikanth, V. V. S. S.; Mosnier, J.-P., Crystalline ZnO/Amorphous ZnO Core/Shell Nanorods: Self-Organized Growth, Structure, and Novel Luminescence, The Journal of Physical Chemistry C, **2015**, 119, 4848-4855.

9. **Marka, S. K.**; Petnikota, S.; Srikanth, V. V. S. S.; Reddy, M. V.; Adams, S.; Chowdari, B. V. R., Germanium/reduced Graphene Oxide Composites: Synthesis, Characterization and their Electrochemical Properties (Manuscript to be submitted).
10. **Marka. S. K.**; Sindam, B.; James Raju, K. C.; Srikanth, V. V. S. S., Graphene-wrapped Magnesium Oxide/polyvinyl alcohol (G@MgO/PVA) Composites: Dielectric and EMI shielding properties in the x-band frequency range at elevated temperatures. (Manuscript to be submitted)

Conference Proceedings

1. Anil, T.*; **Marka, S. K.***; Srikanth, V. V. S. S.; James Raju, K. C., Dielectric properties of novel composites prepared with few layered graphene (FLG)-lithium triniobate ($LiNb_3O_8$), AIP Conference Proceedings, **2015**, 1675, 020043(-1)–020043(-3). (* equally contributed)
2. Petnikota, S.; **Marka, S. K.**; Reddy, M. V.; Srikanth, V. V. S. S.; Chowdari, B. V. R., Synthesis of EG-Ge Composite by Novel Graphenothermal Reduction and its Anodic Studies for Lithium Ion Batteries, Proceedings of the 14th Asian Conference on Solid State Ionics (ACSSI 2014) **2014**, 279-288.
3. Petnikota, S.; Teo, K. W.; Chen, L.; Reddy, M. V.; **Marka**, **S. K.**; Srikanth, V. V. S. S.; Chowdari, B. V. R., Electrochemical Studies of 'Exfoliated Graphene Oxide-MoO_2' Composite Synthesized by Novel Graphenothermal Reduction, Proceedings of the 14th Asian Conference on Solid State Ionics (ACSSI 2014) **2014**, 259-269.

Table of Contents

Abstract i

Chapter 1 Introduction 1

1.1 General Background 1

1.2 Graphene-Based Anode Materials in Li-ion Batteries 1

1.3 EMI Shielding 5

1.3.1 General background 5

1.3.2 EM wave propagation in a medium-Basic EM wave equations 7

1.3.3 Materials for EMI shielding: Development of graphene-based polymer composites 8

1.4 Problem Definition 12

1.5 Objectives of the Thesis 13

1.6 Overview of the Thesis 14

Chapter 2 Literature Review 15

2.1 Electrochemical Energy Storage Performance of Graphene Nanosheets (GNS) 15

2.2 Germanium/Graphene Composites as Anode Materials in LIBs 19

2.3 Molybdenum Based Oxysalts/Graphene Composites as Anode Materials in LIBs 26

2.3.1 $MMoO_4$ (i.e., M = Fe, Co, Ni, Ca, Mn, Zn, and Cu) 27

2.3.2 Mo-cluster oxysalts (i.e., $A_2Mo_3O_8$ type, A=Fe, Co, Mn, and Zn or $LiHoMo_3O_8$) 30

2.4 EMI shielding properties of graphene/polymer composites 31

2.4.1 Epoxy composites 32

2.4.2 PVA composites 32

2.4.3 PMMA composites 33

2.4.4 PVDF composites 35

2.4.5 PS composites 35

2.4.6 PANi composites 36

2.4.7 PEI composites 37

Chapter 3 Experimental Work 45

3.1 Materials Synthesis 45

3.1.1 Few layered graphene (FLG) 45

3.1.2 Graphene-wrapped MgO (G@MgO) composite 46

3.1.3 $Co_2Mo_3O_8$/rGO composite 46

3.1.4 Ge/rGO composite 46

3.1.5 FLG/PVA composite 47
3.1.6 Graphene-wrapped MgO/PVA composite 48
3.2 Characterization of Materials 49
3.2.1 Scanning electron microscopy 49
3.2.2 Transmission electron microscopy 49
3.2.3 X-ray diffraction 50
3.2.4 Raman spectroscopy 50
3.2.5 BET surface area measurements 51
3.2.6 X-ray photoelectron spectroscopy 51
3.2.7 Thermogravimetric analysis 51
3.2.8 UV-VIS-NIR spectroscopy 51
3.3 Li-ion Battery Fabrication and Testing 52
3.3.1 Coin cell fabrication 52
3.3.2 Galvanostatic cycling 52
3.3.3 Cyclic Voltammetry (CV) 53
3.3.4 Electrochemical impedance spectroscopy 53
3.4 AC Conductivity Measurements 54
3.5 Testing EMI Shielding 54
Chapter 4 Results and Discussion 56
4.1 Novel Anode Materials in Li-ion Batteries 56
4.1.1 $Co_2Mo_3O_8$/rGO composite 56
4.1.2 Ge/rGO composite 67
4.2 Novel EMI Shielding Materials 78
4.2.1 Flexible FLG/PVA composite sheets 78
4.2.2 Graphene wrapped MgO/PVA (G@MgO/PVA) composite 88
Chapter 5 Conclusions and Future Aspects 114
5.1 Conclusions 114
5.2 Future Aspects 117
References 118
Annexures 130
Annexure 1 130
Annexure 2 138

Abstract

In this thesis, few layered graphene (FLG) and its composites are synthesized using easy and novel synthesis routes. The synthesized composites are tested as anode materials in Li ion batteries and as materials for electromagnetic interference (EMI) shielding. Two novel graphene based composites namely $Co_2Mo_3O_8$/reduced graphene oxide ($Co_2Mo_3O_8$/rGO) and Germanium/reduced graphene oxide (Ge/rGO) composites are synthesized and tested as anode materials in Li ion batteries while two other novel composites namely few layered graphene (FLG)/poly vinyl alcohol (PVA) and graphene wrapped magnesium oxide (G@MgO)/PVA composites are synthesized and tested as EMI shielding materials. $Co_2Mo_3O_8$/rGO composite is constituted with hierarchical and submicron sized $Co_2Mo_3O_8$ hexagonal nanoplatelets (50 nm thick) entrenched in between thin graphene layers. When cycled in the voltage range of 0.005-3.0 V at a current density of 60 mA/g, $Co_2Mo_3O_8$/rGO composite delivered an excellent reversible specific capacity of ~954 mA h/g that corresponds to 82% capacity retention at the end of the 60th cycle which is higher than the theoretical capacity of both $Co_2Mo_3O_8$ and graphene. $Co_2Mo_3O_8$/rGO composite also showed excellent rate capability. Electrochemical conversion and electrochemical adsorption and desorption are found to be the primary reasons for Li storage in $Co_2Mo_3O_8$/rGO composite. Excellent synergy between $Co_2Mo_3O_8$ and rGO in the composite is attributed for the observed high specific capacity, long cycle life and good rate capability. When Ge/rGO composite was cycled in the voltage range of 0.005-3.0 V at a current density of 160 mA/g, it showed an excellent reversible capacity of ~539 mA h/g that corresponds to 98% capacity retention at the end of the 100th cycle. Ge/rGO composite also showed high reversible capacity retention, good rate capability, and excellent cycle life. Alloying, de-alloying and electrochemical adsorption and desorption type reaction mechanism are the primary reasons for lithium storage in germanium and graphene, respectively. In the case of EMI shielding materials, 1 mm thick FLG/PVA composite sheets containing 0.2 and 0.6 wt.% of FLG as filler are prepared using a simple casting process. A maximum electromagnetic interference (EMI) shielding effectiveness (SE) of ~19.5 dB (in the X-band, 8.2–12.4 GHz) was obtained in case of the FLG/PVA composite with 0.6 wt.% of FLG. Absorption is found to be the dominant mechanism for EMI shielding. The high EMI SE is attributed to the network-like features formed by FLG in PVA matrix. In another work, temperature (30-120 °C) dependent complex permittivity of 1 mm thick G@MgO/PVA_Coag (0.4, 0.6, 0.8, 1.0, 3.0, 10.0, and 15.0wt.%) and G@MgO/PVA_ac (0.4, and 3.0wt.% as-casted) composite samples in low frequency (20 Hz - 2 MHz), and high frequency (i.e., 8.2-12.4 GHz)

ranges are measured. In both the frequency ranges, G@MgO/PVA_Coag composites performed superior dielectric properties than PVA, and G@MgO/PVA_ac composites. A strong interfacial polarization (from M" vs. log (f) plots) is observed in coagulated, and as-casted G@MgO/PVA composites. It is noticed from the calculated activation energies that conduction is the dominating mechanism for energy transfer in both the composites, however, it is predominant in G@MgO/PVA_Coag composites than in G@MgO/PVA_ac composites. In the X-band, EMI SE of the G@MgO/PVA_Coag composites is greater than that of the G@MgO/PVA_ac composites at a particular weight fraction of G@MgO. At 30 and 120 °C, the average EMI SE values of ~14.2 and ~18.9 dB, respectively, are measured for 10.0 G@MgO/PVA_Coag while 15.0G@MgO/PVA_Coag composite showed EMI SE of ~20.6 and ~27.5 dB, respectively. In the case of G@MgO/PVA_Coag and G@MgO/PVA_ac composites too absorption is found to be the dominating mechanism for EMI SE.

Chapter 1 Introduction

1.1 General Background

Among the wide range of applications of the graphene and its composites, energy storage [1] and electromagnetic interference (EMI) shielding [2] applications have gained a great prominence in the recent past. For example, graphene based composites such as graphene-metal [3], graphene-metal oxide [1], and graphene-oxysalt [4] composites etc., are considered as promising anode materials in Li-ion battery (LIB). In the composite, graphene is expected to provide not only the chemical functionality but also the compatibility for the formation of particular composition during the composite synthesis. It is expected that such a composite will suppress (owing to the expected synergy between the components) the agglomeration of materials, volume change of these materials and restacking of graphene layers during cycling. Other characteristics that are expected in such composites are highly conducting networks, a high specific surface area which helps to obtain high specific capacity and excellent rate capability, improved cycling stability and required energy/power density. On the other hand, graphene based composites constituted by conducting, dielectric, and magnetic constituents are considered as excellent EMI shielding materials. Similarly, graphene filled polymer composites are touted as excellent (light weight and flexible) EMI shielding materials. In this thesis work, two novel graphene based composites namely $Co_2Mo_3O_8$/reduced graphene oxide (rGO) and Ge/rGO composites are synthesized and tested as anode materials in LIBs and another two novel graphene based composites namely few layered graphene (FLG)/poly vinyl alcohol (PVA) and graphene wrapped magnesium oxide (G@MgO)/PVA composites are synthesized and tested as EMI shielding materials.

1.2 Graphene-Based Anode Materials in Li-ion Batteries

In the last decade, use of portable electronic devices such as mobile phones, laptops, iPods, etc., have enormously increased. As a consequence, substantial interest is generated in developing compact, light-weight, efficient and more importantly environmental friendly batteries that give the required electric power such that the above mentioned electronic devices work efficiently. In this context, LIBs have emerged as the most preferrable batteries in comparison to other rechargeable batteries such as Pb acid, Ni-Cd and Ni-metal hydride batteries [5]. Amongst the rechargeable batteries, LIBs offer the highest specific energy. Apart from powering portable electronic devices, LIBs can also power electric vehicles (EV), plug-in hybrid electric vehicles (PHEV) and hybrid electric vehicles (HEV) [6-8].

In the 1990s, Sony Co., Japan first developed the commercial LIBs in which lithium cobalt oxide ($LiCoO_2$) and graphite (C) were used as the cathode and anode materials, respectively, while a non-aqueous compound, lithium hexafluorophosphate ($LiPF_6$) was used as the electrolyte. In a LIB, which can be considered as a typical electrochemical cell, Li^+ cycling between anode and cathode takes place through intercalation and de-intercalation reactions (Eq. 1.1 to 1.3).

$$\text{At cathode: } Li_{1-x}CoO_2 + xLi^+ + xe^- \rightarrow LiCoO_2 \qquad (1.1)$$

$$\text{At anode: } Li_xC_6 \rightarrow xLi^+ + xe^- + C_6 \qquad (1.2)$$

$$\text{Overall: } Li_{1-x}CoO_2 + Li_xC_6 \rightarrow LiCoO_2 + C_6 \qquad (1.3)$$

In an electrochemical cell, reaction continues to takes place as long as the change in Gibbs free energy is negative as given in Eq. 1.4.

$$\Delta G = -nFE^o \qquad (1.4)$$

where F is Faraday constant (i.e., 96,496 Coulombs per mole), n is number of electrons that participate in the chemical reaction, and E° is the cell's standard potential. The total potential of the cell E^o_{Cell} is the potential difference of the cathode potential (E^o_{pos}) and the anode potential (E^0_{neg}) as given in Eq. 1.5.

$$E^0_{Cell} = E^0_{pos} - E^0_{neg} \qquad (1.5)$$

The cell's potential is measured by the actual potential difference between the cathode and the anode and it is correlated to the standard potential by Nernst equation given in Eq. 1.6.

$$\Delta E = \Delta E^0 - \frac{RT}{nF} \ln \frac{a_i(A)}{a_i(C)} \qquad (1.6)$$

where R is gas constant, T is the absolute temperature, and a_i (C) and a_i (A) are the activities of the cathode and anode materials, respectively. The theoretical specific capacity (C_{th}) (Eq. 1.7) provides the necessary information to develop and/or to choose new electrode materials.

$$C_{th} = \frac{N \text{ x } F \text{ x } 1000}{3600 \text{ x } M} \qquad (1.7)$$

In Eq. 1.7, F is Faraday constant (obtained by multiplying electron charge (1.6 x 10^{-19} C) and

Avogadro's number (6.02 x 10^{23}/mol)), N is number of moles of Li^+ ions or electrons that participate in the electrochemical reaction per mole of the electrode material, and M is the molar mass of the compound in g/mol. For example, theoretical capacity of the $Co_2Mo_3O_8$ is (16 x 96500 x 1000/(3600 x 471.76)) = 909.12 mA h/g as 16 moles of Li^+ ions participate in the lithium storage per a mole of $Co_2Mo_3O_8$. The excellent Li cycling reversibility of an electrode is often related to the high capacity retention at end of a large number of cycles and is usually represented as a plot of specific capacity versus cycle number. The current rate to test the battery is often selected depending on the theoretical capacity. For example, a current of 0.1 C for $Co_2Mo_3O_8$ implies a theoretical capacity of 90.9 mA/g which means that the current density applied is equivalent to 10 h of discharge or charge time.

For a long time, graphite has been used as an ideal commercial anode material in LIBs. However, graphite has a low theoretical capacity (~372 mA h/g) and encounters problems like Li plating and large volume expansion during cycling and therefore it has limited usage in LIBs intended for high energy capacity applications such as powering electric vehicles. Therefore, over many years' different anode materials, which work on different mechanisms were developed. The mechanisms are: (i) Intercalation-deintercalation based mechanism: Oxides of transitional metals and related compounds with 2D layered structure or 3D network structure that can reversibly intercalate Li into their lattice, similar to graphite, with crystal structure conservation have been explored. In this category, for example, Titanium (Ti) based oxides were well studied; (ii) alloying and dealloying reaction based mechanism: Alloys (intermetallic compounds) are formed by elements (A) or metals (M) with Li metal. For example elements like Si [9, 10], Ge [11], and Sb [12,13] and metals like Sn [14,15], Zn [12], In [12], Bi [12], and Cd [12] have been explored extensively as potential anode materials that follow alloying and dealloying reaction based mechanism. The reversible Li cycling takes place in these materials through Li alloying-dealloying reactions at low potentials (≤ 1.0 V vs. Li, For example, $\mathrm{Ge\,(or\,Si)} + 4.4\mathrm{Li} \leftrightarrow \mathrm{Li_{4.4}Ge\,(or\,Si)}$); (iii) Of late, nanosized transition metal oxides (TMO) [16] and other materials [17-19] which work on "conversion reaction" mechanism were introduced as prospective anode materials in LIBs. In this mechanism reversible Li cycling takes place via decomposition of electrochemically inactive lithium oxide (Li_2O), in the presence of nanosized transition metal particles, as shown by the following reaction: $\mathrm{nano-CoO} + 2\mathrm{Li} \leftrightarrow \mathrm{nano-Co} + \mathrm{Li_2O}$. Conversion reaction is applicable to large number of metallic compounds such as metal oxides, fluorides, oxyfluorides, sulfides, nitrides, phosphides, etc., which include binary, ternary complex metal oxides and oxysalts.

The desirable characteristics of an anode material in LIBs are: (i) it must be a low density material that can accommodate more number of Li ions in its crystal structure, and are reversible on demand, to yield large, stable, and reversible gravimetric (mA h/g) and volumetric (mA h/cm^3) capacities, (ii) its potential must be not far off that of Li metal and even with changes in the Li content in its active material, (iii) it must be chemically stable in the presence of electrolyte, (iv) it must hold good electronic and ionic conductivities which reduces electrode impedance during cycling within the anode material and (v) it should be available at low price, it should be industrially viable and most importantly environmentally benign. Graphite possesses most of these characteristics and therefore it has been a commercial anode material in LIBs, however, for mostly low energy capacity applications. Worldwide, efforts are being put to commercially introduce new anode materials that support high energy applications. Some of such anode materials with their characteristics are tabulated in **Table 1.1**.

Novel materials (such as those tabulated in **Table 1.1**) which work on the above mentioned Li-ion mechanisms were proposed as alternative anode materials in LIBs due to their better Li^+ storage capacities (theoretical as well as experimental capacities), no Li-dendrite growth, no current rate restrictions, very low irreversible capacity loss (ICL), and greater positive intercalation voltage in comparison to Li/Li^+ [8]. However, drawbacks such as poor electrical conductivity (except metals), significant volume changes and severe agglomeration pertaining to these materials have hindered their commercial viability as anode materials in LIBs. On the other hand, of late, graphene has emerged as an excellent alternative anode material (instead of graphite) in LIBs due to its superior specific surface area (calculated value, 2,630 $m^2\ g^{-1}$) [20], superior electrical conductivity i.e., mobility of charge carriers (200,000 $cm^2V^{-1}s^{-1}$) [21], excellent mechanical strength (Young's modulus (~1,100 GPa) [22], fracture strength (125 GPa) [22], and thermal conductivity (~5,000 $Wm^{-1}K^{-1}$) [23], high chemical inertness towards Li-ions, high theoretical capacities in the range of 744 to 1116 mA h/g, and in-situ electrochemical exfoliation over long-term cycling. However, disadvantages associated with graphene are high reducing nature towards electrolyte molecules, high ICL, high voltage hysteresis, poor cycling performance, chances to form Li-dendrite at high current rates, and low volumetric capacity. To overcome these drawbacks, composites constituted by graphene and metal oxides (or metals or metal oxysalts) are proposed The advantages of such composites have already been described in section 1.1.

1.3 EMI Shielding

1.3.1 General background

Electromagnetic interference (EMI) is an undesirable disturbance that affects an electrical circuit through electromagnetic induction from an external source. EMI shielding is the practice of reducing the electromagnetic field induction in space by blocking the field with a barrier made of suitable materials (typically conductive or magnetic materials). The shielding efficiency (SE) is generally measured in terms of reduction in the magnitude of the incident field upon transition across the barrier material. Three different mechanisms (as shown in **Fig. 1.1**) namely SE due to reflection (SE_R), absorption (SE_A) and multiple internal reflections (SE_M) contribute to the overall reduction of the incident electromagnetic wave. Mathematically shielding effectiveness (SE) can be articulated in logarithmic scales as the ratio of transmitted to the incident electric or magnetic powers [24] (Eq. 1.8). In general, SE (Eq. 1.8) is measured in decibels (dB) units.

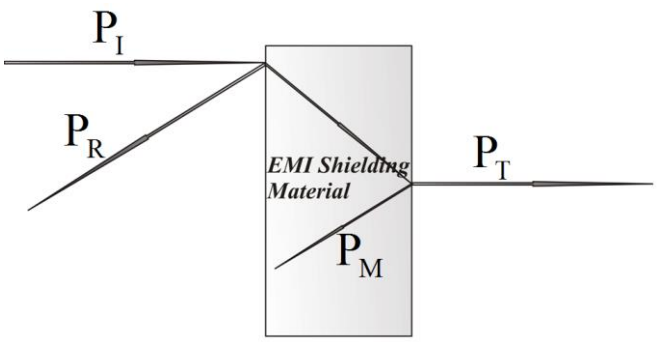

Figure 1.1 Schematic representation of EMI shielding.

$$SE(dB) = SE_R + SE_A + SE_M = -10\log_{10}\left(\frac{P_T}{P_I}\right) = -20\log_{10}\left(\frac{E_T}{E_I}\right) = -20\log_{10}\left(\frac{H_T}{H_I}\right) \quad (1.8)$$

where P_I (E_I or H_I) and P_T (E_T or H_T) are the powers (electric or magnetic field intensity) of the incident and transmitted EM waves, respectively.

Table 1.1 Modern anode materials in Li-ion batteries.

Anode Material	Company	Capacity	Nominal Voltage	Specific Energy	Cycle life	Application
Tin based amorphous materials [25]	Sony-Japan	900 mAh	4.2-2.5/V	158 Wh/kg	-	Handycam Camcorders
$Li_4Ti_5O_{12}$ [26]	Toshiba-SCiB™ 2P12S	40 Ah	27.6 V (18-32.4 V)	79 Wh/kg	10000	HEV, PHEV, EV busses and trams, Grid energy storage, Off-Grid/Micro-Grid storage, and uninterruptible power systems
	Toshiba-SCiB™ 20 Ah Cell	20 Ah (0.2 C)	2.3 V (1.5-2.7 V)	177 Wh/L	10000	
Si-C [27]	Envia	40 Ah	3.74	215 Wh/kg	>1000	EV
		27 Ah	3.74	184 Wh/kg	5000	PHEV
Si@SiO_2 core@shell [28]	Ampirus	1566 Ah/kg	-	-	6000	Laptops, EV, and Grid-scale storage

In recent years, for faster data processing, electronic systems are employed with high operating frequencies and bandwidth especially in X-band and broadband frequencies. Due to the extensive expansion of electronics industry, EMI shielding has become essential in many applications related to telecommunication systems, aerospace, automobiles, medical, computer, aircraft, etc [29]. In addition to this, there are serious health concerns for human beings resulting from the exposure to electromagnetic waves [30]. Nowadays, EMI is considered as one form of pollution. In view of the above, research related to EMI shielding assumes a paramount position.

1.3.2 EM wave propagation in a medium-Basic EM wave equations

Whenever an EM wave is normally incident on a different medium in space, two underlying mechanisms namely Reflection (R) and Transmission (T) are expressed by following Eq. (1.9-1.10)

$$R = \frac{\eta_2 - \eta_1}{\eta_2 + \eta_1} \qquad (1.9)$$

$$T = \frac{2\eta_2}{\eta_2 + \eta_1} \qquad (1.10)$$

where, R-Reflection coefficient, T-Transmission coefficient and η_i-complex impedance of ith medium and it given as Eq. (1.11),

$$\eta = \sqrt{j\omega\mu / \sigma + j\omega\varepsilon} \qquad (1.11)$$

where, η-complex impedance of the medium, ω–the angular velocity of the wave, μ-magnetic permeability of the material, σ-electrical conductivity of the material, and ε-permittivity of the material.

Another important parameter called skin depth explains the mechanism of microwave absorption within a material. It is conductivity and permeability dominated. Skin depth can be physically described as the Ohmic and hysteresis loss suffered by the microwave through leakages while being transmitted through the material thickness, respectively. Skin depth (δ-depth of penetration or skin depth of the material i.e., the thickness at which incident wave intensity reduces to 1/e=0.368 of original) is given by Eq. (1.12),

$$\delta = 1 \Big/ \sqrt{\pi f \mu \sigma} \qquad (1.12)$$

where, f-frequency of the incident microwave.

Penetration depth can be further explained in a better way by the propagation constant (γ) given by Eq. (1.13)

$$\gamma = \alpha + i\beta \qquad (1.13)$$

where α-attenuation constant, and β-phase constant.

Now, the attenuation and phase constants are defined as shown in Eq. (1.14-1.15),

$$\alpha = \lambda_m \omega^2 (\varepsilon' \mu'') + \frac{\varepsilon'' \mu'}{4\pi} \qquad (1.14)$$

$$\beta = 2\pi \Big/ \lambda_m \qquad (1.15)$$

where, λ_m-wavelength of the microwave in the material, ε' and ε'' are real and imaginary part of the complex permittivity of the material, respectively, and μ' and μ'' are real and imaginary part of complex permeability of the material, respectively.

The absorption index (k) of a material is then defined as shown in Eq. (1.16)

$$k = \alpha \Big/ \beta \qquad (1.16)$$

It is clearly observed from the above equation that for a given incident radiation, the change of absorption capability of the material depends on both real and imaginary parts of the dielectric permittivity and magnetic permeability.

1.3.3 Materials for EMI shielding: Development of graphene-based polymer composites

Metals are excellent conductors of electricity and heat. They can absorb, reflect and transmit electromagnetic fields. But metals are heavy; undergo corrosion when exposed to harsh environments and most importantly their production involves difficult processing steps. Especially due to their high weight, metals are not suitable for aerospace applications. The best way to mitigate limitations of metals is to use polymers/plastics. But plastics are insulating in nature and are therefore not suitable for EMI shielding applications. However, in the available literature three approaches namely applying conductive coatings on plastics, compounding

with conductive filler materials, preparing intrinsically conductive polymers (ICPs) have been majorly followed to tune the electrical conductivity of polymers/plastics such that they are suitable for EMI shielding applications.

Ion plating, zinc flame spraying, zinc arc spraying, conductive paints, cathode sputtering, electroplating, vacuum metallization and electroless plating [31-34] are the different methods that have been established for metallizing plastic surfaces for EMI shielding applications. **Table 1.2** shows conductive coatings on plastics and glassy materials exhibited good EMI SE. The main drawbacks of these coatings have been their poor wear and scratch resistances.

Conventional plastic materials are electrical insulators having resistance in the range of 10^{15} – 10^{18} Ω cm. However, they are mechanically stable. The conductivity of conventional polymers like epoxy or polyester can be varied by incorporating conducting filler materials like carbon black [35] into their matrices. It was reported that conductive carbon black and short carbon fiber filled natural rubber (C-SCF-NR) and ethylene vinyl acetate (C-SCF-EVA) composites exhibited excellent EMI shielding characteristics [36]. C-SCF-EVA composites exhibited EMI shielding characteristics for X-band frequency range (8-12 GHz) and have been found technically viable (SE ≥ 20 dB) in X-band region. It was also reported that laminated epoxy carbon fiber composites [37] exhibited conductivity and electromagnetic losses (as a function of frequency and specimen spacing). The study revealed that optimum SE of the laminated epoxy composite of ~62 dB occurs at about 30 mm specimen spacing and at frequency ~ 9 GHz. Exceptionally high EMI shielding effect 130 dB at 1-2 GHz of flexible graphite was also reported [38]. Stainless steel, aluminum, copper, brass and nickel coated graphite fibers are also used as filler materials in conventional polymers which showed EMI SE in the range of 36-45 dB at different frequency regimes and some of them were commercialized [39-42]. Thus conductivity of non-conducting plastics was modified by adding some conducting filler materials. Even though good results were obtained there are certain limitations such as high material costs, problems with materials' processing, poor surface finish, less satisfactory performance levels and most importantly non-uniform conductivity of the composites.

Recently, grapheme based polymer composites have attracted considerable attention due to their exceptional electrical, thermal, and mechanical properties and as a consequence their potential in a variety of commercial applications from the high strength, light weight structural units to conductive components in the majority of fields. To obtain desired properties, homogenous dispersion of graphene nanofillers in the polymer matrices is mandatory. Unlike

CNTs, graphene-related materials have flat surfaces which are useful to avoid entangled bundles. But restacking of graphene layers is a major challenge in fabricating graphene/polymer composites, which directly influences the functional properties of these composite materials. In general graphene/polymer composites are prepared by three major processes namely solution mixing, *in situ* polymerization, and melt processing processes.

Solution mixing is the most widely used mixing process to prepare graphene/polymer nanocomposites. This process involves mixing of graphene and polymer in aqueous or organic solvents under continuous stirring or sonication and later removing the solvent via evaporation or precipitation/coagulation. GO is in-situ reduced to get conductive rGO. The hydrophilic GO is easily dispersed in water soluble polymers such polyvinyl alcohol (PVA), polyethylene glycol (PEG), and conjugated polymers to form nanocomposites [43-46]. On the other hand, low solubility of GO and rGO in the organic solvents pose a great challenge for mixing with hydrophobic polymers. The penetration of organic aprotic solvents, such as N, N-dimethylformamide (DMF), dimethyl sulfoxide (DMSO), and tetrahydrofuran into the interlayer spaces of GO is a highly tedious job, which prevents its exfoliation. Therefore, surface modification of GOs with functional molecules is the way to disperse GO in organic solvents and it leads to enhanced interaction with the polymer matrix. Surface functionalization of GO can be done with covalent functionalization or non-covalent functionalization. In covalent functionalization, GOs are reacted with organic isocyanates or long alkyl molecules such that covalent linkage can be established with polymer matrix of the resultant nanocomposite. For example, the reaction of GO with organic isocyanates causes derivatization of carboxyl and hydroxyl functional groups into amides and carbamate esters, respectively. Thus isocyanate-modified GO can be readily dispersed in DMF and mixed with polystyrene (PS) to form a solution mixture. By reducing the GO component with dimethyl hydrazine, a graphene/PS composite is precipitated out by adding methanol to the DMF solution [47,48]. On the other hand, noncovalent functionalization primarily involves hydrophobic, van der Waals, and electrostatic interactions that require physical adsorption of suitable molecules on the graphene surface. It is typically achieved by polymer wrapping, adsorption of surfactants or small aromatic molecules [49,50]. For example, GO sheets can be functionalized noncovalently using pyrene and polythiophene moieties through the π-π interactions [51-53]. The pyrene derivative has a strong affinity for reacting with the basal plane of graphene to form a stable π-stacking bond. The graphene/polymer nanocomposites prepared with solution mixing are polystyrene (PS) [48], poly(methyl methacrylate) (PMMA) [54,55],

poly(vinylidene fluoride) (PVDF) [56,57], polypropylene (PP) [58], polyethylene [59,60], polyurethane (PU) [61,62], etc.

In-situ polymerization is an effective way to homogeneously disperse graphene in the polymer matrix. In this process, initially, graphene nanofillers are mixed in a monomer, sometimes in presence of a solvent. Then, polymerization is initiated by heating with a suitable initiator. Recently, ε-caprolactam monomer, 6-aminocaproic acid initiator and GO was used as initial reagents and later GO was reduced during in situ polymerization process to prepare rGO/PA6 nanocomposites via in situ polymerization [63]. In another work, graphene/poly (vinyl acetate) nanocomposite was prepared using GO, n-octanol, vinyl acetate monomer and azo bis (isobutyronitrile) (AIBN). In this work, at first n-octanol-GO compound was prepared, later vinyl acetate monomer was dispersed into the interlayer of the modified GO, followed by thermal polymerization of the monomer in the presence of AIBN initiator. Several other graphene-polymer composite systems wherein polymers such as polycaprolactone (PCL) [64], PU [62], PMMA [65], PS [66], PP [67], polyimides [68, 69], and polybutylene terephthalate (PBT) [70] are used as the matrix materials.

Melt mixing is commercially attractive for large-scale production with thermoplastic polymers using conventional mixing facilities such as a twin-screw extruder, internal mixer and/or injection molder [71-77]. In this process, polymers are melted above their melting point and fillers are dispersed in the melt using high shear rates. This process is suitable for thermoplastic polymers which are not soluble in the organic solvents. The properties of the prepared nanocomposite are altered by optimizing screw rotation speed, mixing temperature and time. The shortcoming of this technique is it requires higher amounts of filler materials. Compared with solution mixing and in-situ polymerization methods, melt compounding is less effective in dispersing graphene nanofillers in the polymer matrices. High shear forces used during the melt compounding can damage the graphene layers, resulting in poorer mechanical and physical properties of the final nanocomposite. Several polymer nanocomposites with graphene as filler and polymers namely linear low density PE [60], PU [62], PVDF [78], polyethylene terephthalate (PET) [79], and polycarbonate [80] as matrices were prepared using this technique.

ICPs are best candidates for EMI shielding applications. Owing to their good electrical conductivities and ease of preparation, ICPs also aid in overcoming limitations imposed by applying conductive coatings on plastics and compounding with conductive filler materials.

The idea of ICPs was initiated by iodine exposed polyacetylene film, which attained metallic conductivity [81]. Among the conducting polymers, polyaniline (PANI) and polypyrrole (PPY) were extensively studied for EMI shielding applications. The main drawbacks of these conducting polymers are i) difficulty in processing them into different shapes and ii) poor mechanical properties [82]. PANI coated fabrics (E-glass fabric) were prepared using p-toluene sulfonic acid (PTSA) or camphor-10-sulfonic acid (CSA) and 4-chloro-3-methyl phenol (CMC) as a primary and secondary dopant, respectively. These fabrics exhibited EMI SE of ~54 dB at 1000 MHz [83]. PANI-Ag and PANI-graphite composites [84] and PANI coated nickel carbon black composite were composited with co-poly (ethylene-propylene) as the host material [85] and also found as suitable EMI shielding composites. EMI SE of Ag-PPY-AQSA-AgPd-PE-Ag composites layers on the fabric was found to be ~80 dB and was found to be useful in military applications [86]. It was also reported that the far-field EMI SE of PPY impregnated microporous polyethylene tapes was ~40-50 dB [87]. All the above-discussed materials are tabulated in **Table 1.2**.

Table 1.2. Comparison of EMI SE of different materials.

Reference	Type of the method	Frequency range (GHz)	EMI SE (dB)
M. Stefecka et al. [32]	Coatings	0.05-1.5	85-78
H. Liu et al. [33]		0.01-1.5	> 60
T. Yamada et al. [34]		1.7-2.6	47.4 at 2.54 GHz
N. C. Das et al. [35]	Compounding with Conductive Filler	8-12 & 0.1-2	≥ 20
Y. Ramadin et al. [37]		9	~ 62
X. C. Luo et al. [38]		1-2	130
S. Geetha et al. [83]	ICP	0.0001–1	54 at1000 MHz
C.Y. Lee et al. [84]		0.01 – 1	~27 PANI/graphite ~46 PANI/Silver
P. Kathirgamanathan [85]		0.00001-0.1	>20
Hong et al. [86]		0.05 – 1.5	~ 80
P. Kathirgamanathan [87]		0.00001-1	40-50

A thorough literature review of the materials relevant to this thesis work are elaborately discussed in **Chapter 2** of this thesis work.

1.4 Problem Definition

Graphene based composite materials (useful as anode materials in LIB) are normally synthesized by using wet-chemical procedures that involve time consuming multi-steps and use of hazardous chemicals, and that yield low quantities of the end product. In view of this

there is great need to use a method which is a solid state method while the quantity of the end product is high. In this thesis one such method namely graphenothermal reduction method was used to synthesize $Co_2Mo_3O_8$-rGO and Ge-rGO composites. This method uses carbons of exfoliating graphite oxide (GO) to reduce metal precursors to metal oxides and metals. Simultaneous exfoliation of GO to rGO and reduction of metal precursors results in the in-situ formation of a composite. Similarly, in the case of graphene/polymer composites for EMI shielding application, non-covalent modification which strongly protects the conjugated structure of graphene is developed as an easy method to synthesize FLG/PVA and G@MgO/PVA composites. Ultra-sonication was effectively used to disperse FLG and G@MgO powders in ethanol and later carefully mixed with PVA solution. Then the composite solutions were separately cast into a mould and coagulated in ethanol to obtain FLG/PVA and G@MgO/PVA composites, respectively. $Co_2Mo_3O_8$-rGO and Ge-rGO composites were prepared with the intention of using them as anode materials in LIB while FLG/PVA and G@MgO/PVA composites were prepared with the intention of using them as EMI shielding materials. Therefore, appropriate tests were carried out to known the capability of the synthesized graphene based composites in the respective applications.

1.5 Objectives of the Thesis

Keeping in view the problem definition, the objectives of this thesis work have been decided. The first objective of this thesis is to develop easy and single-step synthesis routes to obtain $Co_2Mo_3O_8$/rGO, Ge/rGO, FLG/PVA, and G@MgO/PVA composite materials. For this purpose, Graphenothermal reduction method is developed to synthesize $Co_2Mo_3O_8$/rGO, Ge/rGO composites and microwave irradiation of GO and combustion of Mg in presence of solid CO_2 (dry ice) to obtain FLG and G@MgO materials, respectively. Simple solution mixing process is adopted to synthesize FLG/PVA and G@MgO/PVA composites.

The second objective of this thesis is to characterize the synthesized materials using a multitude of complementary characterization techniques to confirm the formation of the anticipated composites.

The third objective of this thesis work is to test the potential applications of $Co_2Mo_3O_8$/rGO and Ge/rGO composites as anode materials in electrochemical Li-ion storage and FLG/PVA and G@MgO/PVA composites as EMI shielding materials at room temperature and elevated temperatures, respectively.

1.6 Overview of the Thesis

Chapter 1 discusses about the introduction of Li-ion batteries and EMI shielding. Existing materials and the need of graphene based composites to overcome limitations posed by conventional materials are also presented in **Chapter 1**. In **Chapter 2** literature survey of graphene-based composite materials and their applications as anode materials in Li-ion batteries and EMI shielding materials is presented. **Chapter 3** discusses the detailed experimental work carried out in this thesis work. The experimental work consists of synthesis of materials, general characterization and testing of the materials in concerned applications. **Chapter 4** covers results and discussions of the present thesis work. **Chapter 5** presents conclusions of the thesis work. Chapter 5 also presents immediate future scope of research in relation to this work. All the references that have been cited in the thesis have been arranged and numbered in the order they appear in the main text under the heading '**References**' at the end of the thesis. Certain data that have not been used in the main text of the thesis are included under the heading '**Annexures**'. For clarity purposes, certain words in the text and figures (throughout the thesis) are typed in **bold**. **Equations, Figures** and **Tables** are numbered according to the order they appear in a particular chapter.

Chapter 2 Literature Review

2.1 Electrochemical Energy Storage Performance of Graphene Nanosheets (GNS)

In the recent years, different names are used in the literature w.r.t graphene-like materials. These are graphene, few-layered graphene, multi-layered graphene, graphene flowers, graphene foam etc. To avoid any ambiguity all these structures (which vary with a number of layers) are named as graphene nanosheets (GNS) in this chapter. Similarly, all GNS supported metal oxides (MO) are named as GNS/MO composites. However, at this juncture it is important to know the nomenclature [88] w.r.t graphene and its analogues. The word graphene is explained in the previous chapter. The word graphene is a combination of the words 'graphite' and the suffix '-ene'. A stack of multiple layers of graphene held by van der Waals's interactions is known as multi-layered graphene (MLG). Similarly, a stack of only few (2-10) layers of graphene held by van der Waals's interactions is known as few-layered graphene (FLG). Graphene oxide (GO) is analogous to multi-layered graphene but attached with numerous oxygen containing functional groups namely, hydroxyl (-OH), carbonyls (C=O), carboxylic (-COOH) etc., groups on the basal planes and edges of the graphene layers that are stacked together. Due to the presence of these functional groups the inter-layer distance in GO is greater than that of MLG. Reduced graphene oxide (r-GO) has only few oxygen functional groups attached to the basal planes and edges of the graphene layers stacked together. r-GO is obtained by chemically (or thermally etc.) reducing and exfoliating GO. By controlling the reduction process, number of residual oxygen functional groups can be controlled. Most of the researchers worldwide are trying to replace graphite with graphene and related materials as anode materials in Li-ion batteries due to their unique physical and chemical properties such as, (i) superior electrical conductivity that allows faster electron transport throughout the electrode, (ii) low density, higher specific surface area, (i.e., theoretical specific surface area is 2620 $m^2 g^{-1}$) and ultra-low thickness resulting in a high specific surface area, which offers more active surface sites for ion adsorption and/or electrochemical reactions, (iii) ultra-low thickness, which helps in faster diffusion of ions in the electrode, (iv) thermal, chemical and mechanical flexibility favoring their use in harsh environments, (v) broad electrochemical window that is decisive for increased energy density, which is proportional to square of the window voltage. Lithium storage of graphene was first reported by Yoo et al., [89] and a specific capacity of 540 mA h/g was reported. This value was further enhanced up to 730 and 784 mA h/g by embedding CNTs and fullerene macromolecules into GNS layers, respectively

as shown in **Fig. 2.1 (a)**. Flower-like GNS were synthesized by Wang et al., [90] with improved lithium storage capacity and cycle stability (~960 mA h/g and 460 mA h/g for 1st and 100th discharge cycles, respectively and cycled between 0.02-3.0 V at 1C rate), and claimed that lithium ions can be adsorbed on both surfaces of the graphene, and also be stored on the edges and covalent sites. Mechanically strong (i.e., 41.8 GPa Young's modulus and 293.3 MPa tensile strength) and highly conductive (~351 S/cm) graphene paper was also tested as a flexible electrode material by Wang et al., [91]. However, only limited electrochemical performance was observed owing to the restacking of graphene layers.

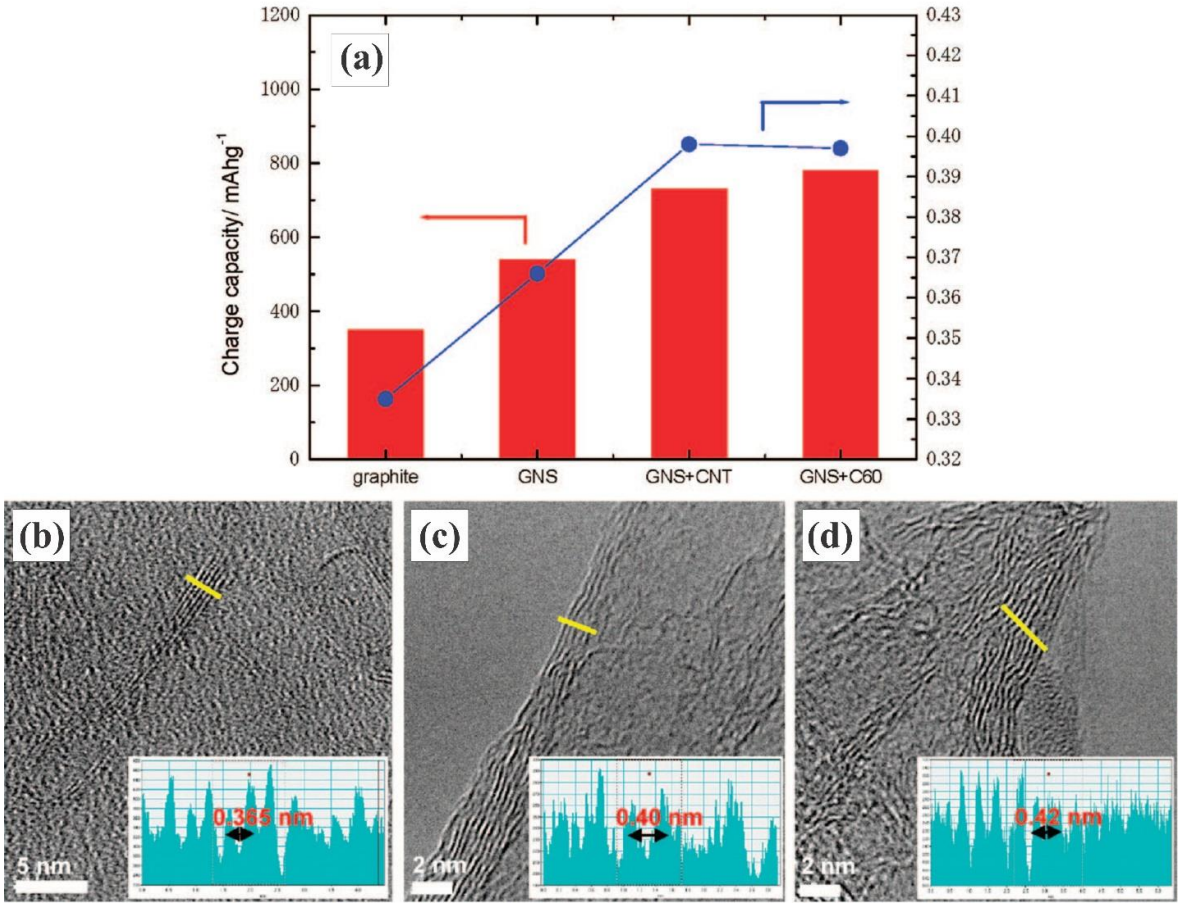

Figure 2.1 (a) The charge capacity and the d-spacing vs the graphite and graphene related materials. **(b), (c)** and **(d)** are the cross-sectional TEM images of graphene families with almost the same numbers (5-6) of graphene stacking layers of G, G+CNT, and G+C_{60} [89].

Pan et al., [92] introduced three different reduction methods namely hydrazine reduction, low-temperature pyrolysis, and electron beam irradiation to systematically tune the structural parameters of graphene such as surface functional groups, specific surface area, inter-layer spacing, defects or degree of disorder and investigated their effects on lithium storage properties. It was observed that Raman intensity ratio of D band to G band was found to be a key parameter to evaluate the reversible capacity and the improved lithium storage properties

and this careful investigation revealed that additional lithium adsorbing places such as surface defects and edges were the dominant factors for better performance as shown in **Fig. 2.2 (a, b, c)**. Lian et al., [93] reported high-quality few layered (~4 layers) graphene with a large specific surface area of 492.5 m^2/g. This sample showed an initial high capacity of 1264 mA h/g at a current density of 100 mA/g. The high capacity of this material has been credited to the few-layered graphene with a large surface to volume ratio, wrinkled graphene layers and disorder in the structure, lot of nanopores, the reversible lithium ions reaction with the residual H, and a broad electrochemical window (0.01- 3.5 V).

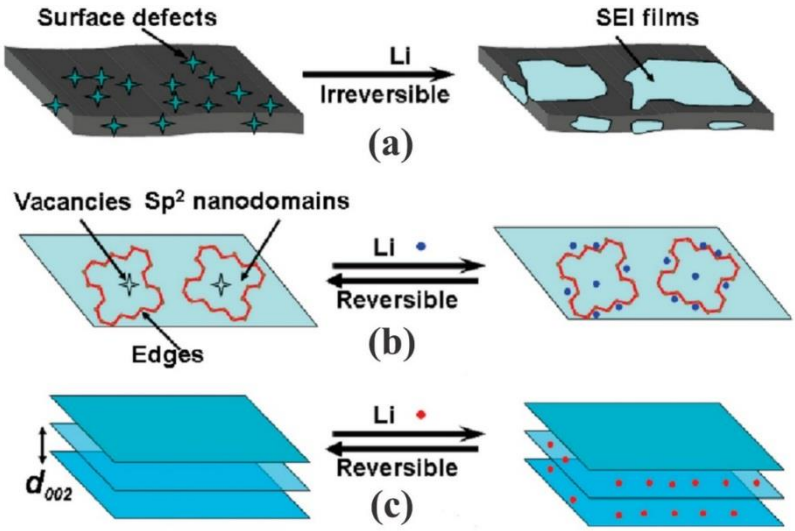

Figure 2.2 (a) Irreversible Li storage at the interface between the GNS and electrolyte; **(b)** Reversible Li storage at edge sites and internal defects (Vacancies etc.) of nanodomains embedded in GNS; **(c)** Reversible Li storage between (002) planes [92].

GNS (few-layered) was prepared by microwave irradiation of graphite oxide (GO) by Shaikshavali et al., [94]. This material showed reversible capacity values of ~400 and ~250 mA h/g at current rates of 0.1 and 1 C, respectively. The key observations are increased capacity from lithium intercalation through prismatic planes and van der Waal gaps in few layered GNS decreased enormously. Capacity above 0.5 V is due to SEI formation and partially due to the reduction of solvent in the electrolyte, originating from a disorder in the layer stacking compared to graphite. Defects, edges, double side absorption of lithium ions are speculated to be main cause in secondary lithium storage. Recently Wu et al., [95] proposed that nitrogen or boron doped graphene can be used as a promising anode material for high-power and high-energy lithium-ion batteries under the fast charge and discharge conditions with large capacity (i.e., >1040 mA h/g), super high-rate and excellent long cycle life. It is also believed that the unique two-dimensional structure, disordered surface morphology,

heteroatom defects, better electrode/electrolyte wettability, increased inter-sheet distance, improved electrical conductivity and thermal stability of the doped graphene are beneficial to rapid surface Li^+ absorption and ultrafast Li^+ diffusion and electron transport. A three-step method including chemical impregnation of the catalyst followed by chemical vapor deposition (CVD) growth of graphene film and then chemical etching of metal catalyst are followed by Goh et al., [96] to fabricate nitrogen (N) doped and undoped graphene egg-shell filled graphene foam (GE@GF) structures. Lithium storage and rate capacity of N-doped GE@GF outperformed the un-doped GE@GF as shown in **Fig. 2.3**. The observed improved reversible capacity and rate capability were attributed to the topological defects on graphene surface caused by the N-doping, leading to a higher electronic conductivity and better electrochemical performance of the active material, which facilitate fast charge and discharge rates.

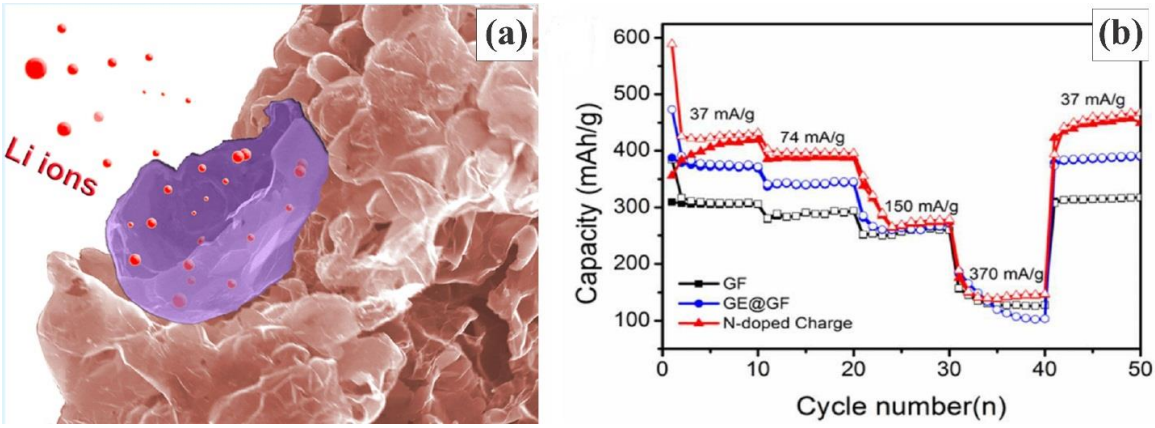

Figure 2.3 (a) Schematic of graphene egg-shell filled graphene foam (GE@GF) structures, **(b)** a comparative rate performance of graphene foam, pristine GE@GF and N-doped GE@GF at current range from 37-370 mA/g [96].

Apart from excellent characteristics of GNS as anode material in LIBs, there are certain challenges that are needed to be overcome to make GNS anode materials as commercially viable. The challenges are: (i) Large-scale synthesis of graphene (at least few-layered graphene) is need to be developed, (ii) Lithium storage mechanism in GNS is not understood well because different models are proposed, such as lithium covalent molecular (Li_2) model predicting the high Li storage capacity i.e., 1116 mA h/g (LiC_2) [92] or electrochemical lithium absorption on both sides of graphene resulting in lithium layer on both sides of GNS to give a Li_2C_6 model [97]. Lithium storage in relation with the number of graphene layers and their lateral size, presence of defect types, and oxygen-containing functional groups, are needed to be investigated, (iii) graphene's initial capacity is much more than the graphite but due to the re-stacking of GNS and side reactions between GNS and electrolytes arising from the presence of abundant functional groups and defects, it suffers from large irreversible capacity, low initial

Coulombic efficiency (QE), and fast capacity fading, (iv) Poor voltage plateau to deliver stable potential outputs, and a large hysteresis between the charge/discharge curves of GNS which will be a major drawback for their practical use in commercial LIBs, and (v) after effective reduction of graphene oxide (GO) the electrical conductivity of the reduced GO (rGO) is usually quite low compared to that of graphite due to the presence of residual functional groups in rGO and poor hexagonal lattice structure of rGO even after proper reduction of GO.

To mitigate the individual drawbacks of graphene and metal oxides, synthesis of graphene/metal oxide (GNS/MO) composites that can provide an effective use of all the potential advantages of graphene as well as metal oxides with improved electrochemical storage are proposed. Excellent reviews on GNS/MO composites as promising anode materials for LIB are available in the literature [1,98-100].

2.2 Germanium/Graphene Composites as Anode Materials in LIBs

Group IVA elements such as silicon (Si), germanium (Ge), and tin (Sn) of the periodic table are promising anode materials for Li-ion batteries. Among the various materials based on the alloying-dealloying type reaction mechanism Si, Ge and Sn show high gravimetric capacities of 4200, 1625 and 994 mA h/g, respectively by forming $Li_{4.4}M$ (where, M=Si, Ge, and Sn) for fully lithiated phase. Among the three, Si and Ge outperformed Sn as anode materials in LIBs. The atomic number of Ge is 32 while its atomic weight is 72.64 amu, with a density of ~5.5 g/cm^3. Ge possess face centered cubic crystal structure (α-Ge) and its lattice parameters are a = b = c = 5.6575 Å, α = β = γ = 90° [101]. Ge is grayish white, lustrous, brittle, and shows similar physical and chemical properties as those of Si under standard conditions. The band gap of Ge can be tuned by doping with arsenic and other elements for the use as a transistor in electronic applications [102]. Ge is non-toxic and in recent years it is used in other areas such as solar cells, polymerization catalysts, phosphors, metallurgy, and chemotherapy [103,104]. It should be noted that Si has been investigated widely as an anode in LIBs due to its intrinsic electrochemical properties, such as its low voltage profile and high theoretical capacity. Also Si is an abundant element in the earth's crust and it is low-cost material. However, there are several challenges when using Si as the anode in LIBs, including its intrinsic poor electrical conductivity, huge volume change (~420% for $Li_{4.4}Si$), and instability of the solid electrolyte interface (SEI) layer [105], which contribute to the destruction of the electrode's structure and the loss of storage capacity. The lithium ion diffusion rate and high electrical conductivity of the Ge are better than the Si, so it is highly suitable for an anode material in LIBs despite its

cost. During the lithiation process, Ge can react with Li to form Li-Ge alloy. Bulk Ge materials undergo huge volume change during charging and discharging processes, which results in severe agglomeration of the active materials. In addition, the integrity of the electrode structure is damaged and SEI layers are formed subsequently. It should be mentioned that nanostructured Ge materials possess large surface area which increases the area of contact between the electrode and electrolyte. The enlarged contact area also greatly accelerates the exchange of ions and electrons at the electrode/electrolyte interfaces. In addition, nanostructured Ge provides much smaller conduction paths when compared with their bulk counterpart, thereby significantly improving the diffusion coefficient of the active material.

To overcome the above challenges w.r.t Ge, different strategies were tried. They are, preparing (i) nanostructured Ge, including nanoparticles (NPs), nanowires (NWs), and nanotubes (NTs), (ii) porous anode materials, (iii) coating or doping designs, including Ge/C composites, core-shell nanocomposites, and other designs, (iv) alloyed germanium anodes, including binary and ternary alloys, and (v) GeO_2-based anode materials. To keep the austerity of the thesis even though many excellent studies are available on Ge in combination with different materials in above five categories, this section only discusses Ge/graphene composites based on the shape dimension of germanium i.e., zero-dimensional (0D), one-dimensional (1D), and two-dimensional (2D) shapes.

S. T. Lee and coworkers [3] synthesized a Ge-graphene composite by evaporating high-purity Ge powder on graphene sheets using a horizontal three-zone CVD tube furnace. Ge-graphene composite consisted of 200 nm Ge particles sandwiched between graphene layers. Further, the Ge-graphene composite electrodes were galvanostatically tested at different current rates such as 100 mA/g in the first cycle, 200 mA/g for the next two cycles and 400 mA/g for the subsequent cycles. The discharge and charge capacities of 1156 mA h/g and 930 mA h/g, respectively were delivered in the first cycle. The high initial Coulombic efficiency (QE) of 80.4% found in their study was attributed to the oxide-free crystalline Ge, the low surface area of 2.669 m^2 g^{-1} of the composite (which avoids side reactions during first cycle), and high-quality Ge active material. Increasing the current density to 400 mA/g resulted in the reduction of the specific reversible capacity to 795 mA h/g. Ge-graphene composite showed long-term stability i.e., 675 mA h/g capacity was retained after 400 full cycles. In addition, the composite had a QE of over 99% after five cycles and over 99.5% after 40 cycles. The Ge-graphene composite showed high rate capabilities when operated at current rates of 0.1, 0.2, 0.5, 1, 2, and 5 A/g; the composite exhibited reversible capacities of 915, 838, 736, 620, 484 and 273

mA h/g, respectively and the capacity recovered to 882 mA h/g when the current rate was returned to 0.1 A/g.

M. Zhu and coworkers [106] used dielectric barrier discharge plasma assisted ball milling and conventional ball milling processes to synthesize P-milling Ge/C, P-milling Ge5h/EG, and C-milling Ge/C composite materials, respectively. Except P-milling Ge5h/EG composite remaining two composites consisted of some amount of GeO_2 in their composition. These materials are galvanostatically tested as anode materials in the Li-ion battery in the voltage range of 0 to 1.5 mV and at different current rates. At low current rate (0.05C), the first discharge and charge capacity of C-milling Ge/C composite were 2151.5 and 979.8 mA h/g, respectively. Similarly, the first discharge and charge capacity of P-milling Ge/C composite were 2081.8 and 1213.8 mA h/g, respectively, and those of P-milling Ge5h/EG composite were 1480 and 991 mA h/g, respectively. The P-milling Ge5h/EG composite showed highest first cycle QE (~67%) than the other composite materials. This difference was expected due to pre-processing of Ge particles and heat treatment of graphite powder before P-milling could decrease micro-defects and irreversible capacity loss in the first cycle. The P-milling Ge5h/EG composite exhibited better cycle life and superior rate capability compared with the other two composites. This was expected due to the presence of graphene, which can enhance the electrical conductivity, specific surface area, and diffusion rate. In addition, Ge nanoparticles wrapped by graphene layers' act as a coriaceous wall and which alleviated the volume changes in the Ge nanoparticles during the lithiation-delithiation process.

Polyvinylpyrrolidone (PVP) assisted hydrolysis is applied to synthesize uniformly embed nanometer sized (~5 nm) germanium particles in the N-doped reduced graphene oxide (Ge/RGO) [107]. The Ge content in the Ge/RGO composite was found using thermogravimetric technique i.e., ~24.3 wt.%. Li storage capacity of the Ge/RGO composite was tested using galvanostatic cycling test in the 0 and 1.5 V voltage range and at different current rates. At 0.5 A/g current rate, the prepared composite delivered first discharge and charge capacities of 1475 and 903 mA h/g, respectively and an equivalent QE of 61.2%. Further, a charge capacity of 700 mA h/g (at 0.5 A/g was delivered during the 200th cycle and the Ge/RGO composite also exhibited better rate capabilities when operated between 0.5 and 10 A/g. Even after 200th cycle (at 0.5 A/g current density), the electrode material's microstructure was intact. In addition, the presence of nitrogen doped graphene renders excellent electrical conductivity to the composites as confirmed by EIS.

Recently, Fang et al., [108] used GO, CNTs, and Ge nanoparticles as the precursor materials and they are reduced the mixture at 600 °C in 5% (v/v) H_2 atmosphere to obtain Ge-RGO-CNTs composite in which Ge nanoparticles are tightly attached to the surfaces of RGO and intertwined with CNTs. Similarly, a Ge-RGO composite with CNTs addition was also prepared. TEM images of Ge-RGO-CNT nanocomposite showed that Ge particles (20 to 30 nm in diameter) are uniformly distributed in the composite and that CNTs and transparent RGO layers were clearly visible. The electrochemical performance of Ge-RGO-CNT composite was better than the Ge-RGO and bare Ge. The specific discharge capacity of this composite was measured as 863.8 mA h/g after 100 cycles under a current density of 100 mA/g. It was concluded that presence of RGO and CNTs favors the transport of both ions and electrons in LIBs and RGO and CNTs and strongly attached to Ge nanoparticles which helped in reducing agglomeration. The nanostructured Ge provided the large specific surface area, which promoted the uniform absorption of electrolyte and ultimately improved Li-ion diffusion and helped in mitigating the problem of volume change.

Decorating carbon coated Ge core-shell (Ge@C) structures on graphene was thought to be beneficial in achieving superior electrochemical properties. In recent years, Xue et al., reported Ge@C/graphene composite with stable performance and a prolonged cycle life [109]. In this work, Ge nanoparticles (Ge NPs) for lithium storage were synthesized by the reaction between $GeBr_2$ and oleylamine. Later, it was subsequently calcined at elevated temperatures to obtain the Ge@C structures which were decorated on reduced graphene oxide (RGO) by solvent evaporation. The initial discharge capacity of the prepared Ge@C/RGO composite was 1750 mA h/g and it retained ~1000 mA h/g after 100 cycles at a current density of 50 mA/g. It was noticed that the presence of graphene network confines the Ge NPs efficiently, thereby preventing the agglomeration in these active nanocomposites. In addition, graphene provides high electrical conductivity to the nanocomposite which leads the enhanced reaction activity. The carbon shell alleviated the volume changes by absorbing stresses produced during the lithiation-delithiation processes.

F.-W. Yuan et al., reported highly loaded Ge NPs (around 80 wt. %) on graphene nanosheets using chemical reaction and subsequent annealing at 500 °C for 2 h under 5% H_2/95% Ar atmosphere gives Ge/RGO/C nanocomposite [110]. The transmission electron micrographs of the Ge/RGO/C nanocomposite showed polycrystalline Ge NPs of size 70±30 nm were uniformly distributed on the graphene layers. At 0.2 C rate and in the voltage range of 0.01-1.5 V, the first discharge and charge capacities of the nanocomposite were 2302 and 988 mA h/g,

respectively which corresponds to a QE of 43%. This lesser QE is ascribed to the formation of solid electrolyte interface (SEI) during the first cycle. At 0.2 C, discharge capacities of 1055 and 1166 mA h/g were observed at the end of the 2nd and 75th cycles, respectively. The QE of ~100% was maintained without any fading at this stage. To test the long-term stability of the electrode, it was tested at the 0.2 C rate for initial 20 cycles and at 1 C for remaining 600 cycles. The charge- and discharge-specific capacities of 1042 and 972 mA h/g were observed at the 21st cycle. Similarly, a discharge capacity of 993 mA h/g was observed at the end of the 600th cycle with 100% CE without fading as compared with the 21st cycle. The stability of the Ge/RGO/C nanocomposite was tested at different rates from 0.2 to 20 C in two regimes. First, in the 0.2 to 1.2 C regime, the same charge and discharge current densities were applied for each period. Second, in the 2.4 to 20 C regimes, different discharge current densities for each period, and constant charge rate of 1.2 C were applied. The nanocomposite exhibited discharge capacities of 1166, 1049, 953, 962, 887, 894, 867, 794 and 720 mA h/g at a rate of 0.2, 0.6, 1.2, 2.4, 3.6, 6, 10, 15 and 20 C, respectively. Prepared electrode quickly recovered a discharge capacity of ∼1100 mA h/g even after 350 cycles at the charge/discharge rate of 0.2 C. It was also mentioned that the electrochemical performance of the Ge/RGO/C nanocomposite over a long term cycling at different rates is better than the Ge/RGO nanocomposite and few of the reported Ge nanostructures to that date. Moreover, the electrochemical Li storage of the Ge/RGO/C nanocomposite was investigated at 55 °C in the voltage range of 0.01-1.5 V and at charge/discharge rates ranging from 0.2 to 9.6 C. The electrode delivered discharge capacities of 1131, 1121, 1080, 1017, 950, 901, 879, 852, 813 and 750 mA h/g at current densities of 0.2, 0.6, 1.2, 1.8, 2.4, 3.6, 4.8, 6, 7.2 and 9.6 C, respectively. The observed high electrochemical performance of the Ge/RGO/C nanocomposite is due to the following reasons: First, Ge NPs tightly encapsulated between RGO and a thin carbon layer is beneficial to protect the structural integrity of the electrode. Second, the presence of RGO not only avoids agglomeration of Ge NPs but also provides higher electron and ion migration in the nanocomposite. Third, the carbon coating on the nanocomposite could effectively preserve the integrity of electrode material. Finally, the interfacial interactions between Ge NPs, graphene and carbon layer effectively reduced the volume changes during cycling. A full cell with Ge/RGO/C nanocomposite as anode and $LiCoO_2$ as a cathode was also studied. The full cell delivered a first cycle discharge capacity of 1234 mA h/g in the voltage range of 2.5 and 4.2 V and at a rate of 1 C. However, a stabilized capacity of ~1000 mA h/g was delivered by the full cell in the remaining cycles, and the prepared anode delivered a discharge capacity of 900 mA h/g at end of 100 cycles.

Wang et al., [111] used GO, $GeCl_4$ and PVP as the precursor materials to prepare germanium @ reduced graphene oxide nanofibers (Ge@RGO NFs) composite using electrospinning technique. Morphological analysis showed that NFs had a diameter of ~50 nm and RGO nanosheets were homogeneously distributed throughout these NFs. The electrochemical properties of the Ge@RGO NFs are compared with Ge@CNFs, pure Ge NFs, and commercial Ge and among these materials, Ge@RGO NFs composite delivered the highest specific discharge capacity in each cycle at a constant current density of 200 mA/g with more than 80% capacity retention. Further, Ge@RGO NFs composite exhibited better rate capability when compared with other materials at a high current density of 5 A/g. The enhanced electrochemical properties of Ge@RGO NFs composite are due to the close contact between Ge NFs and RGO and it alleviated volume changes in the Ge NFs during lithiation and delithiation process and in addition, the presence of RGO provided an excellent electrical conductivity to composite.

Further, Wang et al., [112] adopted the above procedure to synthesize Ge@G@TiO_2 composite using graphene (G), germanium tetrachloride ($GeCl_4$), and PVP as precursors and electrospun Ge@G NFs were coated with a thin TiO_2 protective layer using atomic layer deposition technique. Thus prepared NFs had an average diameter of ~100 nm and the surface of these NFs was not smooth due to the existance of nanoparticles. Energy dispersive x-ray spectroscopy mapping of the NFs was also used to confirm the homogeneous distribution of germanium, titanium, and oxygen. The electrochemical Li storage performance of the Ge@G@TiO_2 showed a reversible specific capacity of 1050 mA h/g at current density of 100 mA/g after 100 cycles with a high Coulombic efficiency of ~99% and an excellent rate performance. It is observed that better electrochemical performance of the prepared composite was due to double protection from graphene and TiO_2, where ultrathin TiO_2 layer stabilizes the SEI layer and protect the integrity of the anode material. In addition, graphene provides high specific surface area, excellent electrical conductivity, faster Li-ion diffusion and strong attachment for Ge nanoparticles.

Chen et al. reported the synthesis of $CuGeO_3$ NWs/RGO composite by a simple one-pot hydrothermal reaction [113]. $CuGeO_3$ NWs with an average diameter of 40 nm were obtained after reacting for 24 h and simultaneously GO was reduced to RGO in the hydrothermal environment. $CuGeO_3$ NWs/RGO composite showed a reversible capacity more than 1000 mA h/g after 10 cycles and 780 mA h/g after 130 cycles at a current density of 100 mA/g. the Coulombic efficiency of 100% was maintained after first few cycles due to the reversible alloying and dealloying between germanium and lithium. Upon lithiation $CuGeO_3$ NWs

decomposed into Cu and Ge NPs, and dispersed homogeneously in the mixed Li_2O and CuO matrix, thereby minimizing the volume changes in the $CuGeO_3$ NWs/RGO composite and mitigating the agglomeration of Ge NPs. It was argued that both Ge and CuO served as active materials for Li storage and enhanced the capacity. In addition, RGO network facilitated faster electron transfer for Li-ions during lithiation and delithiation, as well as a buffer layer to ensure the structural integrity of the $CuGeO_3$ NWs/RGO composite electrode.

$CuGeO_3$ NWs/graphene composites (CGCs) were synthesized using a simple hydrothermal reaction at 180 °C [114]. As-prepared $CuGeO_3$ NWs had an average diameter of 300 nm and a length of 10 μm, and they were tightly attached to graphene layers. The presence of graphene provided a much larger specific surface area and higher electron conductivity, and greatly reduced the transmission path for Li-ions. Further, embedded $CuGeO_3$ NWs prevented graphene layers from restacking which helped to maintain the structural integrity of the composite. The reversible capacity of CGC37 (i.e., 37 wt.% of graphene) was 1265 mA h/g for a 1st cycle. This composite also showed excellent cycling performance of 853 mA h/g at the end of 50 cycles and better rate capacity compared with bare graphene and $CuGeO_3$ NWs. The synergistic effect of graphene, $CuGeO_3$ NWs, and Li_2O buffer layer played a key role to maintain excellent electrochemical properties of the composite.

Similarly, $Ca_2Ge_7O_{16}$ NWs were also composited with graphene using a facile one-pot method without addition of any surfactant [115]. In this method, a 10 nm diameter and 1-2 mm length $Ca_2Ge_7O_{16}$ NWs embedded in the graphene layers were synthesized from calcium acetate, graphene, and GeO_2 precursors. The wrinkled graphene sheet network was mainly responsible for electrical conduction in the composite. The electrochemical properties of the synthesized composite were far better than the pristine $Ca_2Ge_7O_{16}$ NWs electrode. The 3D hierarchical $Ca_2Ge_7O_{16}$ NWs/graphene sheet nanocomposite electrode delivered higher capacity retention around 970 mA h/g and Coulombic efficiency >99% even after 100 cycles. The specific capacity of 800 mA h/g was measured even after 300 cycles during the long-term cycling process. The graphene layers served as a matrix, and the $Ca_2Ge_7O_{16}$ NWs were sandwiched between these layers, which prevented the agglomeration of active material, while $Ca_2Ge_7O_{16}$ NWs prevented graphene from restacking. $Ca_2Ge_7O_{16}$ NWs provided the large interfacial contact area with the electrolyte. The lithium inert species such as Li_2O and the CaO formed after initial cycle acted as a buffer layer to prevent the volume changes and maintain the structural integrity.

Zhang et al., synthesized Co_2GeO_4 nanoplatelets (CGO) and CGO/RGO nanocomposite using a simple hydrothermal method followed by annealing at elevated temperatures [116]. CGO and CGO/RGO are first time used as anode materials in LIBs. In this preparation method, GO, CTAB, GeO_2, and $CoCl_2.6H_2O$ were used as precursor materials in the hydrothermal process and the obtained intermittent product was annealed at 400 °C for 6 h under vacuum to obtain CGO/RGO nanocomposite. The reaction mechanism for obtaining CGO at pH 9 was given as follows: $Ge^{4+} + 2Co^{2+} + 4OH^- \rightarrow Co_2GeO_4 + 2H_2O$. Morphological information was investigated by TEM imaging, which showed that the CGO nanoplatelets had diameters of 50-100 nm and thickness of 30 nm, while CGO was observed to be dispersed uniformly on the surface of the graphene nanosheets. CGO and CGO/RGO as anodes in LIBs were galvanostatically tested for their Li-ion storage in the 0.01-3 V voltage range, current density of 100 mA/g, and up to 100 cycles. The electrochemical testing showed that the CGO/RGO nanocomposite exhibited much better cycling stability than that of the pure CGO electrode. The capacity retention of 1125 and 1083 mA h/g for 50th and 100th cycles, respectively was noticed in the case of CGO/RGO nanocomposite. On the other hand, CGO delivered a capacity of 781 and 623 mA h/g at the end of 50th and 100th cycles, respectively. CGO/RGO nanocomposite also showed better rate capability when operated at different rates i.e., 0.1, 0.3, 0.5, 0.7, 0.9, 1.1, 1.3, 1.5, and 1.7 A/g in the voltage range of 0.01-3.0 V.

2.3 Molybdenum Based Oxysalts/Graphene Composites as Anode Materials in LIBs

Molybdenum-based oxysalts and their graphene composites have been explored for high energy density and high power density anode materials in LIBs. Molybdenum-based oxysalts are categorized into five types namely: (i) $MMoO_4$ (i.e., M = Fe, Co, Ni, Ca, Mn, Zn and Cu), (ii) Mo-cluster oxysalts (i.e., $A_2Mo_3O_8$ type, A=Fe, Co, Mn and Zn or $LiHoMo_3O_8$), (iii) Bronze Mo-based oxides, (iv) Mo-based phosphates and (v) Lithium Mo oxides. Materials in the first two categories were explored as anodic materials in LIBs; only these are presented in this section. Materials in the last three categories were explored as cathode materials in LIBs; these are not presented in this section. Details of the all the above mentioned materials are available in the recent review article by X. Hu et al., [117]. Nanosized molybdenum (Mo) oxysalts showed better electrochemical properties than their bulk counterparts due to the advantages such as shortened diffusion path length, excellent buffering towards the physical strains during the lithium cycling and presence of high active surface sites which helps in enough electrolyte adsorption [118]. Apart from these advantages agglomeration of

nanoparticles upon cycling is a significant challenge which leads to crack and pulverization of the electrode. To overcome these disadvantages, hybridization with carbonaceous materials (as the matrix) such as amorphous carbon [119], one and two dimensional [120,121] carbon materials was used. This strategy not only increased the electrical conductivity of the electrode but suppressed the volume changes during cycling.

2.3.1 $MMoO_4$ (i.e., M = Fe, Co, Ni, Ca, Mn, Zn, and Cu)

Recently, mixed transition metal oxides gained interest as prospective anode materials for Li storage due to their high electric conductivity and larger theoretical capacity than that of single transition metal oxides. Among these, $CoMoO_4$ exhibits higher theoretical Li-ion storage capacity of 980 mA h/g based on the completely reversible electrochemical reaction $CoMoO_4 + 8Li^+ + 8e^- \leftrightarrow Co + Mo + 4Li_2O$.

Table 2.1 Theoretical specific capacity of $AMoO_4$ type materials.

Composition	Molecular Weight	Specific Capacity
$FeMoO_4$	215.79	993.76
$CoMoO_4$	218.87	979.78
$NiMoO_4$	218.63	980.86
$MnMoO_4$	214.87	998.02
$CuMoO_4$	223.48	959.57
$CaMoO_4$	200.01	1072.17
$ZnMoO_4$	225.32	951.73

W. Xiao et al., synthesized $AMoO_4$ (A=Co, Ni) nanorods using hydrothermal process [122]. $AMoO_4$ (A=Co, Ni) nanorods were obtained by annealing $CoMoO_4.nH_2O$ (180 °C, 12 h, addition of number of times of ethanol(r)=0) at 300 °C for 1 h and $NiMoO_4.nH_2O$ (150 °C, 6 h, r=0) at 400 °C for 1 h. Thus synthesized $AMoO_4$ (A = Co, Ni) nanorods delivered a stable lithium storage capacity of 120 mA h/g at 50th cycle and at a current density of 50 mA/g and in the voltage range of 1.2 and 3.2 V. Recently, $CoMoO_4$-Polypyrrole ($CoMoO_4$-PPy) core-shell nanowire arrays were constructed on flexible and conductive carbon cloth through a facile two-step solution based approach [123]. The hybrid $CoMoO_4$-PPy NWs electrode as a binder-free anode material exhibited a reversible capacity of around 1427 mA h/g at a current density of 100 mA/g. The electrochemical discharge specific capacities of the fabricated electrode at current densities of 100, 200, 400, 750 and 1200 mA/g were 1427, 1282, 1231, 934 and 753 mA h/g, respectively. An excellent cycling performance with a capacity of 764 mA h/g after 1000 cycles under the current rate of 1200 mA/g was delivered. The full battery was also

constructed with $LiFePO_4$ as the counter electrode. When tested in the voltage range of 2.0-3.8 V, reversible capacities of 745, 592, 460, 280, and 80 mA h/g were delivered for full battery at 100, 200, 400, 800, and 1500 mA/g current densities. When the current density is returned to 100 mA/g, the specific capacity of 592 mA h/g was observed [123]. Two LED bulbs were powered by two full batteries connected in series when demonstrated its potential use for powering electronics. Very recently, a composite consisting of $CoMoO_4$ nanorods (30-40 nm in diameter) wrapped by graphene layers ($CoMoO_4$-G NRs) was synthesized using a hydrothermal route [124]. The obtained composite material was tested as anode material in LIBs in the voltage range of 0.001-3.0 V at different current rates. At 100 mA/g, the fabricated anode material exhibited initial discharge and charge capacities of 1264 and 1046 mA h/g, respectively with the corresponding Coulombic efficiency of 82.7% and it is increased to 95% at the end of the 2nd cycle. The initial discharge and charge capacities of $CoMoO_4$ NRs are similar to $CoMoO_4$-G nanocomposites indicating the advantage of the 1D structure of $CoMoO_4$ NRs. But as the cycles progressed, $CoMoO_4$-G nanocomposite delivered a stable capacity whereas capacity fading was observed in $CoMoO_4$ NRs. An excellent rate performance of $CoMoO_4$-G nanocomposite was observed from 0.1 to 5 A/g. The nanocomposite delivered discharge capacities of 991, 942, 882, and 784 mA h/g at current densities of 0.1, 0.5, 1, and 2 A/g, respectively. The rate performance of $CoMoO_4$-G nanocomposites was better than the 3D $CoMoO_4$ electrode (611 mA h/g at 1.5 A/g) [125], rattle-type $CoMoO_4$ microspheres (783 mA h/g at 1.5 A/g) [126], and $CoMoO_4$ nanoparticle-graphene composite (660 mA h/g at 0.74 A/g) [127]. A smooth and crack free surface of the post cycled (at the end of 30th cycle and at the current density of 0.1 A/g) $CoMoO_4$-G nanocomposite was observed using SEM. The structural integrity of the nanocomposite was attributed to the presence of graphene and well distributed $CoMoO_4$ NRs in the graphene matrix.

Very recently, Zhang et al. synthesized $FeMoO_4$ nanorods using a one-step solvothermal technique [128]. The morphological investigation revealed that synthesized nanorods had a length of 300-500 nm and a diameter of 50-100 nm. It was observed from x-ray diffraction pattern that obtained material was a combination of major β-$FeMoO_4$ and minor α-$FeMoO_4$ phases. TEM images revealed that ~10 nm pores are present on the surface of the synthesized $FeMoO_4$ nanorods and this observation was supported by nitrogen adsorption-desorption test by using BJH method. X-ray photoelectron spectroscopy confirmed the stoichiometric composition of the $FeMoO_4$. The electrochemical lithium storage of the $FeMoO_4$ nanorods as anode material in LIBs was tested in the voltage window of 0.01-3.0 V and at a rate of 1 C. A

drastic capacity loss was noted during the initial cycles and later it reached an utmost value of 1265 mA h/g at 500th cycle and maintained a constant value of 1110 mA h/g until the 1000th cycle. The rate performance of the $FeMoO_4$ nanorods electrode was tested at current rates of 1, 2, 5, 10, 1, and 0.1C at an interval of 50th, 500th, and 1000th cycles and these were called as stage I, II, and III, respectively. When current returned to its initial value during the rate performance test, faster capacity recovery as observed in stage II, and III than stage I. Cyclic voltammetry, electrochemical impedance spectroscopy measurements, and post cycling investigations (at different stages) like morphology, phase, and composition confirmed that conversion type reaction was the major reason for Li-ion storage and it was also observed that crystal structure destruction from single crystalline to amorphous material took place.

In the year 2015, B. Wang et al., [121] published $NiMoO_4$ nanowire array on 3D graphene foam ($NiMoO_4$ NWA/3DGF) nanocomposite as excellent Li storage material. The synthesis process involved two-steps; first 3DGF was deposited on Ni foam using thermal CVD then Ni foam was dissolved and completely removed to get free standing 3DGF. In the second step, NiMoO4 NWA was coated on 3DGF using a hydrothermal process and subsequent annealing at 300 °C in Ar environment to obtain $NiMoO_4$ NWA/3DGF nanocomposite. For comparison purpose, NiMoO4 nanowires (NWs) were synthesized without the incorporation of GF. SEM and TEM images revealed that in the nanocomposite, NWs had a sharp tip with a diameter in the range of 70-150 nm. On the other hand, the diameter of GF less $NiMoO_4$ NWs was 100-300 nm. The BET specific surface area and pore size distribution of $NiMoO_4$ NWA/3DGF nanocomposite were 70.83 m^2/g and 5-11 nm, respectively. XPS analysis showed the presence of stoichiometric $NiMoO_4$ in the nanocomposite. The electrochemical Li storage of the $NiMoO_4$ NWA/3DGF nanocomposite as an anode with Li metal as a cathode was tested in the voltage range of 0.005-3.0 V at various current densities. The first discharge and charge capacities exhibited by the fabricated electrode were 1308.29 and 1110.29 mA h/g in the mentioned voltage range and at 200 mA/g current density. The capacity of conventional $NiMoO_4$ NWs faded rapidly to below 590 mA h/g at the end of the 40 cycles. However, $NiMoO_4$ NWA/3DGF nanocomposite electrode delivered a capacity of 967.86 mA h/g at the 150th cycle. Observed high capacity was credited to free standing $NiMoO_4$ NWA/3DGF nanocomposite which avoided usage of binder while the presence of foam structure absorbed electrolyte uniformly and helped for faster migration of charge carriers. The rate capacity of the nanocomposite as tested at various current rates ranging from 200 to 3200 mA/g. In this test, the current rate was as high as 3200 mA/g, capacity delivered was ~770 mA h/g and after

high rate discharge-charge cycles a capacity of 915 mA h/g was observed when the current rate returned to 200 mA/g. CV and EIS results supported conversion type of reaction for Li storage in the $NiMoO_4$ NWA/3DGF nanocomposite and conventional $NiMoO_4$ NWs.

2.3.2 Mo-cluster oxysalts (i.e., $A_2Mo_3O_8$ type, A=Fe, Co, Mn, and Zn or $LiHoMo_3O_8$)

Among the transition metal oxides, mixed bimetallic oxides (ternary metal oxides) possess the high theoretical capacity and long cycle life and are therefore considered as interesting host materials for Li insertion. Moreover, since these oxides can be easily formed into different crystal structures, a large variety of them can be modeled and explored for Li insertion. In this context, molybdenum (Mo)-based oxides, in particular, have proven their potential as anode materials in LIBs. These oxides exhibit rich electrochemistry associated with multiple oxidation states of the metal ions and high mass density which are favorable for improving the volumetric energy density of the anode. Very few research reports are available on hexagonal Mo_3-cluster compounds namely $LiHoMo_3O_8$ [129], $LiYMo_3O_8$ [130], $Mn_2Mo_3O_8$ [130], and $Co_2Mo_3O_8$ [131] which are synthesized using carbothermal reduction (CTR) method. B. Das et al., [129] synthesized $LiHoMo_3O_8$ in Ar environment at 750 °C by CTR method. X-ray diffraction patterns showed that the synthesized $LiHoMo_3O_8$ belonged to hexagonal P3m1 phase with least square fitted lattice parameters as a = 5.776(2) Å and c = 5.150(2) Å. SEM and TEM images showed that the synthesized $LiHoMo_3O_8$ consisted of submicron sized particles with agglomerated morphology. The electrochemical Li storage of the electrode was tested at 24 °C and 50 °C in the voltage range of 0.005-3.0 V and at a current density of 30 mA/g. The first reversible capacities of the anode at 24 °C and 50 °C were 180 and 315 (±5) mA h/g, respectively, corresponding to ~3.5 and ~6.0 moles of Li per mole of $LiHoMo_3O_8$. Cycling up to 70 cycles at 24 °C showed a reversible capacity of 290±5 mA h/g (~5.6 moles of Li). Similarly, at 50 °C a charge capacity of 470±5 mA h/g was noticed at the end of the 40th cycle. In another work, B. Das et al., [130] synthesized $LiYMo_3O_8$ and $Mn_2Mo_3O_8$ by CTR method. Rietveld refined x-ray diffraction pattern of $LiYMo_3O_8$ showed that compound crystallized in the hexagonal crystal structure with P3m1 space group and Rietveld refined lattice parameters were a = 5.783(2) Å and c = 5.160(2) Å. On the other hand, Rietveld refinement revealed that $Mn_2Mo_3O_8$ crystallized in the hexagonal crystal structure with $P6_3mc$ space group and Rietveld refined lattice parameters were a = 5.795(2) Å and c = 10.254(2) Å. Rietveld refined x-ray diffraction data showed that the amount of MoO_2 impurity was 6.7 wt.% in $LiYMo_3O_8$ and 7.2 wt.% in $Mn_2Mo_3O_8$. At RT, the $LiYMo_3O_8$ compound exhibited a discharge and charge capacities of 305 and 180 mA h/g, respectively at the end of 1st cycle.

Both the discharge and charge capacities were increased as the cycle number progressed and yielded a reversible capacity of 385 ±5 mA h/g at the end of the 120th cycle. Similarly, at 50 °C a reversible capacity of 418 ±5 mA h/g was noticed at the 60th cycle. On the other hand, the $Mn_2Mo_3O_8$ compound showed different Li storage behavior than the $LiYMo_3O_8$. The total first discharge and charge capacities were 710 ± 5 and 565 ±5 mA h/g, respectively, but a drastic capacity fading was observed as cycle number increased. At the 50th cycle, a reversible capacity of only 205 ±5 mA h/g was exhibited. Recently, Y. Huang et al. reported a two-step reduction method to synthesize hierarchically nanostructured $Mn_2Mo_3O_8$-graphene [4] and $Fe_2Mo_3O_8$-graphene [132] nanocomposites. This synthesis process involved the reaction of a phosphomolybdic acid, metal acetate and graphene oxide with hydrazine hydrate and thus formed intermediate product was further treated at 550 °C for 5 h in a reducing H_2/Ar (5/95) atmosphere to obtain the respective material. Excellent reversible specific capacities of ~951 and ~835 mA h/g (after 40 cycles in the 0.01-3.0 V range and at a current density of 200 mA/g) were shown by $Mn_2Mo_3O_8$-graphene and $Fe_2Mo_3O_8$-graphene nanocomposite, respectively.

2.4 EMI shielding properties of graphene/polymer composites

At the outset it is important to state that when this work was conceptualized, very few graphene-filled polymer composites [133,134], have been tested as EMI shielding materials. Microwave mitigating composite materials should possess a minimum of 1 S/m electrical conductivity. This can be achieved either by filling high amounts of electrically conductive fillers into a non-conductive polymer matrix or by using electrically conductive matrix and a reasonable amount of electrically conductive filler. The former may have adverse effects on formability of the composite while the latter is difficult to produce. Nonetheless, there are a good number of carefully designed and performed experiments that have overcome such difficulties. In all of these works, the composite absorber materials are in the form of sheets of different thicknesses. Sheets are the most convenient to fabricate, handle and are industrially viable. The polymers used are epoxy resin, polyvinyl alcohol (PVA), poly(methyl methacrylate) (PMMA), polyvinylidene fluoride (PVDF), polystyrene (PS), polyaniline (PANI), polyetherimide (PEI), poly (ethylene oxide) (PEO) and polypyrrole (PPY). In the following paragraphs, the graphene filled polymer composites in which the filler has no magnetic properties are discussed. Most of the literature on carbon-based materials/polymer composites for EMI shielding was populated by carbon black/polymer, carbon nanotubes/polymer, and carbon nanofibers/polymer composites. Graphene was discovered in 2004 while the first report on graphene-based polymer composite for EMI shielding appeared only in the year 2009 and most of the reports came

*during last four years (i.e., while this work was being carried out). The reports are tabulated mentioned in **Table 2.2**.*

2.4.1 Epoxy composites

J. Liang et al., used a solution processed functionalized-graphene (SPFG) to synthesize SPFG/epoxy composite for EMI shielding in the X-band (8.2-12.4 GHz) [135] frequency range. It was calculated that each SPFG contains 2-3 graphene layers in its structure stacked along c-axis direction. This composite is prepared by solution mixing of epoxy/hardener in 4:1 ratio, to the partially reduced SPFG in acetone suspension and by subsequently casting the resultant solution. SE images (**Fig. 2.4**) of the cross-sectional surface of the composite displayed SPFG sheets homogeneously throughout the epoxy matrix.

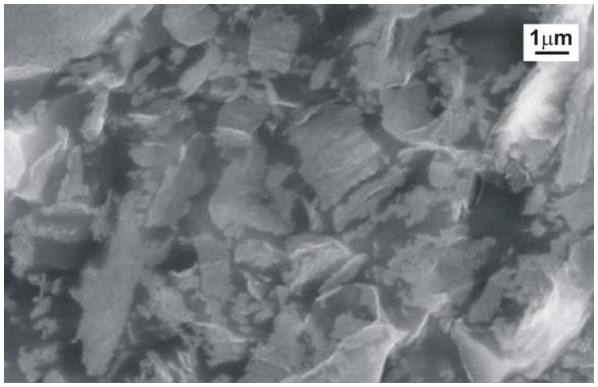

Figure 2.4 Secondary electron micrograph of cross-sectional surface of the graphene/epoxy composite with 7 wt.% loading of SPFG [135].

A low value of percolation threshold of only 0.52 Vol.% was attributed to the high aspect ratio of the graphene layers and their homogeneous dispersion in epoxy matrix. For 8.8 Vol.% (~15 wt.%) of SPFG in epoxy matrix overall SE of ~21 dB was measured and it was attributed to the conducting interconnected network of graphene sheets in the insulating matrix. It was speculated that the SPFG arrangement in the matrix and the measured electrical conductivity of the composite are the major contributions to AE is from absorption.

2.4.2 PVA composites

Anupama Joshi et al., [136] reported the synthesis of graphene nanoribbon-poly vinyl alcohol (GNR-PVA) composite via solution mixing process. In this study, GNR were obtained by unzipping the MWCNTs using chemical process. Synthesized GNR-PVA composite is very thin (0.3, 0.6 mm), lightweight and require very less amount of filler content (0.75, 1.5, and 2.5 wt.%). Raman spectroscopy and atomic force microscopy studies supported the very well

conjugation of GNR with PVA. At a very low concentration of GNR (i.e., 0.75 wt.%), 14 orders of improvement in the electrical conductivity of the composite film compared with the bare PVA film was observed. The average shielding efficiency of -24, -26.8, and -30.92 dB was observed in the x-band frequency range for 0.75 wt.%, 1.5 wt.%, and 2.5 wt.% GNR in PVA with 0.3 mm film thickness. Similarly, the average shielding efficiency of -28, -34, and -45 dB was observed in the x-band frequency range for 0.75 wt.%, 1.5 wt.%, and 2.5 wt.% GNR in PVA with 0.6 mm film thickness. Excellent EMI shielding properties at very low concentrations of GNR were expected due to the better characteristics of GNR. GNR has good dispersion capability in water, the conductive network in the composite shows very high electrical conductivity for a very low concentration of GNR and presence of localized density of states near Fermi energy provides the spin states required for the absorption of incident electromagnetic radiation.

2.4.3 PMMA composites

PMMA is also another interesting polymer similar to the epoxy and PVA. It is transparent to visible light and easy to form a composite with filler materials. Graphene-PMMA foam composites were prepared by solution blending of graphene (or melt compounded for tensile tests) with PMMA followed by foaming with supercritical CO_2 foaming agent [24]. The 3-4 individual graphene layers are present in each graphene platelet construction and BET specific surface area of the graphene is ~700 m^2/g. Prepared composite foams were observed under SEM and 1.8 vol.% graphene/PMMA foam contains nearly spherical cells with an average diameter of ~5 μm were uniformly distributed throughout the matrix. Similarly, homogeneously dispersed graphene sheets throughout the cell walls were observed in the TEM image of a 0.8 vol.% graphene/PMMA foam composite and dispersed graphene formed network type structure in the cell walls and struts of the foam. The insulator-to-semiconductor transition of foam composites was achieved at the lower content of graphene than the bulk composite materials. The 0.6 vol.% graphene nanocomposite foam exhibited an electrical conductivity of 3.80×10^{-5} S/m which was increased to 0.39 S/m for 0.8 vol.% graphene in the nanocomposite foam. Further, a much higher conductivity of 3.11 S/m was achieved in a microcellular foam with 1.8 vol.% graphene sheets in the PMMA. The neat PMMA foam was not shown hardly any EMI SE. But a slight improvement in the EMI SE of nanocomposite foam with 0.6 vol.% graphene was observed. An EMI SE of 7.5 dB in the almost entire frequency range (expect approaches 12 dB in the frequencies around 9.0 and 9.6 GHz) was observed for 0.8 vol.% graphene-containing nanocomposite foam. Further 1.8 vol.% graphene-

containing microcellular nanocomposite foam showed an overall SE of 13-19 dB. It is also found that absorption is the dominant mechanism for EMI SE of all the nanocomposite foam. The mechanical properties of the nanocomposite foam structures were compared with their un-foamed structures. The process of foaming has greatly improved the ductility and tensile toughness of the nanocomposite foam structures than their un-formed counterparts.

In other work [55], the influence of surface chemistry of the graphene on the rheological, electrical, and electromagnetic interference (EMI) shielding properties of the graphene/PMMA composites was investigated. For this purpose, graphene with different C/O ratios were synthesized by varying thermal reduction parameters. Thus synthesized graphene forms are designated as graphene-13.2, graphene-9.6, and graphene-5.0. TEM images of three different graphene sheets are similar and are transparent to the electron beam with slight ripples on their surface. All these graphene platelets contain 3-4 individual graphene layers indicating the similar thickness of these graphene platelets. The surface to volume ratio of the graphene is an extent of degree of exfoliation of graphite oxide. The calculated BET surface areas of graphene-13.2, graphene-9.6, and graphene-5.0 are 700, 660, and 758 m^2/g respectively. The rheological properties are more closely related to dispersion of the filler content in the polymer nanocomposites. The rheological percolation thresholds of 0.30, 0.32, and 0.70 vol.% are derived for graphene-13.2, graphene-9.6, and graphene-5.0, containing PMMA composites respectively. Similarly, the electrical percolation thresholds observed for graphene-13.2, graphene-9.6, and graphene-5.0 were 0.62, 0.77, and 0.92 vol.% respectively. For the same loading of 0.78 vol.%, a conductivity of the graphene-9.6 and graphene-5.0 composites are 3.93×10^{-6} S/m and 1.0×10^{-14} S/m, 4 and 12 orders of magnitude lower than 2.38×10^{-2} S/m of the graphene-13.2 composite were observed. It is reported that EMI SE of PMMA is approximately equal to zero and it increased with increasing filler content in it. The SE_{total} of the graphene-13.2/PMMA composite was 10 dB with only 1.1 vol.% of graphene and it reached above 25 dB for 2.67 vol.% graphene. Further, it reached 30 dB for the loading of 4.23 vol.% of graphene over the frequency range of 8.8-12 GHz. In contrast, the SE_{total} of graphene-9.6 and graphene-5.0 composites are lower than the graphene-13.2 composite. The observed better rheological, electrical, and EMI SE properties of the graphene-13.2 composites than graphene-9.6 and graphene-5.0 composites are expected due to the more amount of oxygen content in other two graphene forms. It is well known that the existence of oxygen functional groups on the graphene disrupts its graphitic sp^2 hybridization network and which reduces its intrinsic conductivity, ultimately it influences the EMI SE properties.

2.4.4 PVDF composites

This polymer is resilient to many chemicals and it can be operated at higher temperatures unlike other polymers discussed so far. PVDF is also high dielectric constant polymer. In a work functionalized graphene/PVDF (f-G/PVDF) foam composites were prepared using solution mixing routes [29]. The thickness of the used graphene was 3-4 nm which equivalent to 9-11 graphene layers in the observed graphene structure. FESEM images clearly showed that synthesized composite materials contain uniformly distributed foams with a pore diameter of 0.5-2.0 μm and these composites contained interconnected f-G in the insulating PVDF matrix. The electrical conductivity of the foam composite also increased with the amount of f-G present in the composite similar to epoxy composite. A conductivity rise of ~10^{-16} S/m for pure PVDF to 10^{-3} S/m for foam composite with 0.5 wt.% f-G in PVDF matrix was observed. It was observed that an EMI SE of 5 wt.% f-G filled PVDF foam composite was 18 and 20 dB in the frequency range of 8-12 GHz and 1-8 GHz, respectively. The observed increase in the EMI SE of foam composite with an increase in the f-G content is expected due to increase in the conductivity of the foam composite through the formation of interconnected network type structures in the PVDF matrix. It was also observed that reflection was the primary mechanism for EMI SE rather than the absorption.

2.4.5 PS composites

High pressure (1000 MPa) compression molding subsequent by salt-leaching procedure [137] was followed to prepare functionalized graphene sheets (FGS) filled PS porous composites. **Fig. 2.4** represents schematic for the synthesis procedure of this composite. A 2.5 mm thick and 0.45 g/cm^3 density FGS/PS composite sheet with 5.6 Vol.% (~30 wt.%) filler shown an admirable microwave absorbing capacity. The electrical conductivity of this composite was 1.25 S/m which is greater than the required value of 1 S/m for optimal attenuation. This composite has shown an average overall AE, AE_A, and AE_R (**Fig. 2.5**) of 29, 27.7, and 1.3 dB, respectively.

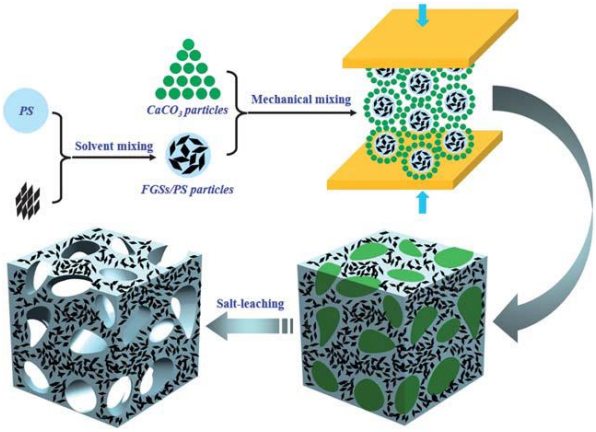

Figure 2.4 Schematic for the production of FGS/PS porous composite [137].

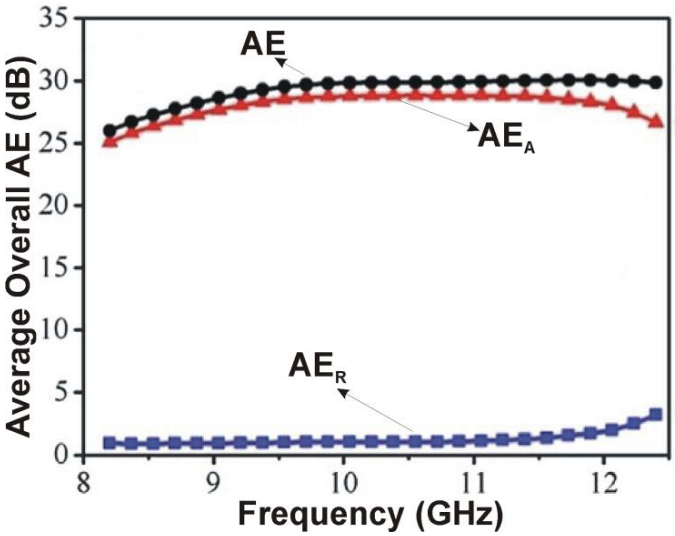

Figure 2.5 Comparison of overall attenuation effectiveness (AE), microwave absorption (AE_A), and microwave reflection (AE_R) [137].

2.4.6 PANi composites

Another interesting polymer PANi was also used for EMI shielding applications. In a report, single-walled carbon nanotubes (SWNT) and graphene nanosheets (GSs) were both synthesized using hydrogen arc-discharge method. TEM observations showed that the obtain GSs consist of 2-10 layers in its construction and SWNTs have a diameter in the range of 0.5-2 nm. SWCNT/PANi and GSs/PANi composites were prepared by simple alcohol-assisted dispersion and pressing process [138]. The prepared 2.4 mm thick composite's morphology showed that GSs are uniformly dispersed in the PANi compared with SWNT and GSs are nicely coated with PANi. The highest EMI SE of 34.2 dB was obtained for 33 wt.% GSs filled PANi composite. Absorption of EM wave was a major reason for EMI shielding in this composite. A SE_A values of 66%, 68%, 75%, 79%, and 81% against the overall EMI SE are

measured at 2, 6, 10, 14 and 18 GHz, respectively. The observed excellent EMI SE was attributed to developed electrically conductive network in the composite.

In another work [139], multi-walled carbon nanotubes-graphene-PANi (PANINGF-MWNTs) multi-phase composite was synthesized by in situ oxidative polymerization of aniline in presence of dispersed graphite flakes (5 wt.%) and subsequent solvent mixing of MWNTs (different wt.%) by high speed homogenization (for functionalization of MWNTs) and ball milling technique. Presence Fe impurities are observed in the as-synthesized MWCNTs and on the other hand defects in the form pits are observed in acid treated MWCNTs. The above observations are corroborated by Raman spectroscopy and FTIR spectroscopy results. TEM images of PANINGF-MWNTs showed not only ball milling exfoliated graphite flakes into semitransparent (to the electron beam) multi-layered graphene but also good contact between graphene layers-MWCNTs and graphene-PANi in the composite. It was observed that the electrical conductivity of 1-2 S/cm for PANi raised to 29.5 S/cm for PCNT 10 (10 wt.% MWCNTs in PANINGF) composite. Similarly, shore hardness measurements were also carried out which showed that shore hardness of 56 for PCNT0 is less than the 91 for PCNT10. SEM images and Raman spectra of the PANINGF-MWNTs composite confirmed the formation of the composite with a homogeneous distribution of filler materials in the composite. EMI shielding measurements were carried out in the frequency range of 12.4 to 18.0 GHz. An EMI SE of -46 dB was observed for PCNT0 which increased with the addition of MWCNTs in the PANINGF matrix. EMI SE values of -48, -69, -78, and -98 dB were observed for PCNT1, PCNT5, PCNT7, and PCNT10, respectively. The measured dielectric constant was only 2.3 for PCNT but was increased from 29 to 168 for PCNT1 to PCNT10, respectively at the 18.0GHz frequency. Similarly, the imaginary part of dielectric constant was only 1.90 for PCNT0 and it was increased from 52 to 206 for PCNT1 to PCNT10, respectively for 18.0 GHz frequency. The observed enhancement in the EMI SE values was supported by calculated dielectric parameters and it was found that interfacial charge polarization was the main reason for these enhanced properties due to the difference in the electrical conductivities of the PANi and filler materials.

2.4.7 PEI composites

Microcellular polyetherimide/graphene (PEI/G) nanocomposite foams were synthesized via water vapor induced phase separation (WVIPS) solution mixing process [140]. Each graphene platelet used in this study had 3-4 individual graphene layers and the BET specific surface area

of graphene was 700 m^2/g. It was observed from SEM images that a strong extensional flow generated during the cell growth induced homogeneous dispersion of graphene on the cell walls. The process decreased the electrical percolation threshold of 0.21 vol.% for PEI/G nanocomposite to 0.18 vol.% for microcellular PEI/G nanocomposite foam. The specific EMI SE of microcellular PEI/G foams was 36.1 and 44.1 $dB/(g/cm^3)$ for 7 and 10 wt.% graphene loading, which was about 2.2 and 2.5 times higher than the unfoamed counterparts. Excellent EMI SE values of microcellular nanocomposite foams than the unfoamed nanocomposites were due to minimizing reflection losses by confining incident microwave in the foam structures.

Table 2.2. Recently reported Electromagnetic interference (EMI) shielding materials.

Filler material[a]	Filler wt.%	Synthesis procedure[b]	Electrical Conductivity (S/m)	Frequency range (GHz)	Shielding effectiveness (dB)	Reflection Loss (dB) below 10 dB
Epoxy composites						
GNs [141]	15	Solution mixing	1.3×10^{-6}	8-20	-	-14.5@18.9 GHz, t=3 mm
Graphene nanosheets [142]	3	Solution mixing	-	2.6-12.4	-	-21.4@4.5 GHz, t=4 mm
Graphene nanoribbon-PANi [143]	2.5	Solution mixing	-	8.2-12.4	-34@ t= 1.7 mm -50@ t= 3.4 mm	-
	5.0				-44@ t= 1.7 mm -68@ t= 3.4 mm	
3wt.%TGO+30wt.%Spherical Carbonyl Iron [144]	30	Planetary centrifugal vacuum mixing	8.38	8.2-12.4	36@9.5-12 GHZ	-
5.6wt.% CNT+0.4wt.% GO [145]	5.6 and 0.4	Solution mixing	-	8-18	-	-14.63@14.32 GHz, t=2 mm
50wt.%HGS@Ag+1wt.%RGO [146]	50 and 1	Solution mixing	-	1-18	-	-46.1@ 10.9 GHz, t=2mm
SMF-RGO [147]	10:1	Wet chemical method	-	0.1-18	-	-23.9@10.8 GHz, t=3 mm
GO coated FeCoB [148]	30	Solution mixing	14	8.2-12.4	-	-22.2@12.4 GHz, t=2 mm
LGA [149]	1	Infiltration method	9.28	10-20	30@t=3 mm	-
rGO-CF60 [150]	1.5 wt.% GO and 60 min deposition GO on CF	Electrophoretic deposition and solution mixing	7.20	8.2-12.4	37.6@t=6 mm	-

TGA [151]	0.8	Solution mixing	120	8.2-12.4	27	-
TAGA_radial [151]	0.8		96		32	
TAGA_axial [151]	0.8		980		25	
HGS@Fe_3O_4-rGO [152]	50:1	Solution mixing	-	1-18	-	-15.8@11.9 GHz, t=2.3 mm
MFGO [153]	40	Solution mixing	-	8.2-12.4	-	-14.8@8.62 GHz, t= 4mm
MFRGO [153]						-25.21@8.62 GHz, t=4mm
PANS@SMF/RGO [154]	1:1	Solution blending	-	1-18	-	-16.1@12.2 GHz, t=2.5mm
Graphene film [155]	-	Vacuum filtration	2.14 x 10^4	0.01-2	51	-
				8.2-12.4	55	
				12-18	60	
Poly Vinyl Alcohol (PVA) composites						
SLGAPC-Fe_3O_4 [156]	15:20	Solution casting	3.37 x 10^{-5}	8.2-12.4	15@t=0.3mm	-
GNS/MWCNTs [157]	0.25:1.25	Solution mixing	42	0.0003-1	18.8@t=0.5 mm	-
				1-2	23.5@t=0.5 mm	
				2-3	24.6@t=0.5 mm	
		melt compounding	1.5x10^{-3}	0.0003-1	0.15@t=0.5 mm	
				1-2	2.20@t=0.5 mm	
				2-3	4.97@t=0.5 mm	
rGO [158]	0.9	Solution mixing	-	2-18	-	-36.4@4.5 GHz, t=5mm

PPC-PVAG-PPC [159]	8:2:8	Melt blending-Solution mixing and hot pressing	0.3	0.0003-1	-34.7$_{@t=1\ mm}$	-
				1-2	-36.7$_{@t=1\ mm}$	
				2-3	-38.7$_{@t=1\ mm}$	
PPC-PVAC-PPC [159]	8:2:8		580	0.0003-1	-22.6$_{@t=1\ mm}$	
				1-2	-24.5$_{@t=1\ mm}$	
				2-3	-23.9$_{@t=1\ mm}$	
Polymethylmethacrylate (PMMA) composites						
Ag-RGO/PMMA [160]	3 vol.%	Solution blending and hot pressing	5	8.2-12.4	26.8$_{@t=2.5\ mm}$	-
SWCNH/GNP/PMMA [161]	1.072 vol.%: 70 vol.%	in-situ polymerization	5	8.2-12.4	-23.6	-
Poly Vinylidene Fluoride (PVDF) composites						
RGO-$MnFe_2O_4$/PVDF [162]	5	Solution mixing and hot pressing	-	2-18	-	-29.0$_{@9.2\ GHz,\ t=3\ mm}$
PVDF/$BaFe_{12}O_{19}$/rGO [163]	PVDF:100:5	Wet chemical method and hot pressing	-	0.5-18	-	-32.0$_{@11\ GHz,\ t=2\ mm}$
rGO@MoS_2/PVDF [164]	5$_{for\ RL}$	Solution mixing and hot molding	-	2-18	27.9	-43.1$_{@14.48\ GHz,\ t=2mm}$
	25 $_{for\ EMI\ SE}$					
rGO/PVDF-HFP [165]	40$_{of\ GO}$	Solution mixing and casting	-	8.2-12.4	30	-

PC/PVDF with 3 wt % MWCNT −MnO2 + r-GO/Fe [166]	-	Melt compounding	-	8-18	-36@t=0.9 mm	-
multilayer assembly 1 [166]					-57@t=0.9 mm	
multilayer assembly 2 [166]					-35@t=0.9 mm	
Polystyrene (PS) composites						
s-rGO/PS [167]	4 (1.95 vol.%)	Solution mixing and solid phase compression molding	~5	8.2-12.4	31.5@t=2.5 mm	-
	7 (3.47 vol.%)		43.5		45.1@t=2.5 mm	
PS/Fe_3O_4@RGO [168]	PS:3.24 vol.%	Solution mixing and Vacuum hot-pressing	0.28	8.2-12.4	<10	-
PS/Fe_3O_4-220/TGO [168]	PS/Fe_3O_4-220: 2.24 vol.%		21		36@11.95 GHz	
PS/MWCNT/SiO_2@rGO [169]	PS/3/SiO_2@rGO	Solution mixing and compression molding	~3	8.2-12.4	30.3@8.2 GHz	-
Polyaniline (PANi) composites						
rGO-γ-Fe_3O_4/PANi (PRF13) [170]	3/1 (aniline)	Chemical oxidative polymerization	$5.4x10^3$	8.2-12.4	51@t=2.5 mm	-

Fe_3O_4- RGO-PANi40 [171]	Fe_3O_4-RGO:40	Chemical oxidative polymerization	-	0.5-18	-	-36.5@7.4 GHz, t=4.5mm
Ni-RGO/PANi [172]	59-41	in-situ polymerization	-	2-18	-	-51.3@4.9 GHz, t=3.5mm
CF/PANi (PCF) [173]	1:1	Chemical oxidative polymerization	2764	8.2-12.4	~31.02	-
MWCNT/PANi (PCNT) [173]			5836		~37.17	
rGO/PANi (PrGO) [173]			6973		~38.52	
PANi-CuS-RGO/wax [174]	30:1	In-situ polymerization	-	0.0003-3	-18@t=3 mm	-
Polyetherimide (PEI) composites						
Double PEI/RGO [175]	0.66 vol.%	Electrophoretic deposition	$1.25x10^3$	0.5-8.5	6.37	-
Polyethylene oxide (PEO) composites						
CR-G/PEO [176]	2.6 vol.%	Solution mixing	-	2-18	-	-38.8@16.5 GHz, t=1.8 mm
Graphene/PEO [177]	1	in-situ reduction	-	1-14	-	-20.1@6 GHz, t=3 mm
Polypropylene (PP) composites						
PP/CNT/xGnP [178]	80:10:10	Solution mixing	-	0.03-1.5	36.5@1.25 GHz,	-
Polypyrrole (PPY) composites						
PPY/MLG/TiO_2 [179]	1:0.05:0.05	in-situ oxidative polymerization	-	12.4-18	53	-

[a]GNs-graphene nanoplatelets; HGS@Ag-Ag coated hollow glass spheres; SMF-surface modified $Fe_{50}Ni_{50}$ nanoparticles; RGO-reduced graphene oxide; LGA-graphene aerogel with large pore size; rGO-CF-reduced graphene oxide-carbon fiber; TGA- thermally annealed graphene aerogels; TAGA-thermally annealed anisotropic graphene aerogel; HGS@Fe_3O_4-lightweight composites comprising Fe_3O_4-coated hollow glass spheres; MFGO-magnetic functionalized graphene oxide ($FeCl_4^-$ magnetic anion); PANS@SMF- surface modified Fe50Ni50-coated poly(acrylonitrile) microspheres; SLGAPC-Fe_3O_4-Fe_3O_4 nanofiller decorated single-layer graphene assembled porous carbon; PPC-PVAG-PPC-Polypropylene/MWCNTs(8 wt.%)-PVA/GNs(2wt.%)- polypropylene/MWCNTs(8 wt.%); PPC-PVAC-PPC-polypropylene/MWCNTs (8 wt.%)-PVA/MWCNTs (2 wt.%)-polypropylene/MWCNTs (8 wt.%); SWCNH-Single wall carbon nanohorn; MoS_2-Molybdenum disulphate; PVDF-HFP- poly (vinylidene-hexafluoropropylene); multilayer assembly 1- PVDF with 3 wt % MWCNT −MnO_2 + r-GO/Fe in the top and bottom layers and PC/PVDF with 3 wt % MWCNT in the middle layer; multilayer assembly 2-PVDF with 3 wt % MWCNT −MnO_2 + r-GO/Fe in the middle layer and PC/PVDF with 3 wt % MWCNT in the top and bottom layers; CR-G- chemically reduced graphene oxide; GnP-exfoliated graphite nanoplatelets; MLG- multilayer graphene;

b- SC-solution chemistry

Chapter 3 Experimental Work

3.1 Materials Synthesis

3.1.1 Few layered graphene (FLG)

Materials used for the synthesis of Graphite Oxide (GO) are graphite flakes (flake size ≤ 47 μm, Nacional de Grafite Ltda), sodium nitrate ($NaNO_3$, Sigma-Aldrich), potassium permanganate ($KMnO_4$, Ajax Chemicals), sulfuric acid (H_2SO_4, concentration ~95-97%, Fluka), and hydrogen peroxide (H_2O_2, concentration ~35%, Riedel-de Haen). All the materials used in this work are as-obtained i.e., without any further purification.

A slightly modified Hummers method [180] was used to synthesize GO in the following manner: 3 g of graphite flakes and $NaNO_3$ were successively added to 69 mL of concentrated H_2SO_4 and the mixture was maintained at 0 °C using an ice bath. To the resultant reaction mixture, 9 g of $KMnO_4$ was added slowly in portions to keep the reaction temperature below 20 °C. Then the reaction mixture was warmed to 35 °C and stirred for 0.5 h. Additional $KMnO_4$ (9.0 g, 3 wt.% equiv.) was added in one portion and again stirred for 0.5 h at 35 °C. Later, 150 mL of distilled water was added to the reaction mixture and eventually, the mixture was stirred at its raised temperature of 98 °C for an hour. Later the reaction mixture was cooled to room temperature, and 5 mL of 30% H_2O_2 was added to it. Then the obtained reaction mixture was allowed to settle down for a few hours before decanting the supernatant solution. The sediment was washed several times with warm distilled water and ethanol until the pH of the solution became neutral (i.e., pH ~7). After the final wash and discarding the water, the obtained GO is dried in an oven at 100 °C for 12 hours.

GO powder was subsequently irradiated with microwaves in a household microwave oven (IFB Industries Ltd, 30SC2, India) for 2 minutes (60s in 2 cycles) to obtain puffy graphene worms (GWs) [181]. The puffy GWs were then uniformly dispersed in distilled water mixed slightly with ethanol AR (99.9% purity, Hangzhou Chemical Co. Ltd. China) using probe sonicator (SONICS Vibra-Cell TM, 750 Watt Ultrasonication Processor). The sonication was done in the continuous pulse mode for 1 h at 50% amplitude. The reaction vessel was kept in an ice bath to remove excess heat generated during the process and the resultant solution was freeze-dried to obtain FLG.

3.1.2 Graphene-wrapped MgO (G@MgO) composite

Magnesium metal turnings (Mg, 99.8% purity, Alfa Aesar) and dry ice (solid CO_2) and hydrochloric acid (HCl, concentration ~37%, Merck).

Graphene-wrapped magnesium oxide (G@MgO) composite powder was synthesized using a combustion process [182]. As shown in **Eq. (3.1)**, combustion process involves ignition and complete combustion of magnesium (Mg) metal turnings in the presence of dry ice at ambient conditions. Then obtained ash-like material was mixed with 1M hydrochloric acid (HCl) to dissolve any unreacted metal and other impurities. Thus resulted material was then filtered and subjected to multiple washes with ethanol and deionized water and finally dried in an oven at 100 °C to obtain Graphene-wrapped MgO composite powder.

$$2Mg + CO_2\ (\text{dry ice}) \rightarrow C\ (\text{Graphene}) + 2MgO \qquad (3.1)$$

3.1.3 $Co_2Mo_3O_8$/rGO composite

Starting materials required for the synthesis of $Co_2Mo_3O_8$/rGO composite are the as-synthesized GO, molybdenum trioxide (MoO_3, Merck), cobalt acetate tetrahydrate ($Co(OOCCH_3)_2{\cdot}4H_2O$, Alfa Aesar). Synthesis of $Co_2Mo_3O_8$/rGO composite was carried out using Graphenothermal reduction (GTR) method. In this method of synthesis, GO, MoO_3 and Co $(OOCCH_3)_2{\cdot}4H_2O$ were taken in 12:3:2 molar ratios and mixed using the mechanical grinder for 30 min. The molecular formula of GO was taken as $C_{2.2}H_{0.8}O_1$ [183] for molar calculations. Then the reaction mixture (12 g) was placed into a ceramic boat and transferred to a tubular furnace (Carbolite, UK). Thermal annealing of the reaction mixture was carried out at 750 °C for 8 h and at a heating rate of 5 °C/min. The furnace was then cooled to room temperature at a cooling rate of 5 °C/min, and a black colored fine powder (6 g) was collected. Heating was started after flushing out air in the furnace with Ar gas while Ar gas flow was maintained throughout the experiment. The as-synthesized final product was directly (i.e., without any further purification or functionalization/modification) used for characterization and electrochemical analysis.

3.1.4 Ge/rGO composite

Germanium dioxide (GeO_2, 99.999 purity, Sigma Aldrich) and as-synthesized GO were used as starting materials to synthesize Ge/rGO composite. Again GTR method is used to synthesize Ge/rGO composite. In this composite preparation, GeO_2 and GO dry powders mechanically mixed in 1:4 molar ratios (and also in another experiment, 1:2 molar ratio) for 30 min. Next,

this dry powder mixture was annealed at 900 ºC for 1 hour in a continuous argon gas flow at 5 ºC/min heating and cooling rates. As a result, black colored Ge/rGO (named as GR14 for GeO_2: GO =1:4) composite powders were produced, and these powders were directly used for further characterization and as anodic material in Li-ion batteries.

3.1.5 FLG/PVA composite

Poly Vinyl Alcohol (M.W. 86000, Fisher Scientific) powder, as-synthesized few-layered graphene (FLG) were used to synthesize FLG/PVA composite sheets. 2.5 g of PVA powder was mixed with 50 ml of deionized water and stirred at 60 °C for 3 h to form a homogeneous solution. 0.2 wt.% (~0.1 Vol.%) of the filler material (named as graphene worms [181]) was dispersed in 50 ml of a solution (de-ionized water + small volume of ethanol AR) by using probe sonicator operated at 750 W for 1 h in continuous pulse mode. This solution was added drop by drop to PVA solution and stirred for 2 h to form a homogeneous solution. Small bubbles present in this solution were removed using mild sonication for few seconds. The bubble free solution was then cast in a borosilicate glass Petri-dish and dried at 60 °C to evaporate residual water and ethanol content. This resulted in obtaining free-standing, flexible and semi-transparent (to visible light) FLG/PVA composite sheets (as shown in **Fig. 3.2**). Like-wise 0.6 wt.% (~0.5 Vol.%) of FLG containing FLG/PVA composite and FLG free PVA sheets were also synthesized. The thickness of all the sheets was maintained 1 mm.

Figure 3.2 Semi-transparent (to visible light) and Flexible 0.2 wt.% FLG/PVA sheet.

3.1.6 Graphene-wrapped MgO/PVA composite

Poly Vinyl Alcohol (PVA, M.W. 86000, Fisher Scientific) powder, as-synthesized G@MgO composite powder were used to synthesize G@MgO/PVA composites. 2.994 g of PVA (M.W. 86000, Fisher Scientific) powder was mixed with 50 ml of deionized water and stirred at 60 °C for 3 h to form a homogeneous solution. 0.4 wt. % of the filler material (G@MgO) was dispersed in 50 ml of a solution (de-ionized water + small volume of ethanol AR) by using probe sonicator operated at 750 W for 1 h in continuous pulse mode. This solution was added drop by drop to already prepared PVA solution and stirred for 2 h to form a homogeneous solution. Small bubbles present in this solution were removed using mild sonication for few seconds. The bubble free solution was then cast in a borosilicate glass Petri-dish and dried at 60 °C to evaporate residual water and ethanol content. This resulted in obtaining free-standing, flexible and semi-transparent (to visible light) G@MgO/PVA sheets. Like-wise 3.0 wt.% of G@MgO containing G@MgO/PVA composite and G@MgO free PVA sheets were also synthesized. The thickness of all the sheets was maintained 1 mm. Since the presence of strong van der Waals forces between graphene particles in G@MgO powder (i.e., appears like clustered particles as shown **Fig. 4.20(a)** of section 4.2.2) make the dispersion highly unstable. To overcome this problem, bubble free solution of a batch of samples (i.e., 0.4, 0.6, 0.8, 1.0, 3.0, 10.0 and 15.0 wt.% of G@MgO containing G@MgO/PVA composites) were coagulated using ethanol and the obtained material is dried at 60 °C for one day to evaporate residual ethanol and water content in it. Later, the casted sheets and coagulated samples were cut into small pieces and hot pressed separately at 140 °C temperature and 3 tons of pressure to form one-inch diameter circular discs with 1 mm thickness as shown in **Fig. 3.3**. Thus prepared composite samples were named as for example, 3.0G@MgO/PVA_ac and 3.0G@MgO/PVA_Coag for as-casted and coagulated samples with 3.0 wt.% G@MgO in PVA, respectively.

Figure 3.3 Circular discs (from left to right) of PVA, 3.0G@MgO/PVA_ac, and 3.0G@MgO/PVA_Coag samples.

3.2 Characterization of Materials

3.2.1 Scanning electron microscopy

In the present work, field emission scanning electron microscopy (FESEM) is used to acquire secondary electron (SE) images of both surface and cross-sectional morphology of the samples based on the requirement. For imagining purpose, sample surface must be electrically conductive otherwise electron beam charge up the sample surface. Since graphene based polymer composites are insulating in nature, their surfaces are coated with thin gold (Au) layer prior to the morphological observation. On the other hand, graphene and graphene-based composite powders are not coated with Au layer due to their inherent electrical conductivity. Carl Zeiss Ultra 55 model high-resolution FESEM is used to obtain secondary electron images at typical 4 mm working distance, accelerating voltage of 5 kV and at various magnifications. The tungsten (W) coated zirconium dioxide (ZrO_2) filament used as the field emission gun (FEG) in this microscope. When high voltages applied, the electron beam released from the FEG was scanned across the sample surface under study. The currents reflected from the surface are collected, amplified and plotted as a two-dimensional image (also called as micrograph) of the signal intensity. As such, SEM can only give information about the appearance, or morphology of the sample surface and not the definitive proof of the surface made of particular composition. Care was taken to avoid charging of the sample surface while imaging; the process of imaging was done as quickly as possible without compromising the quality of the image. The images were digitally recorded and stored immediately.

3.2.2 Transmission electron microscopy

Morphological features were also observed using transmission electron microscope (TEM, model FEI Technai G^2 S-Twin) operated at 5 and 200 kV, respectively. The electron micrographs were acquired at different magnification. Detailed local structural features of the samples were obtained via high-resolution transmission electron microscope (HRTEM) and selected area electron diffraction (SAED) patterns. All the powder samples mentioned in the present study were dispersed in ethyl alcohol using probe/bath sonicator for 30 min. Thus dispersed specimen solution was dropped on a holy carbon coated copper grid. After proper drying, the copper grid with the sample was used for examination under TEM. A special procedure was used to prepare TEM samples of FLG/PVA composites. Initially, borosilicate glass was cleaned in acetone and isopropanol using bath sonication and finally rinsed with deionized water. It was then dried in hot air oven at 100 ºC for 1 h to remove residual alcoholic

contents. Polystyrene was then spin coated on the glass at 1000 rpm. The polystyrene coated glass was then dried at 130 ºC for 1 h. FLG/PVA composite solution was then spin coated at 8000 rpm on the surface of the polystyrene coated glass and subsequently dried at 130 ºC. A part of this film (FLG/PVA composite on top of polystyrene film) was then peeled from the glass and placed on the TEM grid which was then dipped in toluene to dissolve polystyrene leaving a free standing FLG/PVA composite film on TEM grid as shown in **Fig. 3.4**.

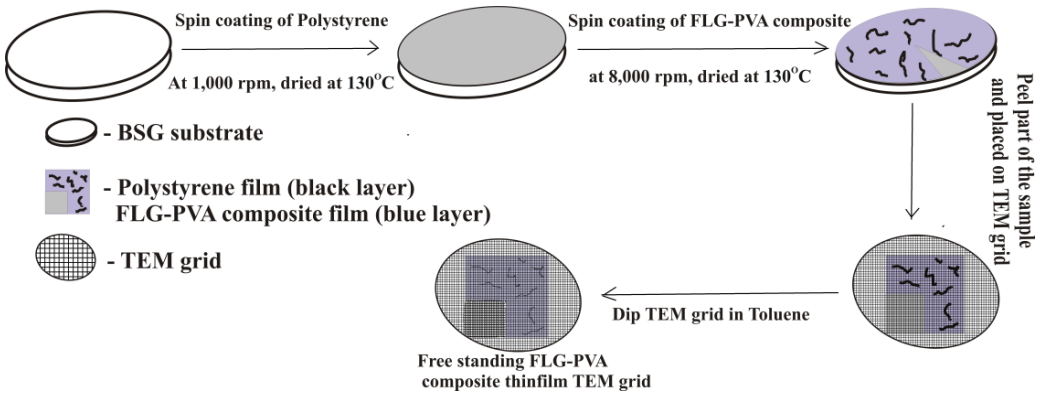

Figure 3.4 Schematic representation of TEM sample preparation of FLG/PVA composites.

3.2.3 X-ray diffraction

The crystallinity of the bulk ensemble of graphene and graphene-based composite powder samples and graphene/polymer composite sheets were determined by using x-ray diffraction (XRD) technique. The XRD patterns were recorded with Bruker AXS model D8 Advanced system in the 2θ range of 5 to 100° (range varies depending on the material) and at a step size of 0.02° using Cu Kα as the X-ray source (λ = 1.54 Å). These XRD patterns are used to determine lattice parameters, space group, crystallite size etc. In some cases, XRD patterns were further analyzed via the Rietveld refinement by using TOPAS (v2.1) software.

3.2.4 Raman spectroscopy

Raman spectra were collected in the air and at room temperature with (Renishaw Raman system 2000) auto-excitation wavelength with 1 µm spot size focused by 50X objective lens. For some other samples, Raman spectra were recorded in air using Nd-YAG laser (wavelength = 532 nm) operated at 40 mW power in the backscattering geometry using CRM spectrometer equipped with a confocal microscope (model alpha 300 of WiTec, Germany). The beam diameter of the laser was 680 nm (at 100X objective) and the resolution of the measurements was ~3 cm^{-1}. Raman spectra were recorded in the spectral region 200-3500 cm^{-1}.

3.2.5 BET surface area measurements

Specific surface area and porosity distribution of the samples were measured by performing N_2 physisorption (on Micromeritics, model Tristar 3000) at 77 K using Brunauer–Emmett–Teller (BET) and Barrett-Joyner-Halenda (BJH) multipoint methods. Samples were preheated under N_2 flow for 1 h at 180 °C. While recording N_2 adsorption and desorption isotherms, NTP conditions were maintained around the sample holder, and a mixture of He and N_2 gasses was flown-in according to the dynamic (flowing gas) technique. The adsorption-desorption isotherms data, specific surface area, pore size and pore volume were imported to an excel sheet using software attached to the Micromeritics instrument.

3.2.6 X-ray photoelectron spectroscopy

X-ray photoelectron spectroscopy measurements were carried out on the synthesized composite powders (especially anode materials) to estimate different bonds and their binding energy values present in the composite. Binding energy values were evaluated using XPS, AXIS Ultra DLD spectrometer (Kratos Analytica) with monochromatic Al Kα radiation. XPS data was analyzed by using Casa XPS software. Survey spectra were recorded in the energy range 0–1200 eV. Charge referencing was carried out against carbon C (C1s binding energy = 284.6 eV). Further bonding possibilities were derived by deconvolution of high-resolution spectra using PeakFit (version 4.01) software.

3.2.7 Thermogravimetric analysis

To know the amount of graphene in the composites, oxidative decomposition of the corresponding composite was performed in the temperature range, 25–1000 ºC at 10 ºC min^{-1} heating rate by using TA Instrument 2960 (DTA-TGA). To probe the formation mechanism of Ge/rGO composite, TG-DTA was also carried on GO, and precursor materials mixture (i.e., $4GO+GeO_2$) in the N_2 atmosphere and in the temperature range, RT to 900 ºC at a heating rate of 10 ºC/min and maintained at 900 °C for 1 hr. This part of the experiment is carried out with TA instrument SDT Q600 V20.9 Build 20 (Module DSC-TGA standard).

3.2.8 UV-VIS-NIR spectroscopy

Optical transmission spectra are recorded in the wavelength range 190-2400 nm by means of a dual beam spectrophotometer UV-vis-NIR model Jasco V-570 having a resolution limit of ±0.2 nm and a sample interval of 2 nm.

3.3 Li-ion Battery Fabrication and Testing

3.3.1 Coin cell fabrication

Prior to coin cell LIBs fabrication, electrodes (anodes) of composite materials prepared as follows. As-synthesized composite material (here $Co_2Mo_3O_8$/rGO or Ge/rGO) as the active material, polyvinylidene fluoride (PVDF) in N-Methyl-2-pyrrolidone (NMP) solvent as a polymer binder, and Super-P carbon (230 m^2g^{-1}) as a conductive additive in the weight ratio of 70:15:15 are mixed in the N-methyl-2-pyrrolidinone solvent at ambient conditions on a magnetic stirrer for 12 h to form electrode slurry. So-prepared electrode slurry was coated as ~25 µm thick film on an etched Cu foil (thickness ~10 µm) by using 'doctor blade' technique. After 12 h drying at 80 °C in a hot air oven, the electrode foil was pressed using stainless steel roller. Subsequently, the foil was cut into 16 mm diameter circular discs. The geometrical electrode area was around 2 cm^2, and mass of active material was estimated to be 2-4 mg (70% of overall electrode mass excluding Cu foil weight). All constituents of the battery namely bottom and top caps, electrodes, and separator were dried in vacuum oven at 80 °C for 12 h before pressing the coin cell type batteries. Coin cells CR2016 were assembled in Ar gas filled glove box (MBraun) by using the fabricated electrodes as anodes and Li metal (16 mm diameter and 0.59 mm thickness, Hohsen Corp.) as the counter electrode. Celgard 2502 polymer membrane was used as the separator while 1 M $LiPF_6$ in ethylene carbonate (EC) and dimethyl carbonate (DMC) (1:1 by volume, Merck Selectipur LP40) was used as the electrolyte. Thus fabricated coin cells are aged for 12 h for good absorption of the electrolyte into the electrode materials before used for electrochemical tests.

3.3.2 Galvanostatic cycling

The Li storage properties of the prepared anode materials are studied using Galvanostatic cycling (or constant current cycling) test on aged coin cells using a computer monitored Bitrode multiple battery tester (GC, model SCN, Bitrode, USA). All the coin cells are tested at room temperature in the voltage range of 0.005-3.0 V and at different current densities (it varies with the material). The storage capacity, cycling performance, stability etc., of the electrode materials, are investigated by carrying out a large number of charge-discharge cycles (a minimum of 50 charge-discharge sweeps). In a typical Galvanostatic cycling test, the lithiation or de-lithiation capacity of an electrode material in the coin cell can be calculated as a function of time taken for either to charge or discharge the cell to a particular voltage and current applied to the cell as expressed by **Eq. 3.2**. The capacity of the electrode is the product of the current

(in Amp) and time (in hours) taken for the complete lithium insertion/ removal and it is equivalent to the total charge stored or released by the electrode material. The capacity per unit mass is specific capacity given by

$$\text{Specific capacity } (C_S) = \frac{\text{Current x time taken}}{\text{mass of the electrode material}} = \frac{I \text{ x } t}{m} \qquad (3.2)$$

3.3.3 Cyclic Voltammetry (CV)

The supporting experiment for Galvanostatic cycling test is a cyclic voltammetry (CV) test which certifies of the electrochemical suitability of the material for lithiation and de-lithiation reactions via redox couple. A computer controlled Mac-pile system (MacPile II Biologic, France) was used to test the aged coin cells at a scan rate of 58 μV/s in the voltage range of 0.005-3.0 V and at room temperature. The current measured versus applied voltage is plotted to acquire the CV curves. The potential applied (between the reference electrode and the working electrode) to the coin cell was ramped at a scan rate of 58 μV/s from open circuit voltage (OCV) of the cell to 0.005 V during discharge and from 0.005 V to 3.0 V during charging for a certain number cycles. As per IUPAC convention, the anodic current is positive and the cathodic current is negative. When the potential applied for discharging and charging sweeps, a current flows through the electrode that either reduces (cathodic scan)/oxidizes (anodic scan) the analyte and the corresponding current (I) between the working electrode and counter electrode were measured and plotted against the potential. Thus observed current peaks at particular voltages in the CV curves were used to analyze and confirm the type of lithiation mechanism (such as intercalation, conversion, etc.,) occurred in the electrode. For example, intense current redox peaks in the voltage range of 0.15-0.25 V in CV curves of the graphite anode arise from Li-ion intercalation and de-intercalation into the van der Waal gaps of graphite through prismatic surfaces [184].

3.3.4 Electrochemical impedance spectroscopy

Electrochemical impedance spectroscopic (EIS) measurements of the coin cells were done with Solartron impedance/gain-phase analyzer (model SI 1255) coupled with a potentiostat (SI 1268) at room temperature in the frequency range 180000 to 0.003 Hz with an AC signal amplitude of 10 mV. The acquired impedance data was analyzed using Z-view software (version 2.2, Scribner Assoc., Inc.). The frequency dependent impedance measurements of electrode material were carried out on a coin cell at various charge states i.e., at OCV, discharged to 0.005 and charged to 3.0 V. The impedance against applied frequency (i.e.,

Nyquist plots) of the electrode plotted and obtained curve fitted to a semicircle in the higher frequency region and a 45° inclined straight line in the lower frequency region in general [185]. Further, the impedance data was modeled to an equivalent circuit (which contains series and the parallel combination of resistor, capacitor etc.,) and the values of the circuit element were acquired by using Z-view software. Thus modeled equivalent circuit and obtained values of circuit elements were used to understand the details of the lithium storage and release kinetics of the electrode and the corresponding consequences.

3.4 AC Conductivity Measurements

Complex permittivity and loss tangent of the samples were measured at room temperature and elevated temperatures (30-120 °C at the interval of 10 °C) in the frequency range of 20 Hz to 20 MHz with an LCR meter (model E4980A precession impedance analyzer, Agilent) in the parallel plate capacitor geometry.

3.5 Testing EMI Shielding

EMI shielding ability of the synthesized composites was studied using Agilent 8722ES vector network analyzer (VNA) as shown in **Fig. 3.5**. The composite sheets were placed in an X-band sample holder between the flanges of two standard X-band waveguides connected to coaxial waveguide adapters which are connected to the ports of the VNA. Full two port TRL calibrations were carried out on the adapter surfaces using the standard X-band waveguide calibration kit before placing the sample holder with samples for the measurements. The measured scattering parameters S_{11} and S_{21} are related to the reflected and transmitted power, respectively w.r.t the power incident on the sample surface. The incident power (P_i) on a shielding material is divided into reflected power (P_r), absorbed power and transmitted power (P_t) at the output of the shielding. The EMI shielding effectiveness (EMI SE) of a material is defined as $SE_{total} = -10\log(P_t/P_i)$ [186]. When an electromagnetic radiation is incident on a shielding material the sum of absorption coefficient (A), reflection coefficient (R) and transmission coefficient (T) must be equal to 1. R, T and A can be calculated from S-parameters using the below-given formulae:

$$
\begin{aligned}
R &= (E_R/E_I)^2 = |S_{11}|^2 = |S_{22}|^2 \\
T &= (E_T/E_I)^2 = |S_{12}|^2 = |S_{21}|^2 \qquad (3.3) \\
A &= 1 - R - T
\end{aligned}
$$

Figure 3.5 Vector Network Analyzer with x-band waveguide adapters and sample holder.

Total EMI SE (SE_{total}) is the sum of reflection from the material surface (SE_R), absorption of electromagnetic energy inside the material (SE_A) and multiple internal reflections (SE_M) of electromagnetic radiation, expressed as, $SE_{total} = SE_R + SE_A + SE_M$. The reflection is related to the impedance mismatch between air and absorber. Absorption is regarded as the energy dissipation of electromagnetic wave in the shielding material over multiple reflections at the interfaces and scattering from inhomogeneity inside the material while the multiple reflections are the consequence of impedance mismatch at the two sample-air interfaces. When $SE_{total} \geq$ 15 dB, it is usually assumed that SE_M is negligible and thus, $SE_{total} \approx SE_R + SE_A$. The effective absorbance (A_{eff}) can be therefore expressed as, $A_{eff} = (1 - R - T)/(1 - R)$. The shielding effectiveness due to reflection and absorption of the shielding material with respect to power of the effective incident electromagnetic wave inside the shielding material are expressed as

$$\begin{aligned} SE_R &= -10\log(1-R) \\ SE_A &= -10\log(T/(1-R)) \\ SE_{total} &= SE_R + SE_A = -10\log(T) \end{aligned} \qquad (3.4)$$

The temperature dependent S parameters (at 30, 60, 90, and 120 °C) were measured by placing the sample in an x-band sample holder between the flanges of two standard x-band waveguides connected to coaxial waveguide adapters in a furnace consisting a circular heating coil. Measurements at a particular temperature are taken by stabilising temperature for 30 min. The permittivity values are evaluated from experimental scattering parameters (S11 and S21) using Nicolson, Ross and Wire algorithms [187,188].

Chapter 4 Results and Discussion

4.1 Novel Anode Materials in Li-ion Batteries

4.1.1 $Co_2Mo_3O_8$/rGO composite

FESEM images of the as-synthesized composite are shown **Fig. 4.1**. The images clearly show that the composite consisted of submicron sized (lateral) and ~50±2 nm thick hierarchical hexagonal nanoplatelets of $Co_2Mo_3O_8$ attached to thin graphene layers of rGO similar to the observations in our previous work [189]. However, the high magnification images (**Figs. 4.1(b)**, **(c)** and **(d)**) show the nanoplatelets are more uniformly distributed and are entrenched between the graphene layers unlike in a previous work [189]. Such an architecture is expected to be beneficial when the material is tested as an anode in LIBs because the conducting graphene sheets facilitate much easier adsorption of electrolyte which leads to better conduction of Li-ions and electrons in the composite upon cycling. Super P carbon does not contribute to the overall electrochemical specific capacity. It provides good contact between the neighboring active anode particles as shown in **Fig. A5** of **Annexure 1**.

The morphology was further confirmed by analyzing TEM images which are shown in **Fig. 4.2**. Here it is very important to note that even after rigorous sonication during TEM sample preparation, $Co_2Mo_3O_8$ particles do not lose their contact with the graphene layers. TEM images clearly show that graphene sheets and some of the $Co_2Mo_3O_8$ nanoplatelets are semi-transparent to the electron beam. The thickness of the $Co_2Mo_3O_8$ nanoplatelets as measured from the TEM images was ~55.0±1.8 nm, a value close to that measured from FESEM images. TEM images also show that each of the $Co_2Mo_3O_8$ nanoplatelets is attached to the graphene sheets which are observed to be wrinkled, a case typical to that of rGO.

The diffraction peaks in the XRD pattern (**Fig. 4.3(a)**) of the composite could be indexed (also matched with the peaks corresponding to the JCPDS data file No. 34-0511 for $Co_2Mo_3O_8$ phase) to the hexagonal crystal structure of $Co_2Mo_3O_8$. Rietveld refined XRD data confirmed the formation of the composite. The refined data showed that 81.3% of it corresponded to the phase pure $Co_2Mo_3O_8$ while the remaining 18.7% corresponded to the combination of intense (002) and broad (004) diffraction peaks of rGO, and monoclinic MoO_2 phase (JCPDS file number #76-1807). (011) and (022) diffraction peaks of monoclinic MoO_2 appeared at 26.5° and 53.6°, respectively. Rietveld refinement showed that Co2Mo3O8 nanoplatelets have cryst-

-allized in hexagonal phase with lattice parameters *a*=5.785(8) Å and *c*=9.923(5) Å. The strong characteristic diffraction peak at 26.5° and a broad diffraction peak at 53.6° (both indicated with an asterisk in the **Fig. 4.3(a)**) correspond to (002) and (004) graphite planes in rGO.

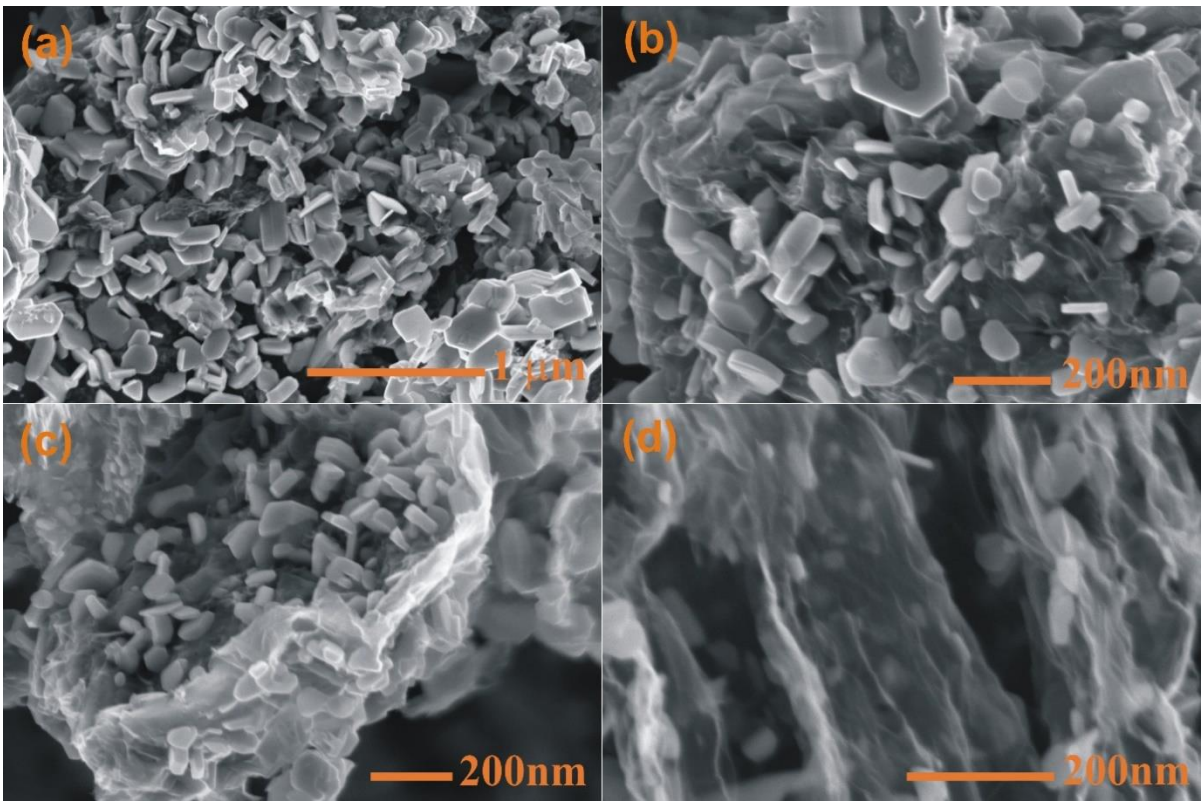

Figure 4.1 FESEM images of $Co_2Mo_3O_8$/rGO composite at different magnifications.

Raman scattering analysis further confirmed the presence of rGO in the composite. The appearance of characteristic Raman bands (as shown in **Fig. 4.3(b)**) namely the D band at ~1345 cm^{-1}, the G band at ~1588 cm^{-1} and the 2D band centered at ~2700 cm^{-1} (please see **Fig. 4.4**) confirmed the presence of rGO [190] in the composite. The intensity ratio I_D/I_G in the case of $Co_2Mo_3O_8$/rGO is ~0.92 which is greater than ~0.68 measured in the case of GO, suggesting the presence of more defects in the case of rGO in the composite than in the case of GO. On the other hand, the higher intensity of G band in comparison to that of D band in both rGO and GO cases indicates the presence of good-quality regular carbon hexagons in the material [190]. Raman bands related to $Co_2Mo_3O_8$ in the composite are shown in **Fig. 4.4**. For crystalline $Co_2Mo_3O_8$ (space group, $P6_3mc$), a maximum of 15 Raman active modes ($3A_1+6E_1+6E_2$) are allowed [130]. Raman spectrum of FLG-$Co_2Mo_3O_8$ composite shows 13 peaks and among which 11 of the expected 15 Raman modes correspond to $Co_2Mo_3O_8$. Based on the available literature [129], the bands at 360 and 435 cm^{-1} are assigned to (O-$(Mo\text{-}Mo)_{cluster}$-O) and (Mo-O-Mo) bending vibrations, respectively [130]. The peaks at and below 326 cm^{-1} are assigned

to Co-O bending vibrations of the CoO_4-tetrahedra and CoO_6-octahedra in the structure. Other higher order combinational modes are also observed at 726, 809 and 928 cm^{-1}.

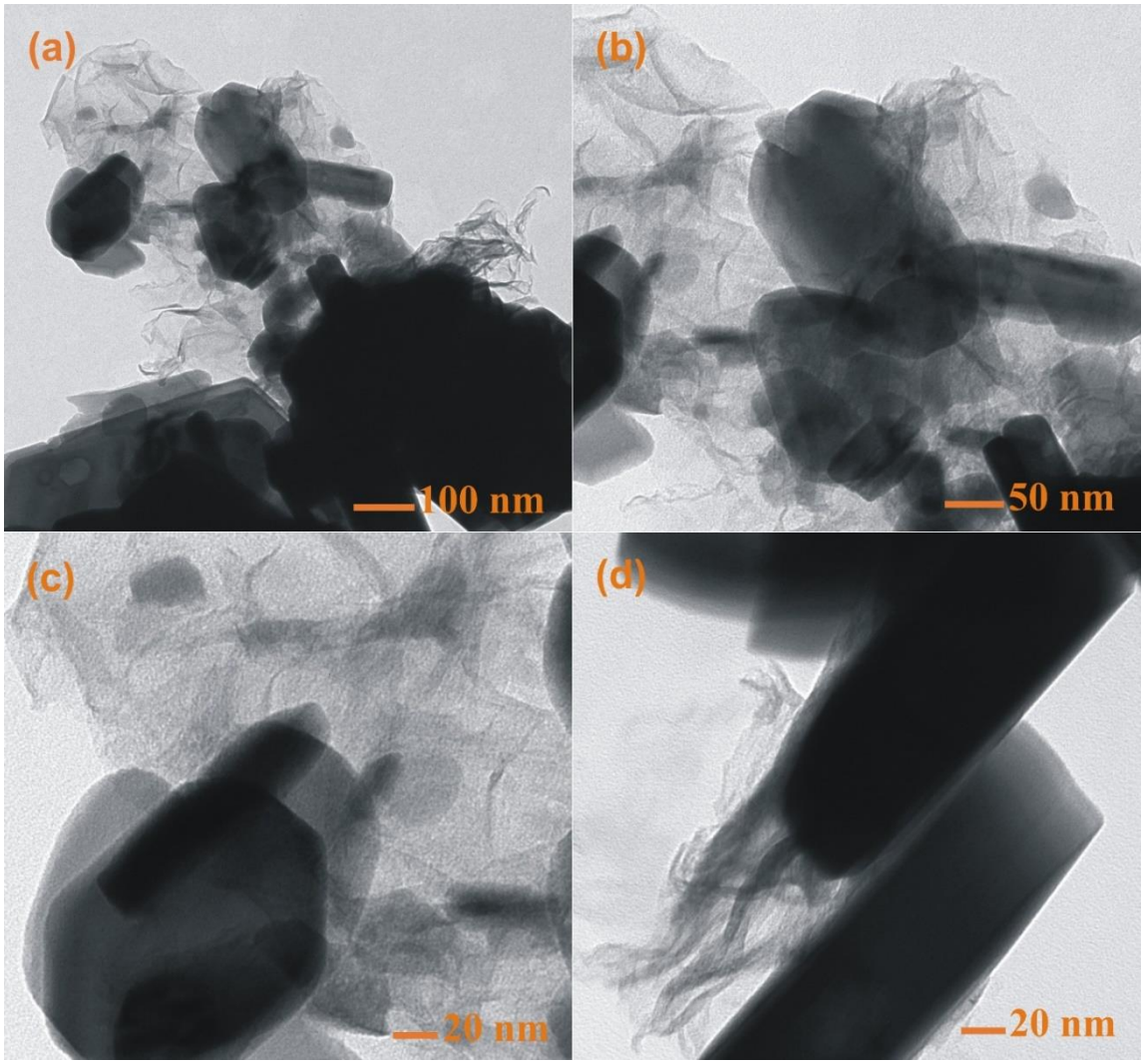

Figure 4.2 TEM images of $Co_2Mo_3O_8$/rGO composite at different magnifications.

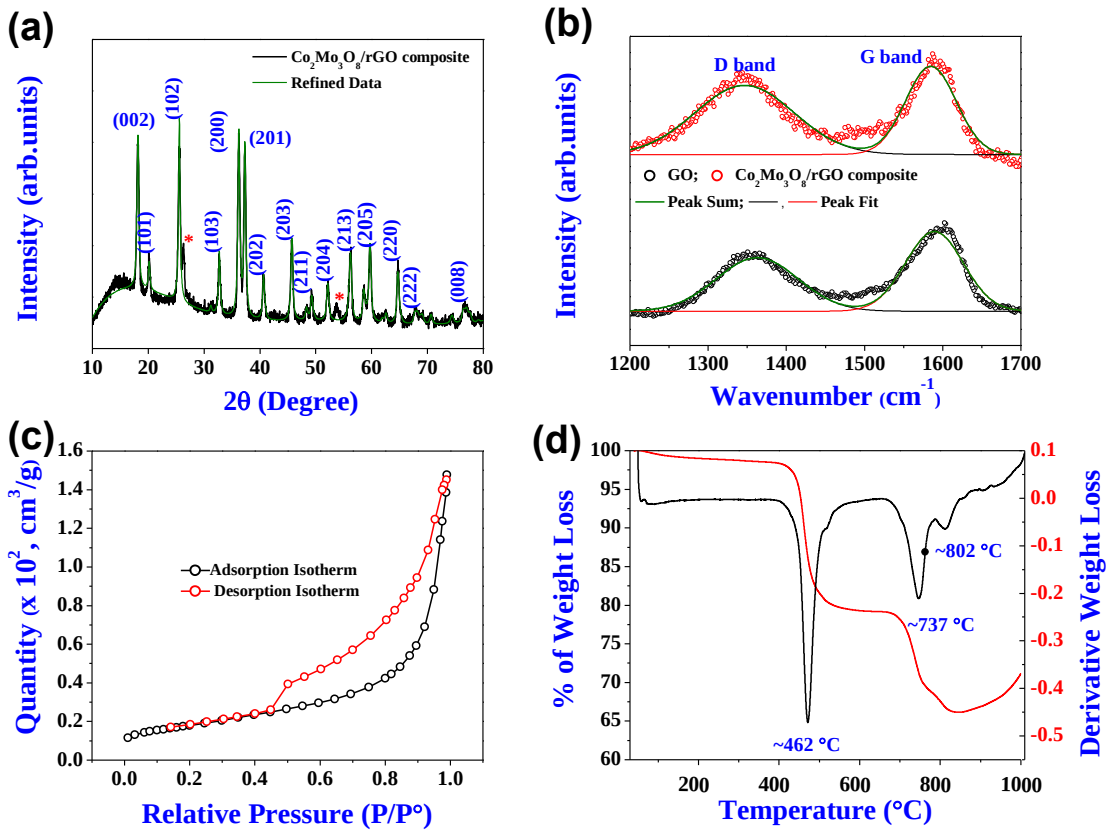

Figure 4.3 (a) X-ray diffractogram, **(b)** Raman spectrum, **(c)** N_2 adsorption and desorption isotherm and **(d)** weight loss versus temperature (TGA) and derivative weight loss versus temperature (DTA) curves of $Co_2Mo_3O_8$/rGO composite, respectively.

$Co_2Mo_3O_8$/rGO composite's N_2 adsorption and desorption isotherm are shown in **Fig. 4.3(c)**. It is representative of the type IV isotherm of IUPAC standard adsorption-desorption isotherms. This observation is similar to that of our previous report [189]. BET specific surface area and average pore diameter values of the composite powder are 63.8 m^2/g and ~11 nm, respectively. Present material is having higher specific surface area (63.8 m^2/g) and pore diameter than a previous report [189]. **Figure 4.3(d)** shows the thermal decomposition characteristics of the composite. It shows that there is a slight weight loss below 350 °C. This loss is attributed to the evaporation of physisorbed water molecules and the decomposition of some residual oxygen-containing groups on the rGO. A rapid weight loss at ~462 °C is attributed to combustion of carbon skeleton in the rGO [191]. Unlike in a previous report, [189] the oxidation of $Co_2Mo_3O_8$ is not observed here in the entire temperature range. This is an indication that $Co_2Mo_3O_8$ nanoplatelets are covered by graphene layers as indicated in by the electron micrographs. From the weight loss characteristics, the calculated weight fraction of rGO in the $Co_2Mo_3O_8$/rGO composite is ~22 wt. %.

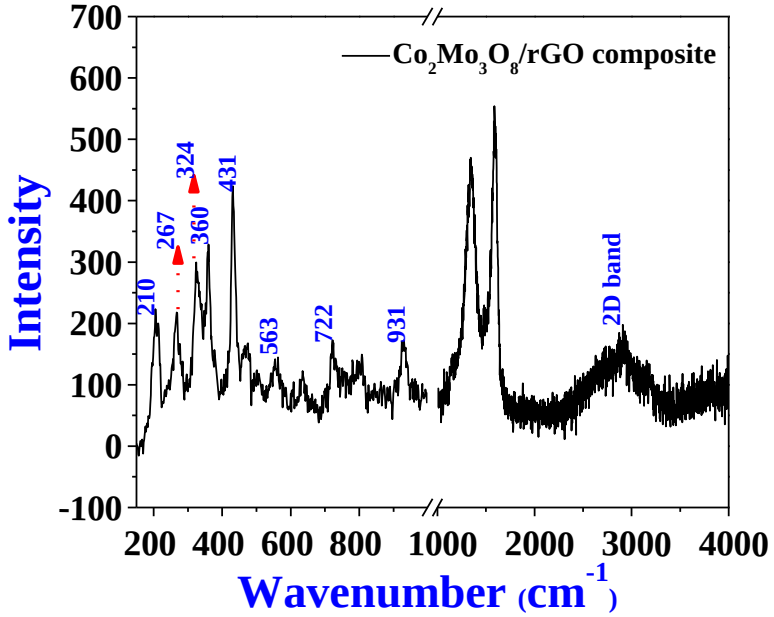

Figure 4.4. Raman spectrum of $Co_2Mo_3O_8$/rGO composite, respectively.

XPS measurements are carried out to evaluate the precise chemical bonding nature in $Co_2Mo_3O_8$/rGO composite. The high-resolution Co 2p X-ray photoelectron spectrum shown in **Fig. 4.5(a)** displays the characteristic Co^{2+} peaks at 778.4 eV and 794.0 eV which are ascribed to $2p_{3/2}$ and $2p_{1/2}$ levels, respectively. Two characteristic satellite peaks of Co^{2+} are identified at 783.8 and 800.1 eV, and the appearance of these peaks is due to the charge transfer from ligand to the metal during the photoemission process [192]. Similarly, as shown in **Fig. 4.5(b)** the spectrum of Mo 3d contains characteristic doublet at 230.5 ($3d_{5/2}$) and 233.6 ($3d_{3/2}$) eV corresponding to Mo^{4+} oxidation state. In addition to Mo^{4+} peaks, Mo^{6+} peaks are also found at 232.3 and 235.5 eV [193]. As shown in **Fig. 4.5(c)**, the characteristic C1s spectrum of the composite is deconvoluted into two peaks. The peak at 284.5 eV is assigned to either sp^2 or sp^3 hybridized carbon atoms in the graphene, and the peak at 285.5 eV arises from C-OH bond in the graphene's basal plane. The spectrum of O 1s shown in **Fig. 4.5(d)** contains two peaks at 527.3 and 529.4 eV which correspond to oxygen atom bonded to the lattice and the surface impurities, respectively [194]. All in all, the XPS analysis confirms the oxidation states of Co and Mo as 2+ and 4+, respectively. The observed Mo^{6+} state is speculated to be either due to surface oxidation of $Co_2Mo_3O_8$ or change in oxygen co-ordination during measurements. However, any features of Mo^{6+} (MoO_3) state are neither identified in XRD analysis nor in CV (redox couple at 2.5V) analysis.

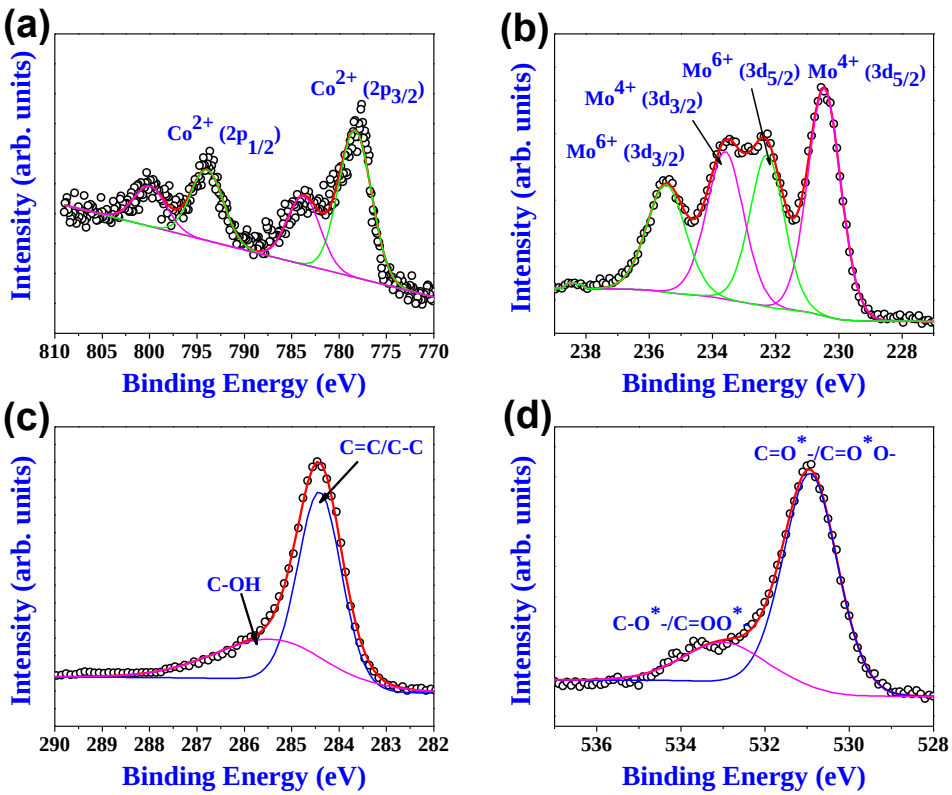

Figure 4.5 X-ray photoelectron spectra of $Co_2Mo_3O_8$/rGO composite: **(a)** Co 2p peak, **(b)** Mo 3d peak, **(c)** C 1s peak and **(d)** O 1s peak.

Owing to the above-discussed characteristics, it is expected that there will be an easy electrolyte access to the electrode material, and there will be low contact and charge transfer impedances and short transport lengths for both Li-ions and electrons when $Co_2Mo_3O_8$/rGO composite is tested as an anode material in LIBs.

A series of electrochemical measurements were carried out to test the potential usage of the $Co_2Mo_3O_8$/rGO composite as anode material in LIBs. **Figure 4.6(a)** shows the CV characteristics of $Co_2Mo_3O_8$/rGO composite during the first six cycles of both cathodic and anodic scans in the voltage range of 0.005-3.0 V and at a scan rate of 58 μV/s. The CV curves are subtly different than those reported previously [189]. In the first cathodic scan, two primary reduction peaks are observed, a peak at 0.6 V and a sudden rapid increase in the cathodic current leading to the appearance of a broad peak in between 0.5 and 0.005 V. Similarly in the first anodic scan, two oxidation peaks at ~1.43 and ~1.78 V are assigned to oxidation of Co^0 and Mo^0 metal nanoparticles (formed during the 1st cathodic scan) to metal oxides, respectively. Asymmetry in the CV curves indicates irreversibility in the Li ions' cycling which resulted in less Coulombic efficiency (~64 %, as shown in **Fig. 4.6(c)**) in the first cycle. From the 2nd cathodic scan onwards, reduction peaks in the 1st cathodic scan have shifted towards higher

voltages (i.e., 0.7 and 0.16 V, respectively and also attained symmetry) with constant reduction currents. New reduction peaks which correspond to Li ions uptake into both rGO and $Co_2Mo_3O_8$ lattice have also appeared [131]. The large current difference between 1st and 2nd cathodic scans and shift in peak positions are expected due to the combined effect of irreversible lithium insertion in the lattice, electrolyte decomposition, solid electrolyte interphase [189], and conversion of Co^{2+} and Mo^{4+} to their metallic states and the formation of amorphous Li_2O phase as shown in **Eq. 4.1**.

$$Co_2Mo_3O_8 + 16Li^+ + 16e^- \rightarrow 2Co^0 + 3Mo^0 + 8Li_2O \qquad (4.1)$$

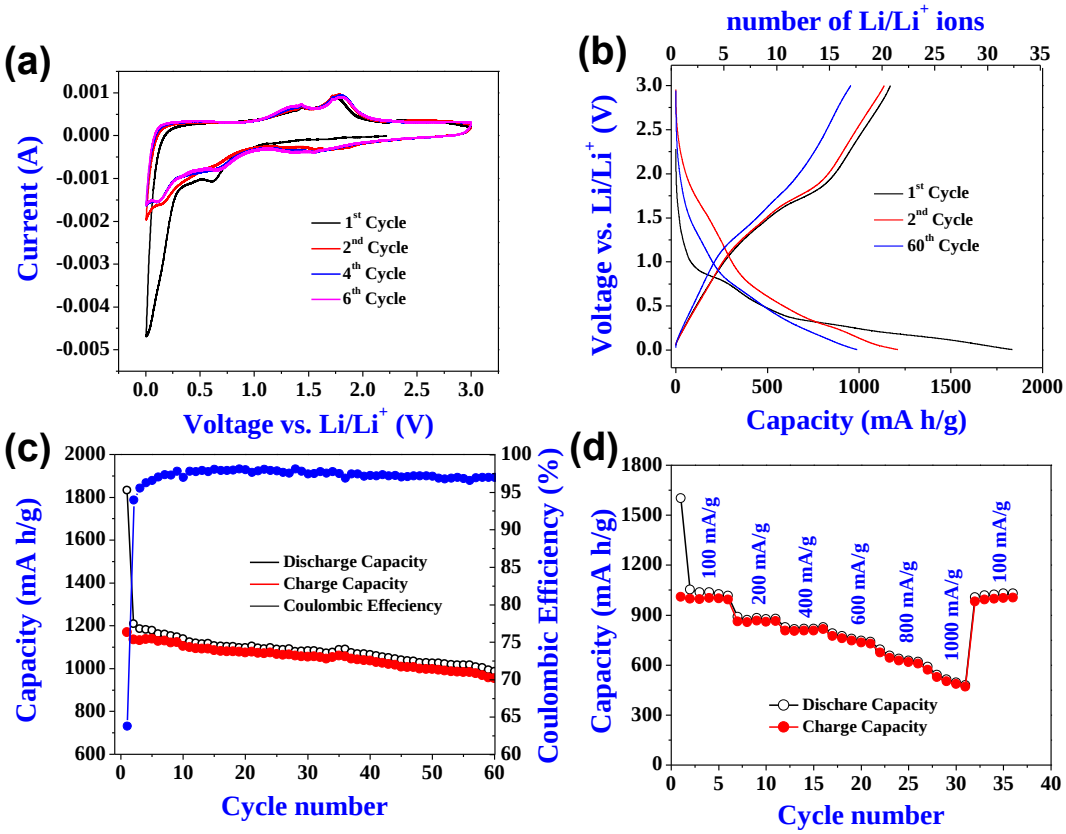

Figure 4.6 (a) Cyclic voltammetry curves at different cycles in the voltage range 0.005-3.0 V vs. Li and at a scan rate of 58 μV/s, **(b)** Galvanostatic discharge and charge curves at 1st, 2nd and 60th cycles in the voltage range of 0.005-3.0 V vs. Li and at a current density of 60 mA/g, **(c)** Discharge-Charge specific capacity and Coulombic efficiency vs. Cycle number and **(d)** rate capability in the voltage range 0.005-3.0 V vs. Li of $Co_2Mo_3O_8$/rGO composite.

From the 2nd cycle onwards, in the cathodic scan, another two broad new reduction peaks centered at 1.30 and 1.70 V are observed, unlike in the previous report [189]. The appearance of these peaks is an indication of an excellent reduction of precursor materials to $Co_2Mo_3O_8$/rGO composite without impurities. The redox couples at 1.70/1.80 and 1.30/1.45 V correspond to the phase transition of MoO_2 due to partially lithiated Li_xMoO_2 phase, i.e., from

monoclinic phase to orthorhombic phase and vice versa during Li insertion and extraction processes, respectively [118]. Evolution of the two extra peaks form the 2nd cathodic scan onwards might have originated due to the formation of MoO_2 formed during the 1st cycle through $Co_2Mo_3O_8$ crystal structure destruction during Li insertion (1st reduction) that eventually lead to the formation of metal nanoparticles surrounded by Li_2O phase (during 1st discharge) and conversion of these metal nanoparticles to metal oxides (during 1st oxidation) as per **Eq. 4.1**. Interestingly, it is noticed that compared with the previous report [189], from the 2nd cycle onwards, the area under the redox curves and intensity of redox peaks are constant throughout the test. This is an indication of stable cyclability which is expected due to the presence of good cooperation between $Co_2Mo_3O_8$ nanoplatelets and graphene layers in the composite material.

Further, to test the composite's cyclability and rate capability, and to support CV observations GC tests were carried out. **Figure 4.6(b)** shows the 1st, 2nd and 60th discharge and charge cycles of $Co_2Mo_3O_8$/rGO composite in the voltage range of 0.005-3.0 V and at a current density of 60 mA/g. In the GC test, it is observed that the composite has delivered an excellent specific capacity of ~1834 mA h/g during the first discharging scan from the open circuit voltage (i.e., ~2.3 V, as shown in **Fig. 4.6(b)**) to a lower cutoff voltage of 0.005 V and as a result of this, a total of 33 Li^+ ions are stored in the electrode.This specific capacity value ~1834 mA h/g is much higher than the theoretical capacity [131,189] value ~873 mA h/g of the $Co_2Mo_3O_8$/rGO composite (theoretical specific capacity of the composite = 78% (theoretical specific capacity of the $Co_2Mo_3O_8$) [131]+22% (theoretical specific capacity of the rGO) [89]). The expected high value of specific capacity is supported by the slope change between 0.9 and 0.3 V accompanied by small voltage plateaus and after that, a continuous decrease in voltage till the lower cutoff voltage 0.005 V is reached. Similarly at the end of first charging curve a reversible specific capacity of ~1170 mA h/g is delivered by the electrode through gradual increase in the voltage (which is started from lower cutoff voltage 0.005 V) and a sudden change in slope at ~1.8 V and thereafter continuous increase in the voltage till it reaches its upper cutoff voltage 3.0 V. As shown in **Fig. 4.5(c)**, at the end of the first cycle ~64 % of Coulombic efficiency (QE) is recorded. This whole cycle resulted in an irreversible capacity loss (ICL) of 664 mA h/g which is equal to a loss of ~12 Li/Li^+ ions (it is in support with observed asymmetry in the CV curves). ICL is expected due to an irreversible transfer of Li/Li^+ ions by the formation of SEI film on the electrode through initial decomposition of electrolyte in the solvent [131, 189, 195-197]. The subsequent cycles (2nd and 60th cycles) have also followed a similar trend as that of the first cycle with much reduced ICL as the cycle number is increased (for example, QE of

~98% is noticed at 30th cycle). The present study also highlights superior cycling behavior of the $Co_2Mo_3O_8$/rGO composite than the other Mo_3-cluster compounds reported to date. When cycled at a current density of 60 mA/g and in the voltage range of 0.005-3.0 V vs. Li, a reversible specific capacity of ~954 mA h/g is delivered by the electrode at the end of the 60th cycle (as shown in **Figs. 4.6(b)** and **(c)**). The higher specific capacity and lower ICL values in this work are much better than the respective values exhibited by pure $Co_2Mo_3O_8$ [131] and FLG-$Co_2Mo_3O_8$ composite [189]. The remaining discharge-charge cycles are shown in **Fig. A4** of **Annexure A1**. Further, the cycling stability of the prepared anode material is studied by conducting rate capability tests. **Figure 4.6(d)** shows specific capacity versus cycle number profiles of $Co_2Mo_3O_8$/rGO composite electrode at different current densities. The reversible specific capacities of 1001, 866, 816, 729, 628, 503 and 1006 mA h/g at current densities of 100, 200, 400, 600, 800, 1000 and 100 mA/g are measured, respectively. A minute capacity decay at higher current densities (i.e., 600 to 1000 mA/g) might have originated from partial loss of contact between $Co_2Mo_3O_8$ nanoplatelets and rGO on cycling at higher current rates. It is observed that even after returning to the current density of 100 mA/g from the highest current density, the discharge specific capacity was 1030 mA h/g (corresponding charge capacity was 1006 mA h/g), which is an indication of the excellent stability of the electrode material even after many cycles at different current rates. The higher specific capacity, longer cycle life and better rate capability of the $Co_2Mo_3O_8$/rGO composite material is expected due to the composite's architecture which facilitates good conduction in the electrode material while the composite's high surface area facilitates easy electrolyte absorption and causes ion/electron diffusion more feasible [4,132]. The excellent electrochemical properties of the present material with the available Mo_3-cluster compounds are compared in **Table 4.1**.

EIS measurements are carried on the cycled coin cell batteries in the frequency range 180000 to 0.003 Hz to understand the Li-ion storage mechanism of the $Co_2Mo_3O_8$/rGO composite and support the GC and CV observations. **Figure 4.7** shows Nyquist plots of the coin cell batteries in different charge states (i.e., at OCV, 1st discharged, and 1st charged). EIS results about all the three stages of are fitted to one equivalent circuit (inset of **Fig. 4.7**), which is similar to the previous report [189].

Table 4.1 Comparison of the present results with the available literature.

Mo_3-cluster compound (or composite)	**Synthesis procedure[a]**	**Voltage range (V)**	**Reversible specific capacity (mA h/g) @ current density (mA/g) & cycle number**
$LiYMo_3O_8$ [130]	CTR	0.005-3.0	385 @ 30 & 120th
$Mn_2Mo_3O_8$ [130]	CTR	0.005-3.0	205 @ 30 & 50th
$Co_2Mo_3O_8$-heat treated [131]	CTR	0.005-3.0	790 @ 60 & 60th
$Cu_3Mo_2O_9$ [198]	SC	0.01-3.0	754 @100 & 80th
			484 @ 500 & 38th
FLG-$Co_2Mo_3O_8$ [189]	GTR	0.005-3.0	607 @ 180 & 50th
FLG-$Mn_2Mo_3O_8$ [189]	GTR	0.005-3.0	518 @ 180 & 50th
FLG-$Zn_2Mo_3O_8$ [189]	GTR	0.005-3.0	579 @ 180 & 50th
$Mn_2Mo_3O_8$-graphene [4]	SC	0.01-3.0	951@ 200 & 40th
			672 @ 1500 & 20th
$Fe_2Mo_3O_8$-graphene [132]	SC	0.01-3.0	835 @ 200 & 40th
			574.8 @ 3000 & 1st
Present study	GTR	0.005-3.0	954 @ 60 & 60th
			729 @ 600 & 21st
			471 @ 1000 & 31st

[a]CTR-Carbothermal reduction, SC- solution chemistry and GTR- Graphenothermal reduction

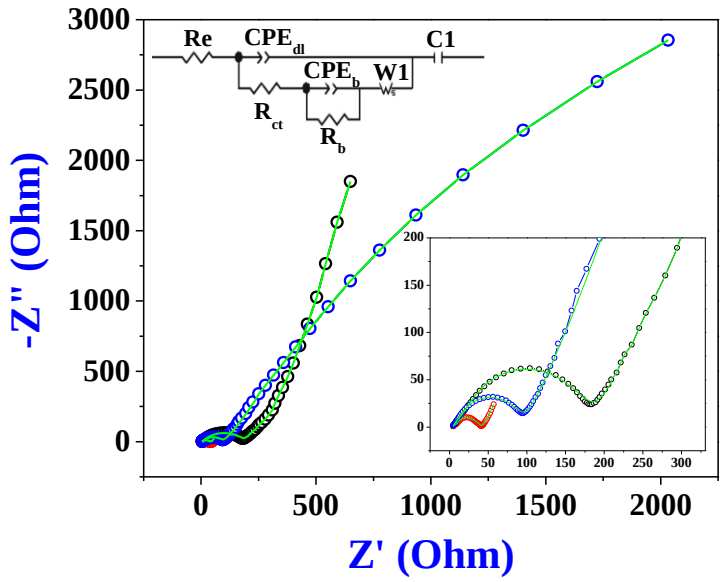

Figure 4.7 EIS curves of $Co_2Mo_3O_8$/rGO composite at different charge states (black, red, and blue color circles represent OCV, 1st discharge, and 1st charge scanned, respectively) with curve fitting (solid line in green color) and the inset shows the magnified portion of the EIS curves at $Z' < 300$ and the equivalent electrical circuit.

Certain elements (related to EIS results) that are necessary to understand the Li-ion storage kinetics and their values are tabulated in **Table 4.2**. The contact (or solvent) resistance (R_e) for

1st discharge scan has decreased and slightly increased for 1st charge scan as compared to OCV. It is expected due to the formation of insulating SEI on the electrode surface during the 1st cycle. Resistance to charge transfer (R_{ct}) in both cases is less than OCV, and it followed a decreasing trend. The lower R_{ct} value of the 1st charge scan than the 1st discharge scan is an indication for easy removal of Li ions due to the presence of highly conducting and high surface area graphene and excellent synergy between graphene and $Co_2Mo_3O_8$ nanoplatelets. After the 1st discharge and charge scans, two orders of increase and one order of decrease in the electric double layer capacitance (CPE_{dl}) values are observed, respectively, and this is expected due to formation of thick SEI film on the electrode surface while first discharge leads to form dense dielectric medium between active electrode and charge carriers in the electrolyte which causes the increase in CPE_{dl}. A continuous decrease in the values of the bulk resistance (R_b) and bulk electric double layer capacitance (CPE_b) are observed, and this is expected due to easy electrolyte access throughout the electrode to make a smooth transfer of ions or electrons in the electrode. Similar to CPE_{dl}, intercalation capacitance (C_i) and Warburg element (Li-ion diffusion, W_i) first increased and then decreased. In all three stages, subtle values of intercalation capacity C_i [199] and very high values of Warburg element W_s (resistance to Li-ion diffusion) are found when compared to R_e and R_{ct}. The very low value of C_i indicates that Li storage preferably takes place either by redox couples of Mo-clusters or electrochemical adsorption by graphene layers [198]. The EIS results supported the GC and CV results in the 1st cycle and are expected to be in line with for other cycles also.

Table 4.2 EIS results of the $Co_2Mo_3O_8$/rGO composite at OCV, 1st discharged, and 1st charged states.

Sample Status	R_e	R_{ct}	CPE_{dl} (μF)	R_b	CPE_b (mF)	C_i (F)
$Co_2Mo_3O_8$/rGO Fresh cell	4.6±0.04	36.5±3.8	39.6±6.1	139.2±3.3	0.02±0.004	0.04
$Co_2Mo_3O_8$/rGO Discharged state	4.0±0.00	16.5±0.0	354.6±0.0	85.0±0.0	0.006±0.0	0.05
$Co_2Mo_3O_8$/rGO Charged state	4.2±0.00	4.5±0.0	1.0±0.0	21.4±0.0	0.004±0.0	0.02

4.1.2 Ge/rGO composite

Morphological features of the GR14 composite powder were studied using TEM. The bright field transmission electron micrographs of GR14 composite shown in **Figs. 4.8(a)** and **(b)**, reveal that clusters of Ge particles are decorated on semi-transparent graphene layers. Enlarged images of the encircled regions in **Fig. 4.8(c)** (high resolution TEM image) show that the Ge nanoparticles are anchored on graphene sheets and the measured d-spacing of 0.21 nm matches with the spacing between (220) planes of the diamond cubic crystal phase of Ge. Also the presence of graphene layers (shown in the rectangular box) is also clearly observed from **Fig. 4.8(c)**. During the synthesis of GR14 composite, as the temperature is applied to reduce the precursor material, the presence of GO in the reaction triggers a combustion type of reaction which produces high temperatures locally. This action stimulates the rapid release of hot gasses and formation of amorphous carbon from GO, and these by-products reduce GeO_2 particles to Ge (as also revealed by Rietveld refinement of XRD data of the precursor material heated at different temperatures). Also, there is every possibility that the rapidly escaping gases can aid in carrying the Ge forming precursor species and spread them on the graphene sheets so as the form individual Ge particles (**Fig. 4.8(b)**) as the solidification took place as the reaction is completed and the temperature gradually decreases. This kind of morphology (two-dimensional- two-dimensional interaction) secures significant bonding between Ge particles and rGO and the composite's high specific surface area, which are the primary requirements for a good anode material in LIB. Further, the selected area electron diffraction pattern shown in **Fig. 4.8(d)** evidences the presence of both hexagonally crystalline graphene and diamond cubic Ge in the composite material.

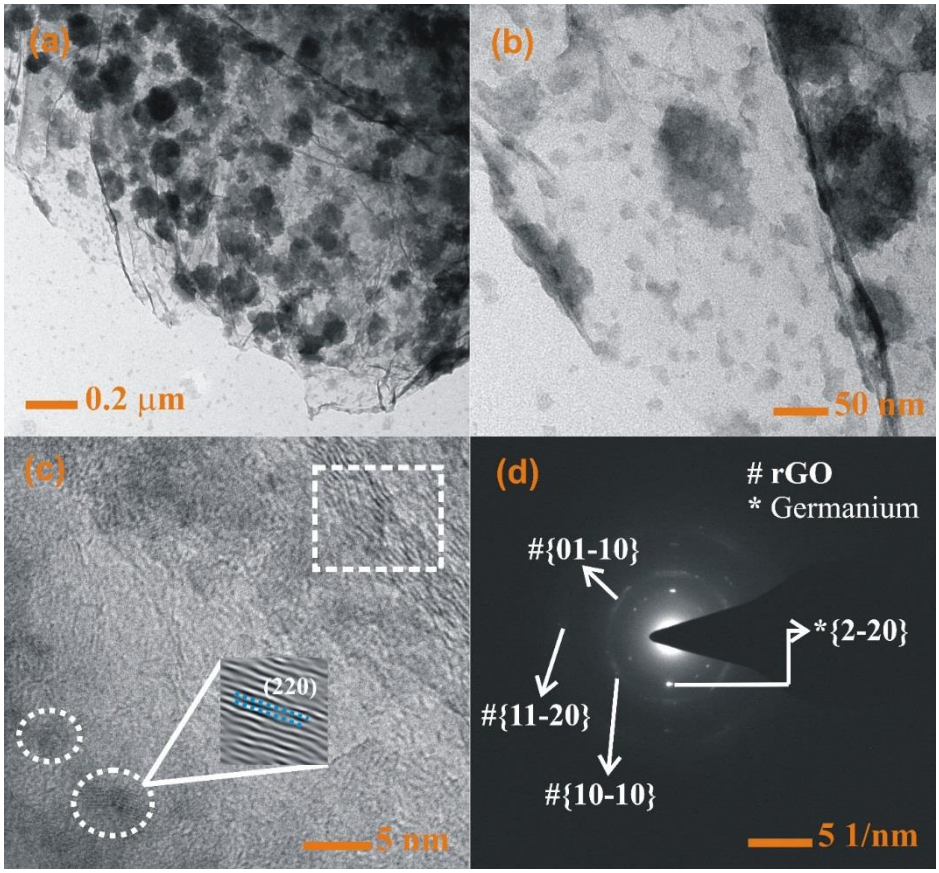

Figure 4.8 (a, b) Bright field transmission electron microscope images, **(c)** high-resolution transmission electron microscope image and **(d)** selected area electron diffraction pattern of the GR14 composite.

X-ray diffractograms of GO, GeO_2, and GR14 composite powders are shown in **Fig. 4.9(a)**. It is observed from x-ray diffractograms that the synthesis conditions are optimal to convert the precursor materials (i.e., GO and GeO_2) into the final composite material (i.e., GR14). (111), (220), (311), (400) and (331) diffraction peaks belong to the diamond cubic crystal structure of Ge while their broadness indicates that the obtained material consists of nanosized crystallites. Using Debye-Scherrer formula $D = k\lambda / \beta\cos\theta$ (D is crystallite size of germanium, k is Scherrer's constant (0.89), λ is wavelength of the X-rays (i.e., ~1.5418Å), $\beta = \sqrt{(\beta_S^2 - \beta_I^2)}$, here β_s and β_I are FWHM of the sample and instrument (i.e., 0.045) and θ is the diffraction angle), the calculated crystallite size of Ge in the GR14 composite is 8.48±0.3 nm. The humps observed at 2θ equals to 26.5° and 44.5° are indexed to graphene's (002) and (004) diffraction peaks. The appearance of these peaks is expected due to complete exfoliation of GO to form graphene layers. In contrast, a sharp X-ray diffraction peak of GO at 2θ equals to ~11° is indexed to (002) graphitic peak as a result of increased d-spacing due to oxidation of graphite to form GO. This peak typically appears at 2θ equals to 26.5° in the case of graphite. Similarly,

X-ray diffractogram of GeO_2 shows that it crystallized in the hexagonal structure. Further, phase information was extracted by analyzing Raman spectra shown in **Fig. 4.9(b)**. The characteristic Raman peaks at 298 and 441 cm^{-1} correspond to the optical mode of crystalline Ge and the symmetric Ge-O-Ge stretching mode of Ge [3, 200]. Raman scattering analysis further confirmed the presence of rGO in the composite. The appearance of characteristic Raman bands such as disorder induced D band, graphitic G band, and 2D band (at ~2682 cm^{-1} as shown in **Fig. A6** of **Annexure 2**) confirmed the presence of graphene in the composite [190]. These bands with their corresponding positions and normalized intensities are tabulated in **Table 4.3**. The I_D/I_G ratio of the GR14 composite and GO are 1.00 and 0.83, respectively suggesting the presence of more defects in graphene (in the composite) than in the GO. On the other hand, the higher intensity of G band in comparison to that of D band in both graphene (in the composite) and GO indicates the presence of good-quality regular carbon hexagons in the material [190]. **Fig. 4.9(c)** represents N_2 adsorption and desorption curves of the GR14 composite. The small hysteresis is the manifestation of the presence of porosity in the material, and it is in tune with average pore size and pore diameter. Calculated BET specific surface area, average pore volume, and average pore size of the GR14 composite material are ~115.45 m^2g^{-1}, ~0.405 cm^3g^{-1}, and ~14 nm, respectively. This specific surface area of the GR14 composite is slightly smaller when compared with thermally reduced GO prepared under similar conditions [201]. The reason for lower specific surface area is expected due to the presence of Ge nanoparticles which are decorated on the active sites of the underlying graphene, and they may not have effectively allowed adsorption of N_2 molecules on the composite's surface. The thermal decomposition (in the temperature range of 50-1000 °C at 10 °C/min scan rate) of the GR14 composite in air was carried out to quantify the amount of graphene in the composite. As shown in **Fig. 4.9(d)**, the weight loss versus temperature and derivative weight loss versus temperature curves of the GR14 composite indicate that decomposition of the composite is majorly a two-step process in the considered broad temperature range. The weight loss below 450 °C (a broad peak centered at 117 °C) is assigned to evaporation of physically adsorbed water molecules and the decomposition of some residual oxygen-containing groups on the graphene. A rapid weight loss at ~613 °C is attributed to combustion of carbon skeleton in the graphene as observed also in a previous report [191]. The oxidation of Ge to GeO_2 was found in the considered temperature range and it is the manifestation of the observed morphology of the composite. The calculated weight fraction of graphene in the GR14 composite is ~66 wt. %.

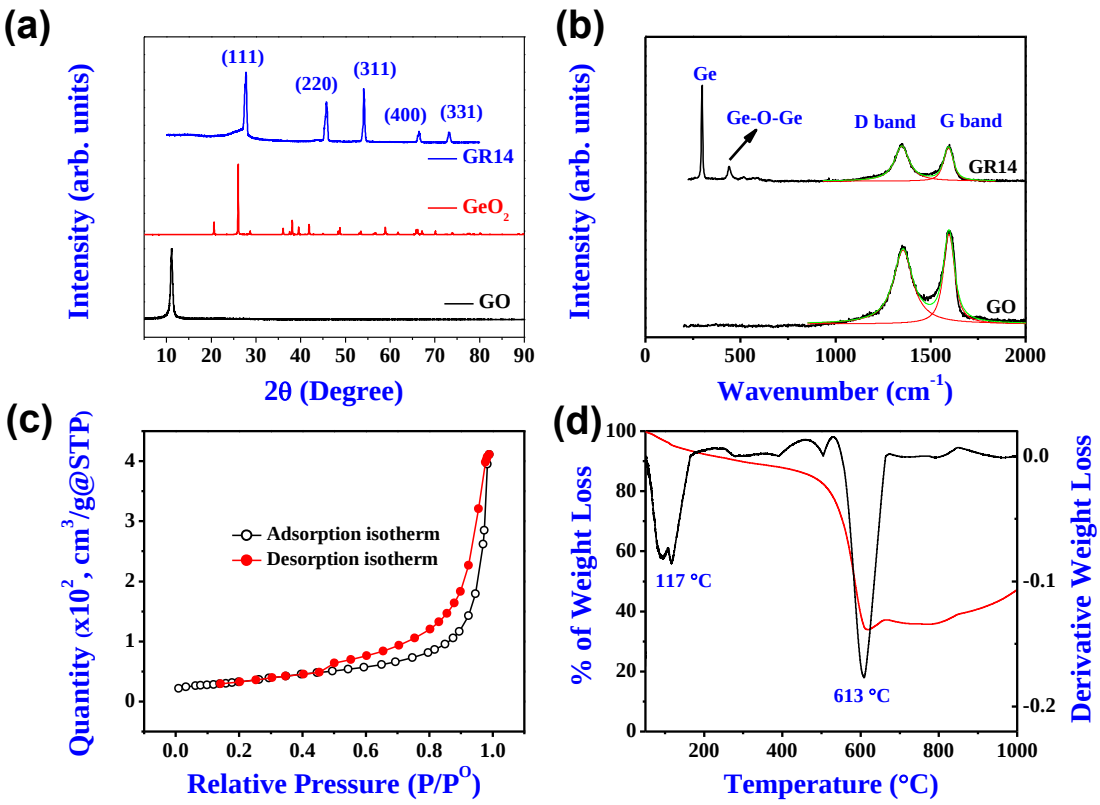

Figure 4.9 (a) X-ray diffractograms of GR14 composite, GeO_2 and GO powders, **(b)** Raman spectra of GR14 composite and GO powder, **(c)** N_2 adsorption and desorption isotherms and **(d)** thermogravimetric (weight loss vs. temperature, black in color) and differential thermogravimetric curves (rate of weight loss vs. temperature, red in color) of GR14 composite, respectively.

Table 4.3. Raman band positions and corresponding normalized intensities of GR14 composite and GO.

Compound	D band		G band	
	ν_D[a]	I_D[b]	ν_G[a]	I_G[b]
GR14	1347/cm	1.875	1593/cm	1.856
GO	1354/cm	0.801	1596/cm	0.965

[a]wavenumber of corresponding band, [b] intensity of the corresponding band

XPS measurements are carried out to know precise chemical composition of the GR14 composite. As shown in **Fig. 4.10(a)**, the spectrum of Ge 3d fitted to single characteristic peak at 30.2 eV arises due to the existence of Ge in its zero valence state (i.e., 3d) [107,200,202,203]. As shown in **Fig. 4.10(b)**, the characteristic C 1s spectrum of the composite is deconvoluted into three peaks. The peak at 284.4 eV is assigned to either sp^2 or sp^3 hybridized carbon (C=O/C-O) atoms in the graphene and the peaks at 285.1 eV and 287.8 eV arise from C-OH and C=O bonds, respectively, in the graphene's basal plane [201-203]. The spectrum of O 1s

shown in **Fig. 4.10(c)** contains two peaks at 530.9 and 532.7 eV which correspond to oxygen atom bonded to the lattice and the surface impurities, respectively [201].

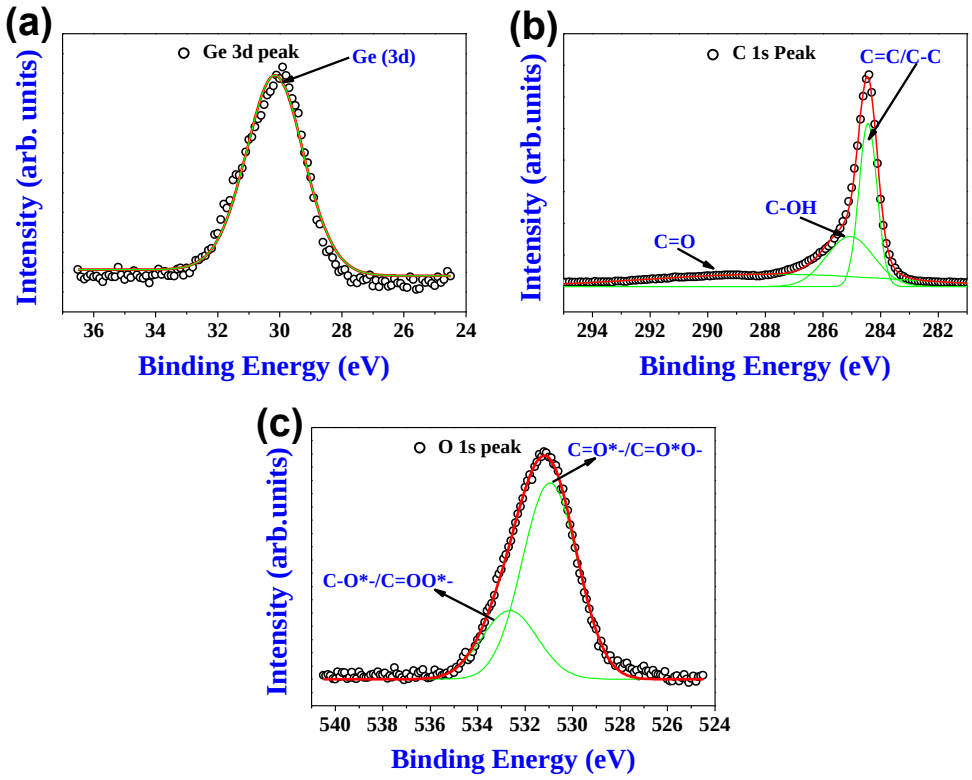

Figure 4.10 X-ray photoelectron spectra of the GR14 composite, **(a)** Ge 3d peak, **(b)** C 1s peak and **(c)** O 1s peak.

In a separate experiment, GeO_2: GO=1:4 mixture (GR14_Raw) was heated in a nitrogen environment to understand the reduction mechanism of GeO_2 to Ge in the presence of GO. This experiment is carried out in the temperature range of 27-900 °C and at a scan rate of 10 °C/min and at a maintained temperature of 900 °C for 1 h (these conditions are similar to the experimental conditions). As shown in **Fig. 4.11(a)**, the recorded TGA curve indicates three stages of reduction of the precursor mixture to form the GR14 composite. Initial two stages show a weight loss of volatile gasses and water molecules from GO and decomposition of various functional groups from GO [204]. The weight loss between 250 and 800 °C is very slow. A sudden drop in weight observed in between 800 and 900 °C is expected due to complete reduction of GeO_2 to Ge in the presence of GO. To further understand the reduction mechanism, ex-situ X-ray diffraction data was collected from heat treated (at different temperatures (i.e., room temperature (RT), and 550, 680, 800, 850 and 900 °C) GR14_Raw sample. **Fig. 4.11(b-h)** represents the Rietveld refined X-ray diffraction data of GR14_Raw at different temperatures in comparison with X-ray diffraction data of GeO_2 (at RT). Rietveld refined X-ray diffraction data of GeO_2 confirms that it crystallizes in hexagonal and tetragonal

phases with R_{wp} of 80.903 and 19.097, respectively. Whereas GR14_Raw sample only refined to hexagonal phase. When GR14_Raw sample is heat treated at different temperatures, along with hexagonal GeO_2 phase, cubic Ge phase is also observed with varying R_{wp}. At 850 °C, Ge cubic phase (with R_{wp} is 57.187) is more than the hexagonal GeO_2 (with R_{wp} is 42.813). At 900 °C GeO_2 is totally converted into Ge as shown in **Fig. 4.11(h)**. Rietveld refinement parameters of GR14_Raw at different temperatures are tabulated in **Table A3** of **Annexure 2**. Rietveld refinement reveals that major reduction of GeO_2 to Ge in the presence of GO took place between 850 to 900 °C. This observation is in line with the observed weight loss as indicated by TG-DTA curves of GR14_Raw. As discussed in the introduction, thermal reduction of GO leads to release of gasses like H^+/H_2, CO, and formation of amorphous carbon and based on the observed Rietveld refinement results of the GR14_Raw sample at different temperatures the following equations are proposed for the formation of Ge from GeO_2.

$$\begin{aligned} C + GeO_2 &\rightarrow Ge + 2CO(g) \\ 2CO + GeO_2 &\rightarrow Ge + 2CO_2(g) \\ 2H_2 + GeO_2 &\rightarrow Ge + 2H_2O \end{aligned} \qquad (4.2)$$

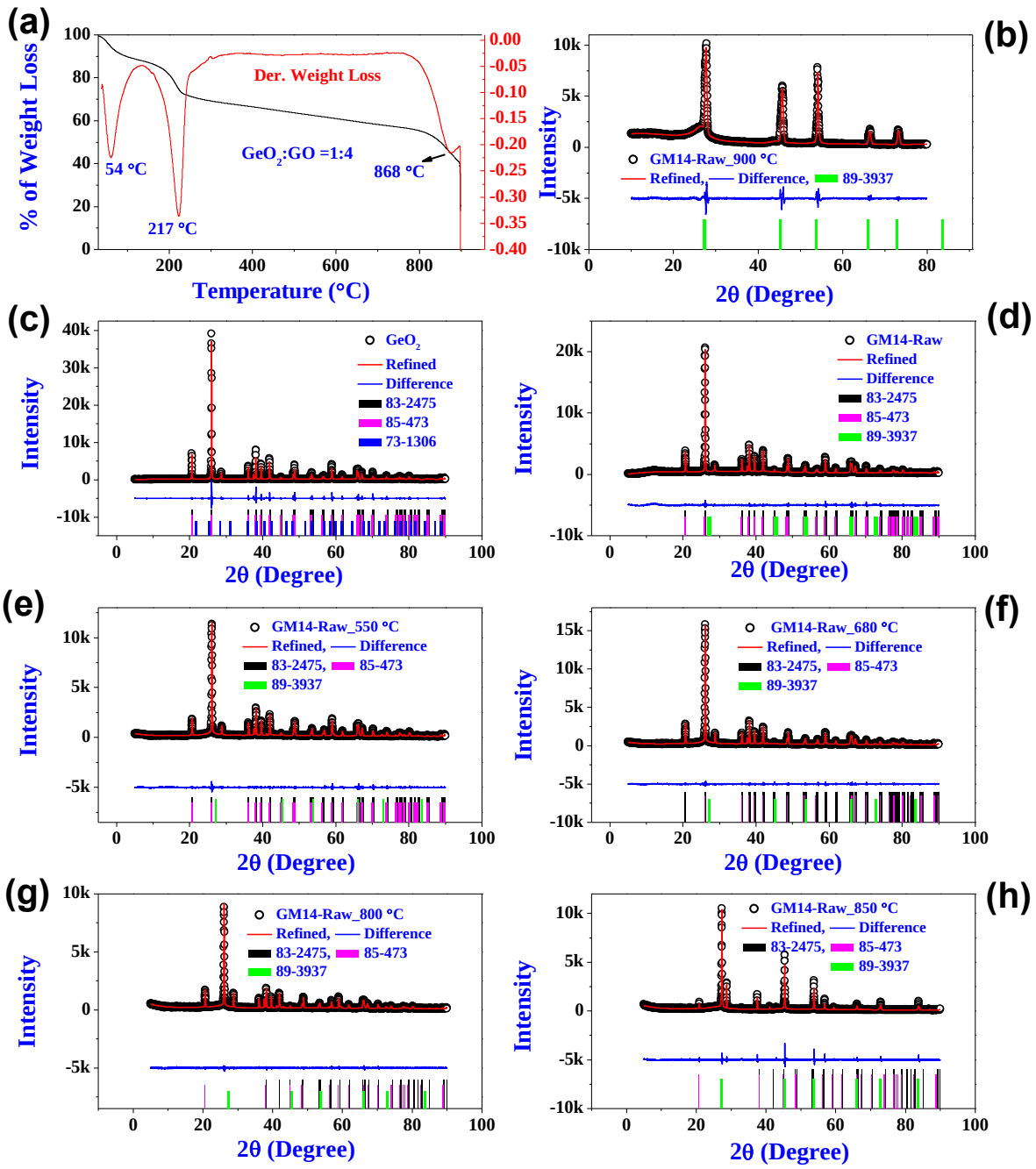

Figure 4.11 (a) Thermogravimetric curve (weight loss vs. temperature, black in color) and differential thermogravimetric curve (rate of weight loss vs. temperature, red in color) of GeO_2:GO (=1:4) mixture, and **(b-h)** Rietveld refined x-ray diffractograms of GeO_2 and GeO_2:GO (=1:4) mixture at different temperatures [i.e., GeO_2 (RT) and GeO_2:GO (RT, 550, 680, 800, 850 and 900 °C)].

Cyclic voltammetry is a fingerprint technique to investigate electrochemical reactions. **Fig. 4.12(a)** shows the cyclic voltammetry profiles of GR14 composite for first six reduction, and oxidation sweeps. As per reported literature, at lower potentials, most of the organic electrolytes (also $LiPF_6$ in EC/DMC) decompose in between 0.2-1.0 V vs. Li/Li^+ and form SEI through multi-electron transfer mechanism [205]. This SEI formation mainly depends on the

many factors such as electrolyte and electrode morphology, chemical composition, surface defects, and temperature [205]. SEI formation also depends on the environment present in the cell, such that SEI formation takes place from first reduction sweep to few reduction sweeps [205]. W. Tang et al., [206] studied Ge/CNT core/shell structures as anode material in the 0.005-1.0 V vs. Li/Li^+ voltage range. This study revealed that lithiation mechanism in Ge took place through four distinct crystal phases namely Li_9Ge_4 (at 0.17V), Li_7Ge_2 (at 0.14 V), $Li_{15}Ge_4$ (at 0.11 V), and $Li_{22}Ge_5$ (0.005 V) as revealed by in-situ ^7Li NMR and ex-situ XRD experiments. CV curves recorded in this study are similar to those reported by W. Tang et al., [206] in the case of Ge/CNT core/shell structures. The first cathodic (i.e., reduction) scan of GR14 started from OCV (i.e., 3.0 V) and a reduction peak centered at 0.60 V is observed which corresponds to the reduction of the electrolyte to form a SEI film on the electrode in response to applied voltage as observed in other related works [189, 207, 208]. The enormous and continuous increase in the reduction current (i.e., 2.1 mA at 0.005 V) after SEI film formation is expected due to a massive transfer of Li ions from the cathode to the anode through SEI film which drives to form different lithium-germanium phases as reported in the reference [206]. In the GR14 composite, the first oxidation scan consists a peak centered around 0.60 V which is accompanied by a flat region with negligible current till the voltage reaches its cutoff value, i.e., 3.0 V. The observed oxidation peak is attributed mainly to the removal of lithium from GR14 composite by de-alloying from $Li_{4.4}Ge$ to form individual Li and Ge phases. The remaining entire oxidation current is due to electrochemical desorption of Li from graphene. Most of the Li-ions consumed in the first cathodic (i.e., reduction) sweep are decomposed and form stable and insoluble (in the electrolyte) inorganic compounds like Li_2O, Li_2CO_3, and LiF, etc., [205]. As compared with the first cycle, a slight decrease in the current is observed in the second cycle. The SEI film formation results in the form of irreversible capacity loss (ICL) which is directly observed as decreased area under the CV curves as shown in **Fig. 4.12(a)**. From the second cycle onwards area under the curves maintained a constant value during the remaining cycles. This is expected due to the good synergy between Ge nanoparticles and graphene layers.

Galvanostatic cycling experiment is performed to evaluate electrochemical performance of the GR14 nanocomposite. The discharge/charge profiles (**Fig. 4.12(b))** are recorded in the voltage range of 0.005-3.0 V and at a current density of 160 mA/g (0.1C). The first discharging curve is very steeper and the voltage dropped below 1.0 V without slope change. The first change in slope is observed in the range 0.9-0.7 V. This corresponds to typical electrolyte decomposition

to form SEI as found in previous reports [189,207,208]. The second change in slope is noticed around 0.3 V (which secured ~394 mA h/g specific capacity) is majorly due to lithiation by Li alloying with Ge. The third change in slope is observed at 0.2 V. This corresponds to the discharging capacity of ~1162 mA h/g, which might be contributed by lithium intercalation into graphene as in graphite. Further, this curve is observed to decline slightly with the same slope till the voltage drops to 0.005 V by securing total discharge capacity of ~1236 mA h/g. The specific capacity ~1236 mA h/g delivered is higher than the theoretical capacity of GR14 composite (i.e., the theoretical capacity of GR14 composite = ~1035 mA h/g = (34 wt.% (theoretical capacity of Ge, i.e., ~1600 mA h/g [209] + 66 wt.% (theoretical capacity of rGO, i.e., ~744 mA h/g) [89]). The first charging curve is inclined steeply up to 0.5 V from where the curve is little horizontally extended up to 0.65 V by securing net charging capacity of ~208 mA h/g, and this capacity is mainly due to partial de-alloying of lithium from Li-Ge alloy formed during cathodic scan and desorption of Li from graphene layers. Above 0.6 V, the slope of the charging curve has changed continually up to 1.5 V from where once again it had a steer inclination up to 3.0 V for which total charging (or reversible) capacity of ~648 mA h/g is observed. Thus more than 52% discharging capacity is reversed while charging by leaving a difference of 588 mA h/g which is also known as an ICL. The observed ICL is majorly considered to originate from lithium loss due to covalent trapping in the form of SEI constituent compounds like Li_2O and Li_2CO_3. However, GR14 composite showed the stable reversible capacity of 466 mA h/g at the 50th cycle and this value again increased to 539 mA h/g at the end of 100th charge curve due to electrode activation effect. From 50th cycle onwards QEs of GR14 composite is 96-98% despite 52% during the first cycle. In the GR14 composite, the second and subsequent discharging and charging curves are found similar to first cycle curves, but their capacity is gradually decreased up to 30th cycle and then after started to increase as shown in **Fig. A7** of **Annexure 2**. This gradual decay is plausibly due to the continuous ceasing of lithium's reversibility through alloying and de-alloying reactions with Ge as like in the case of bare Ge anode. Here, the significant amount of capacity loss occurs only due to continuous shortening of a horizontal portion in the GC curves in the range 0.5-0.65 V indicating that Ge is becoming more and more inactive as cycles progressed and eventually its contribution to total capacities decreases. Finally, there is no sign of alloying, and de-alloying of lithium with Ge and whatever capacity is shown by composite seems to be only contributed by rGO as curves above 40th cycle are found similar to pristine graphene. Here by anchoring Ge nanoparticles onto good conducting type rGO, good electrical contacts are expected during pulverization of Ge crystals upon de-lithiation, unlike bare Ge anode in which pulverization

causes electrical insulation. But decay in capacity due to Ge might be evolved from competition for lithiation between rGO and Ge in which rGO dominates (wt.% of rGO is also more) Ge at current densities equal to C/10. Also, continuous formation of SEI might also be other reason for this decay which might isolate Ge phase from interacting with Li in coupling with its natural pulverization effect.

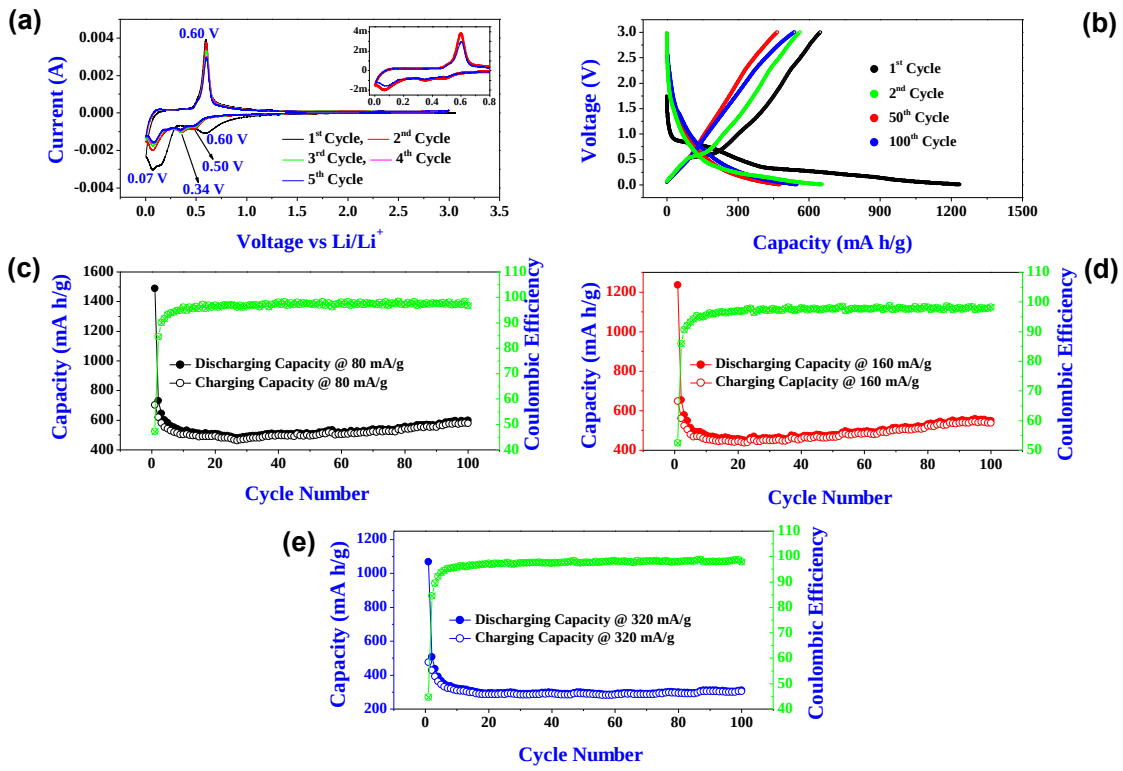

Figure 4.12 (a) Cyclic voltammetry curves at 58 μV/s scan rate (inset shows a comparison of 2nd and 5th cycles), **(b)** Galvanostatic cycling curves at 160 mA/g current density, and **(c-e)** capacity vs cycle number and Coulombic efficiency vs cycle number at different current rates of GR14 composite in the voltage range of 0.005-3.0 V vs. Li/Li^+.

All in all, CV and GC results complemented each other. As shown in GC results where the role of Ge to hold or release Li decreases and became negligible at the end of the test and finally rGO is alone active for (de)lithiation. **Figs. 4.12(c-e)** show cycling stability of the GR14 composite at different current rates i.e., 80, 160 and 320 mA/g in the 0.005-3.0 V voltage range. It is observed that at higher current densities, the specific capacity of GR14 composite faded rapidly i.e., at the end of the 100th cycle a capacity of 304 mA h/g at a current density of 320 mA/g in the voltage range of 0.005-3.0 V was observed. This is less than the theoretical capacity of graphite. Above results are suggesting that lower impedance values can be expected during charging than OCV and discharging cycle signifies the easy extraction of lithium from GR14 composite, and this might appear as high reversible capacity observed in GC results.

EIS measurements are carried on the cycled coin cell batteries in the frequency range 180000 to 0.003 Hz to understand the Li-ion storage mechanism of the GR14 composite and to support the GC and CV results. **Fig. 4.13** shows Nyquist plots of the coin cell batteries in different states (i.e., at OCV, 1st discharged and 1st charged). EIS results about all the three stages are fitted to one equivalent circuit (inset of **Fig. 4.13**). Individual elements (related to EIS results) that are necessary to understand the Li-ion storage kinetics and their values are tabulated in **Table 4.4**. The first circuit element that is contact (or solvent) resistance R_e is observed to decrease from OCV to 1st charge state. It is expected due to good contact between constituents of the anode material as charge states progress. Resistance to charge transfer (R_{ct}) is first increased for 1st discharge state and decreased for 1st charge state than the OCV. The lower R_{ct} value of the 1st charge scan than the first discharge scan is an indication for easy removal of Li ions due to the presence of highly conducting and high specific surface area graphene and excellent synergy between graphene and germanium nanoparticles. Similarly, the electric double layer capacitance (CPE_{dl}) values increased continuously for 1st discharge and 1st charge states, and this is expected due to formation of thick SEI film on the electrode surface while first discharge leads to form dense dielectric medium between active electrode and charge carriers in the electrolyte which causes the increase in CPE_{dl}. Finally, the intercalation capacitance (C_i) and Warburg element (Li-ion diffusion, W_i) first increased and then decreased. In all three stages, subtle values of intercalation capacity C_i [199] and very high values of Warburg element W_s (resistance to Li-ion diffusion) are found when compared to R_e and R_{ct}. The very low value of C_i indicates that Li storage preferably takes place either by redox couples of Ge [203] or electrochemical adsorption by graphene layers [89]. The EIS results supported the GC and CV results in the 1st cycle and are expected to be in line with for other cycles also.

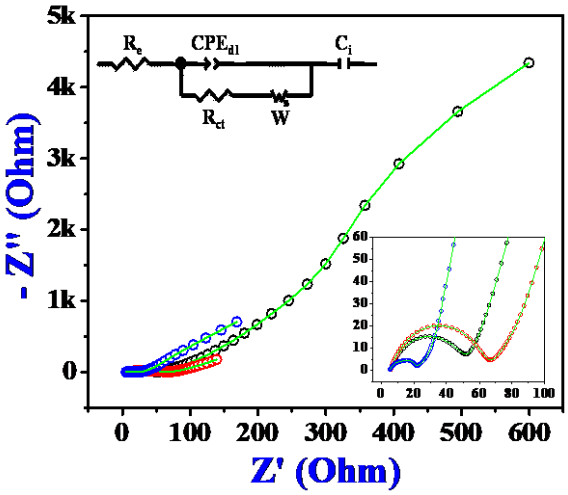

Figure 4.13 EIS curves of GR14 composite at different charge states (black, red and blue color circles represent OCV, 1st discharge, and 1st charge states, respectively) with curve fitting (solid line in green color) and the inset shows the magnified portion of the EIS curves at Z′ < 100 and the equivalent electrical circuit.

Table 4.4. EIS results of the GR14 composite at OCV, 1st discharged, and 1st charged states.

Sample Status	R_e	R_{ct}	CPE_{dl} (μF)	C_i (F)
GR14 Fresh cell	5.69±0.21	46.2±0.0	48.9±0.0	0.01
GR14 Discharged state	5.66±0.01	60.1±0.1	56.9±0.7	0.54
GR14 Charged state	5.03±0.07	18.7±0.2	323.5±25.0	0.09

4.2 Novel EMI Shielding Materials

4.2.1 Flexible FLG/PVA composite sheets

Field emission secondary electron micrographs of graphite flakes (starting material), and FLG are shown in **Fig. 4.14**. It can be observed that graphite flakes are thick (few μm) as shown in **Fig. 4.14(a)**. **Fig. 4.14(b)** shows randomly aggregated thin graphene sheets (few of them stacked together forming independent FLG structures) closely associated with each other and forming a disordered solid. The folded regions of the FLG sheets are found to have an average thickness of few nm. The absence of any surface charging during the imaging indicated that the material was electrically conductive. It can also be observed from **Fig. 4.14(b)** that FLG sheets have lateral dimensions of at least 1 μm^2. **Fig. 4.14** is the evidence that the adopted synthesis method is an optimum one to convert a large number of stacked graphene layers (i.e., graphite flakes, **Fig. 4.14(a)**) into FLG (**Fig. 4.14(b)**). FLG sheets are transparent to the electron beam as observed in electron micrographs (**Fig. 4.14(c)**) indicating the presence of few layers along the c-axis in a single structure. Comparison of XRD data obtained from FLG with graphite (**Fig. 4.14(d)**) showed typically (002) and (004) diffraction peaks with reduced

intensity indicating the formation of FLG. The x-ray diffractogram obtained from FLG also indicated that it is highly ordered. Selective area electron diffraction (SAED) pattern of FLG showed the typical six-fold symmetry as expected for graphene. The regular outer and inner hexagon patterns with varied intensity of the electron diffraction spots as shown inset of **Fig. 4.14(c)** indicate a multi-layer system that is built-in with A-B type of atomic stacking as in graphite [210].

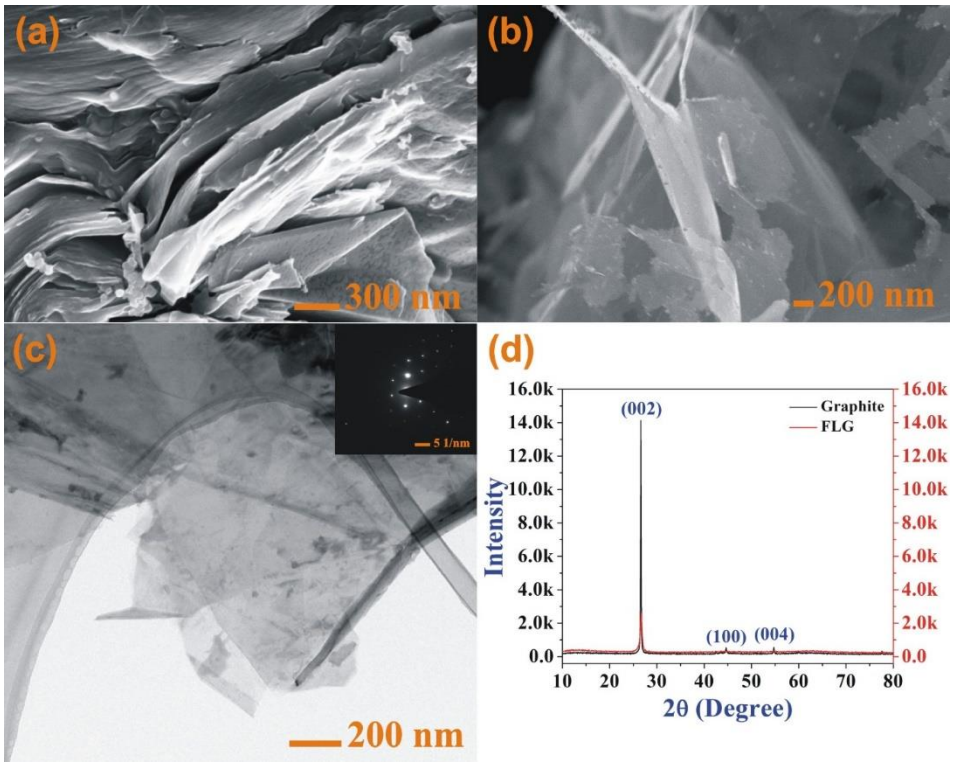

Figure 4.14 Secondary electron micrographs of **(a)** graphite flakes, **(b)** few layered graphene, **(c)** Transmission electron micrograph of few-layered graphene (inset: corresponding diffraction pattern) and **(d)** comparison of x-ray diffraction data of graphite and few-layered graphene.

Cross-sectional FESEM micrographs of PVA and FLG/PVA composites are shown in **Fig. 4.15**. PVA morphology (**Fig. 4.15(a)**) contained a mixture of flat and folded regions and the flat region at higher magnification is shown in **Fig. 4.15(b)**. 0.2 wt.% FLG/PVA composite shows (**Fig. 4.15(c)**) uniformly distributed filler material (i.e., FLG) which occupied very small regions in the matrix and coated with PVA (as observed at higher magnification, **Fig. 4.15(d)**). 0.6 wt.% FLG/PVA composite contains uniformly distributed but a network of FLG (**Fig. 4.15(e)** and coated with PVA (**Fig. 4.15(f)**). Further investigations like XRD, transmission electron microscopy and Raman spectroscopy have been carried out.

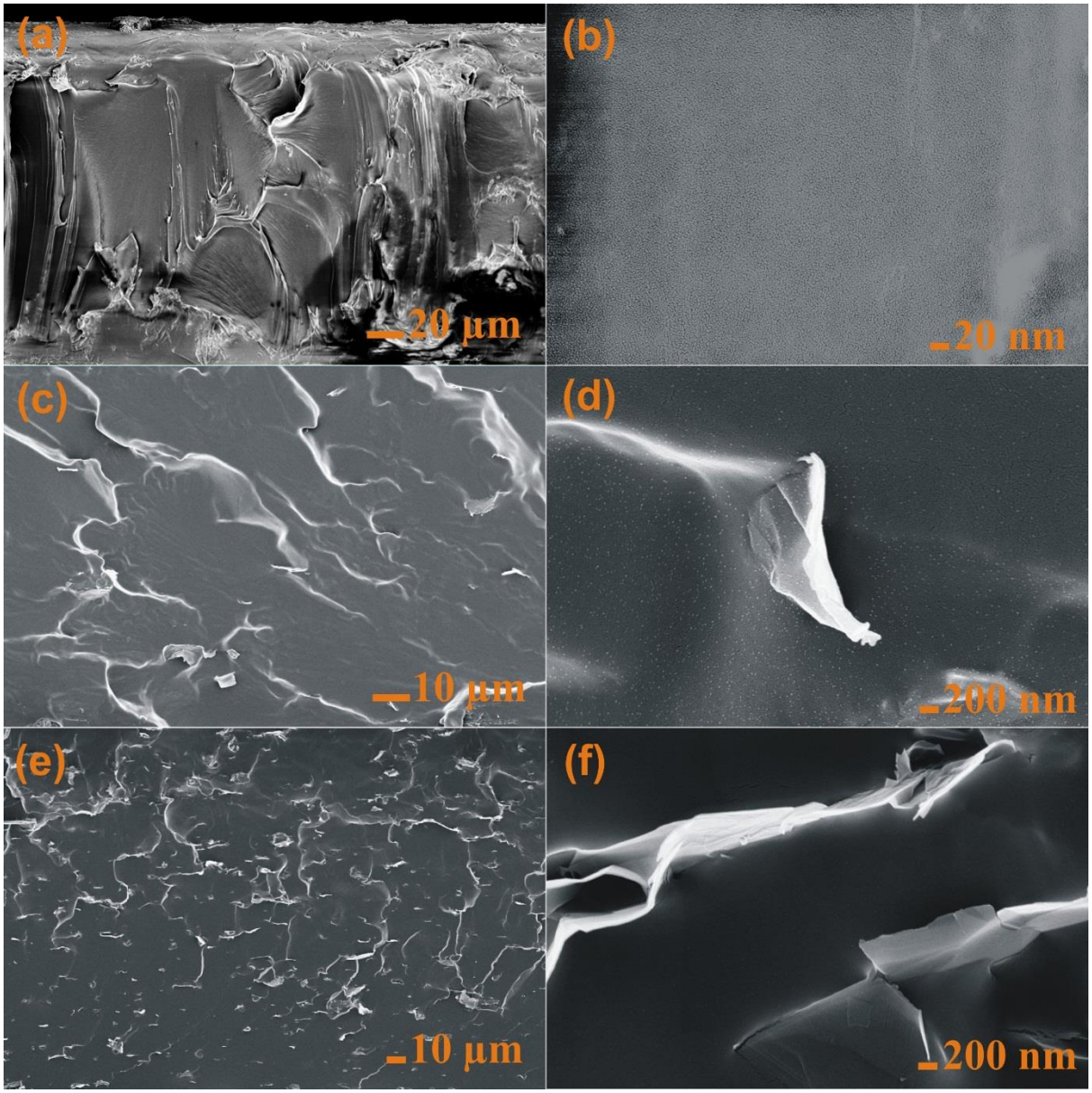

Figure 4.15 Cross-sectional secondary electron micrographs of **(a)**, **(b)** polyvinyl alcohol and FLG/PVA composites with different wt. % of FLG, **(c)**, **(d)** 0.2, and **(e)**, **(f)** 0.6 wt.%.

PVA is a well-known partially crystalline polymer that exhibits a strong (101) x-ray diffraction peak at 2θ=19.5° and a weak broad peak at 2θ=40.4°. On the other hand, FLG has a characteristic (002) diffraction peak at 2θ =26.5° as shown in **Fig. 4.16**. In the case of composites, it was observed that the intensity of (101) peak of PVA increased with FLG is due to uniform distribution of FLG in PVA matrix is acting as nucleation sites for PVA chains to pack together resulting in large size crystallites in PVA sol-gel and thus superior PVA crystallinity in composites [211]. The increase in the intensity of FLG diffraction peak in case of composites with increasing FLG loading is due to increase in the weight content of FLG.

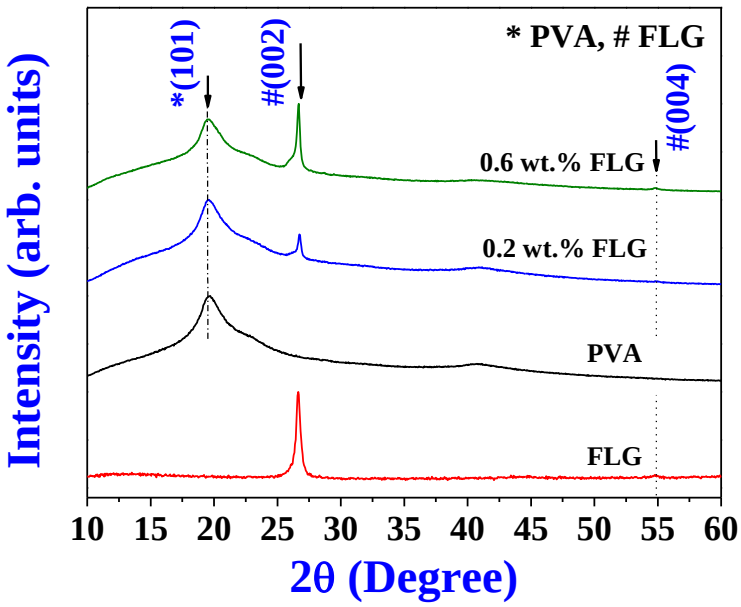

Figure 4.16 X-ray diffractograms of FLG, PVA and FLG/PVA composites.

XRD results are well complemented with transmission electron microscopy results. As shown in **Fig. 4.17**, the micrographs show that all composites are transparent to the electron beam. **Figs. 4.17(a)** and **(b)** show bright field micrograph of 0.2 wt.% FLG loaded PVA composite and high-resolution TEM (HRTEM) micrograph, respectively. Selected area electron diffraction (SAED) pattern indicates one set of six-fold symmetric spots which corresponds to the six-fold symmetry of graphene [212]. HRTEM micrograph clearly shows 2 to 4 graphene layers which confirm that the synthesized composite contains FLG. **Figs. 4.17(c)** and **(d)** show bright field micrograph of 0.6 wt.% FLG loaded PVA composite material and HRTEM micrograph, respectively. SAED pattern contains a family of spots, indicating that field of view contains several grains (individual FLG structures) in different orientations [213]. This is well supported by HRTEM (**Fig. 4.17(d)**) micrograph which shows the presence of several FLG structures in different orientations and that they are interconnected to form a network of structures.

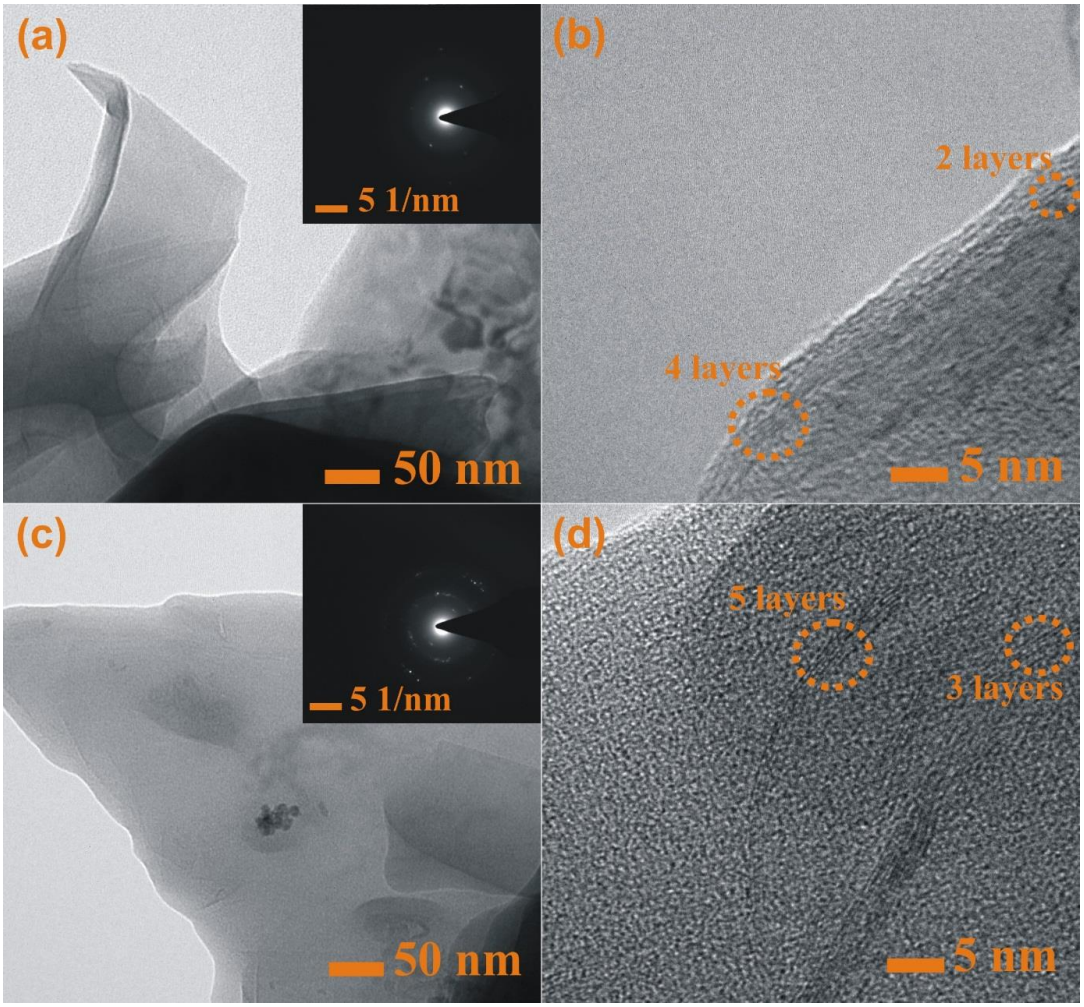

Figure 4.17 Transmission electron microscopy images of FLG/PVA composites at **(a, b)** 0.2 wt.% FLG, **(c, d)** 0.6 wt.% FLG (inset: **(a)** and **(c)** are corresponding SAED patterns respectively).

Raman spectrum of PVA gives the information about the vibrational modes of (-CH_2-CHOH-) monomer, which is expected to have 17-normal modes of vibrations: 6 CH_2 (2 stretching, bending, wagging, twisting and rocking), 3 CH, 3 OH, 3 CO (each consisting of a stretching plus 2 bending modes, one is perpendicular to the chain axis and another one parallel) and 2 CC (skeletal vibrations) [214]. In the present study, an average of six Raman spectra is taken for good accuracy in measurement for each composition. A clear explanation for assignment of bands in PVA [214-216] is available. The Raman spectra corresponding to different samples are shown in **Fig. 4.18**. The Raman bands typically at 2840, 2910, and 2942 cm^{-1} correspond to the stretching modes of CH and CH_2 i.e., υ(CH) and $\upsilon_s(CH_2)$ (and $\upsilon_a(CH_2)$), respectively [214]. In a separate work [215] the same were tentatively assigned to undifferentiated C-H stretching vibrations. The ambiguity for the assignment was removed in a separate work [216]. Based on the previous work [216] the bands at 2835, 2913 and 2935 cm^{-1} in the present work are assigned to $\upsilon_a(CH_2)$, υ(CH), and $\upsilon_s(CH_2)$, respectively. As observed in **Fig. 4.18(b)** there is

a small shift in the peak position and intensity of the peak also increased as the loading level of FLG increased in PVA matrix. The shift is attributed to stresses in the matrix and the reason for the continuous increase in intensity was expected because lower loadings of FLG to PVA matrix cause the CH_2 to form some kind of clustering (i.e., nucleation) which results in enhancement of intensity. The symmetric bending mode of the CH_2 group, $\delta(CH_2)$, was observed (**Fig. 4.18(a)**) in PVA at ~1433 cm^{-1} and in FLG/PVA composites it was observed in between ~1435 and ~1438 cm^{-1}. The wagging and rocking modes of the CH_2 group ($\gamma_w(CH_2)$, $\gamma_r(CH_2)$) are observed (**Fig. 4.18(a)**) in PVA matrix at ~1362 and ~852 cm^{-1} and in FLG/PVA composites at ~1377 cm^{-1} and in between 848 and 856 cm^{-1}, respectively. The twisting mode of CH_2, $\gamma_t(CH_2)$ is too weak to be distinguished from the noise of the spectrum in the present study.

Table 4.5. Graphitic band positions in Raman spectra of FLG and FLG-PVA composites.

Raman Feature	**FLG**	**0.2 wt.%**	**0.6 wt.%**
D-band	1354/cm	1356/cm	1356/cm
G-band	1578/cm	1581/cm	1581/cm
M-K scattering band	2442/cm	2445/cm	2457/cm
2D-band	2702/cm	2712/cm	2716/cm
2D′-band	3234/cm	3242/cm	3243/cm
I_D/I_G ratio	0.6	0.5	0.6
I_G/I_{2D} ratio	1.2	1.4	1.5

The stretching and wagging modes of the OH group, $\upsilon(OH)$ and $\gamma_w(OH)$ are observed in PVA at 3361 and 639 cm^{-1}, respectively and the same are observed in FLG/PVA composites with slight peak shift. The peak at 1440 cm^{-1} in PVA and 1447 cm^{-1} in FLG/PVA composites are attributed to a combined effect of bending mode vibration of CH and OH groups ($\delta(CH+OH)$). A collection of different bands appears in the frequency range 1000–1200 cm^{-1}. However, it is not possible to assign the exact position of the peaks due to lack of crystallinity and limitation of the instrument's resolution (~3 cm^{-1}). The band at ~1096 cm^{-1} is probably due to $\upsilon(CO)$ in both PVA and FLG/PVA composites. The skeletal vibration of the CC group was observed at 922 cm^{-1} in PVA and at 914 cm^{-1} in FLG/PVA composites. A broadband at ~1723 cm^{-1} was observed which is expected due to residual acetate groups from PVA polymer.

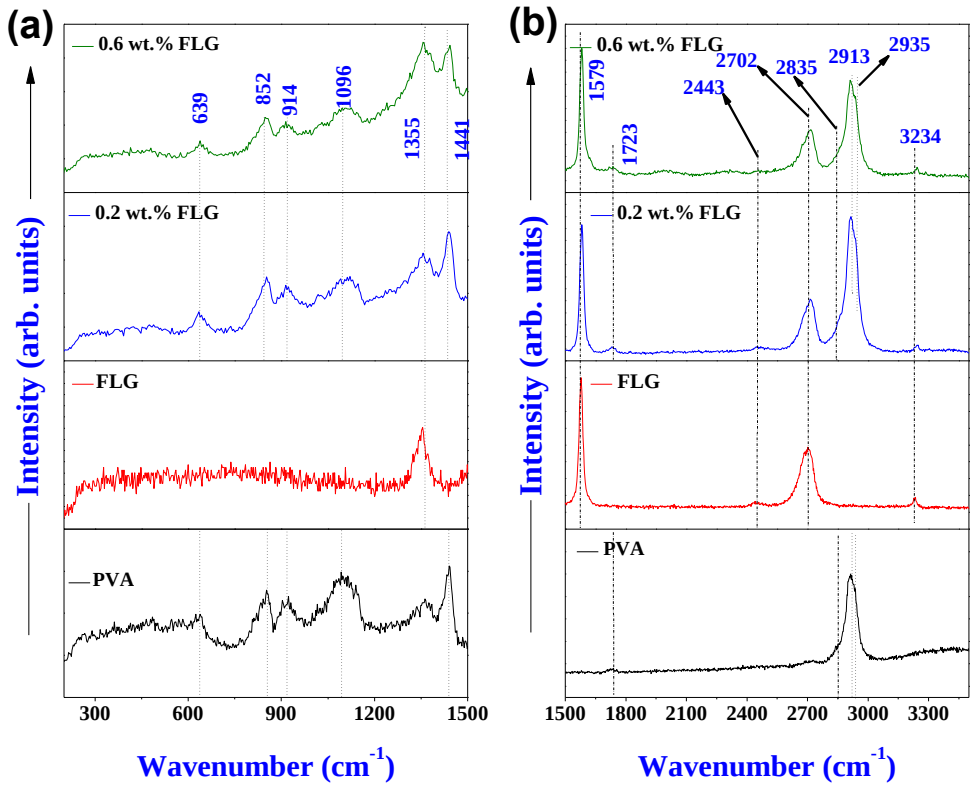

Figure 4.18 Comparison of Raman spectra of PVA, FLG and FLG/PVA composites with different loadings (0.2 and 0.6 wt.%) of FLG **(a)** in 200-1500 cm^{-1} region and **(b)** in 1500-3800 cm^{-1} region.

The Raman spectra of FLG and FLG/PVA composites (**Fig. 4.18**) showed distinctive D and G bands representative of graphitic material. In FLG, D, G, M-K scattering, 2D, and 2D′ bands are observed at 1354, 1578, 2442, 2702 and 3234 cm^{-1}, respectively. Various Raman bands in FLG/PVA composites are shown in **Table 4.5**. Raman peak positions pertaining to FLG in the present study may correspond to Raman scattering in folded graphene, single, double, few layered graphene [217-219]. The intensity ratio I_D/I_G which is a measure of the extent of disorder was ~0.6 indicating higher order graphitization degree while I_G/I_{2D} was ~1.2 corresponding to less than 20 graphene layers [220]. It is well known that 2D band in the Raman spectrum of the graphitic material is a fingerprint for a number of graphene layers in the given graphitic material and one constraint for this technique is that, it is hard to distinguish more than 5 to 6 layers from graphite [219]. The maximum intensity count of the 2D band in FLG was observed at 2702 cm^{-1} with a good center of symmetry around 2700 cm^{-1}. This type of symmetry will be found for single or bilayer or highly ordered pyrolytic graphite (HOPG) [221]. But in comparison to a work reported previously [219], the symmetry of 2D band indicated that the sample in the present study (i.e., FLG) contains very few layers and it is definitely not HOPG. For an ideal and defect-free graphene, it is well known that G and 2D

bands in Raman spectrum are observed at 1590 and 2685 cm^{-1}, respectively. As the number of layers increases the G band shifts towards lower wave number side, 2D band shifts towards higher wave number side and shape of the 2D band will change from sharp, symmetric peak to broad, asymmetric peak. For example, for a single layer graphene, one sharp 2D band can be observed, for a bilayer graphene 2D mode can be decomposed into four components and for HOPG it is best fitted to two components with less intense $2D_1$ component and high intense $2D_2$ component. It was also well observed that as a number of layers increase an increment of the intensity of the higher frequency $2D_2$ component compared to the $2D_1$ component occurs. In the case of FLG/PVA composites, the D and G band observed at 1356 and 1581 cm^{-1} respectively and 2D band shifted to higher wave number side as loading level increased. As the loading level of FLG increased, a number of graphene layers also increased (as observed in HRTEM micrographs) which is reflected as a change in 2D peak position and shape. G band peak position also shifted towards higher wave number side which is a contradictory result. Recently it has been reported [222-224] that such a blue shift in G peak position can be attributed to unintentional doping in graphene by the charge impurities present in the surrounding atmosphere (here may be PVA). It was also reported [225] that defects like edges, dislocations, cracks or vacancies in the sample can cause unintentional doping. Due to this effect, even though the extent of disorder (i.e., I_D/I_G) increased as the loading of FLG increased, the intensity ratio of G to 2D (i.e., I_G/I_{2D}) decreased. It is anticipated that defects in FLG are created during ultrasonication process, which is supported by erosion of FLG edges as observed in **Fig. 4.14(b)**.

The ac-conductivity vs frequency of 0.2 wt.% FLG/PVA and 0.6 wt.% FLG/PVA composites is shown in **Fig. 4.19(a)**. At low frequencies, conductivity of 0.2 wt.% FLG/PVA composite is invariable with frequency and after a certain frequency, a sudden dip in conductivity is observed and thereafter that conductivity increased with frequency. The conductivity of 0.6 wt.% FLG/PVA composite is invariant with frequency and is measured as $5x10^{-1}$ S/cm. This high conductivity at very less volume fraction of FLG is expected because of the presence of well dispersed, conducting network of FLG inside the insulating PVA matrix as observed in the morphology studies. The (visible) light transmittance for PVA, 0.2 wt.% FLG/PVA and 0.6 wt.% FLG/PVA composites are shown in **Fig.4.19(b)**. As the FLG content in the PVA increases, optical transparency of the composite decreased is an indication of an increase in conductivity. As prepared composite sheets exhibited optical transparency of up to 61%, 42% and 0% for PVA, 0.2 wt.% FLG/PVA and 0.6 wt.% FLG/PVA, respectively.

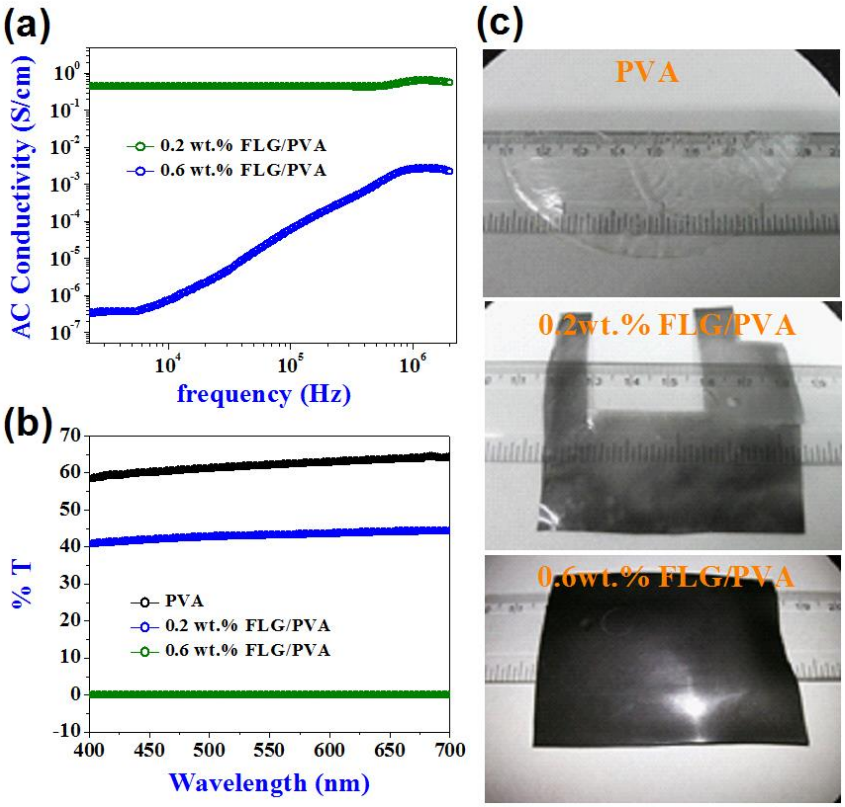

Figure 4.19 (a) Ac conductivity vs. frequency, **(b)** Transmittance spectra and **(c)** digital photographic images of PVA, 0.2 wt.% FLG and 0.6 wt.% FLG composites, respectively.

EMI SE of PVA and FLG/PVA composites are shown in **Fig. 4.20(a)**. The average SE of PVA sheet was measured as ~0.2 dB. Similarly, average SE of 0.2 and 0.6 wt.% FLG loaded PVA matrix is found to be ~13.5 and ~19.5 dB, respectively. High SE at low loadings of FLG in PVA is attributed to the high aspect ratio of graphene layers and formation of network type structure inside the polymer, which leads to more surface sites available for the incoming wave to interact and communicate throughout the network. This inference is well correlated with the observed morphology, structure and phase characteristics. It is also observed that SE of each sample is almost constant in the entire "X band" frequency range. **Figure 4.20(b)** shows variation in average EMI SE due to absorption and reflection with a weight fraction of FLG in PVA matrix. From the figure, it is clear that absorption is the dominant mechanism for EMI shielding. This behavior is well correlated with observed morphology, structure, and phase of the FLG/PVA composites. The EMI SE required for most of the commercial applications is ~20 dB. In the present work, 0.6 wt.% FLG/PVA composite can be used as EMI SE material for commercial applications.

To further understand the reasons behind the observed increase in SE of FLG/PVA composites, complex permittivity, ($\varepsilon^* = \varepsilon' - i\varepsilon''$) is evaluated and is calculated from experimental scattering

parameters (S11 and S21) using theoretical calculations given by Nicholson and Ross and Weir algorithms [187, 188]. The dielectric constant (ε') is mainly concomitant with the amount of polarization occurring in the material and the imaginary part (ε") is a measure of dissipated energy. As shown in **Fig. 4.20(c)**, in the X-band frequency range ε' and ε" values of PVA, 0.2 wt.% FLG/PVA and 0.6 wt.% FLG/PVA composites are slightly decreased with frequency increases and their average values are 2.8 and 0.2, 4.0 and 0.6 and 5.1 and 0.82, respectively. The dielectric performance of the material depends on the ionic, electronic, orientational and space charge (or interfacial) polarization.

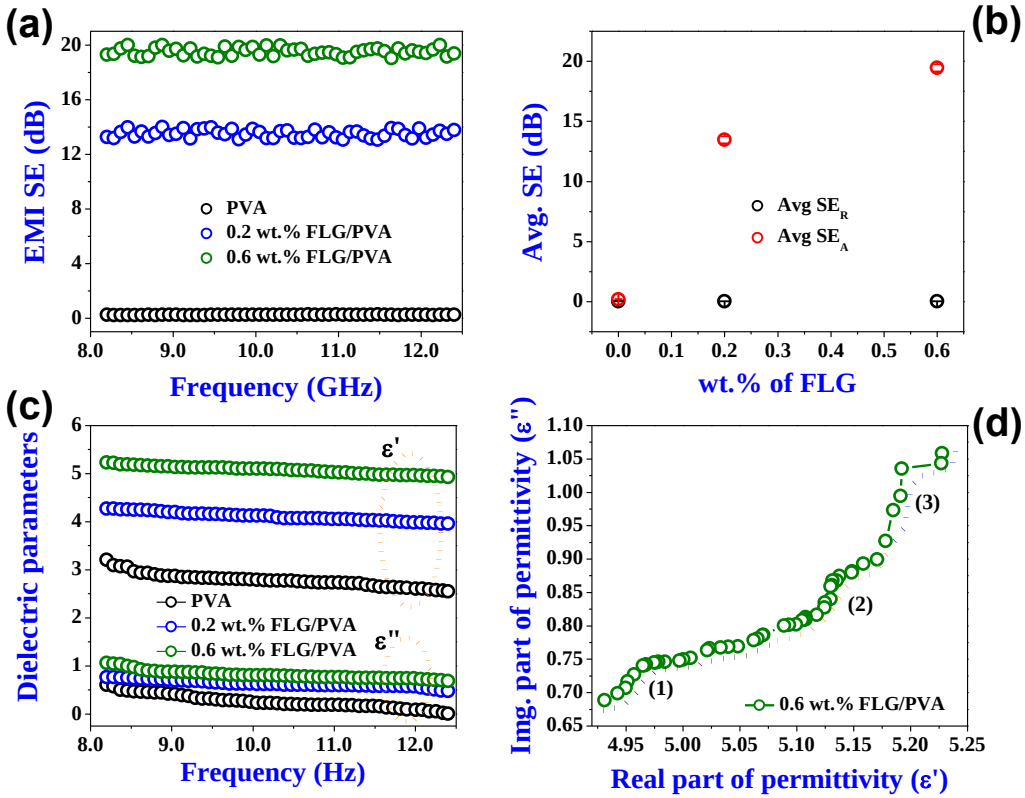

Figure 4.20 (a) EMI shielding effectiveness of the pure PVA and FLG/PVA composites, **(b)** average EMI SE vs. weight fraction of FLG in PVA matrix, **(c)** dielectric parameters of PVA and FLG/PVA composites and **(d)** ε″ vs. ε′ plot of 0.6wt.%FLG/PVA composite.

During the synthesis, a combination of microwave irradiation of graphite oxide and subsequent exposure to ultrasonic waves induce residual groups and defects like missing carbon atoms and sheet corrugation (as shown in **Fig. 4.14(b)**) in the hexagonal carbon lattice of FLG. Energy transition of microwave band involves the electronic spin, which means greater spin states are required for microwave absorption. It has been reported that localized states near to the Fermi level could be created via introducing lattice defects [226]. Thus the existence of defects in FLG favors absorption of electromagnetic energy by the transition from contiguous states to Fermi level when irradiated the absorbing surface.

Cole-Cole diagram gives an idea about relaxation mechanism, observed cole-cole diagram in **Fig. 4.20(d)** consists three semi-circles is a representation of three different relaxation processes involving in the FLG/PVA composite. Defects and groups in the FLG are main reasons for relaxation processes [227]. First, the edge defects that are prominent in these systems gets screened by free charges and can act as polarization centers, which would generate polarization relaxation under the alternating electromagnetic field and attenuate electromagnetic wave, resulting in a profound effect on the loss of microwave energy. Second, the existence of residual oxygen-containing chemical bonds such as C-O, C=O in FLG generates electric dipole polarization due to different ability to catch electrons between a carbon atom and an oxygen atom. Therefore, under the alternating electromagnetic field, electron motion hysteresis in these dipoles can induce additional polarization relaxation processes which are favorable in enhancing microwave absorbing ability. Third, interfacial polarization (or space charge polarization) appears due to the heterogeneity of the material. The presence of well dispersed and network type (as demonstrated in morphological, structural and phase studies) FLG in the insulating matrix results in the formation of more interfaces. Due to the difference in the dielectric constant and conductivity of FLG and PVA, some charge carriers present in FLG are trapped, and, as a result, some charge is developed on the interface between the PVA molecules and the FLG. Which generate space charge at the heterogeneous interface leading to field distortion when an electromagnetic wave passes through it.

Yang et al., [228] studied the EMI SE of ~20 dB at 7 wt.% MWCNT loaded in the solution cast PS/MWCNT composites. Kim et al., [229] synthesized CNT-poly (methyl methacrylate) (PMMA) composites and reported highest EMI SE for raw CNT-PMMA composite as ~ 27 dB. J. Liang et al., [135] reported the EMI SE of ~21 dB at 15 wt.% loading of reduced graphene sheets for the epoxy/reduced graphene-based composites, prepared by solution casting method followed by ultrasonication. Gupta et al., [230] obtained the EMI SE of ~19 dB at 15 wt.% loading of carbon nanofibers (CNF) in solution cast PS/CNF composites. Even though the above-mentioned carbonaceous/polymer composites synthesized through well-established chemical routes have used high wt.% of carbon materials, their EMI SE is comparable to our EMI SE results at very low wt.% of graphene loading in PVA matrix.

4.2.2 Graphene wrapped MgO/PVA (G@MgO/PVA) composite

Fig. 4.20(a) displays secondary electron micrograph of graphene-wrapped magnesium oxide (G@MgO) composite powder. Ultrafine clustered particles, and nanosized particles decorated

on each such particle could be clearly observed in **Fig. 4.20(a)**. Bright field transmission electron micrograph of one such ultrafine particle is shown in **Fig. 4.20(b)**. This semi-transparent ultrafine particle is attached to nanosized MgO particles, and the edge-region of these particles are darker in contrast; these are expected to be graphene layers. High-resolution transmission electron micrograph (HRTEM) shown in **Fig. 4.20(c)** evidences the presence of graphene wrapped MgO nanoparticles, and some of the graphene layers acquired the shape of MgO particle. Measured d-spacing in **Fig. 4.20(c)** (not shown here) matches with the d-spacing of (200) planes of hexagonal MgO. The selected area electron diffraction pattern shown in the inset of **Fig. 4.20(b)** confirms the presence of both hexagonally crystalline graphene and MgO particles in the composite powder. **Fig. 4.20(c)** shows inverse Fourier transform images of HRTEM of G@MgO in **panels 1-4**. **Panels 1-3** show cross over, wrapped (wrapping MgO), touching graphene layers, respectively while **panel 4** shows defects (missing atoms) in the graphene layers. **Fig. 4.20(c)** and **panels 1-4** show 2-10 graphene layers in the G@MgO composite. As shown in **Fig. 4.20(c)**, the presence of defects and multiple interfaces (between graphene-graphene, and graphene-MgO) in the G@MgO are useful for EMI shielding. X-ray diffraction pattern (in **Fig. 4.20(d)**) evidences the presence of both graphene and MgO in the material. An average of eleven graphene layers are present in the G@MgO as calculated from (002) diffraction peak of graphene. Calculated number of layers from x-ray diffraction is closely matching with the HRTEM observations. **Fig.4.20(e)** shows Raman spectrum of G@MgO. The Raman active E_{2g} mode at ~1569 cm^{-1} (G band), characterizing the sp^2-hybridized carbon-carbon bonds in the G@MgO [210] is clearly observed. The defective D band and the 2D band are observed at ~1336 and 2668 cm^{-1}, respectively. The G and 2D band indicate higher order graphene in the G@MgO. The intensity of D band is more than that of the G band (i.e., I_D/I_G=1.18), which is an indication of presence of defects in the G@MgO. The observed sharp intensity of 2D band indicates that G@MgO contains few layered graphene. It is found from weight loss versus temperature, and derivative weight loss versus temperature plots (as shown in **Fig. 4.20(f)**) that G@MgO contains 79 wt. % of graphene and 21 wt. % of MgO in it. The presence of conducting graphene with defects and dielectric MgO in G@MgO is a therefore expected to an excellent candidate for EMI shielding when combined with PVA.

Secondary electron cross-sectional view micrographs of hot-pressed G@MgO/PVA_Coag and G@MgO/PVA_ac composites are shown in **Figs. 4.21(a-h)**. As shown in **Fig. 4.21(a)**, the ultrafine G@MgO filler material in the 0.4G@MgO/PVA_Coag composite is well dispersed in PVA, and thick PVA layer is coated on the G@MgO particle. Similar kind of morphology

is observed in 3.0G@MgO/PVA_Coag composite sample (**Fig. 4.21(b)**). On the other hand, the dispersion of filler material in G@MgO/PVA_ac composites is not proper. Filler material appears to be more agglomerated in comparison to it in the case of the coagulated counterparts. From the morphological observations, it is understood that the distribution of G@MgO particles in coagulated composite samples is better than that in as-casted composites. It is also observed that agglomeration of the filler material in the matrix increases as the weight fraction of filler in the PVA matrix increases.

X-ray diffraction patterns of PVA, all the coagulated (0.4, 0.6, 0.8, 1.0, 3.0, 10.0, and 15.0G@MgO/PVA_Coag) and as-casted (0.4, and 3.0G@MgO/PVA_ac) composites are shown in **Figs. 4.22(a)** and **(b)**, respectively. In all the composites, PVA crystallized in monoclinic crystal system, and G@MgO powder crystallized in hexagonal crystal system. The process of hot pressing at 140 °C and 3 tons of pressure have enhanced the crystallization of PVA with new peaks in all the composite samples. The (10-1) diffraction peak is the major intense peak in the case of PVA [231]. The variation of crystallite size (**Table 4.6**) of PVA (based on (10-1) diffraction peak) with the addition of G@MgO is investigated by applying Scherer's formula. The crystallite size of the PVA is ~65 Å, it is decreased in coagulated samples with increasing filler weight fraction, except for 0.6 and 1.0G@MgO/PVA_Coag composites. It is observed that (as shown in **Fig. 4.22(a)**) in the 0.6 and 1.0G@MgO/PVA_Coag composites (101) diffraction peak evolved at the expense of (10-1) diffraction peak intensity. Further experimentation is needed to understand this observation. It is also observed that the amount of G@MgO added creates compressive stresses in the PVA matrix and these stresses help in the growth of PVA crystals as observed in **section 4.2.1** [211]. The absence of peaks related G@MgO powder in all the composites (except 10.0 and 15.0G@MgO/PVA_Coag) is an indication of excellent dispersion of the filler in the PVA matrix. The appearance of graphene's (002) and MgO's (200) diffraction peaks in the 10.0 and 15.0G@MgO/PVA_Coag composite samples are expected due to the higher amount of G@MgO powder in the PVA matrix.

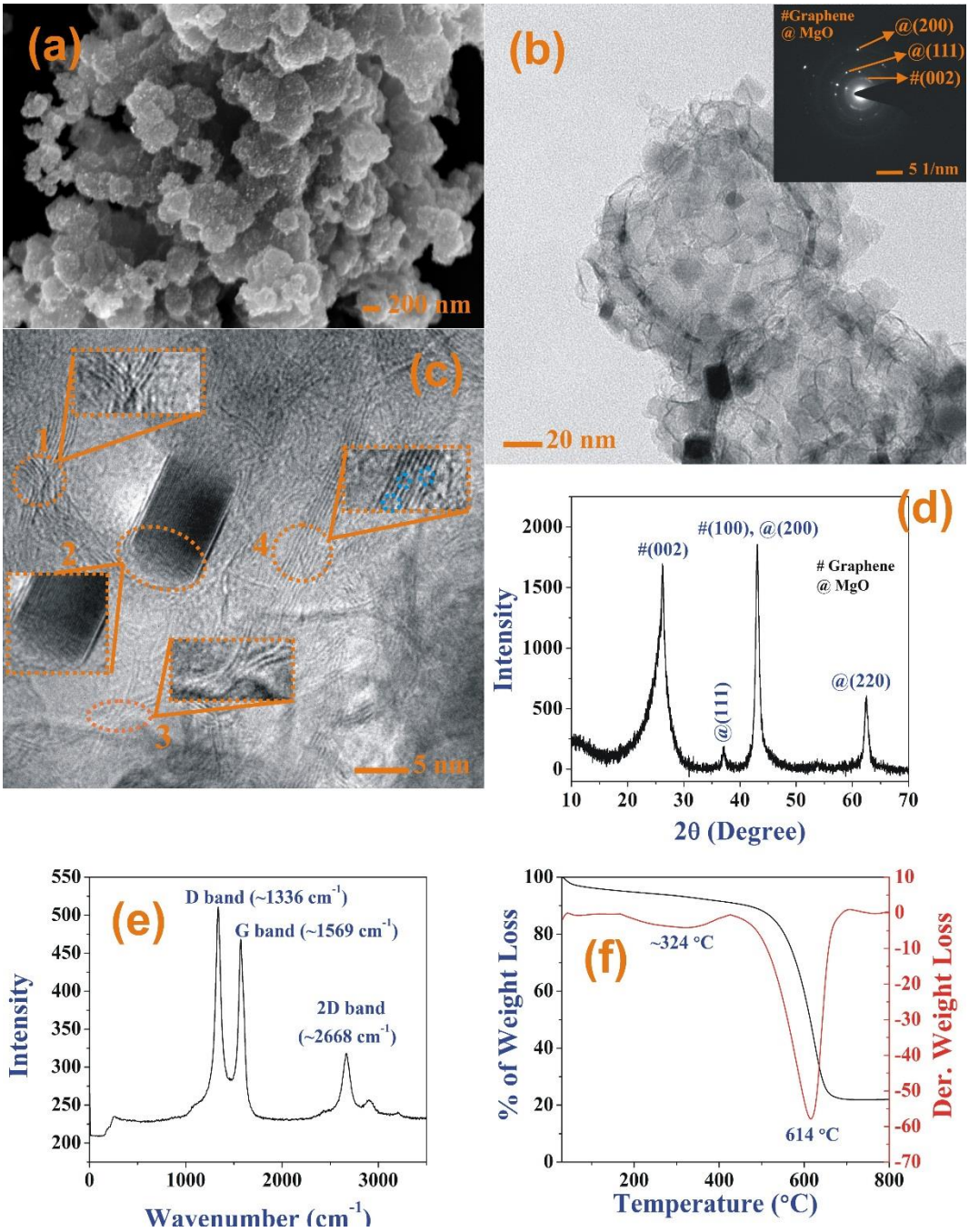

Figure 4.20 (a) Secondary electron micrograph, **(b)** transmission electron micrograph (inset, SAED), **(c)** high-resolution transmission electron micrograph and **(d)** intensity versus 2θ (X-ray diffractogram), **(e)** intensity versus wavenumber (Raman spectrum) and **(f)** weight versus temperature (TGA) and derivative weight loss versus temperature (DTA) of G@MgO composite respectively.

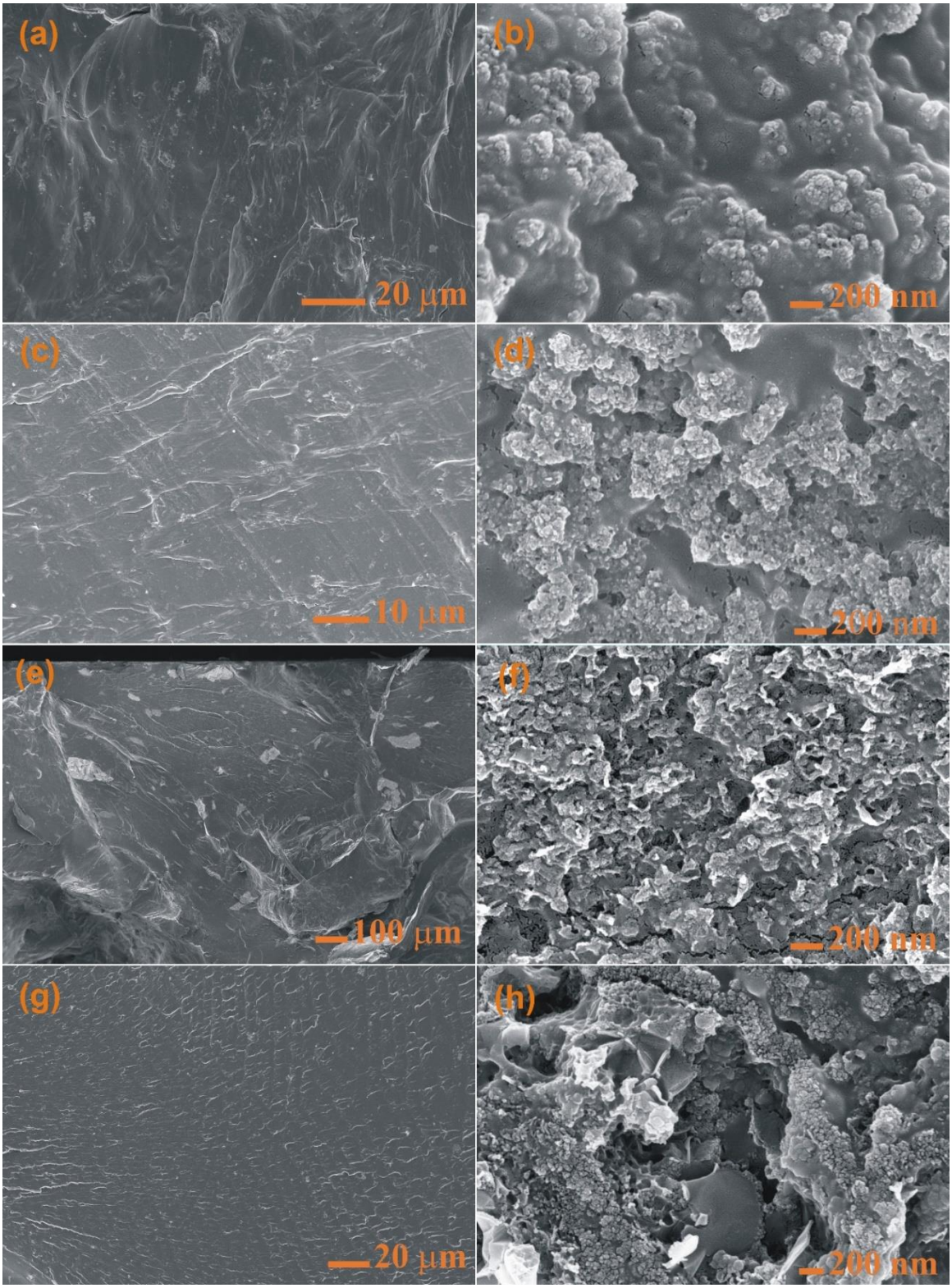

Figure 4.21 Secondary electron micrographs of 0.4 G@MgO/PVA_Coag and _ac **(a, b** and **c, d)** and 3.0G@MgO/PVA_Coag, and _ac **(e, f,** and **g, h)** composites at low and high magnifications, respectively.

The Raman vibrational modes related to PVA namely stretching mode of CH_2, $\nu(CH_2)$, symmetric bending mode of the CH_2 group, $\delta(CH_2)$, wagging, and rocking modes of the CH_2

group ($\gamma_w(CH_2)$, and $\gamma_r(CH_2)$) have appeared at 2910, 1445, 1366, and 859 cm^{-1}, respectively. In the coagulated composite samples (**Fig. 4.22(c)**) a continuous decrease in the intensity of $\nu(CH_2)$ peak and a slight shift in this peak position are observed. This change is attributed to stresses in the matrix and the decrease in intensity can be understood that the filler material in the matrix try to form a network type of structure and which influence the crystalline phase of PVA (it is clearly observed as increased D, G, and 2D bands intensity in the G@MgO/PVA_Coag composites). On the other hand, in the as-casted composite samples (**Fig. 4.22(d)**) the intensity of the $\nu(CH_2)$ peak is increased as the weight fraction of G@MgO in PVA is increased. And the reason for the increase in intensity was expected because loading of G@MgO to PVA matrix cause the CH_2 to form some clustering (i.e., nucleation) which results in enhancement of intensity. These observations are in line with x-ray diffraction results. In both the G@MgO/PVA_Coag and _ac composites, I_D/I_G value is continuously decreased, and again it is an indication of good dispersion of the (formation of network type) filler in the PVA.

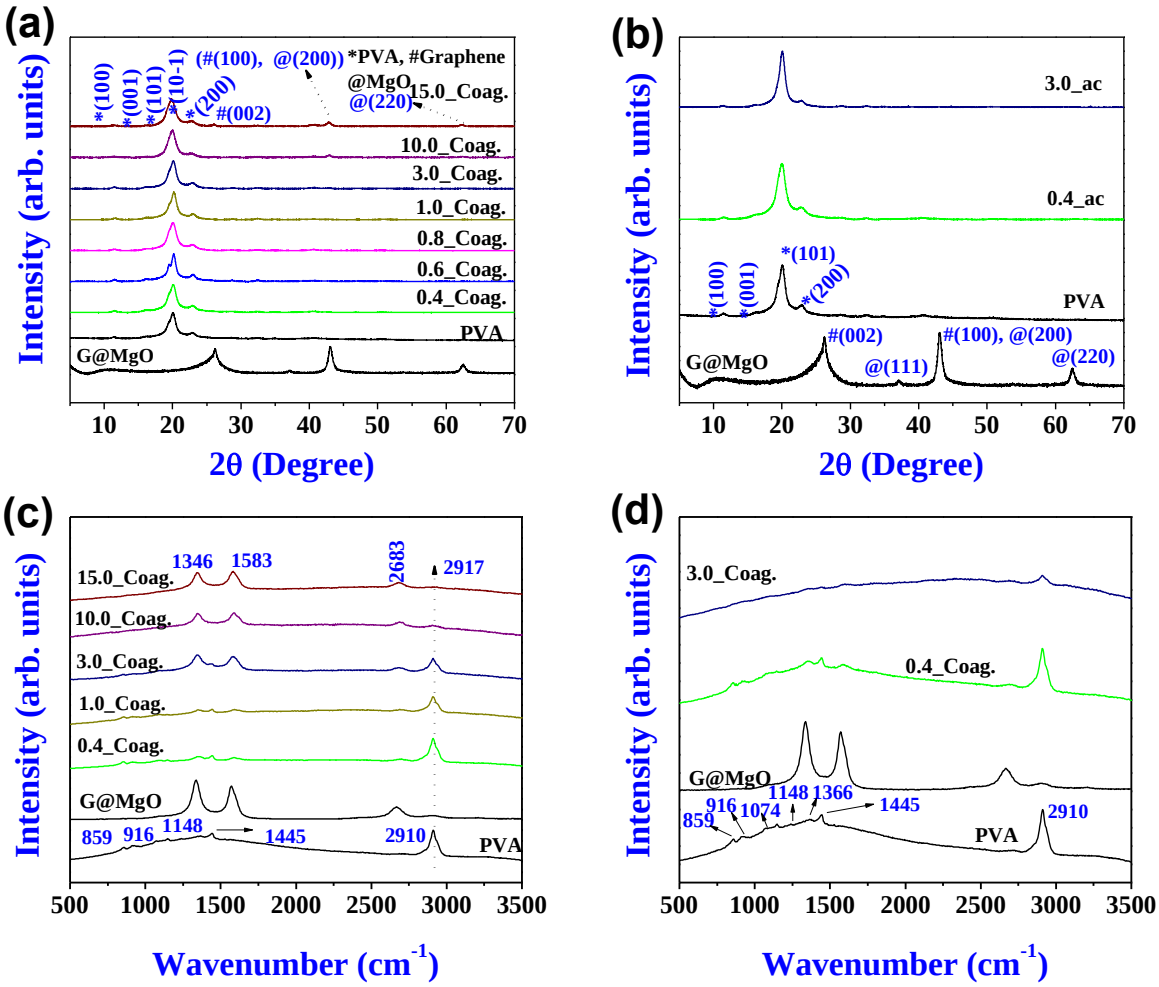

Figure 4.22 X-ray diffractograms and Raman spectra of **(a** and **c)** coagulated, and **(b** and **d)** as-casted G@MgO/PVA composites, respectively.

Table 4.6 2θ, crystallite size, and I_D/I_G ratio of G@MgO/PVA coagulated and as-casted composites.

Material	X-ray diffraction		Raman spectrum
	2θ (Degrees)	**Crystallite size of PVA (Å)**	**I_D/I_G**
PVA	19.97	65.50	-
G@MgO	-	-	1.18
0.4G@MgO/PVA_Coag	19.99	60.90	1.12
0.6G@MgO/PVA_Coag	20.17	114.03	-
0.8G@MgO/PVA_Coag	19.98	57.69	-
1.0G@MgO/PVA_Coag	20.28	113.09	0.97
3.0G@MgO/PVA_Coag	20.01	64.04	1.08
10.0G@MgO/PVA_Coag	19.97	56.16	0.98
15.0G@MgO/PVA_Coag	19.98	53.85	0.95
0.4G@MgO/PVA_ac	19.92	56.30	1.11
3.0G@MgO/PVA_ac	20.01	77.52	0.84

It is predictable that combination of conducting graphene, dielectric MgO and PVA in the synthesized composite materials can produce novel dielectric properties. The dielectric properties of these composite materials are tested in the 20 Hz-2 MHz and in the X-band frequency (i.e., 8.2-12.4 GHz) range.

The **Eq. 4.3** [232] explains the variation of the dielectric constant of material in an alternating electric field,

$$\varepsilon' = \varepsilon_\alpha + \frac{\varepsilon_s - \varepsilon_\alpha}{1 + \omega^2 \tau^2} \qquad (4.3)$$

where ε_s and ε_α are static and infinite dielectric constant values, respectively, ω is the angular frequency, and τ is the relaxation time. At very low frequencies (i.e., $\omega << 1/\tau$), dipoles follow the field and $\varepsilon' = \varepsilon_s$ (dielectric constant at the quasi-static field). As the frequency increases (i.e., $\omega < 1/\tau$), dipoles begin to lag behind the field resulting in a slight decrease in ε' value. When the frequency reaches characteristic frequency (i.e., $\omega = 1/\tau$), the dielectric constant dropped (nothing but the dielectric relaxation). At very high frequencies (i.e., $\omega >> 1/\tau$), dipoles can no longer follow the field and $\varepsilon' \approx \varepsilon_\alpha$ (the value of ε' at high frequencies). The dielectric constant versus frequency of PVA and G@MgO/PVA_Coag composites are shown in **Figs. 4.24 (a-h)**. At low temperatures, a monotonic decrease in the dielectric constant is observed with increasing frequency while it attains a constant value at high frequencies. It is also noted that dielectric constant increases with temperature and it is a typical behavior of a dipolar/polymer materials due to the presence of thermally active defects in the graphene and ionic groups in PVA [232]. Similar behavior is observed in the case of G@MgO/PVA_ac composites as shown in **Figs. 4.25 (a)** and **(b)**. Inset of **Figs. 4.24 (a-h)** and **Figs. 4.25 (a)** and **(b)** are the variation of tangent loss versus frequency at different temperatures. Two loss peaks (one in low-frequency range and other at the high-frequency edge) are observed in PVA and in all the composites (except in 10.0 and 15.0G@MgO/PVA_Coag). It is also observed that as the temperature increases, they shifted towards the high-frequency side. The loss peaks and their shift with temperature suggest thermally activated relaxation mechanisms. In the G@MgO/PVA_ac composites and 0.4-1.0G@MgO/PVA_Coag composites, a shift in loss tangent peak with an increase in temperature and on the other hand a very less shift of loss tangent peak in 3.0-15.0G@MgO/PVA_Coag composites with temperatures is observed. This is expected due to increased conductivity of the 3.0-15.0G@MgO/PVA_Coag composites. In the amorphous phase, dipolar molecules can orient from one equilibrium position to other equilibrium position relatively quickly and contribute to the absorption over a broad frequency range or temperature range. The high dielectric loss observed at low frequencies is due to the accumulation of space charges at the boundaries between fillers and matrix and at high frequencies periodic reversal of the electric field is so high that less charge can diffuse in the electric field direction thereby reducing the accumulation of space charge, and consequently resulting in decrease in the dielectric loss.

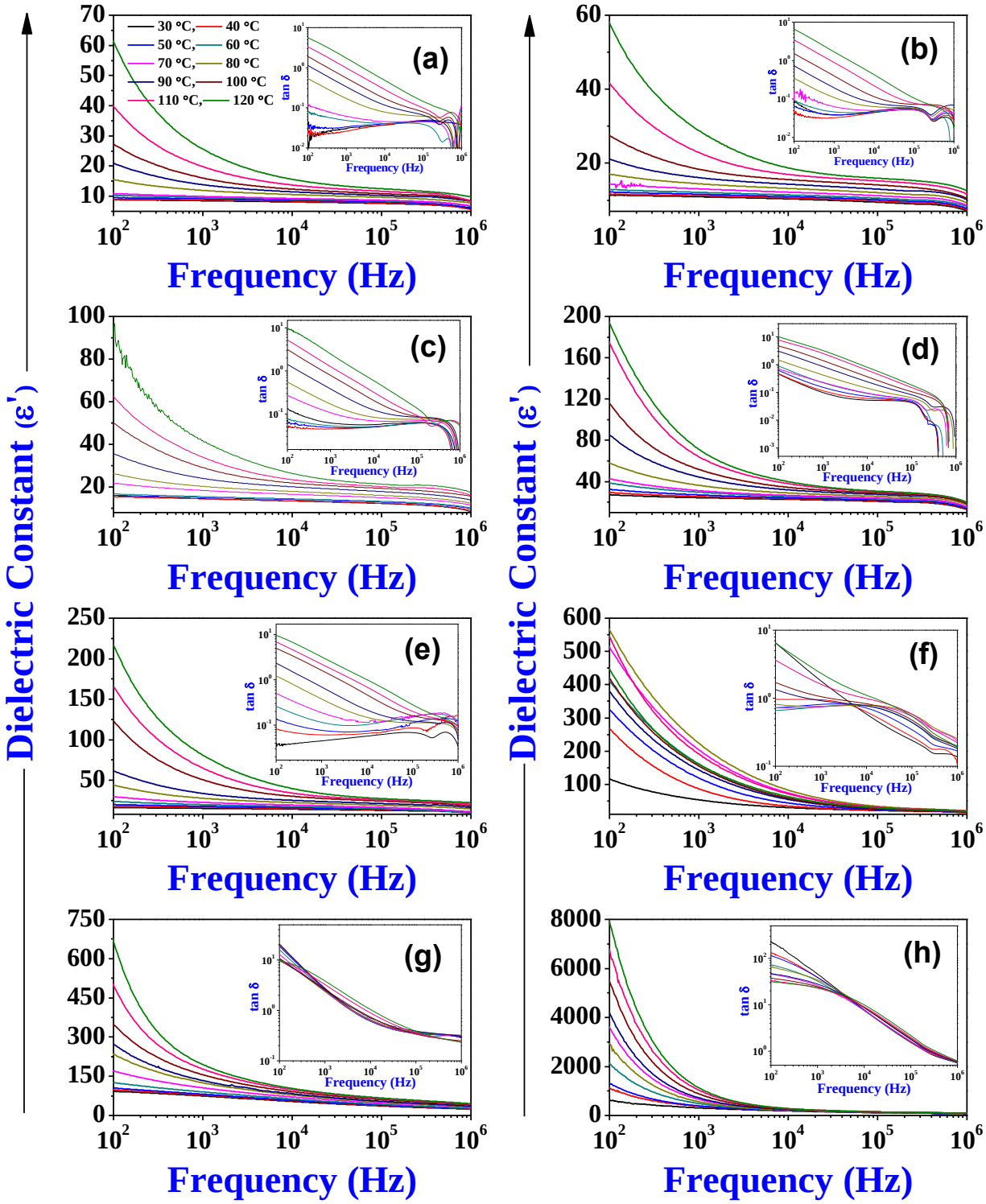

Figure 4.24 Dielectric constant and tangent loss versus frequency at different temperatures of **(a)** PVA, **(b)** 0.4, **(c)** 0.6, **(d)** 0.8, **(e)** 1.0, **(f)** 3.0, **(g)** 10.0 and **(h)** 15.0G@MgO/PVA_Coag composites, respectively.

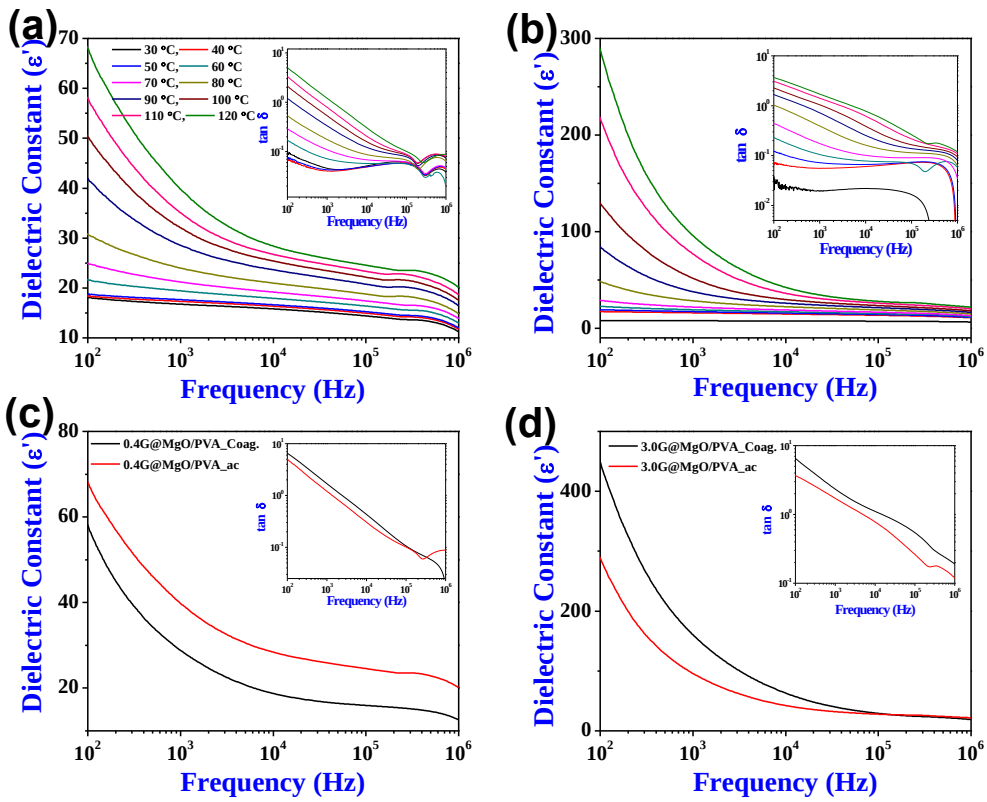

Figure 4.25 Dielectric constant and tangent loss versus frequency at different temperatures of **(a)** 0.4, **(b)** 3.0G@MgO/PVA_ac composites, and a comparison of dielectric constant and tangent loss versus frequency @120 °C of **(c)** 0.4 and **(d)** 3.0G@MgO/PVA_ac, and _Coag composites, respectively.

As shown in **Table 4.7**, at 120 °C and 1 kHz, the dielectric constant of G@MgO/PVA_Coag and G@MgO/PVA_ac composites increase in the range of 1.02-44.78, and 1.55 – 3.75 times more than the pure PVA, respectively. **Figs. 4.25 (c)** and **(d)** display, the comparison of dielectric constant and loss tangent (at 120 °C) of 0.4 and 3.0G@MgO/PVA_Coag and _ac composite samples. It is noticed that at a higher weight fraction of the filler in PVA, dielectric constant and loss tangent of coagulated samples is more than the as-casted composite samples. This is expected in coagulated samples due to good dispersion of filler material in the matrix. This type of distribution creates more filler-matrix interfaces in the coagulated samples than in the as-casted samples. When an electric field is applied on a material, due to different dielectric and conductivities of the filler and matrix charge accumulation takes place at the interface, and it causes interfacial or Maxwell-Wagner-Sillars (MWS) polarisation [233]. To understand the interfacial polarization in the prepared composites, the study of frequency dependent imaginary part of electric modulus at different temperatures is necessary and therefore the study is carried out. The electric modulus is calculated from permittivity using the **Eq. 4.4** as follows,

$$M^* = M' + iM'' = \frac{1}{\varepsilon^*} = \frac{\varepsilon'}{\varepsilon'^2 + \varepsilon''^2} + i\frac{\varepsilon''}{\varepsilon'^2 + \varepsilon''^2} \quad (4.4)$$

where M' and M'' are real and imaginary parts of the electric modulus, respectively.

To investigate the influence of interfacial polarization or MWS polarization on the substantial increase in dielectric constant and loss tangent of the G@MgO/PVA coagulated and as-casted composites, the M'' versus frequency (M'' vs f, at a different temperature) curves of different samples are shown in **Figs. 4.26 (a-h)** and **Figs. 4.27 (a-d)**. As shown in **Figs. 4.26 (a-d)** and **Figs. 4.27 (a-c)** at a certain temperature (here 70 °C or above), in the case of composite materials, the intrinsically immobilized free charges can move freely under the influence of applied field and are blocked at the interface between insulating matrix and conducting filler due to the difference in dielectric response to the applied electric field. Similarly, in the case of PVA (as shown in **Fig. 4.27(a)**), as the temperature increases the segmental motion of polymer chains increases and response of free charges to the applied electric field increases and also charge carrier mobility increases. This causes a decrease in relaxation time of the charges, and it appears as a shift in loss peak towards higher frequency side. On the other hand, 3.0-15.0G@MgO/PVA_Coag composites (**Fig. 4.26(e-g)**) show a huge shift in loss peak compared with PVA and other composites and they mildly respond to the temperature. This is expected due to increased conductivity of these composites. In the conducting materials, charge transport (with temperature) takes place via hopping mechanism or tunneling mechanism [234]. It is observed in literature that, if the composite contains conductive fillers dispersed and separated by insulating matrix hopping mechanism dominates or if the composite contains conductive fillers dispersed by forming a network of fillers throughout the matrix and are separated by thin insulating matrix then tunneling mechanism dominates [234]. The salient feature of these mechanisms is that hopping mechanism depends on temperature whereas tunneling mechanism is independent (or less dependent) of the temperature [234]. **Fig. 4.26(h)** and **Fig. 4.27(d)** represent frequency dependent imaginary part of the electric modulus of coagulated and PVA, as-casted composite samples at 120 °C temperature. With increasing filler content in the matrix the loss peak shifts towards higher frequencies due to increase in new interfaces and thereby reduction in relaxation times. But in the present work, in the case of the first composition (i.e., at 0.4 wt.% of filler in both the composite samples) relaxation peak shifted to lower frequency side. This is attributed to reduction in crystallinity of PVA matrix as shown in **Table 4.6** and lesser amount of filler material. With further increase in filler content in the PVA the loss peak shifts towards higher frequencies. An appreciable amount of shift is observed in as-casted

samples than in the coagulated samples. It is also observed that in the coagulated samples case, as the filler content is equal to or greater than 3.0 wt.% there is huge shift in loss peak towards higher frequencies while the loss peak is not observed at the percolation threshold. A new curve is observed. From above discussion, it is understood that for a critical amount of filler (percolation threshold) addition to PVA different loss mechanism (may be conduction loss) is dominating the interfacial or MWS polarization. To further confirm the above mechanisms the spectra of M'' versus f are scaled as shown in **Figs. 4.28 (a)** and **(b)** for both the composites [235]. In the scaling process, M'' is scaled by M''_{max} (where M''_{max} is the maximum value of M'' in M'' vs. f spectrum) and f is scaled by f_{max} (i.e., the frequency of which maximum of the loss peak appears). It is noted that spectra of all the composites do not merge onto a single master curve, which concludes that relaxation in the material depends on the amount of filler material in the composite. To understand composition dependent transportation, the activation energies [232] of all the composites are calculated using the following equations:

$$\tau_{max} = \tau_0 \exp\left(E_t / kT\right) \qquad (4.5)$$

$$\text{and } \sigma_{dc} = \sigma_0 \exp\left(-E_a / kT\right) \qquad (4.6)$$

where τ_{max} is the relaxation time (i.e., $\tau_{max} = 1/2\pi f_{max}$) for which peak maximum in M'' vs. f appears, τ_0 is the characteristic relaxation time, k is the Boltzmann constant, E_t is the activation energy for the migration of free charges, and T is the applied temperature. In **Eq. 4.6**, σ_{dc} is dc conductivity; σ_0 is the characteristic conductivity. σ_{dc} is calculated from the ac-universality law (i.e., Joschner Law) [234]. According to this law, at constant temperature ac conductivity, is expressed as:

$$\sigma_{ac} = \sigma_{dc} + A\omega^s \qquad (4.7)$$

where ω, A and s are angular frequency (i.e., 2πf), parameters depend on temperature and filler concentration in the composite, respectively.

Table 4.7 Real part of dielectric constant, and activation energies due to conduction and relaxation of G@MgO/PVA_Coag, and _ac composites (values in bracket represents enhancement w.r.t. PVA value).

wt.% of G@MgO	Coagulated composite samples			as-casted composite samples		
	ε′@120 °C & 1kHz	Activation Energy (eV)		ε′@120 °C & 1kHz	Activation Energy (eV)	
		E_a-conduction	E_t-relaxation		E_a-conduction	E_t-relaxation
0	25.5	1.81±0.11	1.28±0.04	25.5	1.81±0.11	1.28±0.04
0.4	28.8(1.13)	0.46±0.08	1.59±0.03	39.7(1.55)	0.47±0.05	1.07±0.09
0.6	41.4(1.62)	0.16±0.03	1.37±0.05	-	-	-
0.8	71.0(2.78)	0.44±0.02	1.04±0.07	-	-	-
1.0	80.7(3.16)	0.99±0.07	1.35±0.08	-	-	-
3.0	159.9(6.27)	0.22±0.04	0.58±0.04	95.5(3.75)	0.87±0.05	1.37±0.11
10.0	194.2(7.62)	0.22±0.03	0.37±0.05	-	-	-
15.0	1124.0 (44.78)	0.07±0.00	0.12±0.01	-	-	-

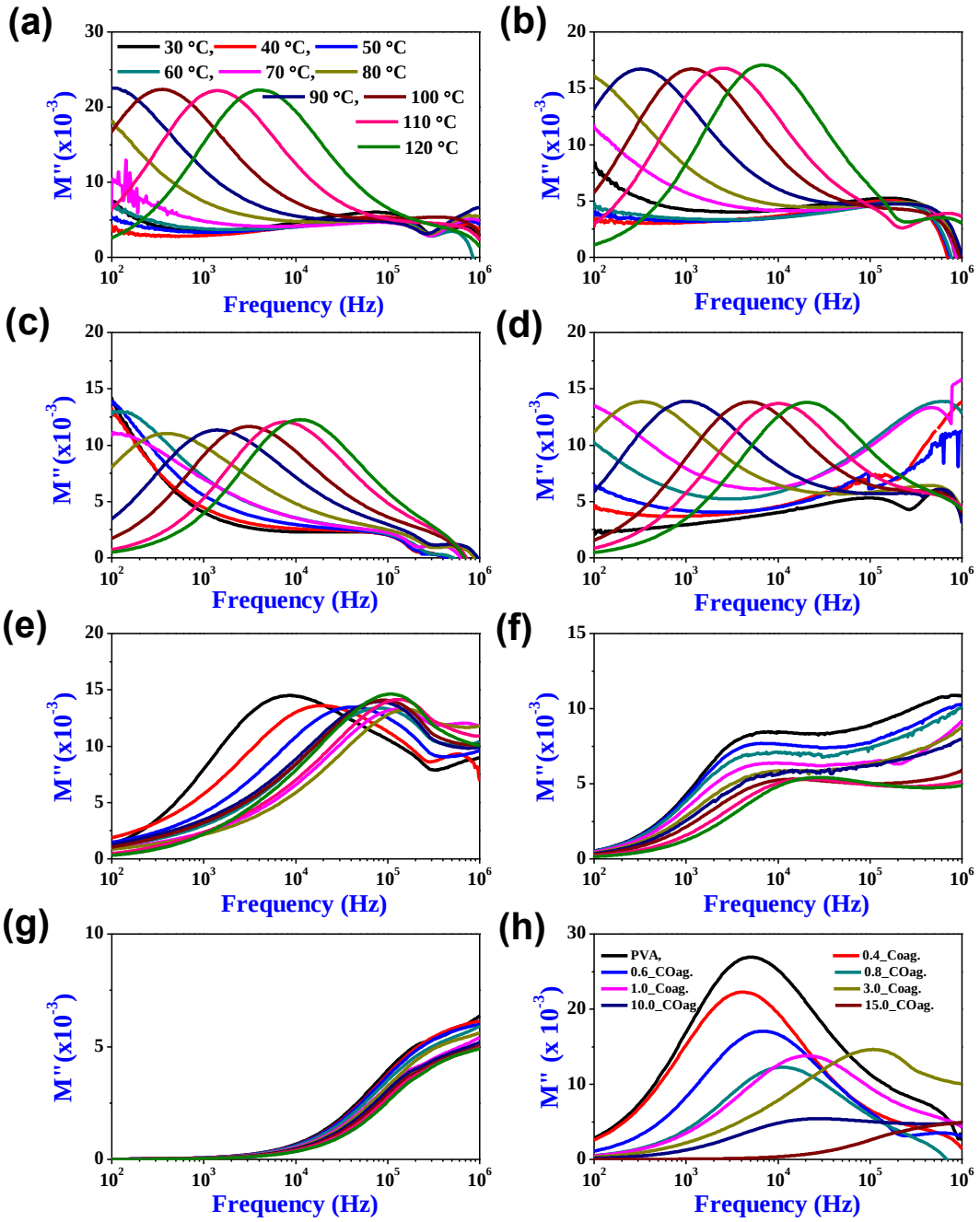

Figure 4.26 The plots of M″ vs. f and temperature of **(a)** 0.4, **(b)** 0.6, **(c)** 0.8, **(d)** 1.0, **(e)** 3.0, **(f)** 10.0, **(g)** 15.0G@MgO/PVA_Coag composites, and **(h)** comparison of **(a)**, **(b)**, **(c)**, **(d)**, **(e)**, **(f)**, and **(g)** at 120 °C, respectively.

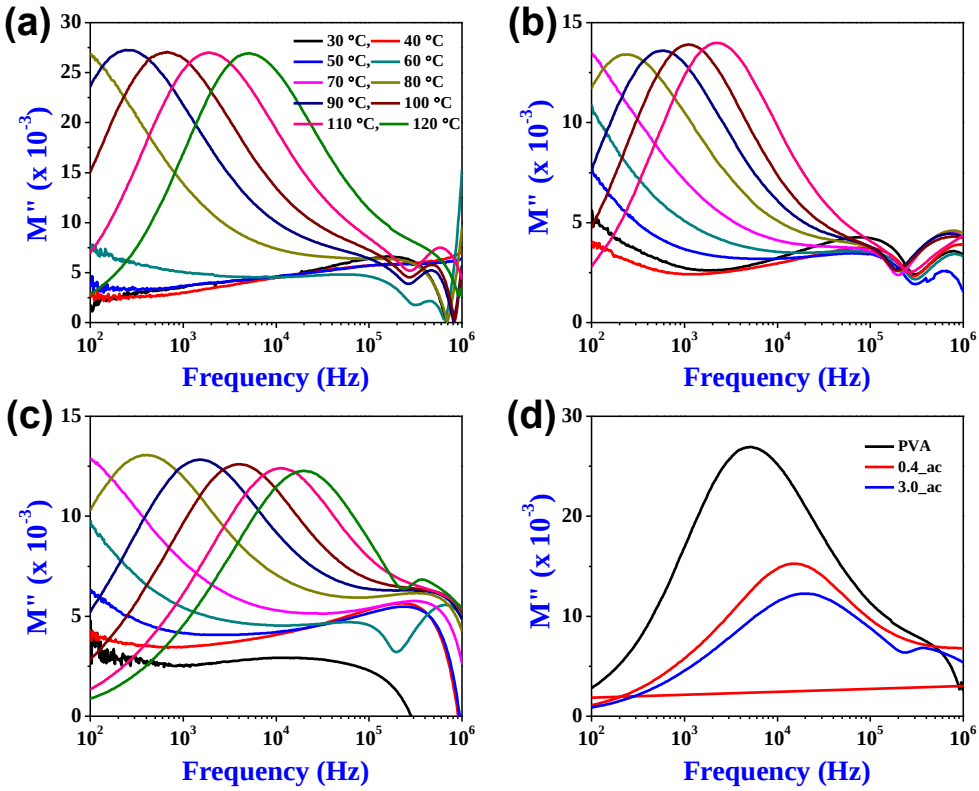

Figure 4.27 Plots of M″ vs. f and temperature of **(a)** PVA, **(b)** 0.4, **(c)** 3.0G@MgO/PVA_ac composites, and **(d)** comparison of **(a)**, **(b)**, and **(c)** at 120 °C, respectively.

The slope of ln(τ_{max}) vs. 1000/T and ln(σ_{dc}) vs. 1000/T curves give activation energies due to relaxation and conduction mechanisms, respectively and those values are presented in **Table 4.7**. As shown in **Figs. 4.28 (a)** and **(b)**, the activation energy due to relaxation mechanism in PVA is less than the conduction mechanism. Which represents polarization is the dominant mechanism for energy transfer in PVA. In both the composite samples, activation energy due to conduction is lesser than the relaxation mechanism, and it is predominate in coagulated samples. In as-casted specimens, activation energy due to conduction mechanism is less than that in PVA due to higher relaxation in comparison to that in PVA. Similarly, in coagulated samples activation energy due to conduction mechanism is less than that in PVA. When compared, the activation energies due to conduction in coagulated samples are less than those in the as-casted samples. It is noticed that in both the composite samples conduction mechanism is the dominating mechanism for energy transfer and it is more active in coagulated composite samples than in the as-casted composites. The excellent charge transport in coagulated samples than as-casted samples is expected due to well dispersed G@MgO in PVA matrix which associates with defects, and the conducting-conducting (graphene-graphene), dielectric-dielectric (MgO-PVA), and conducting-dielectric (graphene-MgO and graphene-PVA) interfaces.

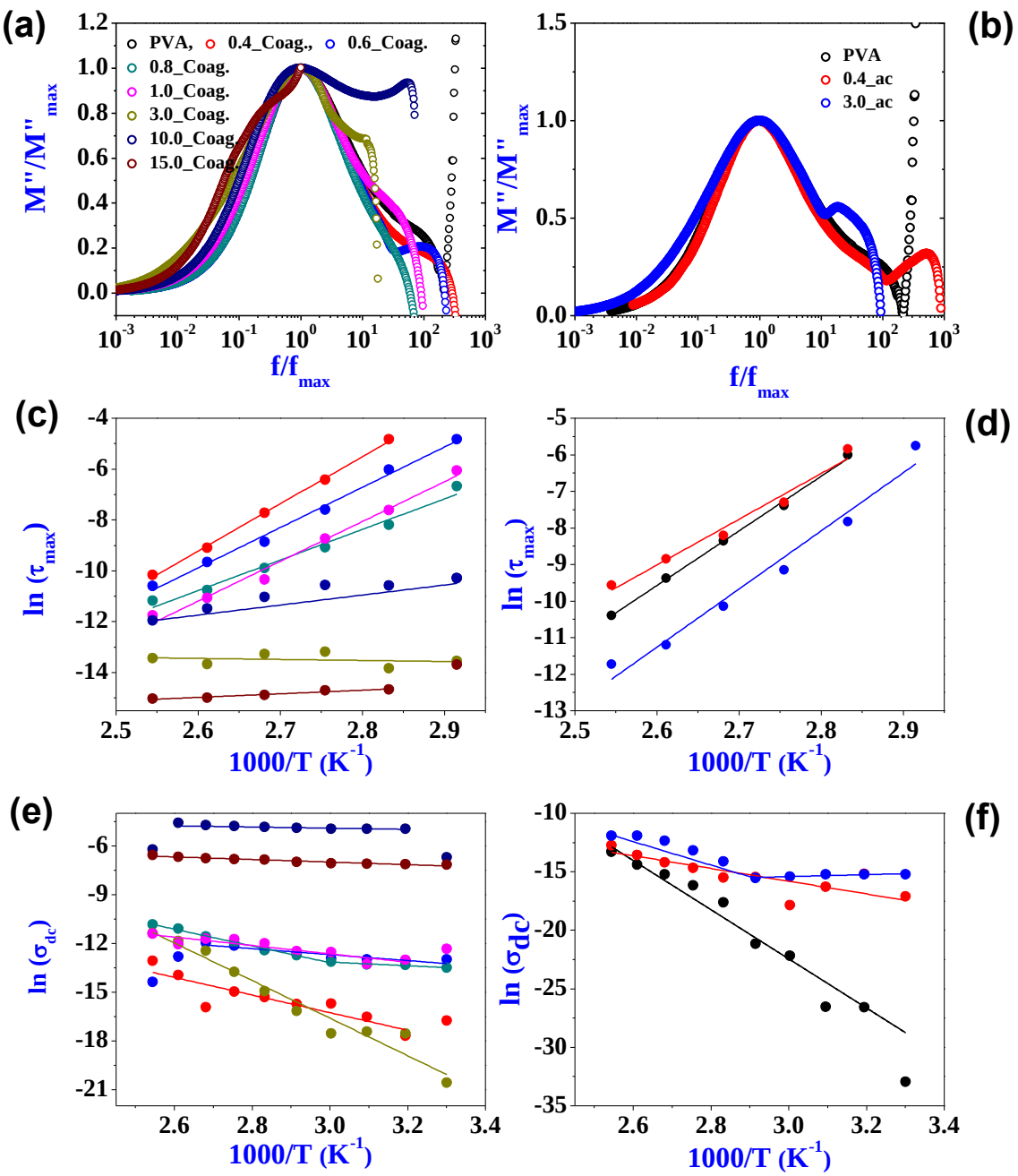

Figure 4.28 Plots of **(a, b)** M''/M''_{max} versus f/f_m, **(c, d)** $\ln(\tau_{max})$ versus 1000/T and **(e, f)** $\ln(\sigma_{dc})$ versus 1000/T of coagulated and as-casted G@MgO/PVA composites, respectively.

EMI SE of PVA, and 0.4, 3.0, 10.0 and 15.0G@MgO/PVA_Coag, and 0.4 and 3.0G@MgO/PVA_ac composites at 30, 60, 90, and 120 °C are shown in **Figs. 4.29 (a)** and **(b)**. A slight increase in the EMI SE value of PVA than both 0.4G@MgO/PVA composites at all the measured temperatures is observed. As shown in **Fig. 4.29(a)**, the EMI SE of coagulated composites is more than that of PVA. Similarly, as **Fig. 4.29(b)** displays, EMI SE of 3.0G@MgO/PVA_ac composite at all the measured temperatures is more than that of PVA. The decrease in EMI SE of 0.4G@MgO/PVA sample in both the composites is expected due

to a reduction in the crystallinity of PVA. At 120 °C and 8.2 GHz, the EMI SE values of PVA, and 0.4 and 3.0G@MgO/PVA_ac composites are ~4.75, and ~3.0, and ~5.91 dB, respectively. On the other hand, EMI SE values of 0.4, 3.0, 10.0, and 15.0G@MgO/PVA_Coag composites are ~4.05, ~16.1, ~19.3, and ~28 dB, respectively. As shown in **Fig. 4.29(c**, **d)**, a continuous increase in the EMI SE values of coagulated composite samples are observed as compared with as-casted composites, i.e., at 120 °C and 12.4 GHz an increase of 1.35 and 3.74 times is found in 0.4 and 3.0G@MgO/PVA_Coag samples, respectively than in their as-casted counterparts. The high SE of coagulated samples than of as-casted samples at the same loadings of G@MgO in PVA is attributed to the formation of network type structure (inside PVA), which leads to more surface sites available for the incoming wave to interact and communicate throughout the network. This inference is well correlated with the observed morphology, structure and phase characteristics. It is also observed that SE of each sample is almost constant in the entire "X band" frequency range. **Fig. 4.30** and **Fig. 4.31** show EMI SE, $SE_{A,}$ and SE_R versus temperature and frequency of G@MgO/PVA_Coag and _ac composites, respectively. From these figures, it is clear that absorption is the dominant mechanism for EMI shielding. This behavior is well correlated with observed morphology, structure, and phase of the G@MgO/PVA composites. The EMI SE required for most of the commercial applications is ~20 dB. In the present work, 10.0 and 15.0G@MgO/PVA_Coag composites can be used as EMI SE materials for industrial applications.

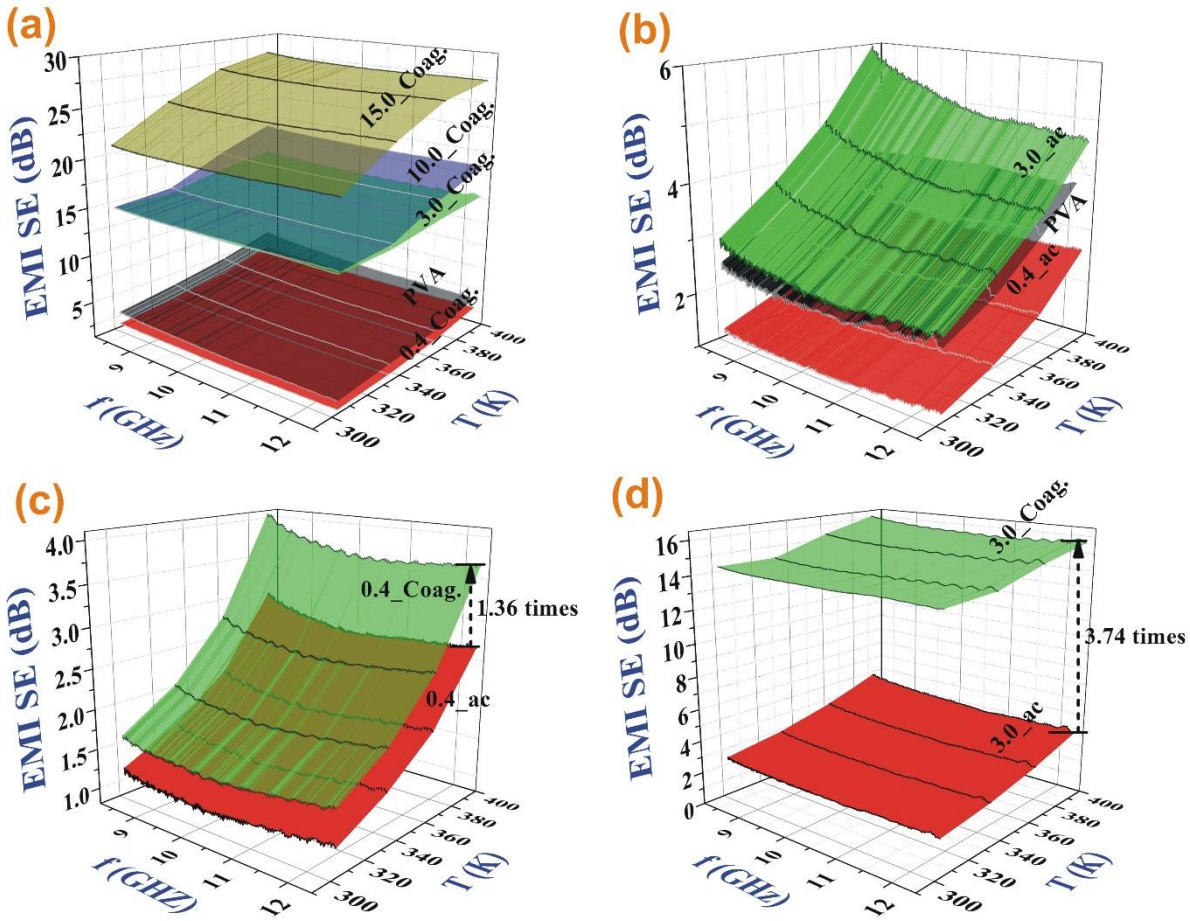

Figure 4.29 3D plots of EMI SE versus frequency and temperature of **(a)** coagulated, **(b)** as-casted composite samples, and a comparison between **(c)** 0.4 wt.%, and **(d)** 3.0 wt.% of G@MgO/PVA composite samples, respectively.

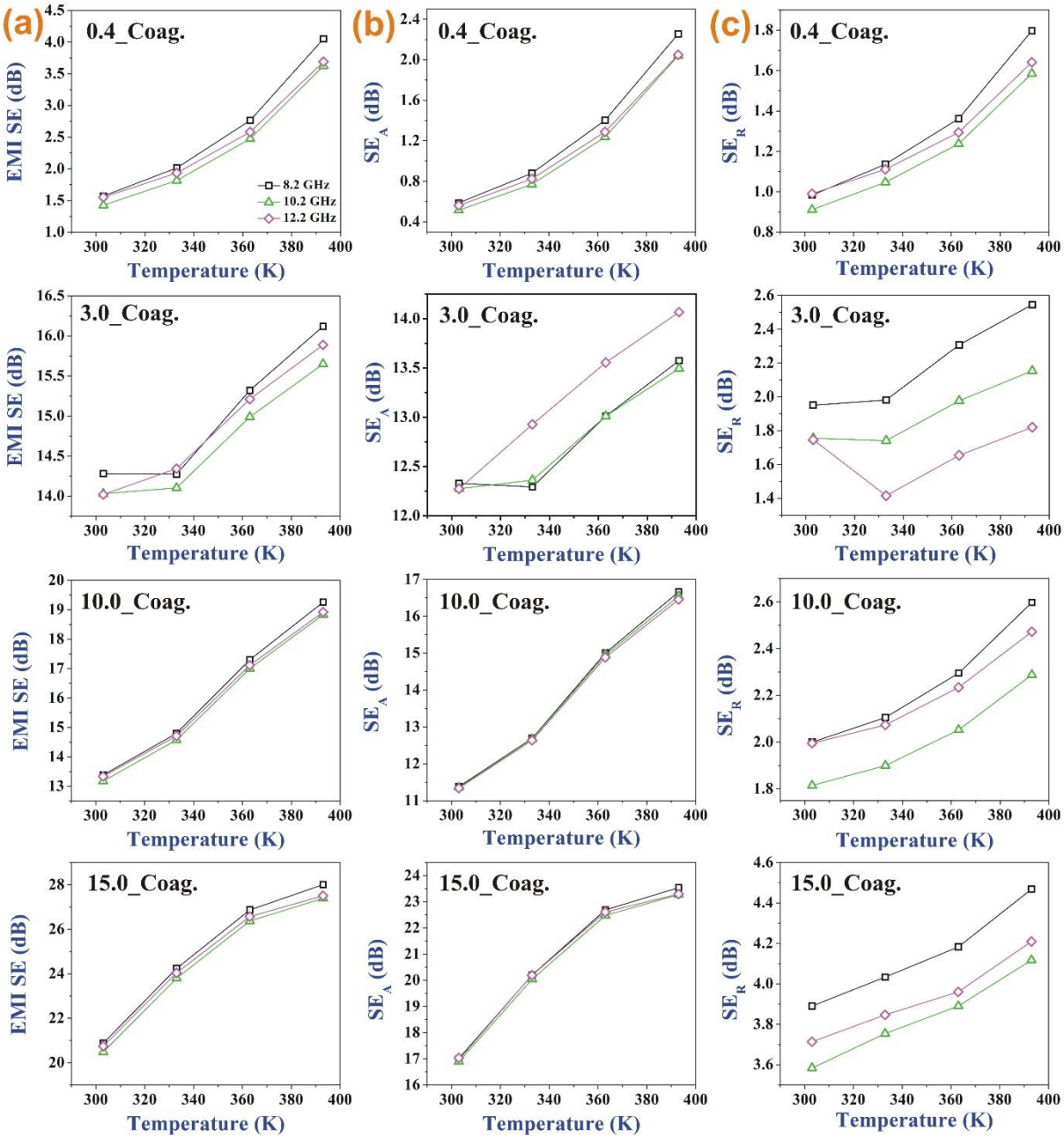

Figure 4.30 Plots of **(a)** EMI SE, **(b)** SE_A, and **(c)** SE_R, of G@MgO/PVA_Coag composites, respectively.

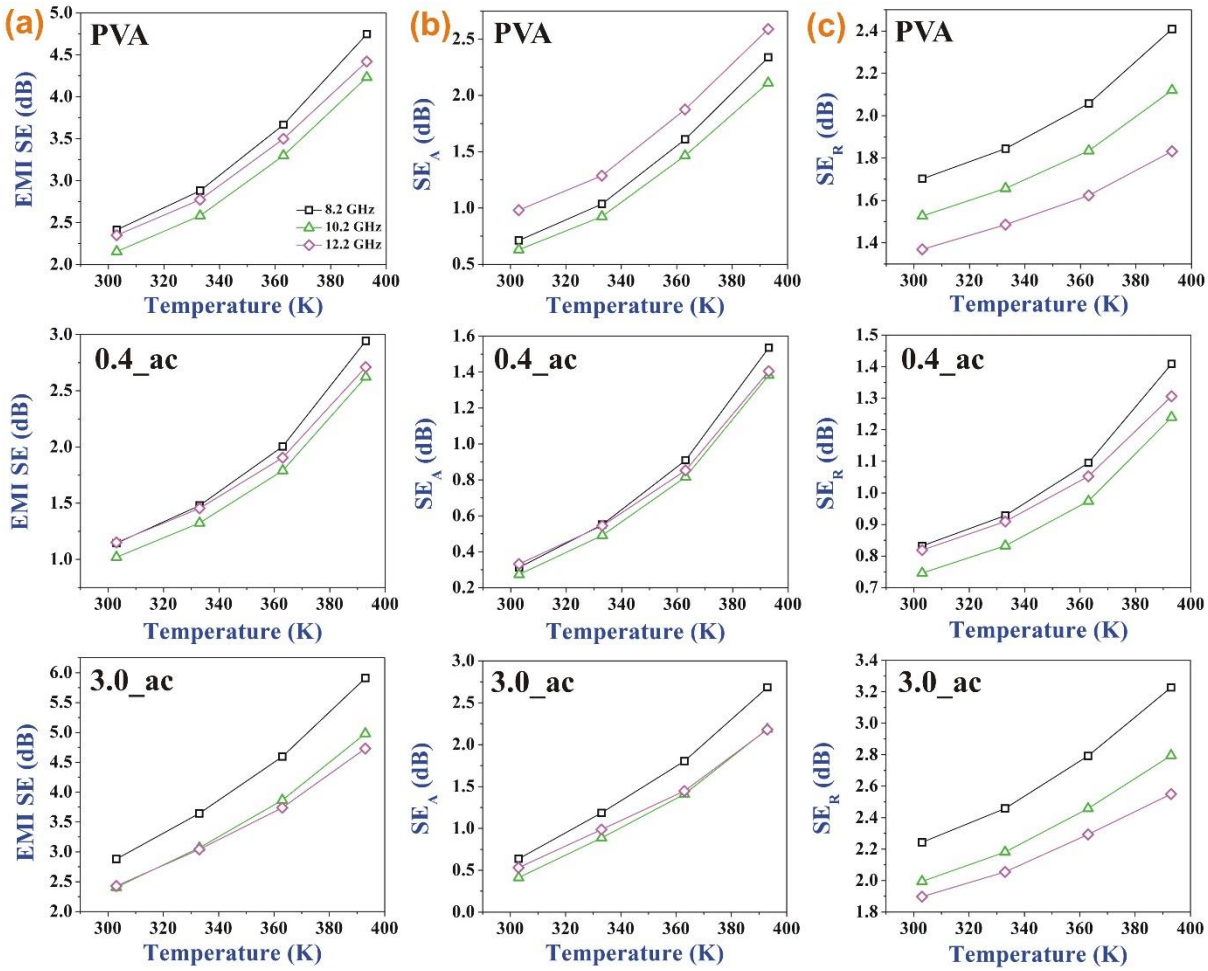

Figure 4.31 Plots of **(a)** EMI SE, **(b)** SE_A, and **(c)** SE_R of G@MgO/PVA_ac composites, respectively.

To further understand the reasons behind the observed increase in EMI SE of G@MgO/PVA composites, complex permittivity, ($\varepsilon^* = \varepsilon' - i\varepsilon''$) is evaluated from experimental scattering parameters (S_{11} and S_{21}) using theoretical calculations given by Nicolson and Ross and Weir algorithms [187, 188]. The dielectric constant (ε') is mainly associated with the amount of polarization occurring in the material, and the imaginary part (ε") is a measure of conduction loss. **Figs. 4.32 (a)** and **(b)** shows 3D plots of complex permittivity versus frequency and temperature of G@MgO/PVA_Coag composites respectively. As shown in **Fig. 4.32(c)**, it is observed that the dielectric constant of 0.4 wt.% coagulated composite is slightly more than that of PVA. An enormous increase in dielectric constant (real and imaginary parts) of the other composites (**Figs. 4.32(d-f)**) is also observed; for example, complex permittivity (real and imaginary parts) of 15.0G@MgO/PVA_Coag composite sample is 5 times more than that of PVA. Similarly, **Figs. 4.33 (a)** and **(b)** represents 3D plots of complex permittivity versus frequency and temperature of G@MgO/PVA_ac composites, respectively. The complex permittivity of 0.4 G@MgO/PVA_ac composite is less than that of PVA, and this is attributed to the less amount of G@MgO addition, and the reduction of PVA crystallinity by adding 0.4G@MgO in the PVA matrix (as shown in **Table 4.7**). The complex permittivity of 3.0G@MgO/PVA_ac composite increased when compared with that of PVA. As shown in **Figs. 4.33(c-e)** (i.e., permittivity versus temperature at 8.2, 10.2, and 12.2 GHz frequency) in all the composites, it is noticed that dielectric constant (real and imaginary part) is increased with temperature and slightly decreased with the frequency at a constant temperature. In all the composites, the dielectric constant (real and imaginary parts) increased with temperature and decreased slightly with increasing frequency. The excellent dielectric performance of the coagulated samples is attributed to the ionic, electronic, and orientational and space charge (or interfacial) polarization, and especially due to improved conduction in the material with a developed network of interconnected conducting fillers in the PVA. In PVA, the observation is attributed to segmental motion of polymer chains with temperature rise [232]. This observation is in support to the observed activation energies of these composite materials in the low-frequency range. The combustion synthesis of G@MgO and subsequent composite preparation can create defects like missing carbon atoms and sheet corrugation in the hexagonal carbon lattice of graphene. Energy transition of microwave band involves the electronic spin, which means greater spin states are required for microwave absorption. It has been reported that localized states near to the Fermi level could be created via introducing lattice defects [227]. Thus the existence of defects in graphene favors absorption of electromagnetic energy by the transition from contiguous states to Fermi level when irradiated the absorbing surface.

As observed from low-frequency dielectric data (**Fig. 4.24 - Fig. 4.28**), relaxation and conduction (dominating) are the main reasons for microwave attenuation in the composite materials. The presence of defects in the graphene, dielectric MgO, the segmental motion of the PVA chains, and interfaces such as conducting-conducting (graphene-graphene, cross over layers), dielectric-dielectric (MgO-PVA), and conducting-dielectric (graphene-MgO and graphene-PVA) are primary reasons for relaxation process. First, the defects that are prominent in these systems get screened by free charges and can act as polarization centers, which would generate polarization relaxation under the alternating electromagnetic field and attenuate electromagnetic wave, resulting in a profound effect on the loss of microwave energy. Second, MgO is a good dielectric material [236] and on the application of electric field, charge separation takes place, which generates electric dipole polarization. Therefore, under the alternating electromagnetic field, electron motion hysteresis in these dipoles can induce additional polarization relaxation processes which are favorable in enhancing microwave absorbing ability. Third, interfacial polarization (or space charge polarization) appears due to the local heterogeneity in the material. The presence of well dispersed and network type (as demonstrated in morphological, structural and phase studies) G@MgO in the insulating matrix results in the formation of more interfaces. Due to the difference in the dielectric constant and conductivity of G@MgO and PVA, some charge carriers present in G@MgO are trapped, and, as a result, some charge is developed at the interfaces between the PVA molecules and the G@MgO. This generates space charges at the various interfaces leading to the distortion of field when an electromagnetic wave passes through the material. Fourth, when electromagnetic energy is incident on the composite material, a part of the energy is absorbed and dissipated as heat due to the formation of network type filler in the composite material.

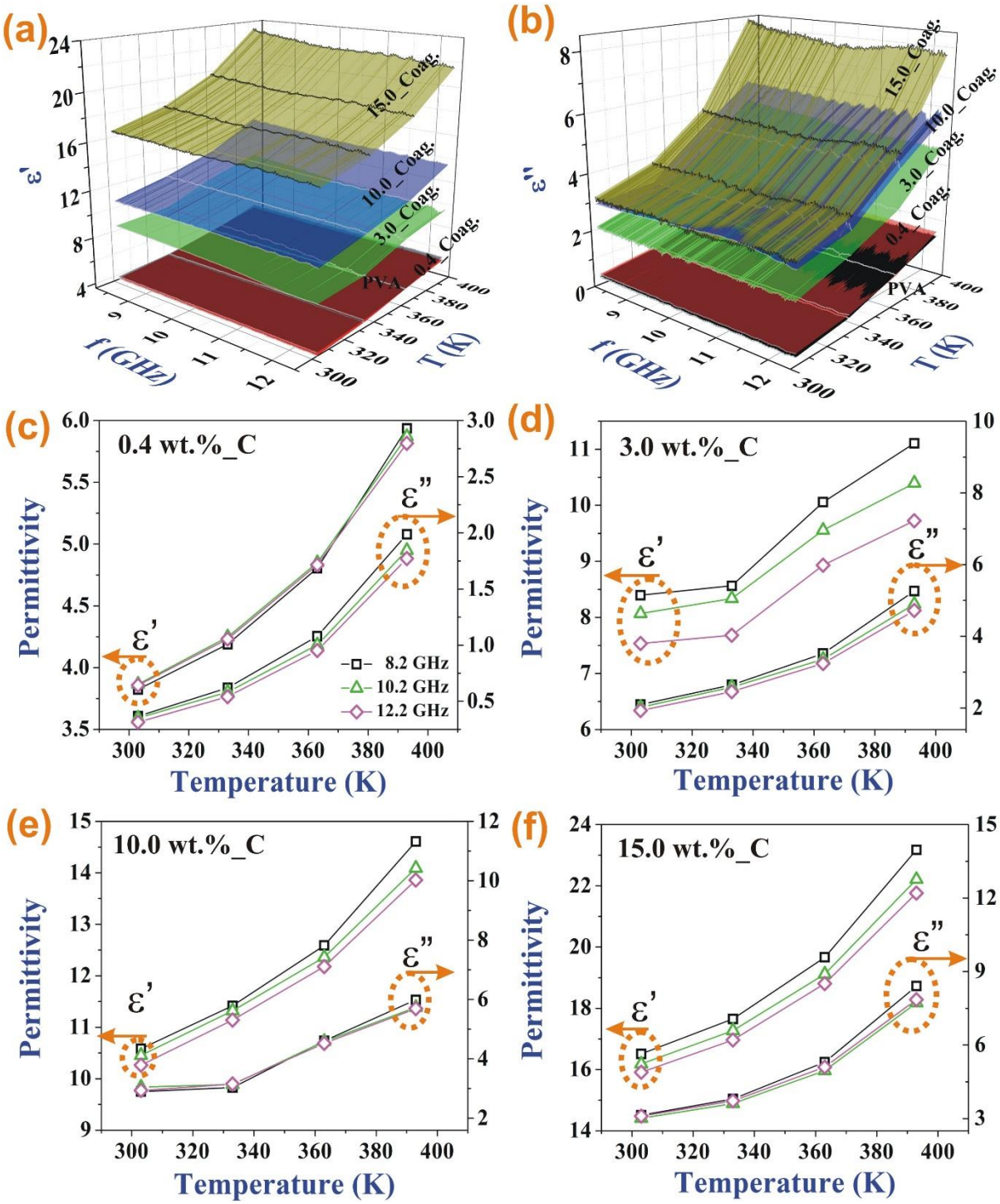

Figure 4.32 3D plots of complex permittivity versus frequency and temperature of **(a, b)** coagulated composite samples, and complex permittivity versus temperature data at a constant frequency of **(c)** 0.4, **(d)** 3.0, **(e)** 10.0 and **(f)** 15.0G@MgO/PVA_Coag composite samples respectively.

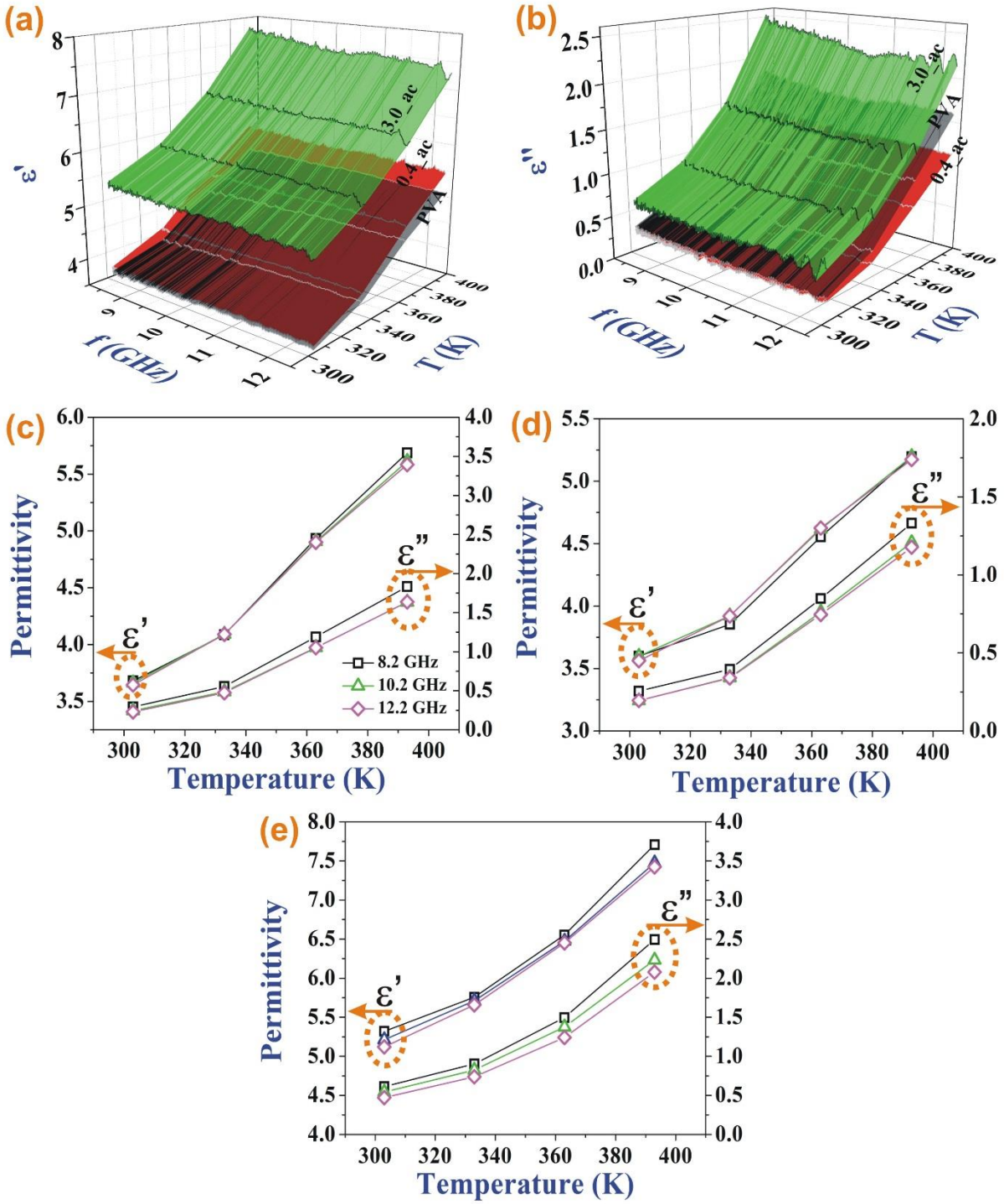

Figure 4.33 3D plots of complex permittivity versus frequency and temperature of **(a, b)** as-casted composite samples, and complex permittivity versus temperature data at a constant frequency of **(c)** PVA, **(d)** 0.4, and **(e)** 3.0G@MgO/PVA_ac composite samples respectively.

Fig. 4.29 to **Fig. 4.32** show that EMI SE, SE_A, SE_R, and complex permittivity of the G@MgO/PVA_Coag and _ac composites increase with temperature rise. It is required to understand temperature dependent dielectric and shielding properties of the composite materials. According to Debye theory of dielectrics, the real and imaginary part of dielectric constant is determined by relaxation loss and electrical conductive losses in the materials [113]. They are expressed as follows,

$$\varepsilon' = \varepsilon_\alpha + \frac{\varepsilon_s - \varepsilon_\alpha}{1+\omega^2\tau^2} \qquad (4.3)$$

$$\varepsilon'' = \frac{(\varepsilon_s - \varepsilon_\alpha)\omega\tau}{1+\omega^2\tau^2} + \frac{\sigma(T)}{\omega\varepsilon_0} \qquad (4.8)$$

where ω is the angular frequency, τ is temperature-dependent relaxation time, ε_s is the static permittivity (i.e., stationary dielectric constant), and ε_α is the relative permittivity (i.e., optical dielectric constant). The real and imaginary part of complex permittivity are determined by relaxation time (τ), and conductance (σ), which are relevant to the temperature as shown below [113],

$$\tau = \frac{1}{2\nu} e^{\frac{U}{kT}} \qquad \text{(4.9, similar to } \textbf{Eq. (4.5)}\text{)}$$

where U is a potential barrier, ν is vibration frequency, k is the Boltzmann constant, and T is the temperature.

The conductance of G@MgO is determined by [113],

$$\sigma(T) = Ae^{\frac{-E}{2kT}} \qquad \text{(4.10, similar to } \textbf{Eq. (4.6)}\text{)}$$

where A is constant and E is the band gap energy of G@MgO.

Shielding effectiveness [237] in terms of dielectric constant (ε), conductivity (σ) and permeability (μ) is,

$$SE_R = 39.5 + 10 \times \log_{10}[\sigma/2\pi f\mu] \qquad (4.11)$$

$$SE_A = 8.7t\sqrt{\pi f\mu\sigma} \qquad (4.12)$$

where $\sigma=\omega\varepsilon_o\varepsilon''$, ω is the angular frequency of the electromagnetic wave, ε_o is the permittivity of free space = 8.854 x 10^{-12} F m^{-1}, ε'' is the imaginary part of complex permittivity. From **Eq. (4.9** and **4.10)** and **Eq. (4.11** and **4.12)**, it is noticed that as the temperature of dielectric material increases, its relaxation time decreases and the conductance of the material increases. As a result, both real and imaginary parts of the complex permittivity increases. At a constant thickness of the composite materials (here 1 mm), as the conductivity of the material increases with temperature both SE_R and SE_A increases and as a consequence the total shielding efficiency of the material increases.

Chapter 5 Conclusions and Future Aspects

5.1 Conclusions

This thesis work has presented development of a simple, single step synthesis procedures to obtain graphene-based materials for Li-ion battery and EMI shielding applications. One such method is graphenothermal reduction (GTR) method which was used to synthesize $Co_2Mo_3O_8$/rGO and Ge/rGO composites. Unlike in other synthesis routes reported in the literature, the GTR method used carbons of exfoliating graphite oxide (GO) to reduce metal precursors to metal oxide ($Co_2Mo_3O_8$) and metal (Ge). At the end of the reaction most of the exfoliated GO is consumed to form respective composites by leaving considerable amount of rGO in the composite. Thus simultaneous exfoliation of GO to rGO and reduction of metal precursors results in the in-situ formation of respective composite. GTR is a single step and scalable process which requires GO and metal precursors as the starting materials. Most importantly, GTR method does not involve use of any hazardous chemicals. Moreover, in this method of synthesis, there is no requirement of any separate reducing agent, there are no hazardous solid-state by-products (only gases like water vapour, CO and CO_2 will be released) and there is no need of any post-synthesis purification. GTR method is industrially viable due to its single step reaction, low cost, and high yield.

The synthesized $Co_2Mo_3O_8$/rGO composite's morphology, crystal structure, and physical properties are studied through various characterization techniques to confirm the formation of the composite. Electrochemical properties of the composite are studied using galvanostatic cycling (GC) and cyclic voltammetry (CV) tests and electrochemical impedance spectroscopy (EIS) technique. Li cycling mechanism (i.e., Li storage and release) as understood using CV, involved redox couples of $Co_2Mo_3O_8$ and electrochemical adsorption and desorption by rGO. In the GC test, high reversible specific capacity of 954 mA h/g (at a current density of 60 mA/g), at the end of 60th cycle (indicating a long cycle life); excellent rate capability of 503 mA h/g (at a current density of 1000 mA/g), at the end of 29th cycle in the case of $Co_2Mo_3O_8$/rGO composite are noticed. EIS results suggested that Li ions experienced low impedance while charging which plausibly secured high reversible capacities. Superior specific capacity, long cycle life and better rate capability are attributed to the excellent synergy between $Co_2Mo_3O_8$ nanoplatelets and rGO in the composite. These results are encouraging for the use of $Co_2Mo_3O_8$/rGO composite as an anode material in the second-generation reversible Li-ion batteries. Similar to the $Co_2Mo_3O_8$/rGO composite, the obtained GR14 (Ge/rGO)

composite's morphology, crystal structure, and physical properties are studied through a multitude of characterization techniques to confirm the formation of the composite. Reduction mechanism of GeO_2 in presence of GO (or rGO) in the RT-900 °C temperature range is understood with the help of Rietveld refinement of XRD data obtained from the product. The redox peaks in the CV curves revealed that alloying-delloying and electrochemical adsorption and desorption type reaction mechanism are the primary reasons for lithium storage in the GR14 composite. When cycled at a current density of 160 mA/g and in the 0.005-3.0 V range, the GR14 composite showed an excellent reversible capacity of ~539 mA h/g that corresponds to 98% capacity retention at the end of the 100th cycle. The GR14 composite also showed high reversible capacity, excellent rate capability, and long cycle life. It is observed that good synergy between Ge nanoparticles and graphene in the GR14 composite and the electrochemical Li storage competition between germanium and graphene are the main reason for the high stability of the electrode material on cycling. The electrochemical performance of the $Co_2Mo_3O_8$/rGO and Ge/rGO composites are compared with existing literature as shown in the **Fig. 5.1**. From **Fig. 5.1** it is observed that $Co_2Mo_3O_8$/rGO composite showed better performance than many other reports and GR14 composite performance is comparable with the existing literature.

In the second part of the work, GO was reduced using microwaves to obtain FLG while graphene-wrapped magnesium oxide (G@MgO) powder is synthesized by ignition and combustion of magnesium metal turnings in the presence of waste solid carbon dioxide and subsequent acid treatment. Thus obtained materials were mixed with PVA to obtain FLG/PVA and G@MgO/PVA composite materials.

Cross-sectional morphology, structure and phase studies of the flexible FLG/PVA composite sheets showed the varied distribution of FLG in PVA matrix. The composite with 0.6 wt.% FLG showed the optimum distribution of FLG in PVA matrix and FLG formed network-like features in PVA matrix. This composite exhibited the highest EMI SE among the prepared composites. Absorption was found to be the dominant mechanism for EMI shielding in the present study. Similarly, morphological and structural and phase characteristics of G@MgO powder is carried out using scanning electron microscopy, transmission electron microscopy, X-ray diffraction, and Raman spectroscopy which confirmed the presence of both graphene and MgO in the powder. TGA-DTA revealed that presence of 79% graphene and 21% MgO in G@MgO. 1 mm thick G@MgO filled PVA coagulated (G@MgO/PVA_Coag) composites are prepared through sonication and coagulation of different weight fractions of G@MgO powder

with polyvinyl alcohol (PVA) solution, and subsequent hot pressing at 140 °C temperature and 3 tons of pressure. Similarly, for comparison, G@MgO filled PVA as-casted (G@MgO/PVA_ac) composites are also prepared. Characterization of these materials with a multitude of techniques confirmed the formation of composite materials. Temperature (30-120 °C) dependent complex permittivity and scattering parameters of these composites are carried out in low frequency (20 Hz - 2 MHz) and high frequency (i.e., X-band, 8.2-12.4 GHz) ranges, respectively. The dielectric properties of G@MgO/PVA_Coag composites are superior to PVA and G@MgO/PVA_ac composites in both the frequency ranges. Electric modulus studies (i.e., M'' vs. log (f) plots) revealed the existence of high interfacial polarization in coagulated and as-casted G@MgO/PVA composites. It is noticed from calculated activation energies that conduction is the dominating mechanism for energy transfer in both the composites and it is predominate in G@MgO/PVA_Coag composites than in the G@MgO/PVA_ac composites. EMI SE of G@MgO/PVA_Coag composites is more than EMI SE of G@MgO/PVA_ac composites having the same amount of G@MgO in PVA. At 30 and 120 °C, the average EMI SE of 10.0 G@MgO/PVA_Coag composite is ~14.2 and ~18.9 dB, respectively and similarly, EMI SE of ~20.6 and ~27.5 dB is found in the case of 15.0G@MgO/PVA_Coag composite, respectively. It is found that the absorption is the dominating mechanism for EMI SE in all the composites synthesized in this work. The observed superior EMI SE of G@MgO/PVA_Coag is attributed mainly to the excellent dispersion of G@MgO in PVA matrix.

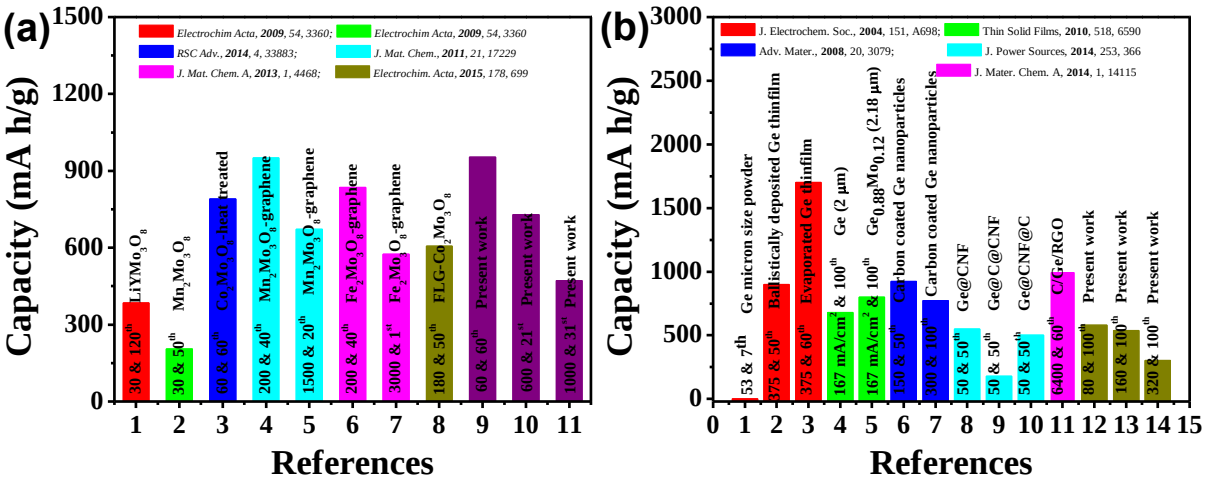

Figure 5.1 A comparison of the electrochemical performance of the **(a)** $Co_2Mo_3O_8$/rGO and **(b)** Ge/rGO composites with existing literature.

5.2 Future Aspects

In the immediate future $Co_2Mo_3O_8$/rGO and Ge/rGO composite materials can be tested as anode materials in Na-ion batteries.

In this work, GTR method was used to prepare $Co_2Mo_3O_8$/rGO and Ge/rGO composites. However, it is still unclear which released species of GO during its reduction are actually causing reduction of metal precursors. It is important to understand this aspect because knowing it would help in controlling many such solid state reactions involving reduction of GO. For this purpose, in-situ observation of reduction of the precursors using TG-DTA in combination with FTIR or mass spectroscopy is required.

The other scope is to find out uniform dispersion of metal or metal oxides on rGO in such a way that there is no impurity left after complete reaction.

In the case of EMI shielding materials, it is observed that absorption is the dominating EMI shielding mechanism for FLG/PVA and G@MgO/PVA composites. For a good absorption material impedance mismatch between sample surface and air must be as minimum as possible. Porous structures are suitable for this purpose. Therefore, immediate future scope of the present work is to synthesis graphene/polymer composites with controlled porosity and testing these samples for their potential EMI shielding applications.

References

1. Wu, Z.-S., et al., *Graphene/metal oxide composite electrode materials for energy storage.* Nano Energy, 2012. **1**(1): p. 107-131.
2. Dhakate, S.R., K.M. Subhedar, and B.P. Singh, *Polymer nanocomposite foam filled with carbon nanomaterials as an efficient electromagnetic interference shielding material.* RSC Advances, 2015. **5**(54): p. 43036-43057.
3. Ren, J.-G., et al., *Germanium-graphene composite anode for high-energy lithium batteries with long cycle life.* Journal of Materials Chemistry A, 2013. **1**(5): p. 1821-1826.
4. Sun, Y., et al., *Hierarchical self-assembly of $Mn_2Mo_3O_8$-graphene nanostructures and their enhanced lithium-storage properties.* Journal of Materials Chemistry, 2011. **21**(43): p. 17229-17235.
5. Nazri, G.A. and G. Postoia, *Lithium Ion Batteries: Science and Technology* Springer Publishers, Newyork, 2009. **First edition**.
6. Tarascon, J.M. and M. Armand, *Issues and challenges facing rechargeable lithium batteries.* Nature, 2001. **414**(6861): p. 359-367.
7. Armand, M. and J.M. Tarascon, *Building better batteries.* Nature, 2008. **451**(7179): p. 652-657.
8. Reddy, M.V., G.V. Subba Rao, and B.V.R. Chowdari, *Metal Oxides and Oxysalts as Anode Materials for Li Ion Batteries.* Chemical Reviews, 2013. **113**(7): p. 5364-5457.
9. Hatchard, T.D. and J.R. Dahn, *In Situ XRD and Electrochemical Study of the Reaction of Lithium with Amorphous Silicon.* Journal of The Electrochemical Society, 2004. **151**(6): p. A838-A842.
10. Kim, I.-S. and P.N. Kumta, *High capacity Si/C nanocomposite anodes for Li-ion batteries.* Journal of Power Sources, 2004. **136**(1): p. 145-149.
11. Graetz, J., et al., *Nanocrystalline and Thin Film Germanium Electrodes with High Lithium Capacity and High Rate Capabilities.* Journal of The Electrochemical Society, 2004. **151**(5): p. A698-A702.
12. Obrovac, M.N., et al., *Alloy Design for Lithium-Ion Battery Anodes.* Journal of The Electrochemical Society, 2007. **154**(9): p. A849-A855.
13. Ionica, C.M., et al., *Study of Li insertion mechanisms in transition metal antimony compounds as negative electrodes for Li-ion battery.* Journal of Power Sources, 2005. **146**(1–2): p. 478-481.
14. Huggins, R.A., *Lithium alloy negative electrodes.* Journal of Power Sources, 1999. **81–82**: p. 13-19.
15. Todd, A.D.W., et al., *Tin-based materials as negative electrodes for Li-ion batteries: Combinatorial approaches and mechanical methods.* International Journal of Energy Research, 2010. **34**(6): p. 535-555.
16. Poizot, P., et al., *Nano-sized transition-metal oxides as negative-electrode materials for lithium-ion batteries.* Nature, 2000. **407**(6803): p. 496-499.
17. Aragón, M.J., C. Pérez-Vicente, and J.L. Tirado, *Submicronic particles of manganese carbonate prepared in reverse micelles: A new electrode material for lithium-ion batteries.* Electrochemistry Communications, 2007. **9**(7): p. 1744-1748.
18. Grugeon, S., et al., *Combining Electrochemistry and Metallurgy for New Electrode Designs in Li-Ion Batteries.* Chemistry of Materials, 2005. **17**(20): p. 5041-5047.
19. Balaya, P., et al., *Fully Reversible Homogeneous and Heterogeneous Li Storage in RuO_2 with High Capacity.* Advanced Functional Materials, 2003. **13**(8): p. 621-625.
20. Stoller, M.D., et al., *Graphene-Based Ultracapacitors.* Nano Letters, 2008. **8**(10): p. 3498-3502.
21. Bolotin, K.I., et al., *Ultrahigh electron mobility in suspended graphene.* Solid State Communications, 2008. **146**(9–10): p. 351-355.
22. Lee, C., et al., *Measurement of the Elastic Properties and Intrinsic Strength of Monolayer Graphene.* Science, 2008. **321**(5887): p. 385-388.
23. Balandin, A.A., et al., *Superior Thermal Conductivity of Single-Layer Graphene.* Nano Letters, 2008. **8**(3): p. 902-907.

24. Zhang, H.-B., et al., *Tough Graphene−Polymer Microcellular Foams for Electromagnetic Interference Shielding.* ACS Applied Materials & Interfaces, 2011. **3**(3): p. 918-924.
25. Sonypressnews(2005)(http://www.sony.net/SonyInfo/News/Press/200502/05-006E/).
26. Toshibapressnews(2014)(https://www.toshiba.com/tic/industrial/rechargable-battery).
27. EnviaWebsite(2013)(http://www.enviasystems.com/#!cell/ch8s).
28. Amprius(2013)(https://gigaom.com/2012/05/14/look-to-silicon-nanotubes-for-really-long-lasting-batteries/).
29. Eswaraiah, V., V. Sankaranarayanan, and S. Ramaprabhu, *Functionalized Graphene–PVDF Foam Composites for EMI Shielding.* Macromolecular Materials and Engineering, 2011. **296**(10): p. 894-898.
30. Hardell, L. and C. Sage, *Biological effects from electromagnetic field exposure and public exposure standards.* Biomedicine & Pharmacotherapy, 2008. **62**(2): p. 104-109.
31. Huang, J.-C., *EMI shielding plastics: A review.* Advances in Polymer Technology, 1995. **14**(2): p. 137-150.
32. Štefečka, M., et al., *Electromagnetic shielding efficiency of plasma treated and electroless metal plated polypropylene nonwoven fabrics.* Journal of Materials Science, 2004. **39**(6): p. 2215-2217.
33. Liu, H., J. Li, and L. Wang, *Electroless nickel plating on APTHS modified wood veneer for EMI shielding.* Applied Surface Science, 2010. **257**(4): p. 1325-1330.
34. Yamada, T., et al., *Application of low resistivity Ga-doped ZnO films to transparent electromagnetic interference shielding material.* Thin Solid Films, 2008. **517**(3): p. 1027-1031.
35. Bowyer, W.H. and M.G. Bader, *On the re-inforcement of thermoplastics by imperfectly aligned discontinuous fibres.* Journal of Materials Science, 1972. **7**(11): p. 1315-1321.
36. Das, N.C., et al., *Electromagnetic interference shielding effectiveness of carbon black and carbon fibre filled EVA and NR based composites.* Composites Part A: Applied Science and Manufacturing, 2000. **31**(10): p. 1069-1081.
37. Ramadin, Y., et al., *Electrical and electromagnetic shielding behavior of laminated epoxy–carbon fiber composite.* Polymer International, 1994. **34**(2): p. 145-150.
38. Xiangcheng Luo, D.D.L.C., *Electromagnetic Interference Shielding Reaching 130 dB Using Flexible Graphite.* MRS Proceedings, 2011. **445**.
39. Baker, Z.Q., M.K. Abdelazeez, and A.M. Zihlif, *Measurements of the "Magnex DC" characteristics at microwave frequencies.* Journal of Materials Science, 1988. **23**(8): p. 2995-3000.
40. Osawa, Z. and K. Kobayashi, *Thermal stability of shielding effectiveness of electromagnetic interference of composites.* Journal of Materials Science, 1987. **22**(12): p. 4381-4387.
41. Huang, C.-Y. and J.-F. Pai, *Studies on processing parameters and thermal stability of ENCF/ABS composites for EMI shielding.* Journal of Applied Polymer Science, 1997. **63**(1): p. 115-123.
42. Huang, C.-Y. and J.-F. Pai, *Optimum conditions of electroless nickel plating on carbon fibres for EMI shielding effectiveness of ENCF/ABS composites.* European Polymer Journal, 1998. **34**(2): p. 261-267.
43. Wang, J., et al., *Preparation of graphene/poly(vinyl alcohol) nanocomposites with enhanced mechanical properties and water resistance.* Polymer International, 2011. **60**(5): p. 816-822.
44. Wu, H., et al., *Study of the Structure and Electrical Properties of Chemically Reduced Graphene/Polyvinyl Alcohol Composite Films.* Journal of Nanoscience and Nanotechnology, 2013. **13**(3): p. 1752-1758.
45. Li, Y., et al., *The effect of the ultrasonication pre-treatment of graphene oxide (GO) on the mechanical properties of GO/polyvinyl alcohol composites.* Carbon, 2013. **55**: p. 321-327.
46. Jung, S.T., et al., *The Optical and Electrical Properties of Graphene Oxide with Water-Soluble Conjugated Polymer Composites by Radiation.* Journal of Nanoscience and Nanotechnology, 2013. **13**(11): p. 7358-7364.

47. Stankovich, S., et al., *Synthesis and exfoliation of isocyanate-treated graphene oxide nanoplatelets.* Carbon, 2006. **44**(15): p. 3342-3347.
48. Stankovich, S., et al., *Graphene-based composite materials.* Nature, 2006. **442**(7100): p. 282-286.
49. Kuila, T., et al., *Chemical functionalization of graphene and its applications.* Progress in Materials Science, 2012. **57**(7): p. 1061-1105.
50. Choi, E.-Y., et al., *Noncovalent functionalization of graphene with end-functional polymers.* Journal of Materials Chemistry, 2010. **20**(10): p. 1907-1912.
51. An, X., et al., *Stable Aqueous Dispersions of Noncovalently Functionalized Graphene from Graphite and their Multifunctional High-Performance Applications.* Nano Letters, 2010. **10**(11): p. 4295-4301.
52. Zu, S.-Z., et al., *Supramolecular Surface Modification and Dispersion of Graphene in Water and Organic Solvents.* Journal of Nanoscience and Nanotechnology, 2013. **13**(2): p. 946-953.
53. Lingappan, N., et al., *Noncovalent Grafting of Poly(3-octylthiophene) at the Edges of the Graphene Nanosheets.* Journal of Nanoscience and Nanotechnology, 2013. **13**(11): p. 7439-7443.
54. Erickson, K., et al., *Determination of the Local Chemical Structure of Graphene Oxide and Reduced Graphene Oxide.* Advanced Materials, 2010. **22**(40): p. 4467-4472.
55. Zhang, H.-B., et al., *The effect of surface chemistry of graphene on rheological and electrical properties of polymethylmethacrylate composites.* Carbon, 2012. **50**(14): p. 5117-5125.
56. Han, P., et al., *Structure, Thermal Stability and Electrical Properties of Reduced Graphene/Poly(vinylidene fluoride) Nanocomposite Films.* Journal of Nanoscience and Nanotechnology, 2012. **12**(9): p. 7290-7295.
57. Ping, F., et al., *Graphene/poly(vinylidene fluoride) composites with high dielectric constant and low percolation threshold.* Nanotechnology, 2012. **23**(36): p. 365702.
58. Yun, Y.S., et al., *Reinforcing effects of adding alkylated graphene oxide to polypropylene.* Carbon, 2011. **49**(11): p. 3553-3559.
59. Pang, H., et al., *An electrically conducting polymer/graphene composite with a very low percolation threshold.* Materials Letters, 2010. **64**(20): p. 2226-2229.
60. Kim, H., et al., *Graphene/polyethylene nanocomposites: Effect of polyethylene functionalization and blending methods.* Polymer, 2011. **52**(8): p. 1837-1846.
61. Seveyrat, L., et al., *Preparation of graphene nanoflakes/polymer composites and their performances for actuation and energy harvesting applications.* Journal of Applied Physics, 2012. **111**(10): p. 104904.
62. Kim, H., Y. Miura, and C.W. Macosko, *Graphene/Polyurethane Nanocomposites for Improved Gas Barrier and Electrical Conductivity.* Chemistry of Materials, 2010. **22**(11): p. 3441-3450.
63. Zheng, D., et al., *In situ thermal reduction of graphene oxide for high electrical conductivity and low percolation threshold in polyamide 6 nanocomposites.* Composites Science and Technology, 2012. **72**(2): p. 284-289.
64. Dao, T.D., et al., *The Effect of Oxidation on Properties of Graphene and Its Polycaprolactone Nanocomposites.* Journal of Nanoscience and Nanotechnology, 2012. **12**(11): p. 8420-8430.
65. Luo, X. and D.D.L. Chung, *Improved properties of chemically modified graphene/poly(methyl methacrylate) nanocomposites via a facile in-situ bulk polymerization.* eXPRESS Polymer Letters, 2012. **6**(10): p. 847-858.
66. Lee, J., et al., *Nanocomposites of Polystyrene/Polystyrene-Grafted Graphene Oxides Synthesized by In-Situ Bulk Polymerization.* Journal of Nanoscience and Nanotechnology, 2013. **13**(3): p. 1769-1772.
67. Milani, M.A., et al., *Polypropylene/graphene nanosheet nanocomposites by in situ polymerization: Synthesis, characterization and fundamental properties.* Composites Science and Technology, 2013. **84**: p. 1-7.

68. Hu, N., et al., *Graphene Oxide Reinforced Polyimide Nanocomposites via In Situ Polymerization.* Journal of Nanoscience and Nanotechnology, 2012. **12**(1): p. 173-178.
69. Luong, N.D., et al., *Enhanced mechanical and electrical properties of polyimide film by graphene sheets via in situ polymerization.* Polymer, 2011. **52**(23): p. 5237-5242.
70. Fabbri, P., et al., *Preparation and characterization of poly (butylene terephthalate)/graphene composites by in-situ polymerization of cyclic butylene terephthalate.* Polymer, 2012. **53**(4): p. 897-902.
71. Tjong, S.C., S.L. Liu, and R.K.Y. Li, *Mechanical properties of injection moulded blends of polypropylene with thermotropic liquid crystalline polymer.* Journal of Materials Science, 1996. **31**(2): p. 479-484.
72. Meng, Y.Z. and S.C. Tjong, *Rheology and morphology of compatibilized polyamide 6 blends containing liquid crystalline copolyesters.* Polymer, 1998. **39**(1): p. 99-107.
73. Tjong, S.C. and Y.Z. Meng, *Performance of potassium titanate whisker reinforced polyamide-6 composites.* Polymer, 1998. **39**(22): p. 5461-5466.
74. Tjong, S.C. and Y.Z. Meng, *Impact-modified polypropylene/vermiculite nanocomposites.* Journal of Polymer Science Part B: Polymer Physics, 2003. **41**(19): p. 2332-2341.
75. Li, X.H., et al., *Completely biodegradable composites of poly(propylene carbonate) and short, lignocellulose fiber Hildegardia populifolia.* Journal of Polymer Science Part B: Polymer Physics, 2004. **42**(4): p. 666-675.
76. Tjong, S.C., S.P. Bao, and G.D. Liang, *Polypropylene/montmorillonite nanocomposites toughened with SEBS-g-MA: Structure–property relationship.* Journal of Polymer Science Part B: Polymer Physics, 2005. **43**(21): p. 3112-3126.
77. Bao, S.P. and S.C. Tjong, *Impact essential work of fracture of polypropylene/montmorillonite nanocomposites toughened with SEBS-g-MA elastomer.* Composites Part A: Applied Science and Manufacturing, 2007. **38**(2): p. 378-387.
78. El Achaby, M., et al., *Preparation and characterization of melt-blended graphene nanosheets–poly(vinylidene fluoride) nanocomposites with enhanced properties.* Journal of Applied Polymer Science, 2013. **127**(6): p. 4697-4707.
79. Zhang, H.-B., et al., *Electrically conductive polyethylene terephthalate/graphene nanocomposites prepared by melt compounding.* Polymer, 2010. **51**(5): p. 1191-1196.
80. Kim, H. and C.W. Macosko, *Processing-property relationships of polycarbonate/graphene composites.* Polymer, 2009. **50**(15): p. 3797-3809.
81. Shirakawa, H., et al., *Synthesis of electrically conducting organic polymers: halogen derivatives of polyacetylene, (CH).* Journal of the Chemical Society, Chemical Communications, 1977. **0**(16): p. 578-580.
82. Trivedi, D.C. and S.K. Dhawan, *Grafting of electronically conducting polyaniline on insulating surfaces.* Journal of Materials Chemistry, 1992. **2**(10): p. 1091-1096.
83. Geetha, S., K.K. Satheesh Kumar, and D.C. Trivedi, *Polyaniline reinforced conducting E-glass fabric using 4-chloro-3-methyl phenol as secondary dopant for the control of electromagnetic radiations.* Composites Science and Technology, 2005. **65**(6): p. 973-980.
84. Lee, C.Y., et al., *Electromagnetic interference shielding efficiency of polyaniline mixtures and multilayer films.* Synthetic Metals, 1999. **102**(1): p. 1346-1349.
85. Kathirgamanathan, P., *Unusual electromagnetic shielding characteristics of inherently conducting polymer-coated metal powder/polymer composites.* Journal of Materials Chemistry, 1993. **3**(3): p. 259-262.
86. Hong, Y.K., et al., *Electromagnetic interference shielding characteristics of fabric complexes coated with conductive polypyrrole and thermally evaporated Ag.* Current Applied Physics, 2001. **1**(6): p. 439-442.
87. Kathirgamanathan, P., *Novel cable shielding materials based on the impregnation of microporous membranes with inherently conducting polymers.* Advanced Materials, 1993. **5**(4): p. 281-283.

88. Bianco, A., et al., *All in the graphene family – A recommended nomenclature for two-dimensional carbon materials.* Carbon, 2013. **65**: p. 1-6.
89. Yoo, E., et al., *Large Reversible Li Storage of Graphene Nanosheet Families for Use in Rechargeable Lithium Ion Batteries.* Nano Letters, 2008. **8**(8): p. 2277-2282.
90. Wang, G., et al., *Graphene nanosheets for enhanced lithium storage in lithium ion batteries.* Carbon, 2009. **47**(8): p. 2049-2053.
91. Wang, C., et al., *Electrochemical Properties of Graphene Paper Electrodes Used in Lithium Batteries.* Chemistry of Materials, 2009. **21**(13): p. 2604-2606.
92. Pan, D., et al., *Li Storage Properties of Disordered Graphene Nanosheets.* Chemistry of Materials, 2009. **21**(14): p. 3136-3142.
93. Lian, P., et al., *Large reversible capacity of high quality graphene sheets as an anode material for lithium-ion batteries.* Electrochimica Acta, 2010. **55**(12): p. 3909-3914.
94. Petnikota, S., et al., *Electrochemical studies of few-layered graphene as an anode material for Li ion batteries.* Journal of Solid State Electrochemistry, 2014. **18**(4): p. 941-949.
95. Wu, Z.-S., et al., *Doped Graphene Sheets As Anode Materials with Superhigh Rate and Large Capacity for Lithium Ion Batteries.* ACS Nano, 2011. **5**(7): p. 5463-5471.
96. Goh, B.-M., et al., *Filling the Voids of Graphene Foam with Graphene "Eggshell" for Improved Lithium-Ion Storage.* ACS Applied Materials & Interfaces, 2014. **6**(12): p. 9835-9841.
97. Murugan, A.V., T. Muraliganth, and A. Manthiram, *Rapid, Facile Microwave-Solvothermal Synthesis of Graphene Nanosheets and Their Polyaniline Nanocomposites for Energy Strorage.* Chemistry of Materials, 2009. **21**(21): p. 5004-5006.
98. Sun, W. and Y. Wang, *Graphene-based nanocomposite anodes for lithium-ion batteries.* Nanoscale, 2014. **6**(20): p. 11528-11552.
99. Luo, B. and L. Zhi, *Design and construction of three dimensional graphene-based composites for lithium ion battery applications.* Energy & Environmental Science, 2015. **8**(2): p. 456-477.
100. Luo, B., S. Liu, and L. Zhi, *Chemical Approaches toward Graphene-Based Nanomaterials and their Applications in Energy-Related Areas.* Small, 2012. **8**(5): p. 630-646.
101. Park, C.-M., et al., *Li-alloy based anode materials for Li secondary batteries.* Chemical Society Reviews, 2010. **39**(8): p. 3115-3141.
102. Crisp, D., A. Pathare, and R.C. Ewell, *The performance of gallium arsenide/germanium solar cells at the Martian surface.* Acta Astronautica, 2004. **54**(2): p. 83-101.
103. Wang, G.H., et al., *Fabrication of amorphous silicon–germanium thin film solar cell toward broadening long wavelength response.* Journal of Alloys and Compounds, 2016. **658**: p. 543-547.
104. Collord, A.D. and H.W. Hillhouse, *Germanium Alloyed Kesterite Solar Cells with Low Voltage Deficits.* Chemistry of Materials, 2016. **28**(7): p. 2067-2073.
105. Chan, C.K., et al., *High-performance lithium battery anodes using silicon nanowires.* Nat Nano, 2008. **3**(1): p. 31-35.
106. Ouyang, L., et al., *Facile synthesis of Ge@FLG composites by plasma assisted ball milling for lithium ion battery anodes.* Journal of Materials Chemistry A, 2014. **2**(29): p. 11280-11285.
107. Xu, Y., et al., *Ge Nanoparticles Encapsulated in Nitrogen-Doped Reduced Graphene Oxide as an Advanced Anode Material for Lithium-Ion Batteries.* The Journal of Physical Chemistry C, 2014. **118**(49): p. 28502-28508.
108. Fang, S., et al., *Ge-graphene-carbon nanotube composite anode for high performance lithium-ion batteries.* Journal of Materials Chemistry A, 2015. **3**(4): p. 1498-1503.
109. Xue, D.-J., et al., *Improving the Electrode Performance of Ge through Ge@C Core–Shell Nanoparticles and Graphene Networks.* Journal of the American Chemical Society, 2012. **134**(5): p. 2512-2515.
110. Yuan, F.-W. and H.-Y. Tuan, *Scalable Solution-Grown High-Germanium-Nanoparticle-Loading Graphene Nanocomposites as High-Performance Lithium-Ion Battery Electrodes: An Example*

of a Graphene-Based Platform toward Practical Full-Cell Applications. Chemistry of Materials, 2014. **26**(6): p. 2172-2179.

111. Wang, T., et al., *Elastic Reduced Graphene Oxide Nanosheets Embedded in Germanium Nanofiber Matrix as Anode Material for High-Performance Li-Ion Battery.* Electrochimica Acta, 2015. **186**: p. 64-70.
112. Wang, X., et al., *Core–Shell Ge@Graphene@TiO_2 Nanofibers as a High-Capacity and Cycle-Stable Anode for Lithium and Sodium Ion Battery.* Advanced Functional Materials, 2016. **26**(7): p. 1104-1111.
113. Chen, Z., et al., *Copper germanate nanowire/reduced graphene oxide anode materials for high energy lithium-ion batteries.* Journal of Materials Chemistry A, 2013. **1**(37): p. 11404-11409.
114. Wu, S., et al., *$CuGeO_3$ nanowires covered with graphene as anode materials of lithium ion batteries with enhanced reversible capacity and cyclic performance.* Nanoscale, 2014. **6**(14): p. 8350-8358.
115. Li, W., D. Chen, and G. Shen, *Encapsulating $Ca_2Ge_7O_{16}$ nanowires within graphene sheets as anode materials for lithium-ion batteries.* Journal of Materials Chemistry A, 2015. **3**(41): p. 20673-20680.
116. Zhang, F., et al., *Hydrothermal growth of Cobalt germanate/reduced graphene oxide nanocomposite as superior anode materials for Lithium-ion batteries.* Electrochimica Acta, 2014. **150**: p. 211-217.
117. Hu, X., et al., *Nanostructured Mo-based electrode materials for electrochemical energy storage.* Chemical Society Reviews, 2015. **44**(8): p. 2376-2404.
118. Ku, J.H., et al., *Thermoelectrochemically Activated MoO_2 Powder Electrode for Lithium Secondary Batteries.* Journal of The Electrochemical Society, 2009. **156**(8): p. A688-A693.
119. Guan, B., W. Sun, and Y. Wang, *Carbon-Coated $MnMoO_4$ Nanorod for High-Performance Lithium-Ion Batteries.* Electrochimica Acta, 2016. **190**: p. 354-359.
120. Xu, X., et al., *Bamboo-like amorphous carbon nanotubes clad in ultrathin nickel oxide nanosheets for lithium-ion battery electrodes with long cycle life.* Carbon, 2015. **84**: p. 491-499.
121. Wang, B., et al., *Hierarchical $NiMoO_4$ nanowire arrays supported on macroporous graphene foam as binder-free 3D anodes for high-performance lithium storage.* Physical Chemistry Chemical Physics, 2016. **18**(2): p. 908-915.
122. Xiao, W., et al., *Synthesis, Characterization, and Lithium Storage Capability of $AMoO_4$ (A = Ni, Co) Nanorods.* Chemistry of Materials, 2010. **22**(3): p. 746-754.
123. Chen, Y., et al., *Coaxial three-dimensional $CoMoO_4$ nanowire arrays with conductive coating on carbon cloth for high-performance lithium ion battery anode.* Journal of Power Sources, 2015. **300**: p. 132-138.
124. Guo, J., et al., *Fast and large lithium storages from $CoMoO_4$ nanorods-graphene composite.* Ionics, 2015. **21**(10): p. 2993-2999.
125. Yu, H., et al., *Hierarchically porous three-dimensional electrodes of $CoMoO_4$ and $ZnCo_2O_4$ and their high anode performance for lithium ion batteries.* Nanoscale, 2014. **6**(18): p. 10556-10561.
126. Ko, Y.N., Y.C. Kang, and S.B. Park, *Superior cycling and rate performances of rattle-type $CoMoO_4$ microspheres prepared by one-pot spray pyrolysis.* RSC Advances, 2014. **4**(34): p. 17873-17878.
127. Yao, J., et al., *$CoMoO_4$ Nanoparticles Anchored on Reduced Graphene Oxide Nanocomposites as Anodes for Long-Life Lithium-Ion Batteries.* ACS Applied Materials & Interfaces, 2014. **6**(22): p. 20414-20422.
128. Zhang, Z., et al., *Iron(ii) molybdate ($FeMoO_4$) nanorods as a high-performance anode for lithium ion batteries: structural and chemical evolution upon cycling.* Journal of Materials Chemistry A, 2015. **3**(41): p. 20527-20534.

129. Das, B., et al., *Synthesis of Mo-cluster compound, $LiHoMo_3O_8$ by carbothermal reduction and its reactivity towards Li.* Journal of Solid State Electrochemistry, 2008. **12**(7): p. 953-959.
130. Das, B., et al., *Carbothermal synthesis, spectral and magnetic characterization and Li-cyclability of the Mo-cluster compounds, $LiYMo_3O_8$ and $Mn_2Mo_3O_8$.* Electrochimica Acta, 2009. **54**(12): p. 3360-3373.
131. Das, B., et al., *A disc-like Mo-metal cluster compound, $Co_2Mo_3O_8$, as a high capacity anode for lithium ion batteries.* RSC Advances, 2014. **4**(64): p. 33883-33889.
132. Sun, Y., et al., *Self-assembly of hybrid $Fe_2Mo_3O_8$-reduced graphene oxide nanosheets with enhanced lithium storage properties.* Journal of Materials Chemistry A, 2013. **1**(14): p. 4468-4474.
133. Du, J. and H.-M. Cheng, *The Fabrication, Properties, and Uses of Graphene/Polymer Composites.* Macromolecular Chemistry and Physics, 2012. **213**(10-11): p. 1060-1077.
134. Kim, H., A.A. Abdala, and C.W. Macosko, *Graphene/Polymer Nanocomposites.* Macromolecules, 2010. **43**(16): p. 6515-6530.
135. Liang, J., et al., *Electromagnetic interference shielding of graphene/epoxy composites.* Carbon, 2009. **47**(3): p. 922-925.
136. Anupama, J., et al., *Graphene nanoribbon–PVA composite as EMI shielding material in the X band.* Nanotechnology, 2013. **24**(45): p. 455705.
137. Yan, D.-X., et al., *Efficient electromagnetic interference shielding of lightweight graphene/polystyrene composite.* Journal of Materials Chemistry, 2012. **22**(36): p. 18772-18774.
138. Bingqing, Y., et al., *Comparison of electromagnetic interference shielding properties between single-wall carbon nanotube and graphene sheet/polyaniline composites.* Journal of Physics D: Applied Physics, 2012. **45**(23): p. 235108.
139. Gupta, T.K., et al., *Multi-walled carbon nanotube-graphene-polyaniline multiphase nanocomposite with superior electromagnetic shielding effectiveness.* Nanoscale, 2014. **6**(2): p. 842-851.
140. Ling, J., et al., *Facile Preparation of Lightweight Microcellular Polyetherimide/Graphene Composite Foams for Electromagnetic Interference Shielding.* ACS Applied Materials & Interfaces, 2013. **5**(7): p. 2677-2684.
141. Wang, Z., J. Luo, and G.L. Zhao, *Dielectric and microwave attenuation properties of graphene nanoplatelet–epoxy composites.* AIP Advances, 2014. **4**(1): p. 017139.
142. Ren, F., et al., *Microwave absorbing properties of graphene nanosheets/ epoxy-cyanate ester resins composites.* Journal of Polymer Research, 2014. **21**(11): p. 585.
143. Joshi, A., et al., *Processing of graphene nanoribbon based hybrid composite for electromagnetic shielding.* Composites Part B: Engineering, 2015. **69**: p. 472-477.
144. Chen, Y., et al., *Magnetic and electrically conductive epoxy/graphene/carbonyl iron nanocomposites for efficient electromagnetic interference shielding.* Composites Science and Technology, 2015. **118**: p. 178-185.
145. Arooj, Y., et al., *Combined effect of graphene oxide and MWCNTs on microwave absorbing performance of epoxy composites.* Polymers for Advanced Technologies, 2015. **26**(6): p. 620-625.
146. Wang, J., et al., *Enhanced microwave absorption performance of lightweight absorber based on reduced graphene oxide and Ag-coated hollow glass spheres/epoxy composite.* Journal of Applied Physics, 2015. **117**(15): p. 154903.
147. Wang, J., et al., *Enhanced microwave absorption properties of epoxy composites reinforced with $Fe_{50}Ni_{50}$-functionalized graphene.* Journal of Alloys and Compounds, 2015. **653**: p. 14-21.
148. Das, S., et al., *Development of FeCoB/Graphene Oxide based microwave absorbing materials for X-Band region.* Journal of Magnetism and Magnetic Materials, 2015. **384**: p. 224-228.

149. Wan, Y.-J., et al., *Tuneable cellular-structured 3D graphene aerogel and its effect on electromagnetic interference shielding performance and mechanical properties of epoxy composites.* RSC Advances, 2016. **6**(61): p. 56589-56598.
150. Wu, J., et al., *Effect of electrophoretic condition on the electromagnetic interference shielding performance of reduced graphene oxide-carbon fiber/epoxy resin composites.* Composites Part B: Engineering, 2016. **105**: p. 167-175.
151. Li, X.-H., et al., *Thermally Annealed Anisotropic Graphene Aerogels and Their Electrically Conductive Epoxy Composites with Excellent Electromagnetic Interference Shielding Efficiencies.* ACS Applied Materials & Interfaces, 2016. **8**(48): p. 33230-33239.
152. Wang, J., et al., *Combined use of lightweight magnetic Fe_3O_4-coated hollow glass spheres and electrically conductive reduced graphene oxide in an epoxy matrix for microwave absorption.* Journal of Magnetism and Magnetic Materials, 2016. **401**: p. 209-216.
153. Kowsari, E. and M. Mohammadi, *Synthesis of reduced and functional graphene oxide with magnetic ionic liquid and its application as an electromagnetic-absorbing coating.* Composites Science and Technology, 2016. **126**: p. 106-114.
154. Zhang, B., et al., *Microwave absorption properties of lightweight absorber based on $Fe_{50}Ni_{50}$-coated poly(acrylonitrile) microspheres and reduced graphene oxide composites.* Journal of Magnetism and Magnetic Materials, 2016. **413**: p. 81-88.
155. Zhang, B., et al., *Fabrication and assessment of a thin flexible surface coating made of pristine graphene for lightning strike protection.* Materials Science and Engineering: B, 2017. **216**: p. 31-40.
156. Bhaskara Rao, B.V., et al., *Single-layer graphene-assembled 3D porous carbon composites with PVA and Fe_3O_4 nano-fillers: an interface-mediated superior dielectric and EMI shielding performance.* Physical Chemistry Chemical Physics, 2015. **17**(28): p. 18353-18363.
157. Lin, J.-H., et al., *Improvement in Mechanical Properties and Electromagnetic Interference Shielding Effectiveness of PVA-Based Composites: Synergistic Effect Between Graphene Nano-Sheets and Multi-Walled Carbon Nanotubes.* Macromolecular Materials and Engineering, 2016. **301**(2): p. 199-211.
158. Wang, T., et al., *Preparation of flexible reduced graphene oxide/poly(vinyl alcohol) film with superior microwave absorption properties.* RSC Advances, 2015. **5**(108): p. 88958-88964.
159. Lin, J.-H., et al., *Polymer composites made of multi-walled carbon nanotubes and graphene nano-sheets: Effects of sandwich structures on their electromagnetic interference shielding effectiveness.* Composites Part B: Engineering, 2016. **89**: p. 424-431.
160. Long, T., et al., *Facile synthesis of Ag-reduced graphene oxide hybrids and their application in electromagnetic interference shielding.* Applied Physics A, 2014. **116**(1): p. 25-32.
161. Bera, R., et al., *Single wall carbon nanohorn (SWCNH)/graphene nanoplate/poly(methyl methacrylate) nanocomposites: a promising material for electromagnetic interference shielding applications.* RSC Advances, 2015. **5**(86): p. 70482-70493.
162. Zhang, X.-J., et al., *Enhanced Microwave Absorption Property of Reduced Graphene Oxide (RGO)-$MnFe_2O_4$ Nanocomposites and Polyvinylidene Fluoride.* ACS Applied Materials & Interfaces, 2014. **6**(10): p. 7471-7478.
163. He, H., et al., *Improved microwave absorption and electromagnetic properties of $BaFe_{12}O_{19}$-poly(vinylidene fluoride) composites by incorporating reduced graphene oxides.* Journal of Applied Physics, 2015. **117**(8): p. 085502.
164. Guo, A.-P., et al., *Excellent Microwave Absorption and Electromagnetic Interference Shielding Based on Reduced Graphene Oxide@MoS_2/Poly(Vinylidene Fluoride) Composites.* ChemPlusChem, 2016. **81**(12): p. 1305-1311.
165. Kumar, P., et al., *An asymmetric electrically conducting self-aligned graphene/polymer composite thin film for efficient electromagnetic interference shielding.* AIP Advances, 2017. **7**(1): p. 015103.

166. Biswas, S., et al., *Absorption-Dominated Electromagnetic Wave Suppressor Derived from Ferrite-Doped Cross-Linked Graphene Framework and Conducting Carbon.* ACS Applied Materials & Interfaces, 2017. **9**(3): p. 3030-3039.
167. Yan, D.-X., et al., *Structured Reduced Graphene Oxide/Polymer Composites for Ultra-Efficient Electromagnetic Interference Shielding.* Advanced Functional Materials, 2015. **25**(4): p. 559-566.
168. Chen, Y., et al., *Enhanced electromagnetic interference shielding efficiency of polystyrene/graphene composites with magnetic Fe_3O_4 nanoparticles.* Carbon, 2015. **82**: p. 67-76.
169. Wu, K., et al., *Largely enhanced electrical properties of polymer composites via the combined effect of volume exclusion and synergy.* RSC Advances, 2016. **6**(57): p. 51900-51907.
170. Singh, A.P., et al., *Encapsulation of [gamma]-Fe_2O_3 decorated reduced graphene oxide in polyaniline core-shell tubes as an exceptional tracker for electromagnetic environmental pollution.* Journal of Materials Chemistry A, 2014. **2**(10): p. 3581-3593.
171. Chen, T., et al., *Enhanced electromagnetic wave absorption properties of polyaniline-coated Fe_3O_4/reduced graphene oxide nanocomposites.* Journal of Materials Science: Materials in Electronics, 2014. **25**(9): p. 3664-3673.
172. Wang, Y., et al., *Facile synthesis of Ni/PANI/RGO composites and their excellent electromagnetic wave absorption properties.* Synthetic Metals, 2015. **210, Part B**: p. 165-170.
173. Mishra, M., et al., *Tunable EMI shielding effectiveness using new exotic carbon: Polymer composites.* Journal of Alloys and Compounds, 2016. **688, Part B**: p. 399-403.
174. Hu, X.-S., et al., *Enhanced electromagnetic interference shielding effectiveness of ternary PANI/CuS/RGO composites.* Journal of Materials Science: Materials in Electronics, 2017: p. 1-8.
175. Kim, S., et al., *Electromagnetic Interference (EMI) Transparent Shielding of Reduced Graphene Oxide (RGO) Interleaved Structure Fabricated by Electrophoretic Deposition.* ACS Applied Materials & Interfaces, 2014. **6**(20): p. 17647-17653.
176. Bai, X., Y. Zhai, and Y. Zhang, *Green Approach To Prepare Graphene-Based Composites with High Microwave Absorption Capacity.* The Journal of Physical Chemistry C, 2011. **115**(23): p. 11673-11677.
177. Liu, H., et al., *Graphene-based composite with microwave absorption property prepared by in situ reduction.* Polymer Composites, 2014. **35**(3): p. 461-467.
178. Kim, M.-S., et al., *Synergistic effects of carbon nanotubes and exfoliated graphite nanoplatelets for electromagnetic interference shielding and soundproofing.* Journal of Applied Polymer Science, 2013. **130**(6): p. 3947-3951.
179. Gupta, A., et al., *Enhanced electromagnetic shielding behaviour of multilayer graphene anchored luminescent TiO_2 in PPY matrix.* Materials Letters, 2015. **158**: p. 167-169.
180. Hummers, W.S. and R.E. Offeman, *Preparation of Graphitic Oxide.* Journal of the American Chemical Society, 1958. **80**(6): p. 1339-1339.
181. Kumar, R.N., et al., *Reducing agent free synthesis of graphene from graphene oxide.* AIP Conference Proceedings, 2013. **1538**(1): p. 262-265.
182. Rotte, N.K., et al., *Equilibrium and kinetics of Safranin O dye adsorption on MgO decked multi-layered graphene.* Chemical Engineering Journal, 2014. **258**: p. 412-419.
183. Brodie, B.C., *On the Atomic Weight of Graphite.* Phil. Trans. R. Soc. Lond. , 1859. **149**: p. 249-259.
184. Gosser, D.K., *Cyclic Voltammetry: Simulation and Analysis of Reaction Mechanisms.* VCH: New York, USA, 1993.
185. Orazem, M.E. and B. Tribollet, *Electrochemical Impedance Spectroscopy.* John Wiley & Sons, Inc.: Hoboken, NJ, USA, 2011.
186. Maiti, S., et al., *Polystyrene/MWCNT/Graphite Nanoplate Nanocomposites: Efficient Electromagnetic Interference Shielding Material through Graphite Nanoplate–MWCNT–*

Graphite Nanoplate Networking. ACS Applied Materials & Interfaces, 2013. **5**(11): p. 4712-4724.

187. Nicolson, A.M. and G.F. Ross, *Measurement of the Intrinsic Properties of Materials by Time-Domain Techniques.* IEEE Transactions on Instrumentation and Measurement, 1970. **19**(4): p. 377-382.
188. Weir, W.B., *Automatic measurement of complex dielectric constant and permeability at microwave frequencies.* Proceedings of the IEEE, 1974. **62**(1): p. 33-36.
189. Petnikota, S., et al., *Elucidation of few layered graphene-complex metal oxide ($A_2Mo_3O_8$, A = Co, Mn and Zn) composites as robust anode materials in Li ion batteries.* Electrochimica Acta, 2015. **178**: p. 699-708.
190. Ferrari, A.C. and D.M. Basko, *Raman spectroscopy as a versatile tool for studying the properties of graphene.* Nat Nano, 2013. **8**(4): p. 235-246.
191. Zhao, J., et al., *Fabrication of Co_3O_4/graphene oxide composites using supercritical fluid and their catalytic application for the decomposition of ammonium perchlorate.* CrystEngComm, 2014. **16**(10): p. 2001-2008.
192. Soriano, L., et al., *Oxidation State and Size Effects in CoO Nanoparticles.* The Journal of Physical Chemistry B, 1999. **103**(32): p. 6676-6679.
193. Ji, W., et al., *Partially nitrided molybdenum trioxide with promoted performance as an anode material for lithium-ion batteries.* Journal of Materials Chemistry A, 2014. **2**(3): p. 699-704.
194. Zhou, L.-N., et al., *Monolayer of close-packed Pt nanocrystals on a reduced graphene oxide (RGO) nanosheet and its enhanced catalytic performance towards methanol electrooxidation.* RSC Advances, 2015. **5**(57): p. 46017-46025.
195. Reddy, M.V., et al., *Energy Storage Studies on $InVO_4$ as High Performance Anode Material for Li-Ion Batteries.* ACS Applied Materials & Interfaces, 2013. **5**(16): p. 7777-7785.
196. Reddy, M.V., et al., *Mixed Oxides, $(Ni_{1-x}Zn_x)Fe_2O_4$ (x = 0, 0.25, 0.5, 0.75, 1): Molten Salt Synthesis, Characterization and Its Lithium-Storage Performance for Lithium Ion Batteries.* The Journal of Physical Chemistry C, 2015. **119**(9): p. 4709-4718.
197. Reddy, M.V., et al., *Li-Cycling Properties of Molten Salt Method Prepared Nano/Submicrometer and Micrometer-Sized CuO for Lithium Batteries.* ACS Applied Materials & Interfaces, 2013. **5**(10): p. 4361-4366.
198. Xia, J., et al., *Construction of $Cu_3Mo_2O_9$ nanoplates with excellent lithium storage properties based on a pH-dependent dimensional change.* Dalton Transactions, 2015. **44**(30): p. 13450-13454.
199. Reddy, M.V., G.V. Subba Rao, and B.V.R. Chowdari, *Long-term cycling studies on 4 V-cathode, lithium vanadium fluorophosphate.* Journal of Power Sources, 2010. **195**(17): p. 5768-5774.
200. Seng, K.H., et al., *Catalytic Role of Ge in Highly Reversible GeO_2/Ge/C Nanocomposite Anode Material for Lithium Batteries.* Nano Letters, 2013. **13**(3): p. 1230-1236.
201. Wang, C., et al., *N/P-Codoped Thermally Reduced Graphene for High-Performance Supercapacitor Applications.* The Journal of Physical Chemistry C, 2013. **117**(29): p. 14912-14919.
202. Liu, X.H., et al., *Reversible Nanopore Formation in Ge Nanowires during Lithiation–Delithiation Cycling: An In Situ Transmission Electron Microscopy Study.* Nano Letters, 2011. **11**(9): p. 3991-3997.
203. Li, D., et al., *A unique sandwich-structured C/Ge/graphene nanocomposite as an anode material for high power lithium ion batteries.* Journal of Materials Chemistry A, 2013. **1**(45): p. 14115-14121.
204. Ganguly, A., et al., *Probing the Thermal Deoxygenation of Graphene Oxide Using High-Resolution In Situ X-ray-Based Spectroscopies.* The Journal of Physical Chemistry C, 2011. **115**(34): p. 17009-17019.
205. An, S.J., et al., *The state of understanding of the lithium-ion-battery graphite solid electrolyte interphase (SEI) and its relationship to formation cycling.* Carbon, 2016. **105**: p. 52-76.

206. Tang, W., et al., *Probing Lithium Germanide Phase Evolution and Structural Change in a Germanium-in-Carbon Nanotube Energy Storage System.* Journal of the American Chemical Society, 2015. **137**(7): p. 2600-2607.
207. Petnikota, S., et al., *Graphenothermal reduction synthesis of 'exfoliated graphene oxide/iron (II) oxide' composite for anode application in lithium ion batteries.* Journal of Power Sources, 2015. **293**: p. 253-263.
208. Petnikota, S., et al., *Exfoliated Graphene Oxide/MoO_2 Composites as Anode Materials in Lithium-Ion Batteries: An Insight into Intercalation of Li and Conversion Mechanism of MoO_2.* ACS Applied Materials & Interfaces, 2016. **8**(17): p. 10884-10896.
209. Cui, G., et al., *A Germanium–Carbon Nanocomposite Material for Lithium Batteries.* Advanced Materials, 2008. **20**(16): p. 3079-3083.
210. Ferrari, A.C., et al., *Raman Spectrum of Graphene and Graphene Layers.* Physical Review Letters, 2006. **97**(18): p. 187401.
211. Hong, P.-D., J.-H. Chen, and H.-L. Wu, *Solvent effect on structural change of poly(vinyl alcohol) physical gels.* Journal of Applied Polymer Science, 1998. **69**(12): p. 2477-2486.
212. Yan, Z., et al., *Toward the Synthesis of Wafer-Scale Single-Crystal Graphene on Copper Foils.* ACS Nano, 2012. **6**(10): p. 9110-9117.
213. Huang, P.Y., et al., *Grains and grain boundaries in single-layer graphene atomic patchwork quilts.* Nature, 2011. **469**(7330): p. 389-392.
214. Krimm, S., C.Y. Liang, and G.B.B.M. Sutherland, *Infrared spectra of high polymers. V. Polyvinyl alcohol.* Journal of Polymer Science, 1956. **22**(101): p. 227-247.
215. Pritchard, J.G., *Poly (vinyl alcohol): Basic Properties and Uses.* Gordan and Breach, London, 1970: p. 17-30.
216. Cooney, T.F., et al., *Raman spectral study of solid and dissolved poly(vinyl alcohol) and ethylene-vinyl alcohol copolymer.* Journal of Polymer Science Part B: Polymer Physics, 1994. **32**(7): p. 1163-1174.
217. Hodkiewicz, J., *Characterizing Graphene with Raman Spectroscopy.* Thermo Fisher Scientific, Application note 51946, Madison, WI, USA.
218. Awnish, K.G., et al., *Curvature-induced D-band Raman scattering in folded graphene.* Journal of Physics: Condensed Matter, 2010. **22**(33): p. 334205.
219. Graf, D., et al., *Spatially Resolved Raman Spectroscopy of Single- and Few-Layer Graphene.* Nano Letters, 2007. **7**(2): p. 238-242.
220. Das, A., B. Chakraborty, and A.K. Sood, *Raman spectroscopy of graphene on different substrates and influence of defects.* Bulletin of Materials Science, 2008. **31**(3): p. 579-584.
221. Zhang, W., et al., *A Strategy for Producing Pure Single-Layer Graphene Sheets Based on a Confined Self-Assembly Approach.* Angewandte Chemie International Edition, 2009. **48**(32): p. 5864-5868.
222. Yan, J., et al., *Electric Field Effect Tuning of Electron-Phonon Coupling in Graphene.* Physical Review Letters, 2007. **98**(16): p. 166802.
223. DasA, et al., *Monitoring dopants by Raman scattering in an electrochemically top-gated graphene transistor.* Nat Nano, 2008. **3**(4): p. 210-215.
224. Pisana, S., et al., *Breakdown of the adiabatic Born-Oppenheimer approximation in graphene.* Nat Mater, 2007. **6**(3): p. 198-201.
225. Peres, N.M.R., F. Guinea, and A.H. Castro Neto, *Electronic properties of disordered two-dimensional carbon.* Physical Review B, 2006. **73**(12): p. 125411.
226. Belavin, V.V., A.V. Okotrub, and L.G. Bulusheva, *A study of the influence of structural imperfection on the electronic structure of carbon nanotubes by x-ray spectroscopy and quantum-chemical methods.* Physics of the Solid State, 2002. **44**(4): p. 663-665.
227. Wang, C., et al., *The electromagnetic property of chemically reduced graphene oxide and its application as microwave absorbing material.* Applied Physics Letters, 2011. **98**(7): p. 072906.

228. Yang, Y., et al., *Novel Carbon Nanotube−Polystyrene Foam Composites for Electromagnetic Interference Shielding.* Nano Letters, 2005. **5**(11): p. 2131-2134.
229. Kim, H.M., et al., *Electrical conductivity and electromagnetic interference shielding of multiwalled carbon nanotube composites containing Fe catalyst.* Applied Physics Letters, 2004. **84**(4): p. 589-591.
230. Yang, Y., et al., *Conductive Carbon Nanofiber–Polymer Foam Structures.* Advanced Materials, 2005. **17**(16): p. 1999-2003.
231. Sato, T. and T. Okaya, *Characterization and Physical Properties of Low Molecular Weight Poly(vinyl acetate) and Poly(vinyl alcohol).* Polym J, 1992. **24**(9): p. 849-856.
232. Senthil, V., et al., *Relaxation and conduction mechanism of PVA: BYZT polymer composites by impedance spectroscopy.* Journal of Polymer Research, 2012. **19**(3): p. 9838.
233. Psarras, G.C., E. Manolakaki, and G.M. Tsangaris, *Electrical relaxations in polymeric particulate composites of epoxy resin and metal particles.* Composites Part A: Applied Science and Manufacturing, 2002. **33**(3): p. 375-384.
234. Psarras, G.C., *Hopping conductivity in polymer matrix–metal particles composites.* Composites Part A: Applied Science and Manufacturing, 2006. **37**(10): p. 1545-1553.
235. Psarras, G.C., E. Manolakaki, and G.M. Tsangaris, *Dielectric dispersion and ac conductivity in—Iron particles loaded—polymer composites.* Composites Part A: Applied Science and Manufacturing, 2003. **34**(12): p. 1187-1198.
236. Jiang, G., et al., *Solution-processed high-k magnesium oxide dielectrics for low-voltage oxide thin-film transistors.* Applied Physics Letters, 2016. **109**(18): p. 183508.
237. Al-Saleh, M.H. and U. Sundararaj, *Electromagnetic interference shielding mechanisms of CNT/polymer composites.* Carbon, 2009. **47**(7): p. 1738-1746.
238. Petnikota, S., et al., *MgO-Decorated Few-Layered Graphene as an Anode for Li-Ion Batteries.* ACS Applied Materials & Interfaces, 2015. **7**(4): p. 2301-2309.
239. DAS, B.K., *Studies on Metal Oxides and Cobalt Nitride as prospective Anodes for Lithium ion batteries*, in *PHYSICS* 2010, National University of Singapore: Singapore. p. 261.
240. Han, P., et al., *Graphene decorated with molybdenum dioxide nanoparticles for use in high energy lithium ion capacitors with an organic electrolyte.* Journal of Materials Chemistry A, 2013. **1**(19): p. 5949-5954.

Annexures

Annexure 1

Figure A1 shows the morphology of the FLG-$Co_2Mo_3O_8$ composite. Secondary electron (SE) micrographs of FLG-$Co_2Mo_3O_8$ composite powder are shown in **Fig. A1(a**, **b)**. The micrograph depicts ~65 nm thick hexagonal shaped sub-micron sized particles that are stacked on one another to form a group of particles. This arrangement left gaps between such neighboring groups. **Figure A1(c)** shows the bright field transmission electron micrograph of FLG-$Co_2Mo_3O_8$ composite platelets. High-resolution transmission electron micrograph (**Figure A1(d)**) confirmed that the sample contains crystalline $Co_2Mo_3O_8$ particles wrapped by FLG. The FLG sheets in FLG-$Co_2Mo_3O_8$ composite are not discernable in **Fig. A1(b)**. However, they are clearly observed in the bright field and high-resolution transmission electron micrographs (**Fig. A1(c**, **d)**).

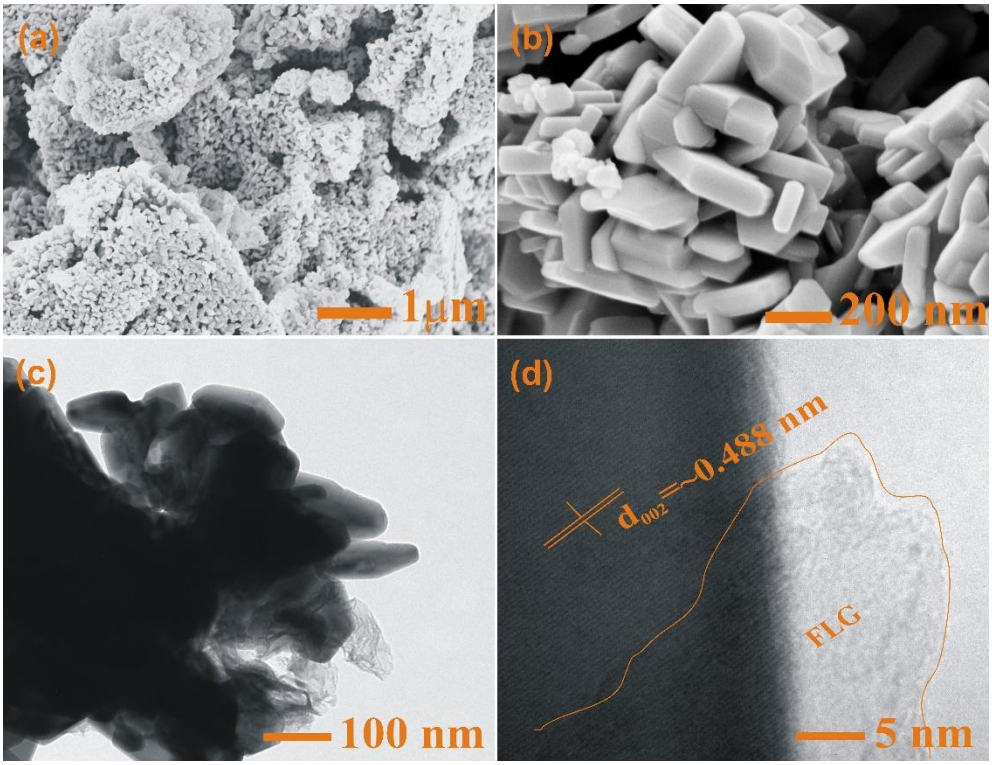

Figure A1. (a, **b)** Secondary electron micrographs of FLG-$Co_2Mo_3O_8$ composite; **(c**, **d)** bright field transmission electron micrograph and high-resolution transmission electron micrograph of FLG-$Co_2Mo_3O_8$ composite.

X-ray diffractogram of FLG-Co2Mo3O8 composite (shown in **Fig. A2 (a)**) is matched with JCPDS data file number #34-0511, respectively. The strong characteristic diffraction peak of graphene (002) at 26.5° and a broad second order diffraction peak (004) at 53.6° are observed

in the composite. This observation is an evidence for the presence of FLG in the composite. It is clear from the observations presented till now that in the composite, FLG sheets are coated densely with mixed metal oxides. Intense and narrow (002) and (004) diffraction peaks result from a combination of FLG and crystalline monoclinic MoO_2 (# JCPDS 76-1807, where (011) and (022) diffraction peaks of MoO_2 also contribute) impurity. It is speculated that presence of minor MoO_2 impurity (in the composite) is due to the fraction of incomplete reaction. Further, Raman spectrum in **Fig. A2(b)** shows D (~1360 cm^{-1}), G (~1599 cm^{-1}) and very weak and broadened 2D (~2700 cm^{-1}) bands which confirm the presence of FLG [210] in the composite. The D-band's high intensity is due to the presence of many defects in the material resulted due to annealing and the presence of complex MO. High intensity of G-band than D-band indicates the presence of more number of regular carbon hexagons which interns imply that FLG of good quality [190]. For crystalline $Co_2Mo_3O_8$ (space group, $P6_3mc$), a maximum of 15 Raman active modes ($3A_1+6E_1+6E_2$) are allowed [130]. Raman spectrum of FLG-$Co_2Mo_3O_8$ composite shows 13 peaks among which 11 of the expected 15 Raman modes correspond to $Co_2Mo_3O_8$. Based on the available literature [16], the bands at 360 and 435 cm^{-1} are assigned to (O-(Mo-Mo)$_{cluster}$-O) and (Mo-O-Mo) bending vibrations, respectively [130]. The peaks at and below 326 cm^{-1} are assigned to Co-O bending vibrations of the CoO_4-tetrahedra and CoO_6-octahedra in the structure. Other higher order combinational modes are also observed at 726, 809 and 928 cm^{-1}. The measured BET surface area, pore size, and pore volume pertaining to FLG-$Co_2Mo_3O_8$ composite are 14.42 m^2/g, 9 nm, and 0.0319 cm^3/g, respectively. N_2 adsorption and desorption isotherms pertaining to the composites are shown in **Figure A2(c)**. The Isotherms (**Figure A2(c)**) resemble the type IV isotherm of IUPAC standard adsorption-desorption isotherms. The measured pore size value categorizes the composite into mesoporous materials. This is owing to the enhanced particle size and agglomeration of particles in the case of higher atomic number elements which in turn leads to the decrease in surface area of the corresponding composite. The low specific surface area is also owing (to the high annealing temperature which leads) to the densely packed hexagonal crystal system of the major $Co_2Mo_3O_8$ phase in the composite. Further, the thermal stability of FLG-$Co_2Mo_3O_8$ composite is carried out in air ambiance, in the temperature range of 50-1000 °C and at a heating rate of 10 °C/min in order to evaluate the amount of FLG present in the composite. As shown in **Fig. A2(d)** the composite showed weight gain between 400 and 600 °C which corresponds to oxidation of $Co_2Mo_3O_8$ composite [4]. The net weight loss found between 200 and 800 °C corresponds to the decomposition of FLG [238]. The calculated amount of FLG in FLG-$Co_2Mo_3O_8$ composite is 17.23 wt.%.

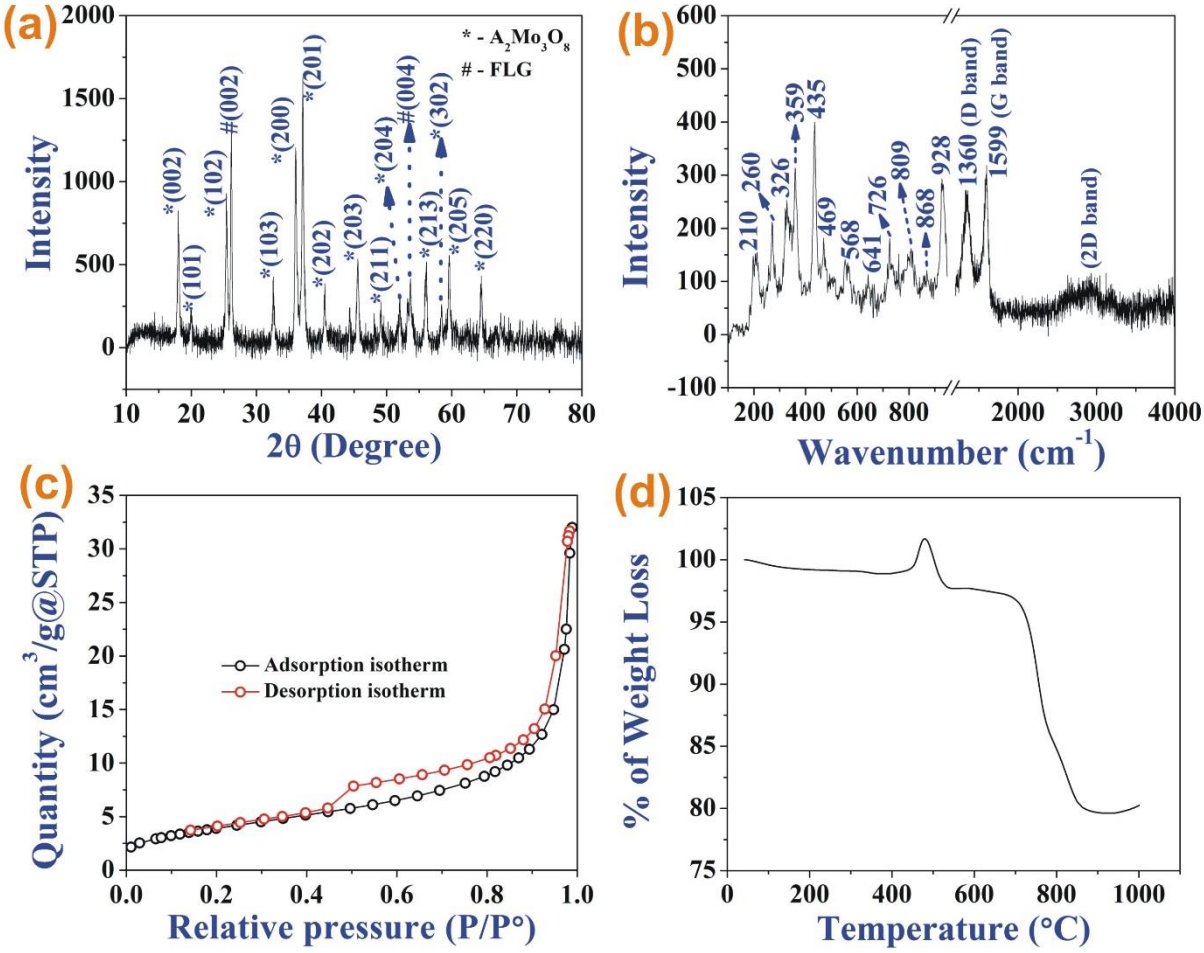

Figure A2. (a) X-ray diffractogram, **(b)** Raman spectrum, **(c)** N_2 adsorption and desorption isotherms and **(d)** weight loss versus temperature (TGA) curve of FLG-$Co_2Mo_3O_8$ composite, respectively.

The voltage versus capacity profiles of the FLG-$Co_2Mo_3O_8$ composite at 60 mA/g current density is shown in **Fig. A3(b)**. It is observed that the first discharging curve is steeper starting from the open circuit voltage (OCV ~2.61 V) with a negligible change in slope up to 1.5 V. Thereafter slope changed continuously until 0.005 V. Change in slope is noticed at 1.25, 0.9 and 0.7 V and a continuous plateau is observed beyond 0.5 V which is in good agreement with CV results shown in **Fig. A3(a)**. The typical slope change between 0.9-0.7 V is attributed to the irreversible reaction between Li^+ and FLG-$Co_2Mo_3O_8$ and initial electrolyte decomposition which leads to the formation of solid electrolyte interphase (SEI) [94, 131]. The first charging curve is steeper up to 1.25 V and thereafter there is a change in slope while a second change is noticed around 1.75 V which continued until the voltage became 2.0 V from which point the charging curve once again became steeper up to a final voltage of 3.0 V with negligible changes in slope. This is again consistent with CV results. The subsequent cycles showed similar

features as that of the first cycle except for a slight decrease in capacity value as the cycle number increased.

The first cycle total discharging and charging capacities of the FLG-$Co_2Mo_3O_8$ composite are 1355 and 907 mA h/g, respectively. These values are greater than the corresponding values pertaining to pure $Co_2Mo_3O_8$ as reported in a previous work [131]. This is expected due to the good interaction between two-dimensional (2D)-$Co_2Mo_3O_8$ and FLG (as observed in **Fig. A1(d)**) and the presence of FLG which facilitates a conducting network for the electrolyte to get absorbed throughout the composite which in turn enhances Li-ion transportation in the composite. The capacity values at different current densities are tabulated in **Table A1**. The net difference (~448 mA h/g) between first discharge and charge is considered as an irreversible capacity loss (ICL) that normally originates from SEI formation in which Li is irreversibly trapped at the anode owing to the formation of covalent compounds [94, 131]. ICL values at current rates of 60, 90 and 180 mA/g are found to be 448, 402 and 330 mA h/g, respectively whilst Coulombic efficiencies (QEs) are more than 67% at all the considered current densities. FLG-$Co_2Mo_3O_8$ composite has shown excellent cycling behavior. QEs fluctuated around 98% up to 50 cycles as shown in **Fig. A3(c)** while the capacity retentions at the end of the tests are found to be greater than 85%.

The CV characteristics of FLG-$Co_2Mo_3O_8$ during both cathodic and anodic scans are shown in **Fig. A3(b)** for the first six cycles. In the 1st cathodic scan two main reduction current peaks are observed, a small peak around 0.7 V and a broad peak between 0.5 to 0.005V with increasing current. From 2nd cycle onwards these peaks are centered at 0.68 and 0.15V with constant reduction currents which correspond to Li intercalation into both FLG and $Co_2Mo_3O_8$ which are active to take Li in this voltage range [131]. The large current difference between 1st and 2nd scans and peak shift towards lower voltages are attributed to SEI formation as well as electrode formation effect [94, 131, 199]. Another two new reduction peaks at 1.25 and 1.53V (which were feebly visible during the 1st cathodic scan) became prominent. Evolution of these peaks might be originated from MoO_2 formed during 1st cycle through crystal structure destruction of $Co_2Mo_3O_8$ during Li insertion (1st reduction) that eventually leads to formation of metal nanoparticles in amorphous Li_2O phase (during 1st discharge) and conversion of these metal nanoparticles to metal oxides (during 1st charging) according to **Equation A1** (after 1st discharge) [131].There are the only two peaks observed at 1.45 and 1.76 V in the case of $Co_2Mo_3O_8$ during the first anodic scan wherein the current decreased up to 3rd scan and then became constant in later scans with a slight shift in the peak position towards higher potential.

The redox couples at 1.53/1.76 and 1.25/1.45 V correspond to phase transition of MoO_2 due to partial lithiated Li_xMoO_2 phase from monoclinic phase to orthorhombic phase and from orthorhombic phase to monoclinic phase during Li insertion and extraction process, respectively [239, 240]. The constant area under these redox curves is in tune with stable cyclability whereas a decrease in current of oxidation peaks indicates slightly capacity fading as observed in GC results while the overall CV features of FLG-$Co_2Mo_3O_8$ are consistent with GC results.

$$Co_2Mo_3O_8 + 16Li^+ + 16e^- \rightarrow 2Co^0 + 3Mo^0 + 8Li_2O \qquad (A1)$$

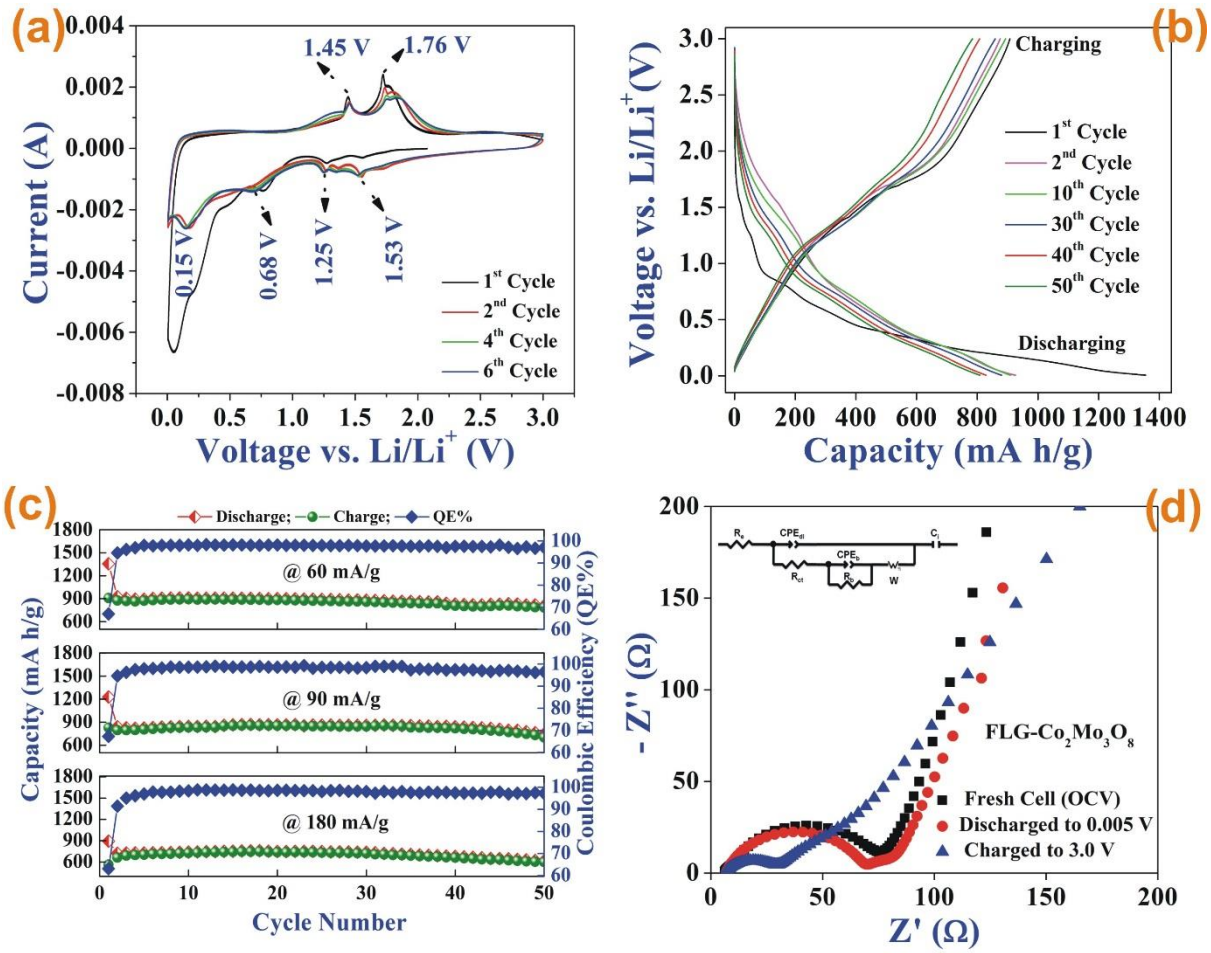

Figure A3. (a) Cyclic voltammetry curves at different cycles at a scan rate of 58 μV/s, **(b)** Galvanostatic discharge and charge curves at different cycles at a current density of 60 mA/g, (c) Capacity vs cycle number and Couloumbic efficiency vs cycle number, and (d) EIS curves of FLG-$Co_2Mo_3O_8$ composite at different charge states (black, red and blue color circles represent OCV, 1st discharge, and 1st charge states, respectively and inset shows equivalent circuit molded) and all these curves are obtained in the voltage range 0.005-3.0 V vs. Li.

Table A1 Specific capacity (mA h/g) of FLG-$Co_2Mo_3O_8$ composite at different current rates and different discharging and charging cycles.

	Current Rate								
	60 (mA/g)			**90 (mA/g)**			**180 (mA/g)**		
Composite	**1D**	**1C**	**QE%**	**1D**	**1C**	**QE%**	**1D**	**1C**	**QE%**
FLG-$Co_2Mo_3O_8$	1355	907	67	1229	827	67	895	599	67
	50D	**50C**	**QE%**	**50D**	**50C**	**QE%**	**50D**	**50C**	**QE%**
FLG−$Co_2Mo_3O_8$	808	785	97	762	733	97	622	607	98

D-Discharge cycle, C-Charge cycle, QE%-Coulombic efficiency

EIS results of FLG-$Co_2Mo_3O_8$ composite is plotted as Nyquist plot and their corresponding equivalent circuit is shown in **Fig. A3(d)**. The impedance data of FLG-$Co_2Mo_3O_8$ is best fitted into an equivalent circuit shown in the inset of **Fig. A3(d)**. The contact (solvent) resistance R_e [195] of the composite is found in between 5.9 and 6.2 Ω as shown in **Table A2**. The resistance to charge transfer Rct [195] values of FLG-$Co_2Mo_3O_8$ composite showed a decreasing tendency when discharged and charged as shown in **Table A2**. The double layer capacitance CPE_{dl} [195] value of FLG-$Co_2Mo_3O_8$ is found to first decrease when discharged and increase when charged. There are two additional circuit elements that represent bulk resistance R_b [195] is decreased mode and the corresponding double layer capacitance CPE_b [195] is continuously increased from OCV. The intercalation capacity C_i [195] is found very small while Warburg element W_s (resistance to Li-ion diffusion) is found relatively very high when compared to R_e and R_{ct}. The relatively very low R_{ct} value during charging signifies easy removal of Li ions that aided in bagging high reversible capacities. The very low value of C_i indicates that Li storage preferably takes place either by redox couples of Mo-clusters or electrochemical adsorption by FLG. The explanation about other two composites (i.e., FLG-$Mn_2Mo_3O_8$ and FLG-$Zn_2Mo_3O_8$ composites) in this work can be found in the reference **Electrochimica Acta 178 (2015) 699–708**.

Table A2 EIS results of the FLG-$Co_2Mo_3O_8$ composite at OCV, discharged and charged states.

Composite	R_e	R_{ct}	CPE_{dl} (μF)	R_b	CPE_b (mF)	C_i (F)
FLG-$Co_2Mo_3O_8$ Fresh cell	5.9±0.09	9.9±0.2	18.9±0.4	58.5±0.03	0.19	0.009
FLG-$Co_2Mo_3O_8$ Discharged state	6.2±0.01	5.1±0.1	8.9±0.3	54.1±0.1	0.23	0.428
FLG-$Co_2Mo_3O_8$ Charged state	6.2±0.02	4.8±0.5	83±1.8	30.8±0.4	26	0.095

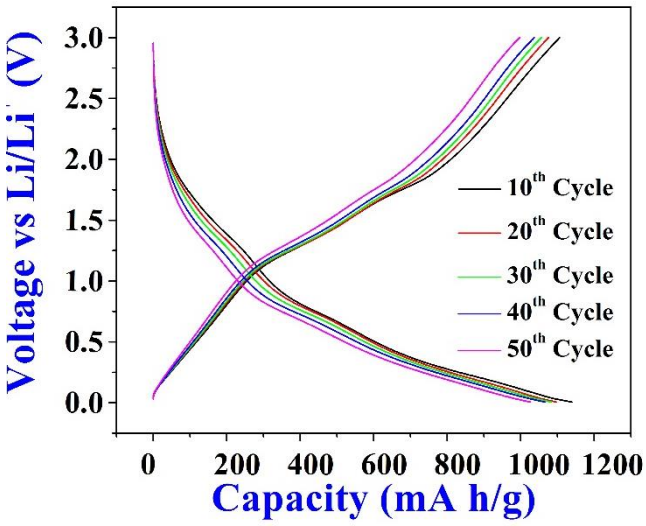

Figure A4. Galvanostatic discharge and charge curves of $Co_2Mo_3O_8$/rGO composite at 10th, 20th, 30th, 40th and 50th cycles in the voltage range of 0.005-3.0 V and at 60 mA/g current density.

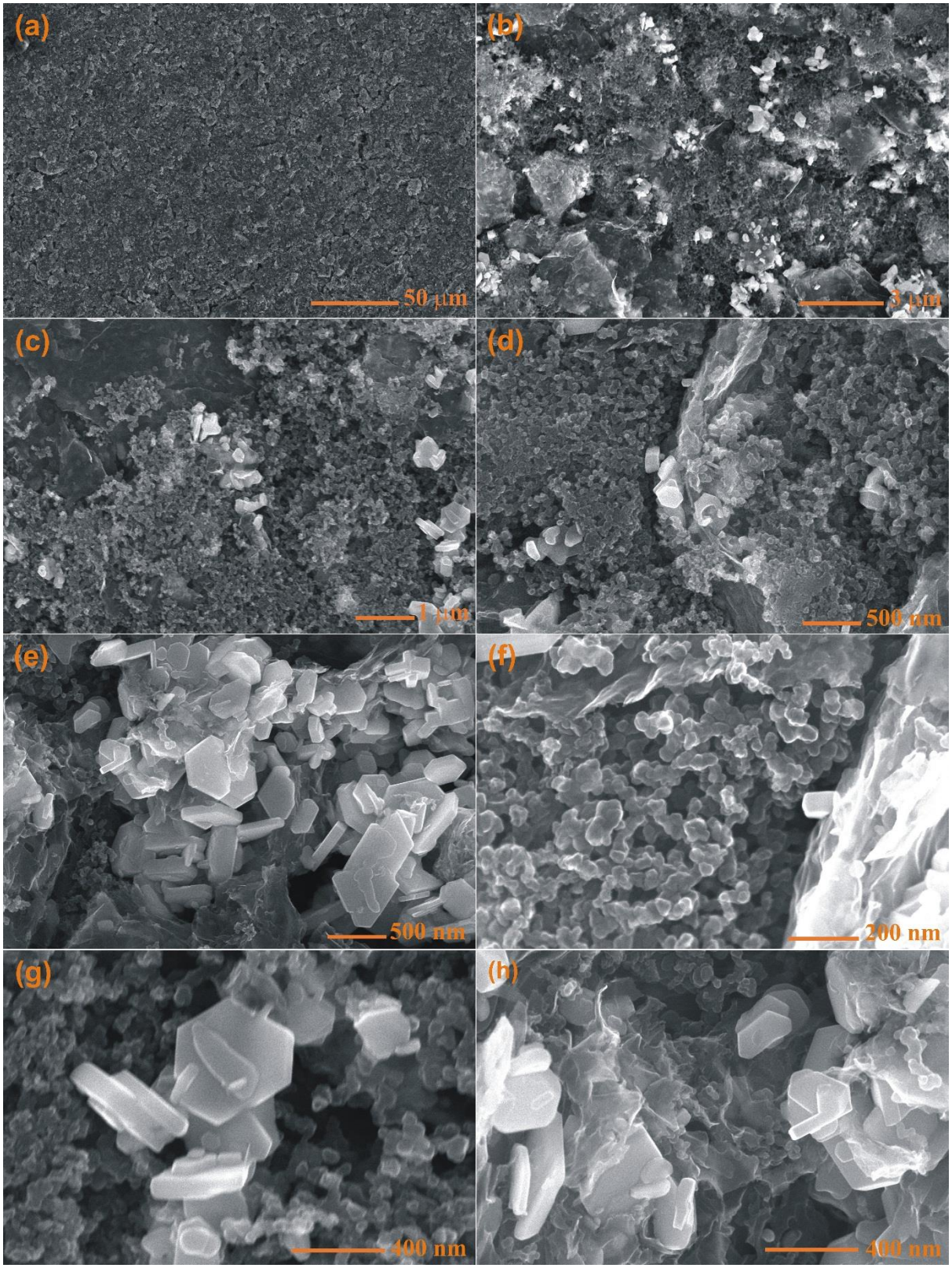

Figure A5. Field emission scanning electron microscope images of $Co_2Mo_3O_8$/rGO composite electrode at different magnifications.

Annexure 2

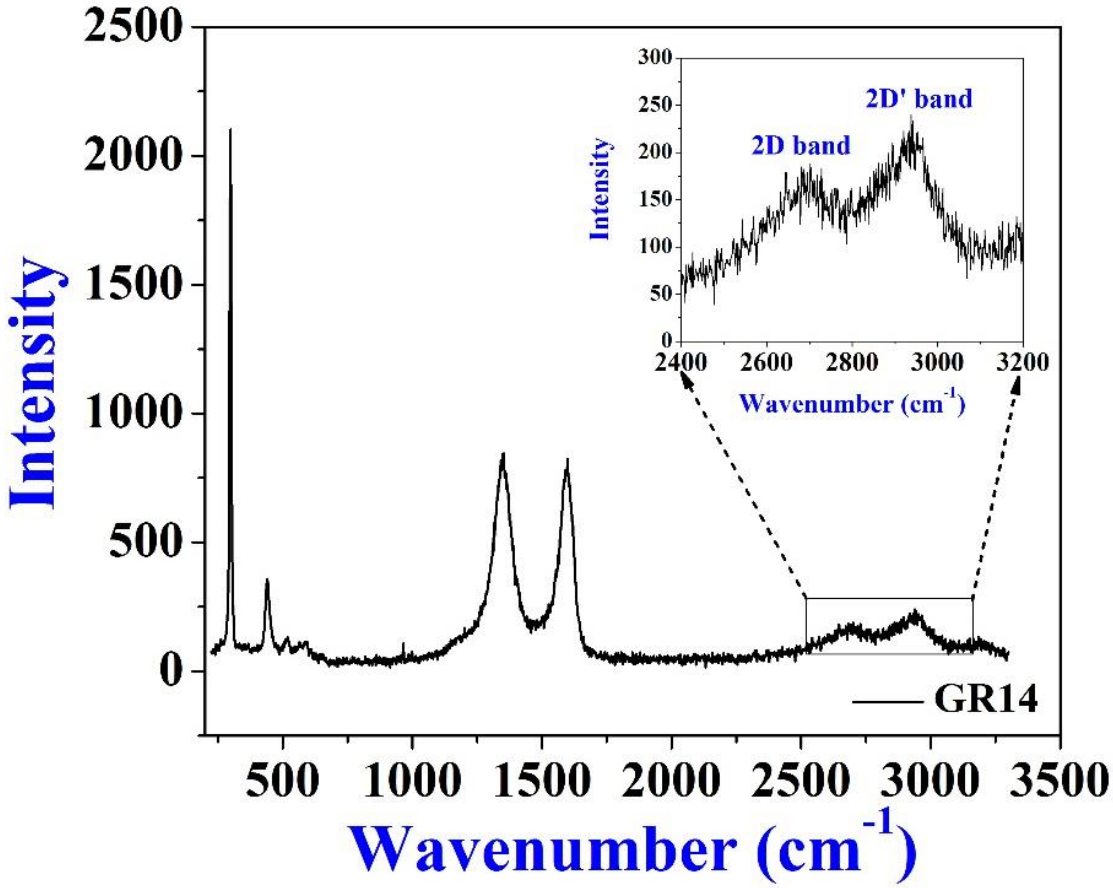

Figure A6. Raman spectrum of GR14 composite and inset shows 2D and 2D′ bands.

Galvanostatic cycling curves shown in **Fig. A7** represent continuous capacity degradation up to 30th cycle and later it increased up to 100th cycle. This kind of behavior is attributed to the electrode activation effect in which initial cycles (here 30 cycles) are utilized for the spread of electrolyte in the electrode and formation of SEI layer and consequently development and release of stresses in the electrode.

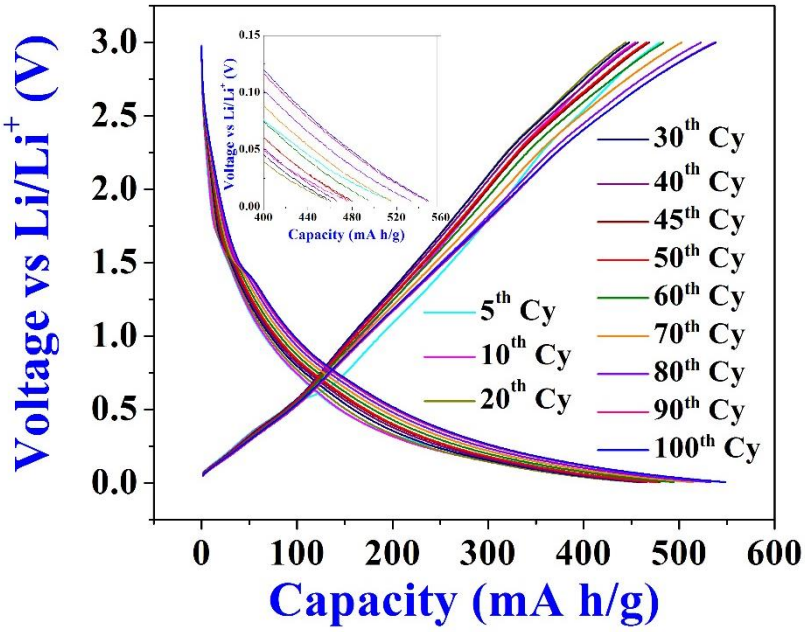

Figure A7. Voltage vs. Capacity profiles of the GR14 composite at 160 mA/g current density, in the voltage range of 0.005-3.0 V, and at different cycles (Inset represents zoomed in portion of the discharge curves).

Table A3. Rietveld refinement data of GR14-Raw composite at different temperatures.

System	Phase	Sp. Gr	R.P.	GeO_2	GR14_Raw	GR14_550°C	GR14_680°C	GR14_800°C	GR14_850°C	GR14_900 °C
GeO_2	Hexagonal	P3221	R_{wp}	30.311	2.644	16.082	0.590	47.704	-	-
			R_B	3.731	2.953	0.684	1.386	0.768	-	-
			a(Å)	4.9873928	3.6787732	4.9755856	4.9616763	4.9834740	-	-
			c(Å)	5.6481235	6.0416610	5.6512439	5.6200730	5.6379690	-	-
			C.S.L. (nm)	71.5	10000.0	115.4	50.4	10000.0	-	-
		P3121	R_{wp}	50.592	95.761	83.836	96.106	52.221	42.813	-
			R_B	2.989	0.274	0.776	0.842	0.970	2.138	-
			a(Å)	4.5600254	4.9482889	3.9625382	3.8665683	5.0784146	5.0227988	-
			c(Å)	5.2683996	5.6374936	5.3160224	5.0925547	5.6954194	5.4517928	-
			C.S.L. (nm)	4.7	124.9	2.8	3.1	2.7	15.3	-
	Tetragonal	P41212	R_{wp}	19.097	-	-	-	-	-	-
			R_B	2.143	-	-	-	-	-	-
			a(Å)	4.9605898	-	-	-	-	-	-
			c(Å)	6.8551680	-	-	-	-	-	-
			C.S.L. (nm)	123.9	-	-	-	-	-	-
Ge	Cubic	Fd-3m	R_{wp}	-	1.595	0.082	3.304	0.075	57.187	100
			R_B	-	2.272	2.531	0.117	0.723	4.498	0.418
			a(Å)	-	5.4224602	5.7352319	5.8017401	5.6728782	5.6589842	5.7888329
			C.S.L. (nm)	-	436.5	86.6	252.6	10000.0	71.5	3.7
			GoF	3.85	2.93	1.84	1.82	1.58	2.44	2.35

Sp. Gr.-space group, **R.P.**-refinement parameters**,** R_w- Wt% - Rietveld, R_B- R-Bragg, **C.S.L.**- Crystallite size Lorentzian and **a(Å)**, **b(Å)**-lattice constants